

NATIONAL AERONAUTICS AND SPACE ADMINISTRATION

Space Programs Summary 37-45, Vol. III

The Deep Space Network

For the Period March 1 to April 30, 1967

GPO PRICE \$ _____

CFSTI PRICE(S) \$ _____

Hard copy (HC) 3.00

Microfiche (MF) .65

ff 653 July 65

FACILITY FORM 602

~~N67-30228~~ N67-30376
(ACCESSION NUMBER) (THRU)
10/19/67
(PAGES) (CODE)
CR 85298-P
(NASA CR OR TMX OR AD NUMBER) (CATEGORY)

JET PROPULSION LABORATORY
CALIFORNIA INSTITUTE OF TECHNOLOGY
PASADENA, CALIFORNIA

May 31, 1967

NATIONAL AERONAUTICS AND SPACE ADMINISTRATION

3 Space Programs Summary ^{NO.} 37-45, Vol. ^{une} III

The Deep Space Network

For the Period March 1 to April 30, 1967. 2#

29B. JPL-SPS-37-45, Vol. III 1#

1 JET PROPULSION LABORATORY
CALIFORNIA INSTITUTE OF TECHNOLOGY
PASADENA, CALIFORNIA 3

9 May 31, 1967 10CN

SPACE PROGRAMS SUMMARY 37-45, VOL. III

Copyright © 1967
Jet Propulsion Laboratory
California Institute of Technology

Prepared Under Contract No. NAS 7-100
National Aeronautics & Space Administration

25
29A CV

PRECEDING PAGE BLANK NOT FILMED

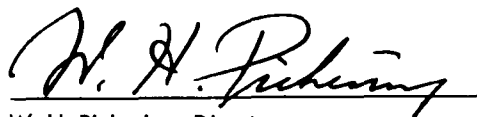
Preface

The Space Programs Summary is a six-volume bimonthly publication designed to report on JPL space exploration programs and related supporting research and advanced development projects. The titles of all volumes of the Space Programs Summary are:

- Vol. I. *The Lunar Program* (Confidential)
- Vol. II. *The Planetary-Interplanetary Program* (Confidential)
- Vol. III. *The Deep Space Network* (Unclassified)
- Vol. IV. *Supporting Research and Advanced Development* (Unclassified)
- Vol. V. *Supporting Research and Advanced Development* (Confidential)
- Vol. VI. *Space Exploration Programs and Space Sciences* (Unclassified)

The Space Programs Summary, Vol. VI, consists of: an unclassified digest of appropriate material from Vols. I, II, and III; an original presentation of the JPL quality assurance and reliability efforts, and the environmental- and dynamic-testing facility-development activities; and a reprint of the space science instrumentation studies of Vols. I and II.

Approved by:



W. H. Pickering, Director

Jet Propulsion Laboratory

PRECEDING PAGE BLANK NOT FILMED

Contents

I. Introduction	1	✓
II. Tracking and Navigational Accuracy Analysis	3	✓
A. DSN Inherent Accuracy Project		
<i>T. W. Hamilton and D. W. Trask</i>	3	
B. Satellite Orbit Determination Accuracy Study Applicable to Voyager Trajectories		
<i>R. K. Russell</i>	3	
C. Polar Motion and DSN Station Locations		
<i>P. M. Muller</i>	10	
D. Theoretical Basis for the Double Precision Orbit Determination Program: VIII. Regression Partial Derivatives		
<i>T. D. Moyer</i>	14	
E. Lunar Orbiter D — Slant Range Rates and Accelerations		
<i>R. A. Wallace</i>	23	
References	31	
III. Communications Research and Development	32	✓
A. Demonstration of Error Detection for DSN Teletype		
<i>H. M. Fredricksen and E. C. Posner</i>	32	
B. Frequency Generation and Control: Phase Modulator for Testing Phase-Lock Loops of the Frequency Agile Receiver		
<i>G. Lutes</i>	36	
C. Frequency Generation and Control: Hydrogen Maser Frequency Standard		
<i>W. Higa</i>	39	
D. Low Noise Receivers: Microwave Maser Development, Block II Traveling Wave Maser		
<i>R. Clauss</i>	40	
E. Efficient Antenna Systems: X-Band Gain Measurements		
<i>D. A. Bathker and B. L. Seidel</i>	42	
F. Multi-feed Cone System for the Advanced Antenna Systems		
<i>G. S. Levy and S. M. Katow</i>	48	
G. Multi-mission Telemetry Demodulator Project		
<i>R. Petrie and J. Layland</i>	51	
References	58	
Erratum	58	
IV. Communications Development Engineering	59	✓
A. Ultra-Stable Oscillators: 24-MHz Low-Noise VCO Development		
<i>A. Kirk</i>	59	

Contents (contd)

B. Improved Calibration Techniques: X-Band Cone Built-in Reflectometer System	
<i>C. T. Stelzried and T. Y. Otoshi</i>	62
C. Experimental Modification of a Cassegrain Cone Assembly to Reduce System Noise Temperature	
<i>R. W. Hartop</i>	65
D. High-Power Transmitter Development	
<i>E. J. Finnegan</i>	66
E. RF Voltage-Controlled Oscillator Development	
<i>J. H. Wilcher</i>	67
F. DSN Receiver Performance, 3-Hz Loop Noise Bandwidth	
<i>J. H. Wilcher</i>	68
G. Receiver Subsystem Development	
<i>C. F. Foster</i>	70
H. Time Synchronization System	
<i>R. C. Coffin, R. F. Emerson, and J. R. Smith</i>	72
V. Facility Engineering and Operations	76 ✓
A. Flight Project Support	
<i>J. Orbison</i>	76
B. Facility Construction and Equipment Installation	
<i>J. Orbison</i>	77
C. Venus DSS Operations	
<i>R. M. Gosline, E. B. Jackson, and A. L. Price</i>	79
D. DSIF Station Control and Data Equipment	
<i>R. Flanders, J. Woo, G. Jenkins, E. Bann, H. Baugh, A. Burke, and E. Garcia</i>	82
E. DSN Discrepancy Reporting System	
<i>G. C. Gilley</i>	86
F. Systems Reliability Study for SFOF Power Design	
<i>D. C. Card</i>	88
G. DSN 16-Month Loading Schedule System	
<i>R. T. Haenle</i>	93
VI. Operations Programming	102 ✓
A. Computer Programming Technology, Part II	
<i>W. Thomas</i>	102

3 I. Introduction 8

The Deep Space Network (DSN) is a facility established by the NASA Office of Tracking and Data Acquisition under the system management and technical direction of JPL, and is responsible for two-way communications with unmanned spacecraft traveling approximately 10,000 miles from Earth to interplanetary distances. The DSN is distinct from other NASA networks such as the Space Tracking and Data Acquisition Network (STADAN), which tracks Earth-orbiting scientific and communication satellites, and the Manned Space Flight Network (MSFN), which tracks the manned spacecraft of the *Gemini* and *Apollo* programs.

The DSN performs four basic functions in support of each space flight project: tracking, data acquisition, command, and control. Tracking is the function of locating the spacecraft, calculating its distance, velocity, and position, and following its course. Data acquisition consists of the recovery of information from the spacecraft in the form of telemetry—the recorded measurements of the condition of, and the scientific data obtained by, the spacecraft. The command function involves the sending of signals to the spacecraft to guide it in its flight and to operate scientific and engineering equipment on board the spacecraft. Control refers to the making of command decisions from a central facility and to the overall direction of flight operations, including the network of ground stations, during a mission. Present facilities permit simultaneous control of a newly launched spacecraft and a sec-

ond one already in flight. In preparation for the increased number of U.S. activities in space, a capability is being developed for simultaneous control of either two newly launched spacecraft plus two in flight, or four spacecraft in flight. With the advanced communications techniques now being implemented, it may soon be possible to obtain data from, and track spacecraft to, planets as far out in space as Jupiter.

The DSN supports, or has supported, the following NASA space exploration projects: *Ranger*, *Surveyor*, *Mariner*, and *Voyager* (JPL); *Lunar Orbiter* (Langley Research Center); *Pioneer* (Ames Research Center); and *Apollo* (Manned Spacecraft Center), as backup to the MSFN.

The main elements of the network are: the Deep Space Instrumentation Facility (DSIF), with space communications and tracking stations located around the world; the Ground Communications System (GCS), which provides communications between all elements of the DSN; and the JPL Space Flight Operations Facility (SFOF), the command and control center.

The DSIF is a worldwide chain of deep space stations that provide radio contact with the spacecraft (Table 1). JPL operates the U.S. and the Ascension Island stations. The overseas stations are normally staffed and operated

Table 1. Deep Space Instrumentation Facility

Deep Space Communication Complex (DSCC)	Deep Space Station (DSS)	DSS serial designation	Geodetic longitude, deg
Goldstone	Pioneer	11	243.1 E
	Echo	12	243.2 E
	Venus	13	243.2 E
	Mars	14	243.1 E
Canberra	Woomera	41	136.9 E
	Tidbinbilla	42	149.0 E
	Booroomba ^a	43	—
	Johannesburg	51	27.7 E
Madrid	Robledo	61	355.7 E
	Cebreros	62	355.6 E
	Rio Cofia ^a	63	—
	Cape Kennedy (Spacecraft Monitoring)	71	279.4 E
	Ascension Island (Spacecraft Guidance and Command)	72	345.7 E

^aStation not yet authorized.

by government agencies of the respective countries, with the assistance of U.S. support personnel. To maintain continuous mission coverage, the stations are placed approximately 120 deg apart in longitude around the Earth, so that the spacecraft is always within the field of view of at least one of the ground stations.

Radio contact with the spacecraft begins when it is poised on the launch pad at Cape Kennedy, and is maintained throughout the mission as the spacecraft passes from the field of view of one station to that of another. The Cape Kennedy tracking facility monitors the spacecraft during and immediately after launch. Later in the launch trajectory, while the spacecraft is relatively low in altitude, the signal is picked up by the 30-ft antenna at Ascension Island. Once the spacecraft is in orbit, the deep space stations with the large antennas, low-noise phase-lock receiving systems, and high-power transmitters take over radio communications and follow the vehicle to its destination. These stations obtain angular position, velocity (doppler), and distance (range) data for the spacecraft, and provide command control (up-link) and data reception (down-link) for the spacecraft. The standard 85-ft-diameter antennas in use at the deep space stations have gains of 53 db at 2295 MHz, permitting the receipt of significant data at distances as far as Mars. To improve the data-rate and distance capability, a 210-ft-diameter antenna having a gain of 61.81 ± 0.32 db at 2295 MHz has been built at DSS 14; two additional antennas of this size are planned for installation at overseas stations. In the

present configuration, with the exception of DSS 51 which has an S-band receiver-exciter subsystem, all stations are full S-band.

The DSN continuously conducts research and development of new components and systems to maintain a state-of-the-art capability. Therefore, the Goldstone DSCC is also used for extensive investigation of space tracking and telecommunications techniques, establishment of DSIF-spacecraft compatibility, and development of new DSIF hardware and software. New DSIF system equipment is installed and tested at the Goldstone DSCC before being accepted for systemwide integration into the DSIF. After acceptance for general use, it is classed as Goldstone Duplicate Standard (GSDS) equipment, thus standardizing the design and operation of identical items throughout the system.

The GCS, using facilities of the worldwide NASA Communications System (NASCOM), provides voice and teletype communications among the overseas DSIF stations, Goldstone, Cape Kennedy, and the SFOF. A special microwave link, which includes a video channel, is used between the SFOF and Goldstone to transmit critical data during a mission. Overseas communications are transmitted by land lines, submarine cables, microwave relays, high-frequency radio circuits, and even communication satellites.

Teletype is the primary means of transmitting tracking and telemetry data from the DSIF stations to the SFOF and sending predictions and other data to the stations. Voice circuits are used for transmission of high-priority communications other than data.

The SFOF at JPL is equipped with operations control consoles, status and operations displays, computers, and data-processing systems, and is the focal point of the DSN. From launch through mission completion, it is the control center for DSIF tracking and data-acquisition activities, as well as for spacecraft trajectory determinations, generation of the commands transmitted to the spacecraft, and analysis and interpretation of the data received.

Internal communications at the SFOF are maintained by means of telephones, voice intercom units, a public address system, closed-circuit TV, and other types of visual displays. Incoming spacecraft telemetry and tracking data from the deep space stations are automatically routed to the SFOF data-processing system, where special telemetry-processing equipment and high-speed digital computers convert the data into information for use by scientific experimenters and spacecraft engineers.

N67-30372

Tracking and Navigational Accuracy Analysis 8

A. DSN Inherent Accuracy Project, T. W. Hamilton and D. W. Trask

The DSN Inherent Accuracy Project was formally established by the DSN Executive Committee in July 1965. The objectives of the Project are:

- (1) Determination (and verification) of the inherent accuracy of the DSN as a radio navigation instrument for lunar and planetary missions.
- (2) Formulation of designs and plans for refining this accuracy to its practical limits.

Achievement of these goals is the joint responsibility of the Telecommunications Division (33) and the Systems Division (31) of JPL. To this end, regular monthly meetings are held to coordinate and initiate relevant activities. The Project leader and his assistant (from Divisions 31 and 33, respectively) report to the DSN Executive Committee, and are authorized to task Project members to (1) conduct analyses of proposed experiments, (2) prepare reports on current work, and (3) write descriptions of proposed experiments. The Project is further authorized to deal directly with those flight projects using the

DSN regarding data-gathering procedures that bear on inherent accuracy.

The various data types and tracking modes provided by the DSIF in support of lunar and planetary missions are discussed in SPS 37-39, Vol. III, pp. 6-8. Technical work directly related to the Inherent Accuracy Project is presented in SPS 37-38, Vol. III, and in subsequent issues, and is continued in the following sections of this volume.

B. Satellite Orbit Determination Accuracy Study Applicable to Voyager Trajectories, R. K. Russell

1. Introduction

This study was undertaken to answer the question: Are there orbits that should be avoided because of their poor orbit determination characteristics? To implement the study, the JPL single precision orbit determination program (SPODP) was used.

The following parametric variations were investigated:

- (1) Variation of in-plane orbital parameters (semimajor axis a ; eccentricity e) while keeping the orientation of the orbit fixed.

- (2) Variation of the inclination of the orbit to the plane of the sky¹ for extremes of a and e .
- (3) Variation of the arrival date while holding orbit characteristics fixed.

In all computer runs, the Cartesian position and velocity of the probe in geocentric-equatorial coordinates of date and the mass of Mars are estimated. The data type for all the runs is two-way doppler. The noise on the doppler is assumed to be 0.001 m/sec for a 1-min sample rate. The *a priori* uncertainties in position, velocity (of the probe), and mass of Mars are: 1000 km on x , y , and z ; 0.1 km/sec on \dot{x} , \dot{y} , and \dot{z} ; and 1 km³/sec² on μ , mass of Mars. Data for all the runs commenced at periapsis passage. Consequently, T , the time of periapsis passage, was chosen to be zero. For all the runs, Mars is assumed to be a transparent body; i.e., data are obtained even if the probe is behind Mars relative to the Earth.

In addition, the ephemeris of Mars is assumed to be perfectly known in all the runs. This limitation was necessary since at present the SPODP is not able to find target-centered covariance matrices when the ephemeris of the target body is estimated.

March 4, 1974, a sample *Voyager* arrival date, was the epoch chosen for this study.

2. Variation of In-Plane Orbital Parameters

a. Discussion. For this part of the study, periapsis altitude h_p was held constant, and apoapsis altitude h_a was varied from an almost circular orbit² ($h_a \approx h_p$) to 20,000 km. This was repeated for several values of h_p ; namely, 500, 1000, and 1500 km, respectively. For these runs, the covariance matrix on the estimated parameters was formed on the basis of 15 hr of tracking data taken from three tracking stations: DSS 51 (Johannesburg), DSS 41 (Woomera), and DSS 11 (Pioneer, Goldstone). For determination of input conditions, R_m , the radius of Mars, was chosen to be 3378 km. The orbit specifications are given in Table 1.

¹The plane of the sky is that plane which is orthogonal to the Earth-Mars vector. This plane was chosen to quote statistics because Ω' , the longitude of the ascending node of the orbit on the plane of the sky, is indeterminate if the orbit does not change its aspect angle relation to the Earth (or tracking station). Thus, Ω' is a rather critical parameter, highly dependent on the relative rate of revolution of Mars with respect to the Earth. For simplicity, the x -axis is chosen to lie in the ecliptic plane (see Fig. 1).

²The reason for not having a circular orbit ($e = 0$; $h_a = h_p$) is that in the conversions from Cartesian statistics to orbital element statistics, terms of $0(1/e)$ appear and hence would be unbounded.

Table 1. Orbit characteristics

Orbit	h_p , km	h_a , km	a , km	e	Period P
1A	500	578.4	3,917.0	0.01000	2 ^h 3 ^m 50 ^s
1B	500	1,000	4,128	0.06056	2 ^h 13 ^m 58 ^s
1C	500	5,000	6,128	0.36717	4 ^h 2 ^m 19 ^s
1D	500	10,000	8,628	0.55053	6 ^h 44 ^m 50 ^s
1E	500	15,000	11,128	0.65151	9 ^h 52 ^m 58 ^s
1F	500	20,000	13,628	0.71544	13 ^h 23 ^m 38 ^s
2A	1,000	1,088.4	4,420.0	0.01000	2 ^h 28 ^m 26 ^s
2B	1,000	5,000	6,378	0.31358	4 ^h 17 ^m 18 ^s
2C	1,000	10,000	8,878	0.50687	7 ^h 2 ^m 33 ^s
2D	1,000	15,000	11,378	0.61522	10 ^h 13 ^m 4 ^s
2E	1,000	20,000	13,878	0.68454	13 ^h 45 ^m 51 ^s
3A	1,500	1,598.5	4,925.0	0.01000	2 ^h 54 ^m 35 ^s
3B	1,500	5,000	6,628	0.26403	4 ^h 32 ^m 34 ^s
3C	1,500	10,000	9,128	0.46560	7 ^h 20 ^m 32 ^s
3D	1,500	15,000	11,628	0.58050	10 ^h 33 ^m 23 ^s
3E	1,500	20,000	14,128	0.65473	14 ^h 8 ^m 16 ^s

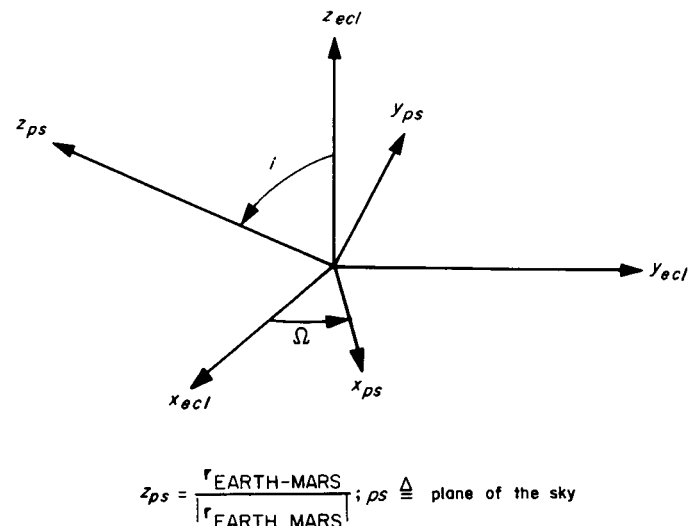


Fig. 1. Plane-of-the-sky coordinates

For these orbits, i' , the inclination with respect to the plane of the sky, was set to 60 deg. See Fig. 2, where

Ω, ω, i are the Euler angles of the plane of the sky with respect to the ecliptic plane.

Ω', ω', i' are the Euler angles of the plane of the orbit with respect to the plane of the sky.

Ω'', ω'', i'' are the Euler angles of the plane of the orbit with respect to the plane of the ecliptic.

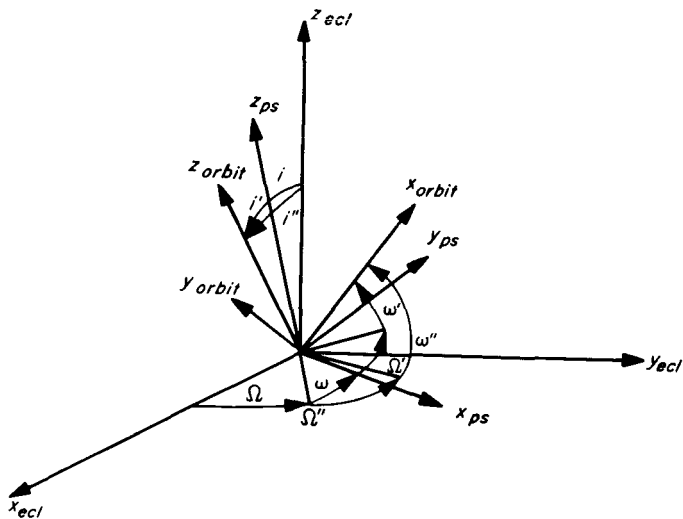


Fig. 2. Plane of the sky and orbit plane relative to the ecliptic

For the epoch chosen,

$$\begin{array}{lll} \Omega = 152^\circ 54' 50.2 & \Omega' = 0^\circ & \Omega'' = \Omega \\ \omega = 0^\circ & \omega' = 0^\circ & \omega'' = 0^\circ \\ i = 88^\circ 41' 62.33 & i' = 60^\circ & i'' = i + i' \end{array}$$

We denote the orbital elements as follows:

a	semimajor axis	
e	eccentricity	
T	time of periapsis passage	
Ω	longitude of ascending node	} relative to ecliptic plane
ω	argument of periapsis	
i	inclination to reference plane	
μ	mass of Mars	

In addition to statistics on these elements, statistics on apoapsis altitude, periapsis altitude, and period of the orbit are also useful. These are computed as follows:

$$\sigma_{h_a}^2 = (1 + e)^2 \sigma_a^2 + a^2 \sigma_e^2 + 2a(1 + e) \rho_{ae} \sigma_a \sigma_e \quad (1)$$

$$\sigma_{h_p}^2 = (1 - e)^2 \sigma_a^2 + a^2 \sigma_e^2 - 2a(1 - e) \rho_{ae} \sigma_a \sigma_e \quad (2)$$

$$\sigma_p^2 = \pi^2 \frac{a}{\mu} \left[9\sigma_a^2 + \left(\frac{a}{\mu} \right)^2 \sigma_\mu^2 - 6 \left(\frac{a}{\mu} \right) \rho_{a\mu} \sigma_a \sigma_\mu \right] \quad (3)$$

It is also desirable to have the statistics on the orbital elements relative to the plane of the sky. Since statistics on a , e , T , and μ are independent of the coordinate system chosen, the only elements affected are Ω'' , ω'' , and i'' . In the above notation, we are seeking statistics on Ω' , ω' , and i' .

Letting

$$\left. \begin{array}{l} \Omega' = \begin{bmatrix} \Omega' \\ \omega' \\ i' \end{bmatrix} \\ \Omega'' = \begin{bmatrix} \Omega'' \\ \omega'' \\ i'' \end{bmatrix} \end{array} \right\} \quad (4)$$

$$\begin{aligned} \Gamma_{\Omega'} &= (\overline{\delta \Omega'} \delta \Omega'^T) = \left(\frac{\partial \Omega'}{\partial \Omega''} \right) (\overline{\delta \Omega'' \delta \Omega''^T}) \left(\frac{\partial \Omega'}{\partial \Omega''} \right)^T \\ &= \left(\frac{\partial \Omega'}{\partial \Omega''} \right) \Gamma_{\Omega''} \left(\frac{\partial \Omega'}{\partial \Omega''} \right)^T \end{aligned} \quad (5)$$

We need to calculate:

$$\frac{\partial \Omega'}{\partial \Omega''} = \begin{bmatrix} \frac{\partial \Omega'}{\partial \Omega''} & \frac{\partial \Omega'}{\partial \omega''} & \frac{\partial \Omega'}{\partial i''} \\ \frac{\partial \omega'}{\partial \Omega''} & \frac{\partial \omega'}{\partial \omega''} & \frac{\partial \omega'}{\partial i''} \\ \frac{\partial i'}{\partial \Omega''} & \frac{\partial i'}{\partial \omega''} & \frac{\partial i'}{\partial i''} \end{bmatrix} \quad (6)$$

Since the formulation and solution of this problem are exceedingly tedious, these are not presented here. Suffice it to say that with the values of the orientation angles, the matrix reduces to

$$\frac{\partial \Omega'}{\partial \Omega''} = \begin{bmatrix} \left(\frac{\sin i''}{\sin i'} \right) & 0 & 0 \\ \left(\frac{-\sin i}{\sin i'} \right) & 1 & 0 \\ 0 & 0 & 1 \end{bmatrix} \quad (7)$$

which implies that the statistics on i'' are unchanged. The factor $(1/\sin i')$ in the partials implies that as the inclination with respect to the plane of the sky tends to

zero, the uncertainties of Ω' and ω' tend to infinity, as is to be expected because of the nature of the Euler rotations.

For comparison with results presented here, the following accuracy goals typical for an orbit photographic mission such as *Voyager* are shown below:

Parameter	3- σ uncertainty
h_p	1-10 km
h_a	1-10 km
P	1-10 sec
ω	4×10^{-3} rad
Ω	4×10^{-3} rad
T	1-10 sec

b. Conclusions. Figs. 3, 4, and 5 are plots of uncertainties in h_p , P , and ω . These data are taken from Table 2. These parameters are of primary importance to *Voyager*-type missions where knowledge of period and suborbit points on the planet's surface are critical.

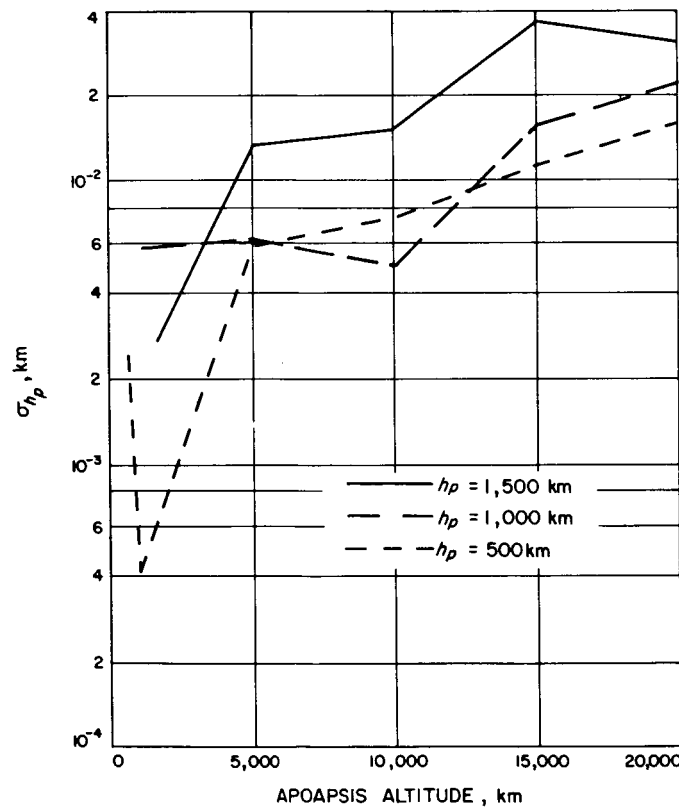


Fig. 3. Uncertainty in periapsis altitude versus apoapsis altitude

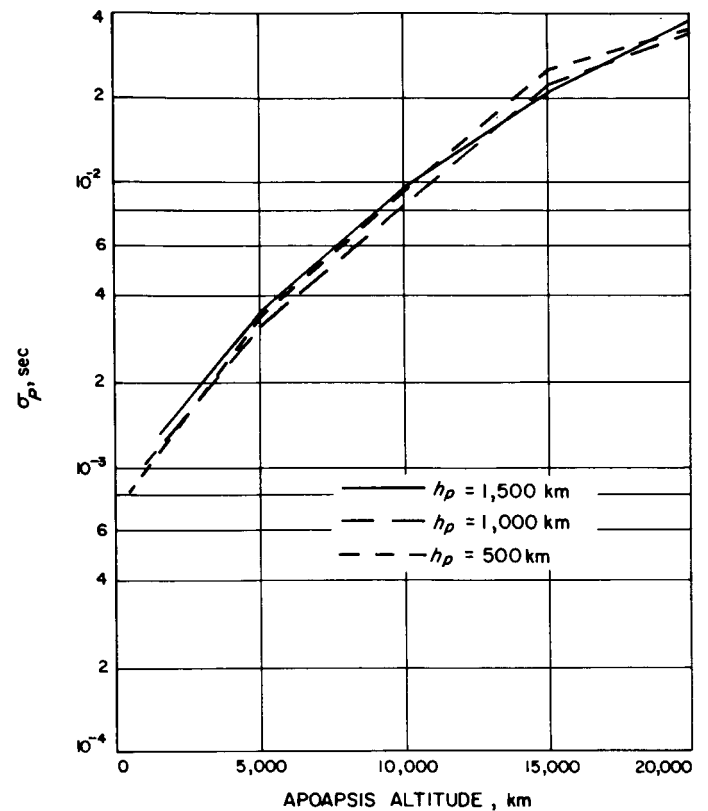


Fig. 4. Uncertainty in period versus apoapsis altitude

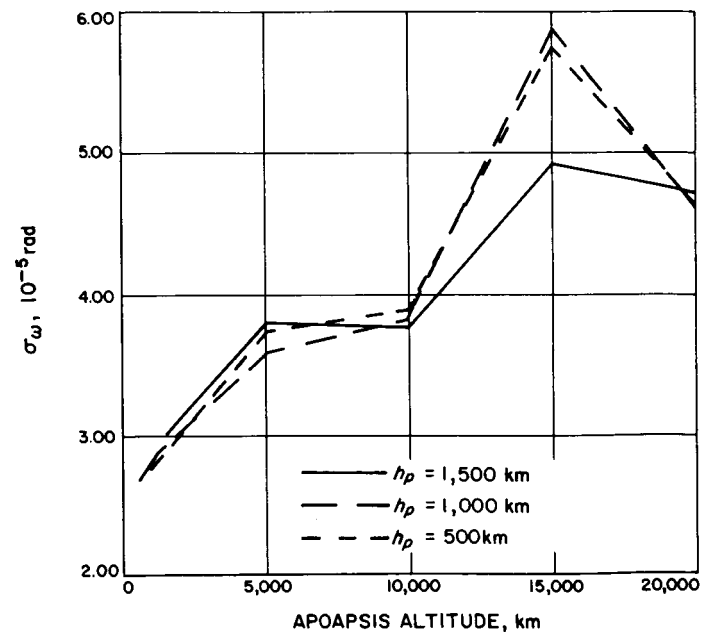


Fig. 5. Uncertainty in argument of periapsis versus apoapsis altitude

Table 2. Orbital element uncertainties for in-plane parameter variations

Orbit	σ_{a_i} , km	σ_e	σ_{T_i} , sec	σ_{Ω_i} , rad	σ_{ω_i} , rad	σ_{i_i} , rad	σ_{μ_i} , km ³ /sec ²	$\sigma_{h_{a_i}}$, km	$\sigma_{h_{p_i}}$, km	σ_{P_i} , sec	$\sigma_{\Omega_{ps_i}}$, rad	$\sigma_{a_{ps_i}}$, rad
1A	2.40×10^{-3}	4.50×10^{-8}	2.66×10^{-3}	2.45×10^{-5}	2.69×10^{-5}	1.05×10^{-6}	7.81×10^{-2}	2.46×10^{-3}	2.34×10^{-3}	8.34×10^{-4}	1.48×10^{-5}	2.27×10^{-6}
1B	1.38×10^{-3}	4.90×10^{-8}	4.72×10^{-4}	2.52×10^{-5}	2.88×10^{-5}	5.60×10^{-7}	4.19×10^{-2}	1.50×10^{-3}	4.11×10^{-4}	9.80×10^{-4}	1.52×10^{-5}	3.70×10^{-7}
1C	9.36×10^{-3}	7.48×10^{-8}	2.28×10^{-4}	3.11×10^{-5}	3.58×10^{-5}	2.64×10^{-6}	1.97×10^{-1}	1.28×10^{-2}	5.92×10^{-3}	3.34×10^{-3}	1.88×10^{-5}	1.04×10^{-7}
1D	1.70×10^{-2}	9.47×10^{-8}	1.71×10^{-4}	3.34×10^{-5}	3.85×10^{-5}	3.28×10^{-6}	2.42×10^{-1}	2.68×10^{-2}	7.36×10^{-3}	9.07×10^{-3}	2.02×10^{-5}	6.88×10^{-8}
1E	3.24×10^{-2}	1.52×10^{-7}	3.32×10^{-4}	5.13×10^{-5}	5.91×10^{-5}	5.03×10^{-6}	3.76×10^{-1}	5.37×10^{-2}	1.13×10^{-2}	2.51×10^{-2}	3.10×10^{-5}	1.03×10^{-7}
1F	5.77×10^{-2}	1.30×10^{-7}	3.52×10^{-4}	3.99×10^{-5}	4.60×10^{-5}	7.02×10^{-6}	5.23×10^{-1}	9.97×10^{-2}	1.58×10^{-2}	3.51×10^{-2}	2.42×10^{-5}	8.30×10^{-8}
2A	5.85×10^{-3}	4.60×10^{-8}	3.13×10^{-3}	2.52×10^{-5}	2.76×10^{-5}	2.28×10^{-6}	1.70×10^{-1}	5.91×10^{-3}	5.80×10^{-3}	1.03×10^{-3}	1.52×10^{-5}	2.23×10^{-6}
2B	8.73×10^{-3}	7.54×10^{-8}	2.56×10^{-4}	3.25×10^{-5}	3.74×10^{-5}	2.39×10^{-6}	1.80×10^{-1}	1.14×10^{-2}	6.08×10^{-3}	3.35×10^{-3}	1.96×10^{-5}	1.16×10^{-7}
2C	1.01×10^{-2}	8.88×10^{-8}	2.83×10^{-4}	3.37×10^{-5}	3.88×10^{-5}	1.97×10^{-6}	1.48×10^{-1}	1.52×10^{-2}	4.99×10^{-3}	8.19×10^{-3}	2.04×10^{-5}	8.75×10^{-8}
2D	3.97×10^{-2}	1.43×10^{-7}	3.97×10^{-4}	4.99×10^{-5}	5.75×10^{-5}	6.09×10^{-6}	4.56×10^{-1}	6.41×10^{-2}	1.55×10^{-2}	2.24×10^{-2}	3.02×10^{-5}	1.11×10^{-7}
2E	7.36×10^{-2}	1.36×10^{-7}	3.85×10^{-4}	4.03×10^{-5}	4.64×10^{-5}	8.84×10^{-6}	6.57×10^{-1}	1.25×10^{-1}	2.24×10^{-2}	3.42×10^{-2}	2.44×10^{-5}	8.88×10^{-8}
3A	2.81×10^{-3}	4.92×10^{-8}	3.92×10^{-3}	2.74×10^{-5}	3.01×10^{-5}	9.83×10^{-7}	7.24×10^{-2}	2.89×10^{-3}	2.76×10^{-3}	1.31×10^{-3}	1.65×10^{-5}	2.38×10^{-6}
3B	1.54×10^{-2}	7.38×10^{-8}	3.18×10^{-4}	3.30×10^{-5}	3.80×10^{-5}	3.98×10^{-6}	2.97×10^{-1}	1.71×10^{-2}	1.33×10^{-2}	3.38×10^{-3}	1.99×10^{-5}	1.26×10^{-7}
3C	2.89×10^{-2}	9.49×10^{-8}	2.56×10^{-4}	3.29×10^{-5}	3.79×10^{-5}	5.34×10^{-6}	3.95×10^{-1}	4.28×10^{-2}	1.50×10^{-2}	8.44×10^{-3}	1.99×10^{-5}	8.42×10^{-8}
3D	8.71×10^{-2}	1.35×10^{-7}	3.37×10^{-4}	4.27×10^{-5}	4.92×10^{-5}	1.27×10^{-6}	9.44×10^{-1}	1.38×10^{-1}	3.58×10^{-2}	2.10×10^{-2}	2.58×10^{-5}	9.13×10^{-8}
3E	9.21×10^{-2}	1.57×10^{-7}	3.96×10^{-4}	4.09×10^{-5}	4.71×10^{-5}	1.07×10^{-6}	7.95×10^{-1}	1.54×10^{-1}	3.03×10^{-2}	3.77×10^{-2}	2.47×10^{-5}	1.03×10^{-7}

Table 3. Orbital element uncertainties for variation of inclination

Orbit	σ_a , km	σ_e	σ_T , sec	σ_{Ω} , rad	σ_{ω} , rad	σ_i , rad	σ_{μ} , km ³ /sec ²	σ_{a_e} , km	σ_{a_p} , km	σ_P , sec	$\sigma_{\Omega_{ps}}$, rad	$\sigma_{\omega_{ps}}$, rad	i' , deg
1A	8.02×10^{-2}	4.40×10^{-5}	4.37×10^0	1.39×10^{-7}	3.64×10^{-3}	8.15×10^{-8}	9.96×10^{-1}	1.38×10^{-1}	2.30×10^{-1}	2.01×10^{-1}	∞	∞	0
1A	3.18×10^{-2}	1.25×10^{-6}	6.76×10^{-2}	1.55×10^{-5}	1.48×10^{-4}	6.90×10^{-7}	9.94×10^{-1}	3.40×10^{-2}	3.02×10^{-2}	1.73×10^{-2}	1.78×10^{-4}	5.73×10^{-5}	5
1A	3.22×10^{-2}	1.18×10^{-6}	3.62×10^{-2}	3.20×10^{-6}	1.65×10^{-4}	1.39×10^{-6}	9.99×10^{-1}	3.46×10^{-2}	3.03×10^{-2}	1.72×10^{-2}	1.82×10^{-4}	3.07×10^{-5}	10
1A	3.09×10^{-2}	1.03×10^{-6}	2.29×10^{-2}	1.15×10^{-4}	2.14×10^{-4}	4.49×10^{-6}	9.96×10^{-1}	3.24×10^{-2}	2.99×10^{-2}	1.64×10^{-2}	2.03×10^{-4}	1.96×10^{-5}	30
1A	3.20×10^{-2}	1.03×10^{-6}	4.25×10^{-2}	5.89×10^{-4}	6.45×10^{-4}	1.34×10^{-6}	9.92×10^{-1}	3.41×10^{-2}	3.03×10^{-2}	2.00×10^{-2}	3.56×10^{-4}	3.66×10^{-5}	60
1A	4.23×10^{-2}	2.48×10^{-6}	1.39×10^{-1}	5.54×10^{-3}	5.50×10^{-3}	4.39×10^{-6}	9.86×10^{-1}	5.03×10^{-2}	3.46×10^{-2}	5.47×10^{-2}	1.13×10^{-3}	1.20×10^{-4}	80
1A	4.12×10^{-2}	4.39×10^{-6}	2.58×10^{-1}	1.81×10^{-2}	1.79×10^{-2}	8.85×10^{-6}	9.86×10^{-1}	5.52×10^{-2}	3.09×10^{-2}	9.91×10^{-2}	2.08×10^{-3}	2.22×10^{-4}	85
1A	3.42×10^0	4.39×10^{-4}	$2.52 \times 10^{+1}$	7.28×10^0	7.25×10^0	6.75×10^{-1}	9.53×10^{-1}	5.17×10^0	1.67×10^0	$1.02 \times 10^{+1}$	2.01×10^{-1}	2.17×10^{-2}	90
1F	1.08×10^{-1}	1.36×10^{-5}	1.61×10^{-1}	1.87×10^{-7}	2.45×10^{-5}	4.45×10^{-8}	9.98×10^{-1}	2.85×10^{-1}	1.82×10^{-1}	2.15×10^{-1}	∞	∞	0
1F	1.15×10^{-1}	1.03×10^{-6}	6.65×10^{-3}	5.17×10^{-6}	5.80×10^{-5}	6.97×10^{-7}	9.81×10^{-1}	2.04×10^{-1}	2.86×10^{-2}	1.83×10^{-1}	5.92×10^{-5}	1.49×10^{-6}	5
1F	1.15×10^{-1}	8.57×10^{-7}	3.41×10^{-3}	1.07×10^{-5}	6.11×10^{-5}	1.38×10^{-6}	9.86×10^{-1}	2.02×10^{-1}	2.92×10^{-2}	1.79×10^{-1}	6.11×10^{-5}	6.88×10^{-7}	10
1F	1.14×10^{-1}	6.69×10^{-7}	1.25×10^{-3}	3.96×10^{-5}	7.89×10^{-5}	4.47×10^{-6}	9.91×10^{-1}	2.01×10^{-1}	2.97×10^{-2}	1.64×10^{-1}	6.96×10^{-5}	3.13×10^{-7}	30
1F	1.14×10^{-1}	6.30×10^{-7}	9.03×10^{-4}	1.99×10^{-4}	2.29×10^{-4}	1.34×10^{-5}	9.94×10^{-1}	2.01×10^{-1}	2.99×10^{-2}	1.69×10^{-1}	1.20×10^{-4}	3.82×10^{-7}	60
1F	1.32×10^{-1}	1.25×10^{-6}	1.28×10^{-3}	1.61×10^{-3}	1.63×10^{-3}	4.37×10^{-5}	9.86×10^{-1}	2.38×10^{-1}	2.98×10^{-2}	3.59×10^{-1}	3.28×10^{-4}	9.27×10^{-7}	80
1F	1.69×10^{-1}	2.21×10^{-6}	1.87×10^{-3}	5.21×10^{-3}	5.23×10^{-3}	8.81×10^{-5}	9.80×10^{-1}	3.14×10^{-1}	2.98×10^{-2}	6.47×10^{-1}	6.00×10^{-4}	1.42×10^{-6}	85
1F	8.80×10^{-1}	1.85×10^{-5}	2.03×10^{-2}	7.93×10^{-2}	7.93×10^{-2}	3.86×10^{-3}	5.50×10^{-1}	1.76×10^0	1.98×10^{-2}	4.94×10^0	2.19×10^{-3}	2.26×10^{-5}	90

These figures show that variations of periapsis altitude from 500 to 1500 km are not of extreme importance, but that variations in apoapsis altitude over the range of 20,000 km are of importance; i.e., the smaller orbits are typically the best. The knowledge of the mass of the target planet also improves as the orbit size is reduced.

In general, all the orbits considered met and well surpassed the accuracy goals shown above.

3. Variation of the Inclination of the Orbit

a. Discussion. In this part of the study the inclination of the orbit relative to the plane of the sky is varied from 0 to 90 deg for two specific orbits; namely, 1A and 1F, described above. The input is obtained as before. All the runs are based on one orbit of tracking data. The results are given in Table 3.

b. Conclusions. As the inclination relative to the plane of the sky decreases from 90 to 0 deg, there is a tremendous improvement in the statistics on the orientation angles Ω , ω , and i . However, near 0 deg, the in-plane parameter statistics a , e , and T become degraded. Statistics on Ω and ω relative to the plane of the sky become unbounded as we near 0 deg, which is as expected. The larger and more eccentric orbits appear to suffer smaller variations in statistics over the interval of inclination than do the smaller, less eccentric orbits, as demonstrated by the differences between orbits 1A and 1F.

In order to meet the orbit determination requirements, the inclination with respect to the plane of the sky should be kept in the 5- to 80-deg region; otherwise, the accuracy can be severely affected.

4. Variation of Arrival Date

a. Discussion. There is good reason to suppose that because the apparent revolution rate of Mars with respect

to the Earth is a function of time, variation of the arrival date will change the statistics. If Mars were at infinity and this rate were zero, the binary star problem would result, in which case it becomes impossible to solve for the longitude of ascending node relative to the plane of the sky. In reality, Mars is not at infinity; however, it does have zero revolution rates relative to the Earth at some times in its orbit. These are the points at the beginning and end of its retrograde motion, which occur approximately 15.4 deg before and after conjunction with the Earth.

To test this hypothesis of orbit determination degradation, four dates were examined:

September 16, 1973—15.4 deg before closest approach

November 22, 1973—15.4 deg after closest approach

October 18, 1973—conjunction

November 13, 1974—opposition

The first and second correspond to zero relative angular velocity. The runs were made using one orbit of tracking data with orbit 1F. The results are given in Table 4.

b. Conclusions. The hypothesis that arrival date does affect the orbit determination accuracy is confirmed. This effect is seen principally in the orientation angles Ω , ω , and i , where changes in statistics by factors of 4 to 10 are seen. Also affected, though not as severely, are the in-plane parameters e and T . Despite this degradation of the solutions, we are still well within the prescribed constraints.

5. Summary

In order to meet the sample constraints, the only parameter that seriously affects the orbit determination characteristics is the inclination with respect to the plane of

Table 4. Orbital element uncertainties for variation of arrival date

Date	σ_a , km	σ_e	σ_T , sec	σ_{Ω} , rad	σ_{ω} , rad	σ_i , rad	σ_{μ} , km ³ /sec ²	σ_{h_a} , km	σ_{h_p} , km	σ_{P_i} , sec
Sept. 16, 1973	1.08×10^{-1}	3.08×10^{-7}	1.82×10^{-4}	2.38×10^{-4}	2.80×10^{-4}	1.13×10^{-4}	9.91×10^{-1}	1.86×10^{-1}	2.98×10^{-2}	1.10×10^{-1}
Nov. 22, 1973	1.10×10^{-1}	7.09×10^{-7}	2.07×10^{-4}	3.40×10^{-4}	4.16×10^{-4}	9.62×10^{-5}	9.93×10^{-1}	1.92×10^{-1}	2.93×10^{-2}	2.18×10^{-1}
Oct. 18, 1973	1.09×10^{-1}	1.19×10^{-7}	1.84×10^{-4}	5.71×10^{-5}	6.66×10^{-5}	1.87×10^{-5}	9.95×10^{-1}	1.88×10^{-1}	3.02×10^{-2}	3.47×10^{-2}
Nov. 13, 1974	1.14×10^{-1}	1.96×10^{-7}	3.93×10^{-4}	3.37×10^{-5}	3.74×10^{-5}	1.16×10^{-5}	9.86×10^{-1}	1.98×10^{-1}	2.98×10^{-2}	5.30×10^{-2}

the sky. All other variations, including arrival date, represent second-order effects.

This study should be further amplified to examine the effect of target ephemeris uncertainty on these results.

C. Polar Motion and DSN Station Locations,

P. M. Muller

1. Introduction

This is the first in a series of articles covering polar motion and DSN station locations, and is a survey of the information being used at present. The Earth's axis of figure is not coincident with the spin axis; it moves with respect to the latter, causing the so-called polar motion. The precision with which we are seeking to evaluate DSN station locations requires consideration of this polar motion and its effects.

Heretofore, station locations have been presumed to be time-invariant. This presumption is doubtful when we become concerned with errors of 10 m or less. In fact, we are anticipating possible reduction of these errors to the range of 1 m.

2. Definition of Terms and Coordinate Systems

Spin axis: The axis of the Earth's rotation; free of gravitational and impulsive forces, it would remain fixed in inertial space. In reality, there are precession and nutation motions. For the purposes of this article, we will assume that these are perfectly known.

Polar motion: A motion of the Earth's axis of figure with respect to its axis of rotation. This manifests itself as a change in the point where the spin axis pierces the Earth's crust. Intuitively, it is best to think of the polar motion as a motion or displacement of the Earth's crust with respect to the spin axis. It is *not* a movement of the spin axis with respect to inertial space.

International Polar Motion Service (IPMS): The IPMS has the task of observing and documenting the polar motion. This international organization began in September 1899 with the construction of five observatories, all at the same north latitude, spaced around the Earth. The observatories are located in Mizusawa, Japan (the current administrative center); Ukiah, California; Gaithersburg, Maryland; Carloforte, Italy; and Kitab, USSR. The IPMS issues yearly reports

(Ref. 1) and monthly bulletins containing observations, results, and all other pertinent information and equations, and also assists scientists needing these results. Dr. Shigeru Yumi, IPMS Observatory, Mizusawa, Japan, is the current director of this well-organized service.

Polar coordinates: This is the standard system adopted by the IPMS for representing the polar motion. It consists of a rectangular coordinate grid (X, Y) centered on the origin defined below. The X - Y plane is tangent to the Earth at the north pole, with $+X$ along the Greenwich meridian, and $+Y$ along the 90 west-longitude meridian. This coordinate system is used in the plot shown in Fig. 6.

New system and origin pole 1900: This refers to a method of data reduction and the resulting origin for the polar coordinates. Ref. 1 documents the equations currently used by IPMS to reduce observations. Since other methods may be, and have been, used in this connection, results based upon this system are denoted "new system." The origin of polar coordinates is uniquely defined by the new-system program.

Old system 1900: This was the program standard of IPMS prior to replacement by the new system in 1955. The origins and results of the two are distinct, and there is no simple relationship between them. To obtain results in a given system, one must process the observations according to the methods that define it. The same situation exists in the JPL orbit determination solutions. Changing one assumption necessary to the data-processing changes all answers in a complex way.

Stellar declination: This is the angular separation of a star from the point determined by the Earth's spin axis. It is a function *only* of the spin axis, and is independent of an observer's location on the Earth, and of the polar motion.

Local vertical: As defined by astronomers, the local vertical is a line perpendicular to the plane determined by local gravity. Because of gravitational anomalies, the local vertical line does not, in general, pass through the spin axis.

Astronomical latitude: This is the complement of the angle between the local vertical, and a line through the observatory parallel to the spin axis. This quantity is definitely a function of the observer's location and of the polar motion. Variations in this observed

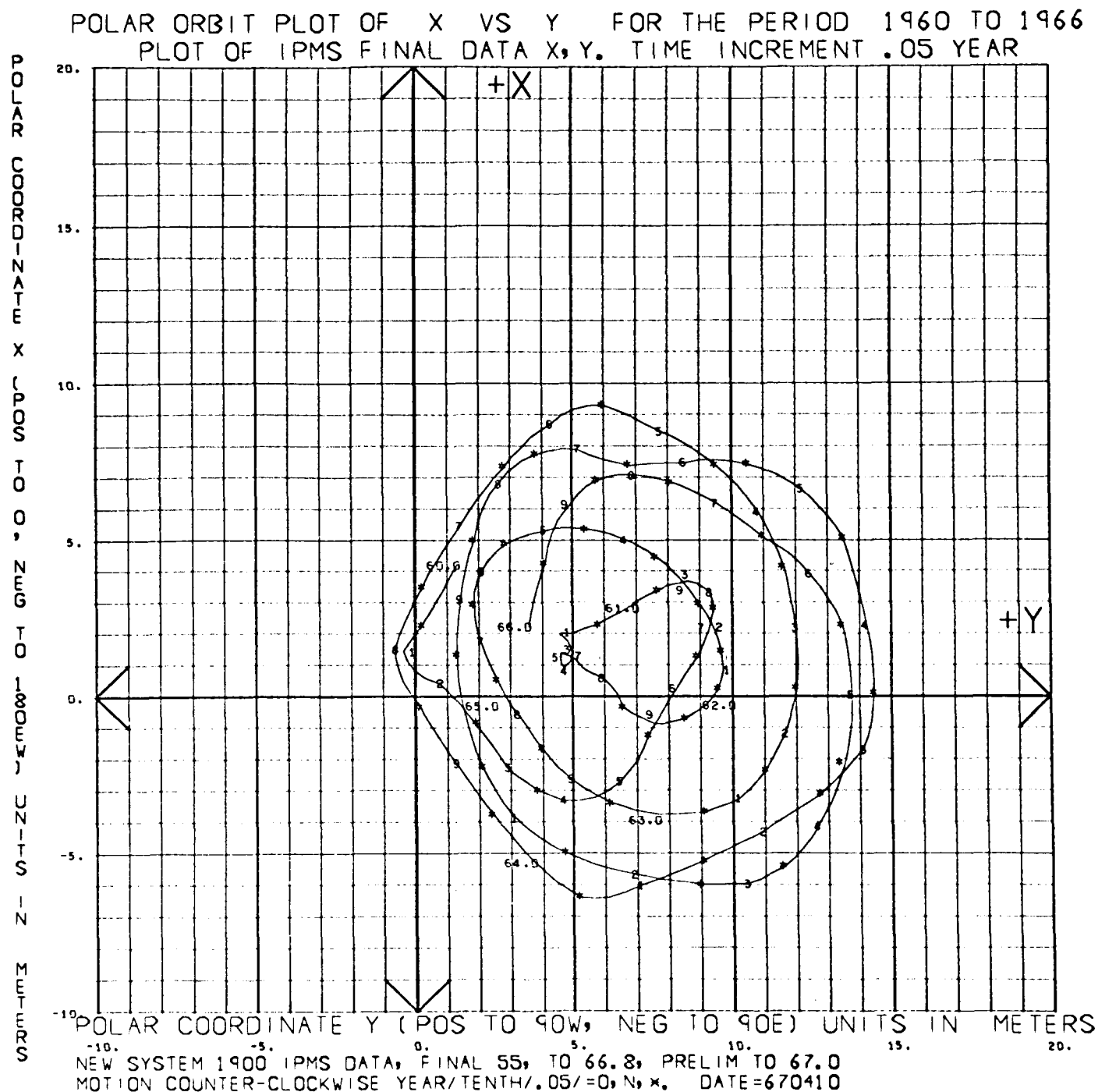


Fig. 6. Computer output plot of X versus Y for the period 1960 to 1966

quantity may be related to polar motion, as will be shown.

Continental drift and crustal slippage: These motions have effects on station locations. The continental drift is a matter of controversy, but most observers believe

that it is small, bounded by about 0.1 m/year. Crustal slippage due to earthquakes and faults has been observed,³ and amounts to 2 m in 50 years. These small motions will be neglected in the current discussion.

³See Ref. 4, p. 327, and bibliography from same.

Earth-fixed system (EFS) coordinates: We shall adopt a system of crust-fixed coordinates as a reference in this article. Let the pole be at the origin for new system 1900. The equator follows from the pole. Choice of the Greenwich meridian is arbitrary, but once chosen, remains fixed and determines EFS station longitudes and the polar coordinates. This is a system of invariant coordinates for any station anchored to the crust, neglecting crustal slippage. In any comparison of station-location solutions such as are obtained from orbit determination (SPS 37-43, Vol. III, pp. 3-11),⁴ we must use time-invariant station coordinates. This will become an important concept in our future analysis of DSN locations.

Instantaneous (INS) coordinates: We shall adopt a system of instantaneous Earth coordinates. Let the pole be at the location (X, Y) given by the IPMS as the current location. The equator is defined from the pole. Consider a small rotation from EFS to the INS coordinate system. Rotate through Y first, followed by X, which is an arbitrary choice in small transformations. The INS Greenwich meridian resulting from the change of coordinates still passes through the intersection of the EFS equator and EFS Greenwich meridian. Therefore, the INS Greenwich meridians all pass through this EFS intersection point. Other definitions of the INS Greenwich meridian would be possible, but they could not be consistent with Eqs. (1a)-(1c).

Longitude, latitude, and r_s : Longitude shall be measured *eastward*, from 0 to 360 deg; latitude is measured positive north and negative south of the equator; r_s is distance from the spin axis, and is the length of the perpendicular through the station. These may be given in either the EFS or INS system, as required below.

3. The Observation and Determination of Polar Motion

It is assumed that the reader is familiar with the several computations required to reduce observations for precession and nutation (Ref. 2). The early background of the IPMS effort, and the theory behind it, may be found in Ref. 3. Polar motion is observed indirectly, through determinations of the variations in latitude of the five IPMS observatories. If we take the nominal station location of any observatory or DSN station in EFS coordinates, and then observe its location in the INS system, there will

be a difference. This is clearly a *coordinate* difference, for the station has not moved with respect to the Earth. Eqs. (1a)-(1c) give INS-EFS coordinate differences for latitude, longitude, and r_s .

$$\Delta\lambda = \lambda_{INS} - \lambda_{EFS} = \tan \phi (X \sin \lambda + Y \cos \lambda) \quad (1a)$$

$$\Delta\phi = \phi_{INS} - \phi_{EFS} = X \cos \lambda - Y \sin \lambda \quad (1b)$$

$$\Delta r_s = -\Delta\phi \cdot \sin \phi \quad (1c)$$

Where X, Y are polar coordinates, ϕ , λ are station latitude and longitude, correct to three significant figures (commensurate with X and Y).

Notice that $\Delta\lambda$ is zero for stations on the equator. This is a consequence of the definition for the INS Greenwich meridian, which requires that it always pass through a fixed point on the equator. One could make other requirements, but first-order changes in the equations would result. These equations agree with others, e.g., Ref. 4 and Footnote 4.

Eq. (1b) is the fundamental equation used by the IPMS for variation in latitude. The same set of 72 star pairs are observed with vertical zenith telescopes at each observatory. Eq. 2 is filled out for an observation from each station, creating five simultaneous equations.

$$\phi_{observed} - \phi_{nominal} = X \cos \lambda - Y \sin \lambda + Z \quad (2)$$

The variable Z is the change introduced by any catalog or proper-motion errors in the adopted declinations. With at least three stations observing the same pair, one may obtain values for X, Y, and Z, independently. If the declination errors could not be removed in this fashion, they would swamp-out the very small latitude variations caused by polar motion.

The use of five stations allows for bad weather, and makes possible data-consistency checks. Such checks (Ref. 1) have revealed good agreement. The IPMS values of X and Y are correct to the order of 1 m. The method of observing each star pair, including reversal of the instrument between observations, eliminates or reduces such instrumental errors as flexure, axis orientation, etc. A micrometer measures positions of the crosshair during the observation. Adoption of "micrometer-coefficients" plays a large part in the data-reduction equations of Ref. 1.

⁴Vegos, C. J., and Trask, D. W., *Tracking Station Locations Determined From Combined Ranger Block III*.

4. Observed Nature of the Polar Motion

Fig. 6 is a plot of IPMS data, X versus Y , for the period 1960 to 1966. (See Table 5 which is included to assist the reader in converting from calendar year to fraction of year.) These so-called polar orbit plots demonstrate the elliptical nature of the motion, and show the period of about 405 days. This motion has been represented as the sum of two basic terms, called Annual and Chandler motion (Ref. 3). Their periods differ, and they repeat phase relationships about every 6.5 years. Their phase-canceling situation is revealed in 1961 as a very small amplitude of motion in the six-month semiperiod. The variation in amplitude over one-half revolution ranges from 1 m to over 20 m (compare 1961 with 1964, for example).

Notice that the ellipses are not centered at the origin. In 1900, they were very nearly so aligned. The change illustrates the secular motion of the pole (Ref. 4), which has covered 10 m in 67 years. This small effect, 0.2 m/year, is well below our 1-m accuracy goal, and will be neglected for the present (SPS 37-44, Vol. III, pp. 4-11).⁵

5. Predictions of the Future Motion

Ref. 5 discusses possible modeling of the polar motion. Hattori was successful in empirically fitting trigonometric equations, with about 15 terms, to the polar motion over one 6.5-year period (minimum-to-minimum amplitude).

⁵Hamilton, T. W., Grimes, D. C., and Trask, D. W., *Critical Parameters in Determining the Navigational Accuracy for a Deep Space Probe During the Planetary Encounter Phase*.

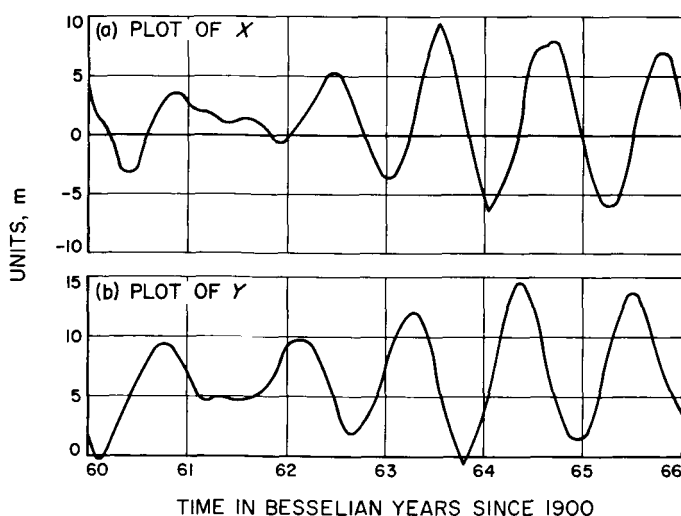


Fig. 7. New system 1900 IPMS final data versus Besselian years 1960 to 1966

The fit was good within 3 m over the entire interval. He found that the phase and amplitude characteristics of the Chandler term undergo unpredictable changes at each minimum.

If these methods cannot be improved, prediction of the polar motion to the desired 1-m accuracy level in the region of the minimum will be impossible. The minima will next occur in mid-September 1967 and in early 1974.

6. DSN Station Location Variations

Figs. 7(a) and (b) give plots of X and Y alone, versus time, for reference. We are interested in using Eqs. (1a)–(1c) to determine INS-EFS coordinate differences for the DSN stations as a function of the station and the polar

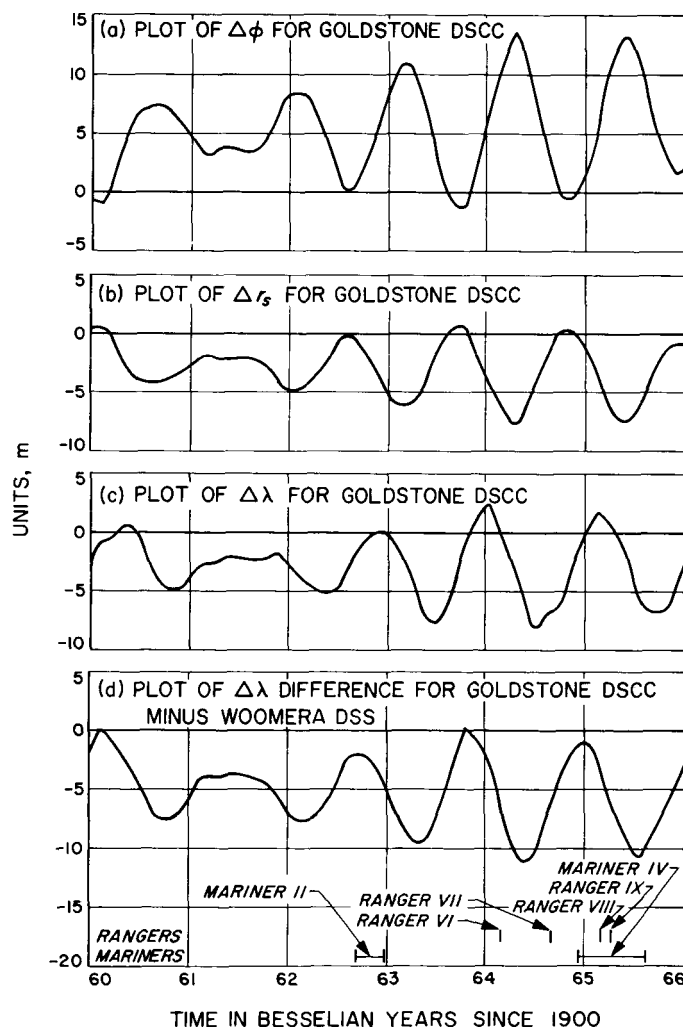


Fig. 8. Station location variations caused by polar motion, 1960 to 1966

motion. In SPS 37-43, Vol. III, pp. 3-18,⁴ the first attempt to do corrections based upon these variations is described. As a sample of DSN station-location variations due to the polar motion, see Figs. 8(a), (b), and (c), which document the results of Eqs. (1a)-(1c) applied to the Goldstone DSCC. These figures, covering the period 1960-1966, are a sample of the magnitudes and variations involved.

Table 5. First of month versus fraction of Besselian years^a

Month	Fraction
January 1	.00
February 1	.08
March 1	.16
April 1	.25
May 1	.33
June 1	.41
July 1	.50
August 1	.58
September 1	.67
October 1	.75
November 1	.83
December 1	.92

^aTo assist reader in converting from calendar date to fraction of year. Note designation of mission time below plots in Fig. 8.

Fig. 8(d) demonstrates that station longitude differences are *not* invariant with the polar motion. The deviation of 10 m seen in the figure is typical. The maximum, however, reaches 23.5 m for some station pairs. This is, perhaps, the most unfortunate result encountered when an orbit determination solves for INS station coordinates. It has been documented in SPS 37-44, Vol. III, pp. 4-11,⁵ that we can solve for longitude differences more readily than for absolute longitudes. In the sequel to this article, the effects of these longitude difference errors on orbit determination will be discussed.

7. Summary

The polar motion affects DSN station locations by amounts ranging up to 23.5 m. In future orbit determination programs it will be necessary to solve for station locations in an Earth-crust-fixed coordinate system such as the EFS proposed here. Prediction of the motion to high accuracy is quite difficult. As further investigation of these areas continues, the results will be reported in future SPS articles.

D. Theoretical Basis for the Double Precision Orbit Determination Program: VIII. Regression Partial Derivatives, T. D. Moyer

1. Introduction

This eighth article in the series presenting the theoretical basis for the double precision orbit determination program (DPODP) gives the formulation for computing the regression partial derivatives. These are the partial derivatives of each observable quantity with respect to the parameter vector q .

Part VII of this series (SPS 37-44, Vol. III) gave the formulation for integrating the variational equations which yield the partial derivatives of the probe state vector at any time t with respect to q . These subpartial derivatives are required to form the regression partial derivatives.

2. General Expression for Regression Partial Derivatives for Doppler and Angular Observables

Let

z = an observable quantity (doppler or angles)

q = total parameter vector

$\mathbf{X}_i^s(t_i) = \begin{bmatrix} \mathbf{r}_i^s(t_i) \\ \dot{\mathbf{r}}_i^s(t_i) \end{bmatrix}$ = column vector of heliocentric S rectangular position and velocity coordinates of direct participant i at its epoch of participation t_i (ET) referred to the Earth's mean equator and equinox of 1950.0. The units are km and km/ephemeris sec.

$$\dot{\mathbf{X}}_i^s(t_i) = \begin{bmatrix} \dot{\mathbf{r}}_i^s(t_i) \\ \ddot{\mathbf{r}}_i^s(t_i) \end{bmatrix}$$

The direct participants i are

- 1 = transmitter on Earth at transmission time t_1 .
- 2 = probe at intermediate time t_2 , or transmission time t_2 for angles.
- 3 = receiver on Earth at reception time t_3 . For doppler, t_3 is the midpoint of the count interval T_c .

For purposes of obtaining partial derivatives of an observable z with respect to the parameter vector q ,

$$z = z[\mathbf{X}_3^s(t_3, q), \mathbf{X}_2^s(t_2, q), \mathbf{X}_1^s(t_1, q), q] \quad (1)$$

Differentiating Eq. (1) with respect to \mathbf{q} gives

$$\begin{aligned}
 \frac{\partial z}{\partial \mathbf{q}} = & \frac{\partial z}{\partial \mathbf{X}_3^S(t_3)} \left[\frac{\partial \mathbf{X}_3^S(t_3)}{\partial \mathbf{q}} \right]_{t_3=\text{constant}} \\
 & + \frac{\partial z}{\partial \mathbf{X}_2^S(t_2)} \left\{ \left[\frac{\partial \mathbf{X}_2^S(t_2)}{\partial \mathbf{q}} \right]_{t_2=\text{constant}} + \dot{\mathbf{X}}_2^S(t_2) \left[\frac{\partial t_2(\text{ET})}{\partial \mathbf{q}} \right]_{c, \text{ time transformations} = \text{constant}} \right\} \\
 & + \frac{\partial z}{\partial \mathbf{X}_1^S(t_1)} \left\{ \left[\frac{\partial \mathbf{X}_1^S(t_1)}{\partial \mathbf{q}} \right]_{t_1=\text{constant}} + \dot{\mathbf{X}}_1^S(t_1) \left[\frac{\partial t_1(\text{ET})}{\partial \mathbf{q}} \right]_{c, \text{ time transformations} = \text{constant}} \right\} \\
 & + \left[\frac{\partial z}{\partial \mathbf{q}} \right]_{c, \text{ time transformations} = \text{variable}} \\
 & + \left[\frac{\partial z}{\partial \mathbf{q}} \right]_{\mathbf{X}_3^S(t_3), \mathbf{X}_2^S(t_2), \mathbf{X}_1^S(t_1) = \text{constant}}
 \end{aligned} \tag{2}$$

The terms of Eq. (2) are of two basic types. The last term gives the direct variation of the observable z due to a variation in \mathbf{q} , holding the state vectors of each participant constant. The remaining terms give the variation in the observable due to variations in the state vectors of each participant. The term on line 1 and the first terms on lines 2 and 3 give the direct variation in the state vector (and hence z) with respect to a variation in \mathbf{q} holding the epochs of participation constant. Since the state vectors are a function of \mathbf{q} , the epochs of participation t_2 (ET) and t_1 (ET) obtained from the solution of the light-time problem will also vary with \mathbf{q} . The second terms on lines 2 and 3 account for this effect. The epochs of participation may also vary due to variations in c , the speed of light,⁶ and the parameters affecting the time transformations which are used in the light-time solution. The partial derivative of z with respect to \mathbf{q} due to these effects is indicated on line 4.

The partial derivatives of the heliocentric state vectors with respect to the parameter vector \mathbf{q} , holding the epochs of participation constant, are given by the following sums:

$$\frac{\partial \mathbf{X}_3^S(t_3)}{\partial \mathbf{q}} = \frac{\partial \mathbf{X}_3^E(t_3)}{\partial \mathbf{q}} + \frac{\partial \mathbf{X}_E^S(t_3)}{\partial \mathbf{q}} \tag{3}$$

$$\frac{\partial \mathbf{X}_2^S(t_2)}{\partial \mathbf{q}} = \frac{\partial \mathbf{X}_2^{B2}(t_2)}{\partial \mathbf{q}} + \frac{\partial \mathbf{X}_{B2}^S(t_2)}{\partial \mathbf{q}} \tag{4}$$

$$\frac{\partial \mathbf{X}_1^S(t_1)}{\partial \mathbf{q}} = \frac{\partial \mathbf{X}_1^E(t_1)}{\partial \mathbf{q}} + \frac{\partial \mathbf{X}_E^S(t_1)}{\partial \mathbf{q}} \tag{5}$$

⁶The speed of light is an adopted constant that defines the light-second as the basic length unit. It is not normally included in the solution vector.

where

$B2$ = center of integration for free probe or body (other than Earth) on which a station is located

E = Earth

S = Sun

The partial derivatives $\partial z / \partial \mathbf{X}_3^S(t_3)$, $\partial z / \partial \mathbf{X}_2^S(t_2)$, and $\partial z / \partial \mathbf{X}_1^S(t_1)$ for doppler and angular observables are given in Section 3 of this article.

For a free probe, $\partial \mathbf{X}_2^{B2}(t_2) / \partial \mathbf{q}$ is obtained from the solution of the variational equations (see Part VII, SPS 37-44, Vol. III, pp. 33-44).

In Section 4, the formulation is given for computing $\partial \mathbf{X}_3^E(t_3) / \partial \mathbf{q}$, $\partial \mathbf{X}_1^E(t_1) / \partial \mathbf{q}$, and $\partial \mathbf{X}_2^{B2}(t_2) / \partial \mathbf{q}$ (if point 2 is a station on a celestial body).

The partial derivatives $\partial \mathbf{X}_E^S(t_3) / \partial \mathbf{q}$, $\partial \mathbf{X}_{B2}^S(t_2) / \partial \mathbf{q}$, and $\partial \mathbf{X}_E^S(t_1) / \partial \mathbf{q}$ are computed from the following (where E = Earth, M = Moon, B = Earth-Moon barycenter, p = planet, S = Sun):

$$\frac{\partial \mathbf{X}_E^S}{\partial \mathbf{q}} = \frac{\partial \mathbf{X}_B^S}{\partial \mathbf{q}} - \frac{\partial \mathbf{X}_B^E}{\partial \mathbf{q}} \tag{6}$$

$$\frac{\partial \mathbf{X}_M^S}{\partial \mathbf{q}} = \frac{\partial \mathbf{X}_B^S}{\partial \mathbf{q}} + \frac{\partial \mathbf{X}_M^B}{\partial \mathbf{q}} \tag{7}$$

$$\frac{\partial \mathbf{X}_p^S}{\partial \mathbf{q}} = \frac{\partial \mathbf{X}_p^S}{\partial \mathbf{q}} \tag{8}$$

where the right-hand terms are obtained from Eqs. (73), (75), and (76) of Part VII (Eq. 73 applies also for $p = B$).

The columns of Eqs. (6)–(8) are nonzero only for the reference parameters A_E , R_E , μ_E , μ_M , and osculating orbital elements \mathbf{E} for the ephemeris of a planet, the Earth–Moon barycenter, or the Moon.

The derivatives $\partial t_2(\text{ET})/\partial \mathbf{q}$ and $\partial t_1(\text{ET})/\partial \mathbf{q}$ are obtained by differentiating the light-time equation (Part IV, SPS 37-41, Vol. III, p. 33, Eqs. 16 or 19), ignoring the relativity term. The results are

$$\frac{\partial t_2(\text{ET})}{\partial \mathbf{q}} = \frac{1}{c} \frac{\mathbf{r}_{23}^T}{r_{23}} \left[\frac{\partial \mathbf{r}_2^S(t_2)}{\partial \mathbf{q}} - \frac{\partial \mathbf{r}_3^S(t_3)}{\partial \mathbf{q}} \right] \left(1 + \frac{\dot{p}_{23}}{c} \right) \quad (9)$$

$$\begin{aligned} \frac{\partial t_1(\text{ET})}{\partial \mathbf{q}} &= \frac{\partial t_2(\text{ET})}{\partial \mathbf{q}} \left(1 - \frac{\dot{r}_{12}}{c} \right) \\ &+ \frac{1}{c} \frac{\mathbf{r}_{12}^T}{r_{12}} \left[\frac{\partial \mathbf{r}_1^S(t_1)}{\partial \mathbf{q}} - \frac{\partial \mathbf{r}_2^S(t_2)}{\partial \mathbf{q}} \right] \left(1 + \frac{\dot{p}_{12}}{c} \right) \end{aligned} \quad (10)$$

where, from Part V,

$$\dot{p}_{12} = \frac{\mathbf{r}_{12}}{r_{12}} \cdot \dot{\mathbf{r}}_1 \quad (11)$$

$$\dot{p}_{23} = \frac{\mathbf{r}_{23}}{r_{23}} \cdot \dot{\mathbf{r}}_2 \quad (12)$$

In Eqs. (9) and (10), the partial derivatives of heliocentric position with respect to \mathbf{q} are simply the first three rows of Eqs. (3), (4), and (5).

The last two terms of Eq. (2) are evaluated in Sections 5 and 6 of this article.

For angular observables, Eq. (2) is evaluated with the state vector \mathbf{X} of each participant taken to be its position vector only. Also, since angular observables involve only two participants, the third line is omitted.

3. Partial Derivatives of Doppler and Angular Observables With Respect to State Vectors of Each Direct Participant

a. Two-way doppler. The formulation for computing two-way doppler \dot{f} consists of Eqs. (6), (34), and (60) of Part V (SPS 37-42, Vol. III, pp. 15–21). The partial derivatives of \dot{f} with respect to the heliocentric state vectors of the three participants are obtained by a straightforward differentiation of these formulas.

In Eq. (34) for $(1 - f_R/f_T)$, the $1/c$ and $1/c^2$ terms are differentiated. However, the relativistic terms $(\phi_1 - \phi_3)$ and $\frac{1}{2}(\dot{s}_1^2 - \dot{s}_3^2)$ are ignored. The potential term contributes a maximum of only 10^{-4} m/sec to range rate. The velocity term has a maximum value of about 0.1 m/sec, but its variation due to a variation in the parameter vector \mathbf{q} is very small.

In Eq. (60) for $(1 - f_R/f_T)^{**}$, only the $1/c$ terms are differentiated.

Near Earth, with a range $\rho = r_{12}, r_{23} = 100$ km, and a count time $T_c = 10$ sec, the partial derivatives from $(1 - f_R/f_T)^{**}$ are the same order of magnitude as those from $(1 - f_R/f_T)$. Since the $1/c^2$ terms of $(1 - f_R/f_T)^{**}$ were not differentiated, the partial derivatives for this extreme near-Earth case are good to about four figures.

The ratio of the partial derivatives derived from $(1 - f_R/f_T)^{**}$ to those derived from $(1 - f_R/f_T)$ is proportional to $(T_c/\rho)^2$. For ρ increasing from 100 km (with $T_c = 10$ sec) to 10^6 km (with $T_c = 1000$ sec), the factor $(T_c/\rho)^2$ reduces by four orders of magnitude, and the partials from $(1 - f_R/f_T)^{**}$ are the same order of magnitude as those from the $1/c^2$ terms of $(1 - f_R/f_T)$. Since, effectively, all terms of the second order of $1/c$ were differentiated, the partial derivatives for this case ($\rho = 10^6$ km, $T_c = 1000$ sec) are accurate to seven or eight figures.

In deriving Eq. (2) of this article, the dependency of the observable z on the acceleration and jerk vectors⁷ of each participant was ignored. This omission limits the accuracy of the partial derivatives to 4 or 5 significant figures for $\rho = 100$ km, and 7 or 8 significant figures for $\rho = 10^6$ km. This limitation on accuracy is the same as that resulting from truncating the doppler formulas before differentiating.

The partial derivatives are computed from the following quantities (see Part V for definitions of terms):

$$\begin{aligned} D &= \frac{1}{c} \left[-\frac{(\dot{\mathbf{r}}_{12})^T}{r_{12}} + \frac{\dot{r}_{12}}{r_{12}} \frac{(\mathbf{r}_{12})^T}{r_{12}} \right] \left[1 + \frac{1}{c} (\dot{p}_{12} - \dot{r}_{23}) \right] \\ &+ \frac{1}{c^2} \left[-\frac{(\ddot{\mathbf{r}}_1)^T}{r_{12}} + \frac{\dot{p}_{12}}{r_{12}} \frac{(\mathbf{r}_{12})^T}{r_{12}} \right] \dot{r}_{12} \\ &+ \frac{T_c^2}{24cr_{12}} \left[\left(\ddot{\mathbf{r}}_{12} - 6 \frac{\ddot{r}_{12} \dot{\mathbf{r}}_{12}}{r_{12}} + 6 \frac{\dot{r}_{12}^3}{r_{12}^3} \right) \frac{(\mathbf{r}_{12})^T}{r_{12}} \right. \\ &\left. + 3 \left(\ddot{r}_{12} - 2 \frac{\dot{r}_{12}^2}{r_{12}} \right) \frac{(\dot{\mathbf{r}}_{12})^T}{r_{12}} + 3 \frac{\dot{r}_{12}}{r_{12}} (\ddot{\mathbf{r}}_{12})^T - (\ddot{\mathbf{r}}_{12})^T \right] \end{aligned} \quad (13)$$

⁷The jerk vector is the time derivative of the acceleration vector.

$D \begin{pmatrix} 12 \leftrightarrow 23 \\ 1 \rightarrow 2 \end{pmatrix}$ = Eq. (13) with subscript 12 changed to 23 and vice versa, and subscript 1 changed to 2.

$$E = -\frac{1}{c} \frac{(\mathbf{r}_{12})^T}{r_{12}} \left[1 + \frac{1}{c} (\dot{\mathbf{p}}_{12} - \dot{\mathbf{r}}_{23}) \right] + \frac{T_c^2}{8c r_{12}} \left[\left(\ddot{\mathbf{r}}_{12} - 2 \frac{\dot{\mathbf{r}}_{12}^2}{r_{12}} \right) \frac{(\mathbf{r}_{12})^T}{r_{12}} + 2 \frac{\dot{\mathbf{r}}_{12}}{r_{12}} (\dot{\mathbf{r}}_{12})^T - (\ddot{\mathbf{r}}_{12})^T \right] \quad (14)$$

$E(12 \leftrightarrow 23)$ = Eq. (14) with subscript 12 changed to 23 and vice versa.

$$\Delta E = \frac{1}{c^2} \frac{(\mathbf{r}_{12})^T}{r_{12}} \dot{\mathbf{r}}_{12} \quad (15)$$

The partial derivatives are of the form

$$\frac{\partial \bar{f}}{\partial \mathbf{X}_i^s(t_i)} = \left[\frac{\partial \bar{f}}{\partial \mathbf{r}_i^s(t_i)} \mid \frac{\partial \bar{f}}{\partial \dot{\mathbf{r}}_i^s(t_i)} \right] \quad (16)$$

Specifically, they are given by

$$\frac{\partial \bar{f}}{\partial \mathbf{X}_1^s(t_1)} = C_3 f_q(t_1) \left[D \mid E + \Delta E \right] \quad (17)$$

$$\frac{\partial \bar{f}}{\partial \mathbf{X}_2^s(t_2)} = C_3 f_q(t_1) \left[D \begin{pmatrix} 12 \leftrightarrow 23 \\ 1 \rightarrow 2 \end{pmatrix} - D \mid E \begin{pmatrix} 12 \leftrightarrow 23 \\ 1 \rightarrow 2 \end{pmatrix} + \Delta E \begin{pmatrix} 12 \leftrightarrow 23 \\ 1 \rightarrow 2 \end{pmatrix} - E \right] \quad (18)$$

$$\frac{\partial \bar{f}}{\partial \mathbf{X}_3^s(t_3)} = C_3 f_q(t_1) \left[-D \begin{pmatrix} 12 \leftrightarrow 23 \\ 1 \rightarrow 2 \end{pmatrix} \mid -E \begin{pmatrix} 12 \leftrightarrow 23 \\ 1 \rightarrow 2 \end{pmatrix} \right] \quad (19)$$

b. Angular observables. The partial derivatives of angular observables with respect to the heliocentric position vectors of the transmitter and receiver are given by Eqs. (62)–(74) and auxiliary formulas of Part VI (SPS 37-43, Vol. III, p. 36).

4. Partial Derivatives of Body-Centered State Vector of Station With Respect to Parameter Vector

This section gives the partial derivatives of $\mathbf{X}_5^E(t_3)$, $\mathbf{X}_1^E(t_1)$, and $\mathbf{X}_2^{B2}(t_2)$ (if point 2 is a station on a celestial body other than the Earth) with respect to the parameter vector \mathbf{q} . Each of these state vectors will be denoted here by

$$\mathbf{X}_{50} = \begin{bmatrix} \mathbf{r}_{50} \\ \dot{\mathbf{r}}_{50} \end{bmatrix} \quad (20)$$

From Article IV (SPS 37-41, Vol. III, p. 36, Eqs. 43 and 44),

$$\mathbf{r}_{50} = T \mathbf{r}_b \quad (21)$$

$$\dot{\mathbf{r}}_{50} = \dot{T} \mathbf{r}_b \quad (22)$$

The transformations T, \dot{T} from body-fixed to space-fixed coordinates are not functions of solve-for parameters. The one exception to this is \dot{T} for a fixed Earth station which is a function of Δf_{cesium} . However, it affects the magnitude of $\dot{\mathbf{r}}_{50}$ by less than 10^{-5} m/sec, and hence is ignored in the partial derivatives. Thus, for a fixed station on any body,

$$\frac{\partial \mathbf{X}_{50}}{\partial \mathbf{q}} = \begin{bmatrix} T \frac{\partial \mathbf{r}_b}{\partial \mathbf{q}} \\ \dot{T} \frac{\partial \mathbf{r}_b}{\partial \mathbf{q}} \end{bmatrix} \quad (23)$$

The partial derivatives are nonzero only for the three spherical or cylindrical coordinates of the station. The partial derivatives of \mathbf{r}_b with respect to spherical station coordinates are obtained by differentiating Eq. (23) of Part IV:

$$\frac{\partial \mathbf{r}_b}{\partial r} = \begin{bmatrix} \cos \phi \cos \lambda \\ \cos \phi \sin \lambda \\ \sin \phi \end{bmatrix} = \frac{\mathbf{r}_b}{r} \quad (24)$$

$$\frac{\partial \mathbf{r}_b}{\partial \phi} = \begin{bmatrix} -r \sin \phi \cos \lambda \\ -r \sin \phi \sin \lambda \\ r \cos \phi \end{bmatrix} \quad (25)$$

$$\frac{\partial \mathbf{r}_b}{\partial \lambda} = \begin{bmatrix} -r \cos \phi \sin \lambda \\ r \cos \phi \cos \lambda \\ 0 \end{bmatrix} \quad (26)$$

The partial derivatives of \mathbf{r}_b with respect to cylindrical station coordinates are obtained by differentiating Eq. (24) of Part IV:

$$\frac{\partial \mathbf{r}_b}{\partial u} = \begin{bmatrix} \cos \lambda \\ \sin \lambda \\ 0 \end{bmatrix} \quad (27)$$

$$\frac{\partial \mathbf{r}_b}{\partial v} = \begin{bmatrix} 0 \\ 0 \\ 1 \end{bmatrix} \quad (28)$$

$$\frac{\partial \mathbf{r}_b}{\partial \lambda} = \begin{bmatrix} -u \sin \lambda \\ u \cos \lambda \\ 0 \end{bmatrix} \quad (29)$$

The right-hand terms of Eqs. (24)–(29) are evaluated from coordinates referenced to the instantaneous pole. The partial derivatives, however, apply to the solve-for station coordinates, whether they are referenced to the true pole or to the mean pole of 1900–05, and are accurate to approximately seven significant figures.

5. Partial Derivatives of Doppler and Angular Observables With Respect to Speed of Light and Parameters Affecting Time Transformations

a. Introduction. This section gives the partial derivatives indicated on line 4 of Eq. (2). These are the partial

derivatives of doppler and angular observables z with respect to q due to (1) variation in the speed of light c in the light-time solution only, and (2) variation in the time transformations used in the light-time solution. The parameters affecting the time transformations are ΔT_{1958} and Δf_{cesium} which affect (ET – A1), and a , b , and c (by time block) which affect (UTC – ST) for the receiving station. Additional terms for $\partial z / \partial \Delta T_{1958}$, Δf_{cesium} arise from the variational equations. These partials are substituted into the first term of Eq. (4), and hence appear on line 2 of Eq. (2). The speed of light c appears explicitly in the expression for computing two-way doppler. Hence, an additional term for $\partial z / \partial c$ appears on line 5 of Eq. 2.

b. Speed of light c . Given the reception time $t_3(\text{ET})$, the solution of the light-time problem for $t_2(\text{ET})$ and $t_1(\text{ET})$ is affected by the value used for c . For angular observables, however, a change in c of 3 km/sec along with a probe velocity of 300 km/sec will produce a maximum change of only 0.003. Hence, this partial derivative is ignored for angular observables. The partial derivative of a doppler observable z with respect to a change in c in the light-time equation is given by

$$\frac{\partial z}{\partial c} = \frac{\partial z}{\partial \mathbf{X}_2^s(t_2)} \dot{\mathbf{X}}_2^s(t_2) \frac{\partial t_2(\text{ET})}{\partial c} + \frac{\partial z}{\partial \mathbf{X}_1^s(t_1)} \dot{\mathbf{X}}_1^s(t_1) \frac{\partial t_1(\text{ET})}{\partial c} \quad (30)$$

Differentiating the light-time equations for the down and up legs with respect to c gives

$$\frac{\partial t_2(\text{ET})}{\partial c} = \frac{t_3(\text{ET}) - t_2(\text{ET})}{c} \left(1 + \frac{\dot{p}_{23}}{c} \right) \quad (31)$$

$$\frac{\partial t_1(\text{ET})}{\partial c} = \frac{\partial t_2(\text{ET})}{\partial c} \left(1 - \frac{\dot{r}_{12}}{c} \right) + \frac{t_2(\text{ET}) - t_1(\text{ET})}{c} \left(1 + \frac{\dot{p}_{12}}{c} \right) \quad (32)$$

where \dot{p}_{12} and \dot{p}_{23} are given by Eqs. (11) and (12). Substituting Eqs. (31) and (32) into Eq. (30) gives

$$\begin{aligned} \frac{\partial z}{\partial c} = & \frac{\partial z}{\partial \mathbf{X}_2^s(t_2)} \dot{\mathbf{X}}_2^s(t_2) \frac{t_3(\text{ET}) - t_2(\text{ET})}{c} \left(1 + \frac{\dot{p}_{23}}{c} \right) \\ & + \frac{\partial z}{\partial \mathbf{X}_1^s(t_1)} \dot{\mathbf{X}}_1^s(t_1) \left\{ \frac{t_3(\text{ET}) - t_2(\text{ET})}{c} \left[1 + \frac{1}{c} (\dot{p}_{23} - \dot{r}_{12}) \right] + \frac{t_2(\text{ET}) - t_1(\text{ET})}{c} \left(1 + \frac{\dot{p}_{12}}{c} \right) \right\} \end{aligned} \quad (33)$$

c. **Parameters affecting transformation (ET - A1):** ΔT_{1958} and Δf_{cesium} . The observables are computed from the state vectors

$$\mathbf{X}_3^S(t_3) = \mathbf{X}_3^E(t_3) + \mathbf{X}_E^S(t_3) \quad (34)$$

$$\mathbf{X}_2^S(t_2) = \mathbf{X}_2^{B2}(t_2) + \mathbf{X}_{B2}^S(t_2) \quad (35)$$

$$\mathbf{X}_1^S(t_1) = \mathbf{X}_1^E(t_1) + \mathbf{X}_E^S(t_1) \quad (36)$$

The state vectors $\mathbf{X}_E^S(t_3)$, $\mathbf{X}_{B2}^S(t_2)$, $\mathbf{X}_E^S(t_1)$, and $\mathbf{X}_2^{B2}(t_2)$ are functions of ephemeris time. The state vectors $\mathbf{X}_3^E(t_3)$ and $\mathbf{X}_1^E(t_1)$ are functions of both the UT1 and ET values of the epoch. However, the variation in $\mathbf{X}_i^E(t_i)$ due to δt_i (ET) is insignificant compared with the variation due to δt_i (UT1). Thus, for purposes of taking partial derivatives, $\mathbf{X}_3^E(t_3)$ and $\mathbf{X}_1^E(t_1)$ are considered to be functions of UT1 only.

Given the data time tag t_3 (ST) (the midpoint of the count interval for doppler observables), the values of t_3 (ET) and t_3 (UT1) are computed from

$$t_3(\text{ET}) = t_3(\text{ST}) + (\text{UTC} - \text{ST})_{t_3} + (\text{A1} - \text{UTC})_{t_3} + (\text{ET} - \text{A1})_{t_3} \quad (37)$$

$$t_3(\text{UT1}) = t_3(\text{ST}) + (\text{UTC} - \text{ST})_{t_3} + (\text{A1} - \text{UTC})_{t_3} - (\text{A1} - \text{UT1})_{t_3} \quad (38)$$

Using the expressions for these time transformations from Part II (SPS 37-39, Vol. III, pp. 36-38), we obtain

$$\frac{\partial t_3(\text{ET})}{\partial \Delta T_{1958}} = \frac{\partial (\text{ET} - \text{A1})_{t_3}}{\partial \Delta T_{1958}} = 1 \quad (39)$$

$$\frac{\partial t_3(\text{ET})}{\partial \Delta f_{cesium}} = \frac{\partial (\text{ET} - \text{A1})_{t_3}}{\partial \Delta f_{cesium}} = - \frac{[\text{JD}(t_3) - 243,6204.5] 86,400}{9,192,631,770} \quad (40)$$

$$\frac{\partial t_3(\text{UT1})}{\partial \Delta T_{1958}, \Delta f_{cesium}} = 0 \quad (41)$$

Differentiating the light-time equation for the down leg with respect to ΔT_{1958} , Δf_{cesium} using Eqs. (39), (40), and (41) gives

$$\frac{\partial t_2(\text{ET})}{\partial \Delta T_{1958}} = \left(1 - \frac{\mathbf{r}_{23}^*}{c}\right) \frac{\partial (\text{ET} - \text{A1})_{t_3}}{\partial \Delta T_{1958}} \quad \Delta T_{1958} \rightarrow \Delta f_{cesium} \quad (42)$$

where

$$\mathbf{r}_{23}^* = \frac{\mathbf{r}_{23}}{r_{23}} \cdot [\mathbf{r}_E^S(t_3) - \mathbf{r}_2^S(t_2)] \quad (43)$$

Differentiating the light-time equation for the up leg with respect to ΔT_{1958} , Δf_{cesium} using Eq. (42) and

$$t_1(\text{UT1}) = t_1(\text{ET}) - (\text{ET} - \text{A1})_{t_1} - (\text{A1} - \text{UT1})_{t_1} \quad (44)$$

gives [assuming $\partial(\text{ET} - \text{A1})_{t_1}/\partial\Delta f_{\text{cesium}}$ appearing in a $1/c$ term equals $\partial(\text{ET} - \text{A1})_{t_3}/\partial\Delta f_{\text{cesium}}$]:

$$\frac{\partial t_1(\text{ET})}{\partial \Delta T_{1958}} = \left[1 - \frac{1}{c} (\dot{r}_{12}^* + \dot{r}_{23}^*) \right] \frac{\partial(\text{ET} - \text{A1})_{t_3}}{\partial \Delta T_{1958}} \quad \Delta T_{1958} \rightarrow \Delta f_{\text{cesium}} \quad (45)$$

where

$$\dot{r}_{12}^* = \frac{\mathbf{r}_{12}}{r_{12}} \cdot [\dot{\mathbf{r}}_2^s(t_2) - \dot{\mathbf{r}}_E^s(t_1)] \quad (46)$$

The result (Eq. 45) also follows directly from differentiation of the light-time equations, holding t_3 (UT1) and t_1 (UT1) constant. Differentiating Eq. (44) with respect to ΔT_{1958} and Δf_{cesium} using Eqs. (39), (40), and (45) gives

$$\frac{\partial t_1(\text{UT1})}{\partial \Delta T_{1958}} = -\frac{1}{c} (\dot{r}_{12}^* + \dot{r}_{23}^*) \quad (47)$$

$$\frac{\partial t_1(\text{UT1})}{\partial \Delta f_{\text{cesium}}} = \frac{[\text{JD}(t_1) - 243,6204.5] 86,400}{9,192,631,770} - \left[1 - \frac{1}{c} (\dot{r}_{12}^* + \dot{r}_{23}^*) \right] \frac{[\text{JD}(t_3) - 243,6204.5] 86,400}{9,192,631,770} \quad (48)$$

Using Eqs. (39)–(42) and Eq. (45), the partial derivative of a doppler observable with respect to ΔT_{1958} or Δf_{cesium} due to a variation in $(\text{ET} - \text{A1})$ in the light-time solution is:

$$\begin{aligned} \frac{\partial z}{\partial \Delta T_{1958}} = & \left\{ \frac{\partial z}{\partial \mathbf{X}_3^s(t_3)} \dot{\mathbf{X}}_E^s(t_3) + \frac{\partial z}{\partial \mathbf{X}_2^s(t_2)} \dot{\mathbf{X}}_2^s(t_2) \left(1 - \frac{\dot{r}_{23}^*}{c} \right) + \frac{\partial z}{\partial \mathbf{X}_1^s(t_1)} \dot{\mathbf{X}}_E^s(t_1) \left[1 - \frac{1}{c} (\dot{r}_{12}^* + \dot{r}_{23}^*) \right] \right\} \frac{\partial(\text{ET} - \text{A1})_{t_3}}{\partial \Delta T_{1958}} \\ & + \frac{\partial z}{\partial \mathbf{X}_1^s(t_1)} \dot{\mathbf{X}}_1^E(t_1) \frac{\partial t_1(\text{UT1})}{\partial \Delta T_{1958}} \quad \Delta T_{1958} \rightarrow \Delta f_{\text{cesium}} \end{aligned} \quad (49)$$

where use is made of Eqs. (39), (40), (47), and (48). For angular observables, there are only two participants and the terms containing the factor $\partial z/\partial \mathbf{X}_1^s(t_1)$ are omitted.

d. Parameters affecting transformation (UTC – ST): a , b , and c . The transformation from station time ST at the receiving station to UTC is given by

$$(\text{UTC} - \text{ST}) = a_R + b_R t + c_R t^2 \quad (50)$$

where the coefficients a_R , b_R , and c_R are specified by time block (the subscript R denoting the receiving station for the observable), and the argument t is seconds past the start of the time block.

The values of a_R , b_R , and c_R affect the value of t_3 (equally in all time scales), and hence also affect the values of t_2 and t_1 from the light-time solution. From Eqs. (37), (38), and (50) above and Eqs. (44) and (45) of Part V (SPS 37-42, Vol. III, p. 19), the derivative of a doppler observable with respect to a_R is given by

$$\frac{\partial z}{\partial a_R} = \frac{\partial z}{\partial \mathbf{X}_3^s(t_3)} \dot{\mathbf{X}}_3^s(t_3) + \frac{\partial z}{\partial \mathbf{X}_2^s(t_2)} \dot{\mathbf{X}}_2^s(t_2) \left(1 - \frac{\dot{r}_{23}^*}{c} \right) + \frac{\partial z}{\partial \mathbf{X}_1^s(t_1)} \dot{\mathbf{X}}_1^s(t_1) \left[1 - \frac{1}{c} (\dot{r}_{12}^* + \dot{r}_{23}^*) \right] \quad (51)$$

For angular observables, omit the last term of Eq. (51). For doppler or angular observables,

$$\frac{\partial z}{\partial b_R} = \frac{\partial z}{\partial a_R} t_3 \quad (52)$$

where t_3 is the reception time of the signal measured in seconds past the start of the current time block for a_R , b_R , and c_R . Similarly,

$$\frac{\partial z}{\partial c_R} = \frac{\partial z}{\partial a_R} t_3^2 \quad (53)$$

6. Partial Derivatives of Doppler and Angular Observables With Respect to Parameter Vector, Holding State Vectors Fixed

a. Introduction. This section gives the partial derivatives of doppler and angular observables with respect to those parameters that affect the data directly, holding the state vectors of each participant constant. The only parameters in this category that significantly affect the observables are the speed of light c appearing in the doppler formulation and the small rotations η' , ϵ , ζ' or η , ϵ , ζ of the reference coordinate system for angular observables at the tracking station.

The unit vectors **P**, **Q**, **E** to which HA, δ are referenced, and **N**, **E**, **Z** to which σ , γ ; X , Y ; and X' , Y' are referenced,⁸ are functions of the station coordinates. However, for a 100-m change in station location, the maximum change in orientation of any of these unit vectors is only 3", which is less than the 36" accuracy of directly observed angular position. Thus, the partial derivatives of angular observables with respect to this particular effect of change in station coordinates are ignored.

In order to compute the unit vectors **P**, **Q**, **E** and **N**, **E**, **Z**, the sidereal time θ is also required, which is primarily a function of the reception time t_3 in the UT1 time scale. The solve-for parameters that affect t_3 (UT1) are a , b , and c at the receiving station. The uncertainty in $a + bt + ct^2$ should be of order 10^{-3} sec. Multiplying this by the rotation rate of the Earth (15"/sec) gives an uncertainty of 0.015 in sidereal time, which is negligible in view of the 36" accuracy of directly observed angular position. Therefore, the partial derivatives of angular observables with respect to this particular effect of a change in a , b , and c at the receiving station are ignored.

b. Speed of light c . Two-way doppler is computed from Eqs. (6), (34), and (60) of Part V (SPS 37-42, Vol. III, pp. 15-21). The speed of light c appears explicitly in the

latter two expressions, which may be written as

$$\left(1 - \frac{f_R}{f_T}\right) = \frac{D_1}{c} + \frac{D_2}{c^2} + \dots \quad (54)$$

$$\left(1 - \frac{f_R}{f_T}\right)^{**} = \frac{\ddot{D}_1}{c} + \frac{\ddot{D}_2}{c^2} + \dots \quad (55)$$

The derivative of \bar{f} with respect to c appearing explicitly in the formulation is given by

$$\frac{\partial \bar{f}}{\partial c} = -\frac{1}{c} C_3 f_q(t_1) \left[\left(\frac{D_1}{c} + 2 \frac{D_2}{c^2} \right) + \frac{T_c^2}{24} \left(\frac{\ddot{D}_1}{c} + 2 \frac{\ddot{D}_2}{c^2} \right) \right] \quad (56)$$

c. Rotations η' , ϵ , ζ' or η , ϵ , ζ of reference coordinate system for angular observables. Eqs. (49), (51), and (56)-(61) of Part VI (SPS 37-43, Vol. III, pp. 34-35) give corrections to the computed values of the directly observed angles as linear functions of the small rotations of the reference coordinate system about each of its three mutually perpendicular axes. The coefficients of each equation are the partial derivatives of the angular observable with respect to the three rotations affecting it.

7. Partial Derivatives of Range Observables With Respect to Parameter Vector

a. Observable formulation. The formulation for computing range observables was given in Section 3 of Part V (SPS 37-42, Vol. III, p. 21); it is repeated here in more detail. The general expression for the range observable ρ is

$$\rho = \left[t_3(\text{ST}) - t_1(\text{ST}) + \frac{R_c}{10^3 c} + \frac{\Delta_r \rho_3 + \Delta_r \rho_1}{c} \right] F \quad (57)$$

where

$t_3(\text{ST})$ = data time tag, reception time of signal at tracking station, station time

$t_1(\text{ST})$ = transmission time of signal at tracking station, station time

R_c = a constant solve-for range bias, m. R_c is specified for each station by time block

c = solve-for value of speed of light, km/sec

$\Delta_r \rho_3$ = down-leg refraction correction, km

$\Delta_r \rho_1$ = up-leg refraction correction, km

F = units conversion factor

⁸Terms are defined in Part VI; SPS 37-43, Vol. III.

For ρ in pseudo-one-way kilometers,

$$\rho \text{ (km/2)}; \quad F = 149,896.25 \text{ km/sec}$$

For ρ in range units (RU), where 1 RU \approx 1.04 one-way meters, mod 785762208,

$$\rho \text{ (RU)}; \quad F = \frac{96}{16} \frac{240}{221} f_q(t_1)$$

where

$f_q(t_1)$ = transmitter reference oscillator frequency (S-band) at time t_1 relative to transmitter rubidium frequency standard.

For ρ in nanoseconds, mod 1.00947×10^9 ,

$$\rho \text{ (nsec)}; \quad F = 10^9$$

Time is accounted for in the DPODP as double precision seconds past January 1, 1960, 0^h. From approximately 1953 to 1982, time is represented to a precision of 10^{-7} sec. For each observable, the light-time problem is solved giving the epochs of participation t_3 , t_2 , and t_1 to 10^{-7} sec. A precision value of the light time $(t_j - t_i)_{ET}$ for each leg of the light path is then computed from the light-time equation (Eqs. 16 or 19 of Part IV; SPS 37-41, Vol. III, p. 33), with the right-hand side evaluated with the epochs of participation accurate to 10^{-7} sec. For a participant heliocentric velocity of 1000 km/sec, the precision light time for each leg of the light path will be accurate to at least 0.3×10^{-9} sec or 0.1 m.

The round-trip light time in seconds of ephemeris time is given by

$$(t_3 - t_1)_{ET} = (t_3 - t_2)_{ET} + (t_2 - t_1)_{ET} \quad (58)$$

where $(t_3 - t_2)_{ET}$ and $(t_2 - t_1)_{ET}$ are the precision values of the light time for the down and up legs, respectively, computed as indicated above.

The round-trip light time in seconds of station time is computed from

$$\begin{aligned} t_3(\text{ST}) - t_1(\text{ST}) &= (t_3 - t_1)_{ET} \\ &\quad - (ET - A1)_{t_3} + (ET - A1)_{t_1} \\ &\quad - (A1 - UTC)_{t_3} + (A1 - UTC)_{t_1} \\ &\quad - (UTC - ST)_{t_3} + (UTC - ST)_{t_1} \end{aligned} \quad (59)$$

The transformation of round-trip light time from ephemeris time to station time does not degrade the precision of 10^{-9} sec or better. The maximum value of a time transformation is about 30 sec; therefore, in double precision it is computed to a precision of at least 10^{-14} sec.

b. Partial derivatives. The partial derivative of range ρ with respect to \mathbf{q} is the sum of several terms in this section.

The heliocentric state vectors of each participant are functions of \mathbf{q} , and hence the epochs of participation t_2 and t_1 obtained from the solution of the light-time problem will also vary with \mathbf{q} . The partial derivative of ρ with respect to \mathbf{q} due to this effect is given by

$$\frac{\partial \rho}{\partial \mathbf{q}} = -F \frac{\partial t_1(\text{ET})}{\partial \mathbf{q}} \quad (60)$$

where $\partial t_1(\text{ET})/\partial \mathbf{q}$ is computed from Eqs. (3)–(5), (9), and (10). In the derivation of Eq. (60), the derivative $dt_1(\text{ST})/dt_1(\text{ET})$ is taken to be unity. This is accurate to eight significant figures.

The speed of light c affects the solution of the light-time problem for the epochs of participation and also affects the data directly (see Eq. 57). Hence,

$$\frac{\partial \rho}{\partial c} = -F \left[\frac{\partial t_1(\text{ET})}{\partial c} + \frac{R_c}{10^3 c^2} \right] \quad (61)$$

where $\partial t_1(\text{ET})/\partial c$ is given by Eqs. (31) and (32).

Additional terms to $\partial \rho/\partial \mathbf{q}$ arise due to variation of ΔT_{1958} , Δf_{cesium} , and a , b , and c in the time transformations used in the light-time solution. Considering Eq. (44) and

$$\begin{aligned} t_1(\text{ST}) &= t_1(\text{ET}) - (ET - A1)_{t_1} - (A1 - UTC)_{t_1} \\ &\quad - (UTC - ST)_{t_1} \end{aligned} \quad (62)$$

the partial derivatives of $t_1(\text{ST})$ with respect to ΔT_{1958} and Δf_{cesium} are given by Eqs. (47) and (48); namely,

$$\frac{\partial t_1(\text{ST})}{\partial \Delta T_{1958}} = -\frac{1}{c} (\dot{r}_{12}^* + \dot{r}_{23}^*) \quad (63)$$

$$\frac{\partial t_1(\text{ST})}{\partial \Delta f_{\text{cesium}}} = \frac{[\text{JD}(t_1) - 243,6204.5] 86,400}{9,192,631,770} - \left[1 - \frac{1}{c} (\dot{r}_{12}^* + \dot{r}_{23}^*) \right] \frac{[\text{JD}(t_3) - 243,6204.5] 86,400}{9,192,631,770} \quad (64)$$

The partial derivatives of $t_1(\text{ST})$ with respect to variations of a , b , and c in $(\text{UTC} - \text{ST})_{t_3}$ are given by

$$\frac{\partial t_1(\text{ST})}{\partial a(t_3)} = 1 - \frac{1}{c} (\dot{r}_{12} + \dot{r}_{23}) \quad (65)$$

$$\frac{\partial t_1(\text{ST})}{\partial b(t_3)} = t_3 \left[1 - \frac{1}{c} (\dot{r}_{12} + \dot{r}_{23}) \right] \quad (66)$$

$$\frac{\partial t_1(\text{ST})}{\partial c(t_3)} = t_3^2 \left[1 - \frac{1}{c} (\dot{r}_{12} + \dot{r}_{23}) \right] \quad (67)$$

where t_3 is the reception time of the signal measured in seconds past the start of the time block for a , b , and c containing t_3 . Considering Eq. (62), the partial derivatives of $t_1(\text{ST})$ with respect to variations of a , b , and c in $(\text{UTC} - \text{ST})_{t_1}$ are given by

$$\frac{\partial t_1(\text{ST})}{\partial a(t_1)} = -1 \quad (68)$$

$$\frac{\partial t_1(\text{ST})}{\partial b(t_1)} = -t_1 \quad (69)$$

$$\frac{\partial t_1(\text{ST})}{\partial c(t_1)} = -t_1^2 \quad (70)$$

where t_1 is the transmission time of the signal measured in seconds past the start of the time block for a , b , and c containing t_1 . In general, t_3 and t_1 will fall within the same time block, so that the partial derivatives given by Eqs. (68)–(70) are associated with the same parameters as those in Eqs. (65)–(67).

Letting $p_i = \Delta T_{1958}$, Δf_{cesium} , or a , b , and c at t_3 and t_1 , $\partial \rho / \partial p_i$ due to variation of p_i in the time transformations of the light-time solutions is given by

$$\frac{\partial \rho}{\partial p_i} = -F \frac{\partial t_1(\text{ST})}{\partial p_i} \quad (71)$$

where $\partial t_1(\text{ST}) / \partial p_i$ is given by Eqs. (63)–(70).

The partial derivative of ρ with respect to R_c is given by

$$\frac{\partial \rho}{\partial R_c} = \frac{F}{10^8 c} \quad (72)$$

The partial derivative $\partial \rho / \partial q_i$ for range observables is computed as the sum of the terms given above, where each term $\partial \rho / \partial q_i$ must be placed in the proper column of $\partial \rho / \partial q_i$.

E. Lunar Orbiter D — Slant Range Rates and Accelerations, R. A. Wallace

The first launch dates for *Lunar Orbiter D* are scheduled for early May 1967. Unlike previous *Lunar Orbiter* missions, the primary objective of this mission will be to photograph 85% of the front side of the Moon at resolutions between 50 and 100 m. To do this, a high-altitude lunar orbit will be used in conjunction with the high-resolution (24-in.) telephoto lens. There will be no preliminary orbit; the deboost maneuver will inject the spacecraft directly into the final picture-taking orbit. Some orbital characteristics are given below:

Semimajor axis, 6143.2893 km

Eccentricity, 0.3068543

Inclination (to true lunar equator), 85.00 deg

Period, 720.1 min

Perilune altitude, 2520 km

Apolune altitude, 6290 km

The inertial attitude of this orbit results in two phenomena that did not occur for the first three *Lunar Orbiters*. Because the Sun–Moon line will be almost perpendicular to the spacecraft lunar orbit early in the mission, Sun occultation will not occur until two or three months of orbital flight. The spacecraft will be in sunlight during this whole time. Another characteristic of this trajectory is the absence of Earth occultation for the first ten days of lunar orbit. Continuous tracking may be possible, contingent on tracking station availability.

Since this mission *does* result in a significantly different lunar orbit design than the DSN has seen before, a review of the slant range rate and acceleration variations in lunar orbit is appropriate. The orbital injection conditions (i.e.,

conditions immediately following the powered insertion into lunar orbit) were obtained from The Boeing Company, and a trajectory was computed. The injection conditions used are given below:

Orbit: *Lunar Orbiter D* final orbit

Epoch (post-deboost): May 7, 1967, 14^h30^m32^s GMT

Coordinate system: Selenocentric Cartesian, referenced to Earth equator and equinox of 1950.0

Injection conditions:

$$X = -651.9317 \text{ km}$$

$$Y = +1820.2578 \text{ km}$$

$$Z = -5436.0915 \text{ km}$$

$$\dot{X} = +0.91612277 \text{ km/sec}$$

$$\dot{Y} = -0.21800452 \text{ km/sec}$$

$$\dot{Z} = +0.12077533 \text{ km/sec}$$

Rates and accelerations were determined for two time periods during the mission. The first period covers the first 32 hr in lunar orbit (see Figs. 9-12); the second period covers the time when the orbit is seen edge-on from the Earth (hence, the occurrence of Earth occultations).

The rates and acceleration for the second time period are shown in Figs. 13-16. The highest rates and accelerations occur during the second time period, from injection plus 9 days and 20 hr to injection plus 11 days and 4 hr. Note that the scales on the second time period plots for acceleration differ from those on the first time period plots.

The plots represent the full range of the values of rates and accelerations that can be expected on the *Lunar Orbiter D* mission. Thus, range rates will lie between ± 1.3 km/sec and range accelerations between ± 0.0003 km/sec².

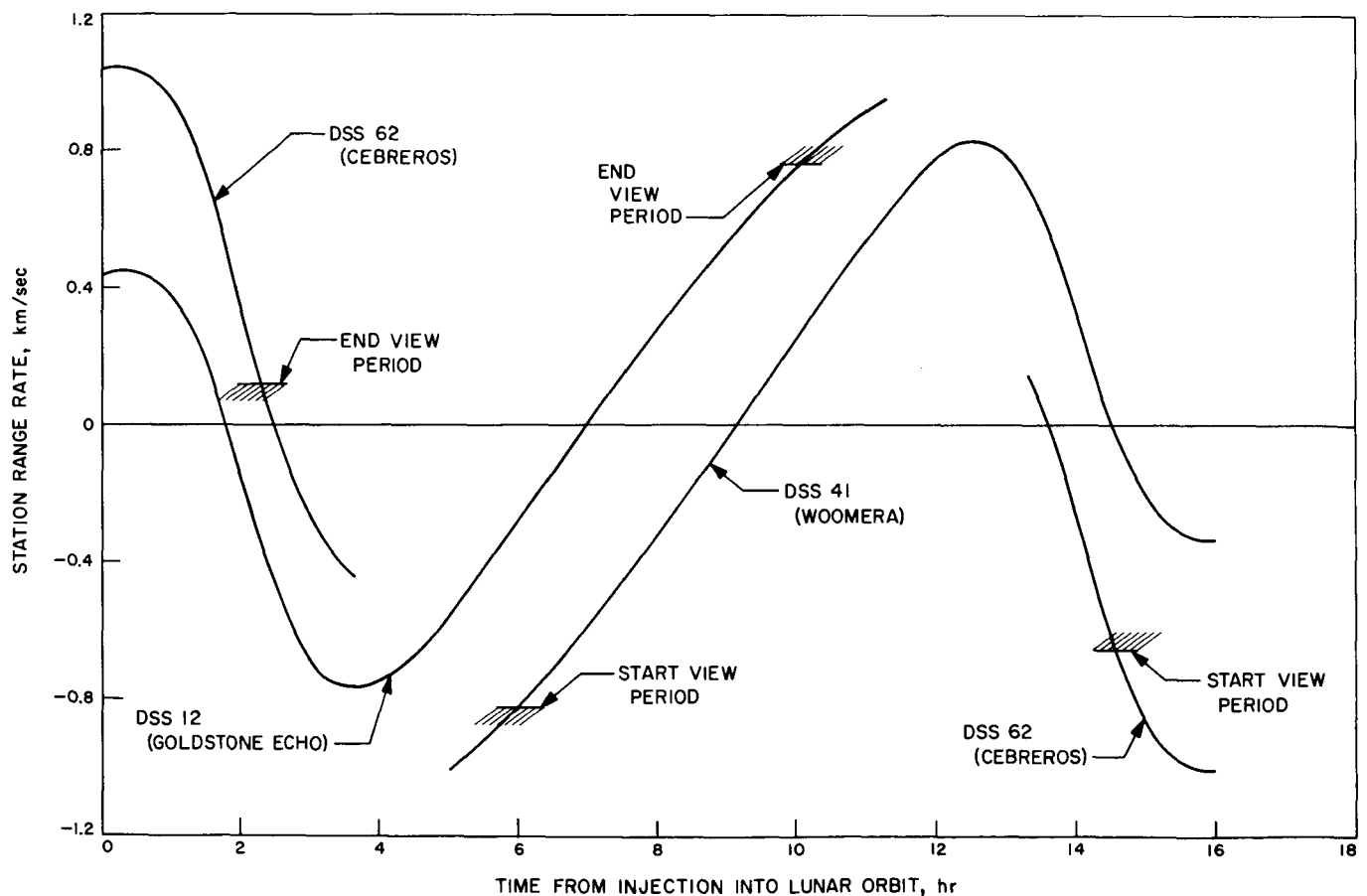


Fig. 9. *Lunar Orbiter D* slant range rate: 0-16 hr from injection into lunar orbit

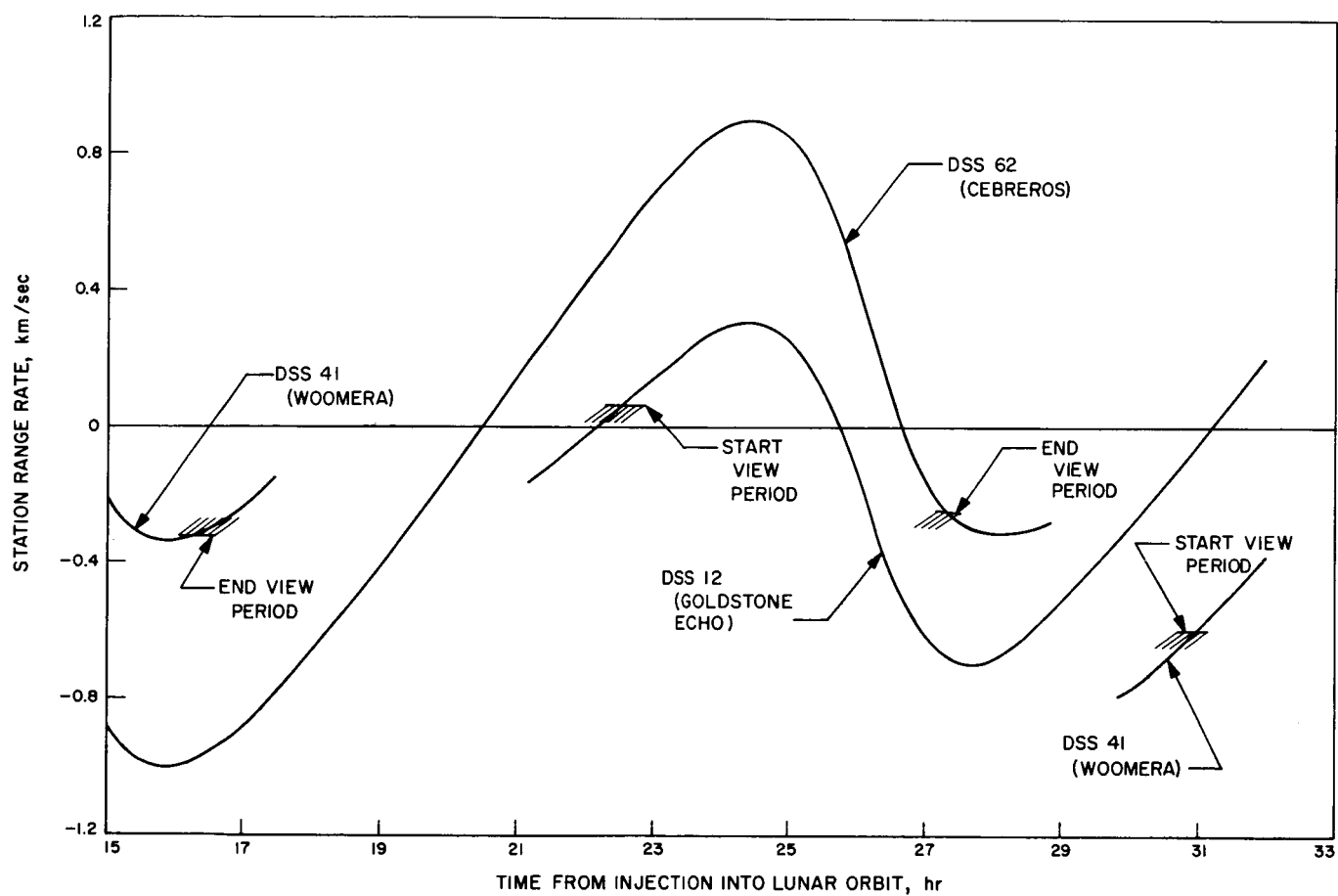


Fig. 10. Lunar Orbiter D slant range rate: 15-32 hr from injection into lunar orbit

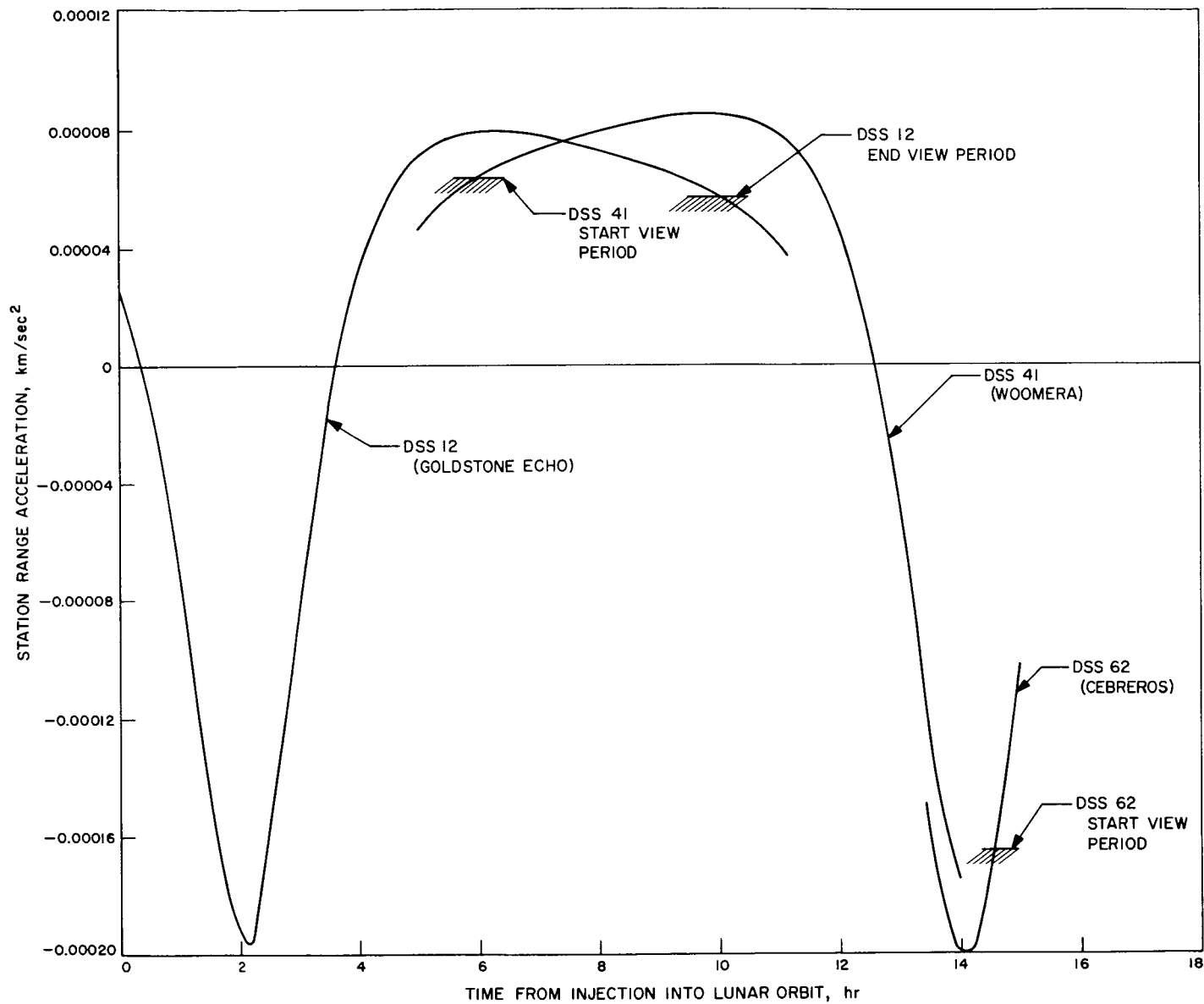


Fig. 11. Lunar Orbiter D slant range acceleration: 0-16 hr from injection into lunar orbit

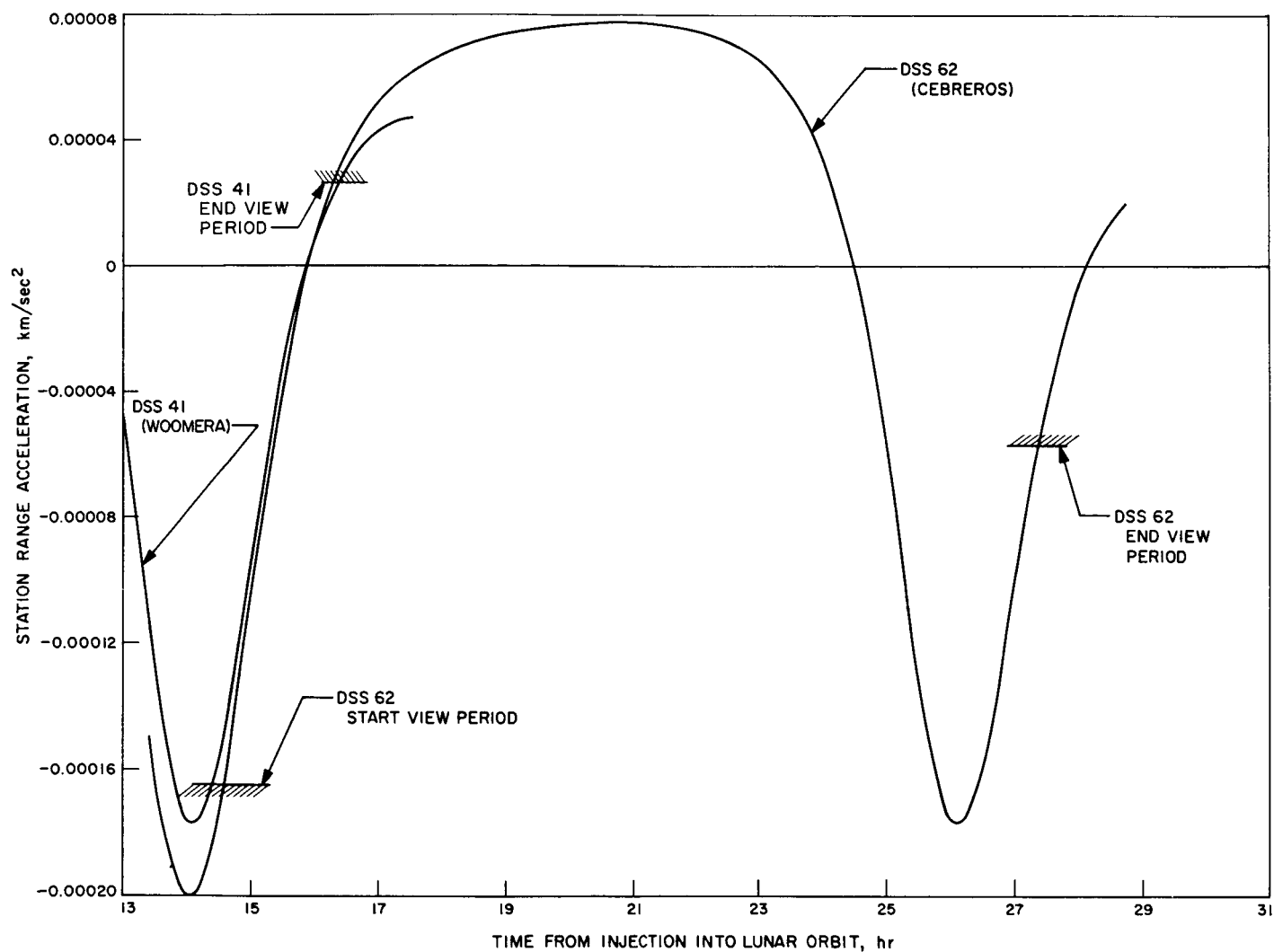


Fig. 12. Lunar Orbiter D slant range acceleration: 13–29 hr from injection into lunar orbit

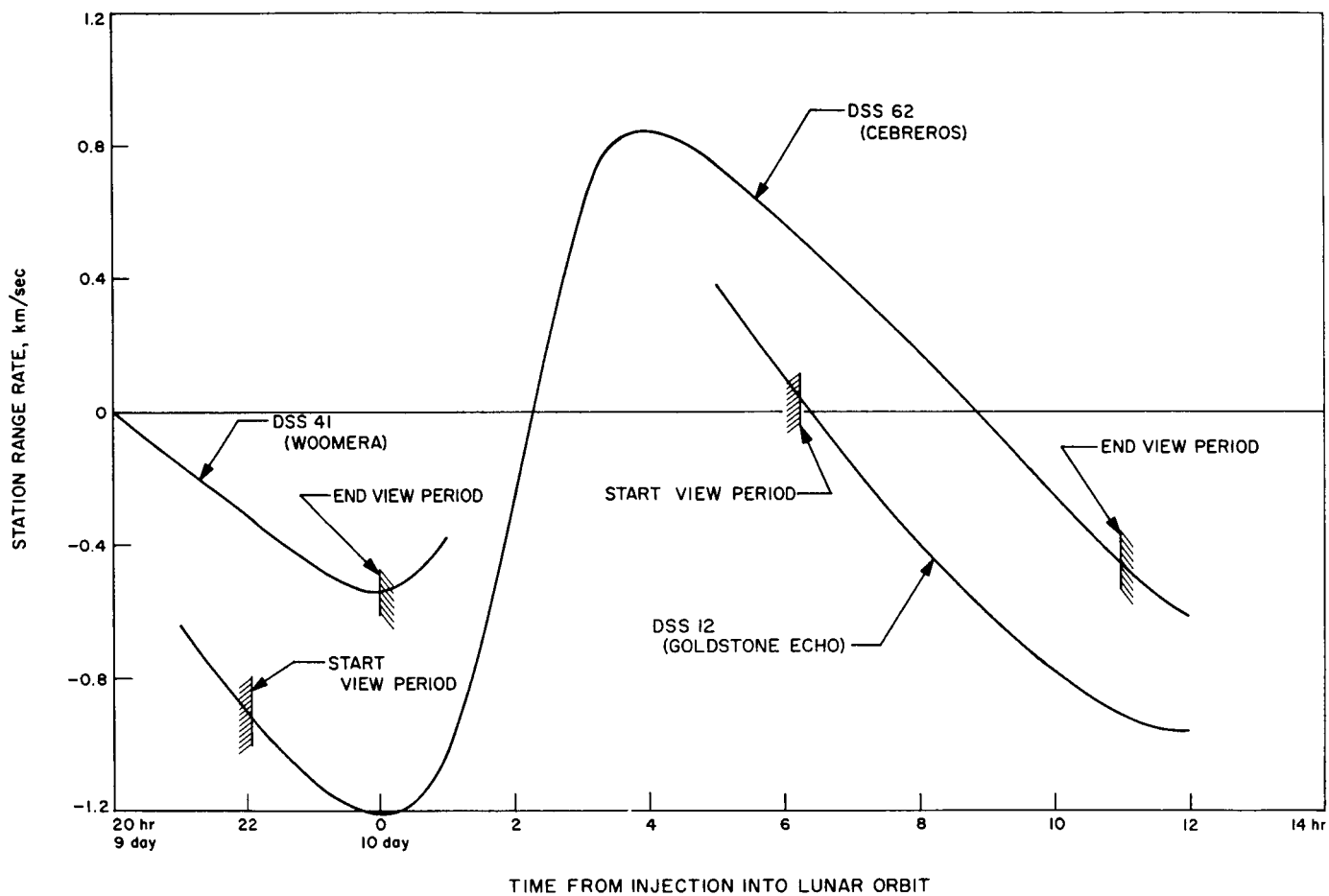


Fig. 13. Lunar Orbiter D slant range rate: 9.8–10.5 days from injection into lunar orbit

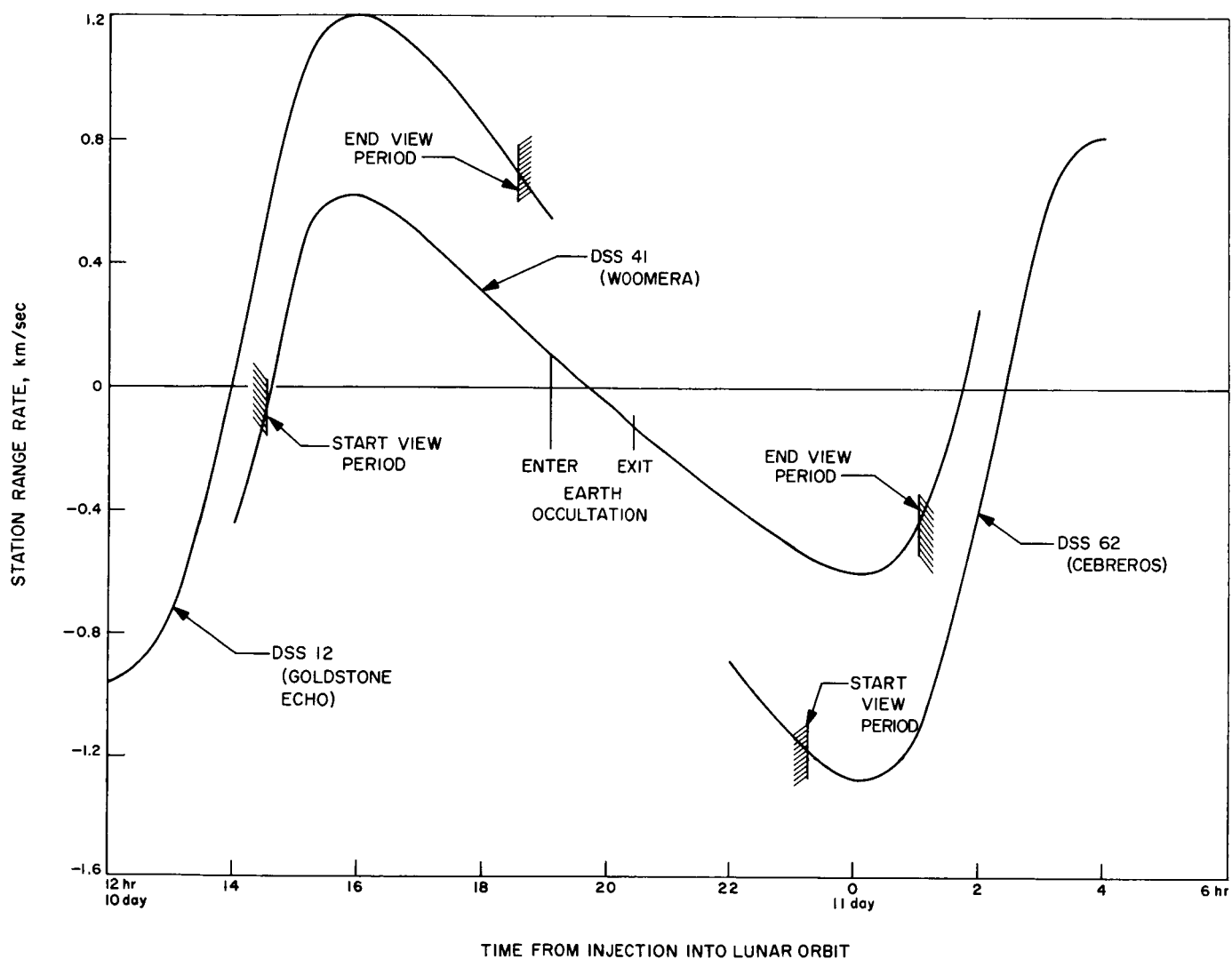


Fig. 14. Lunar Orbiter D slant range rate: 10.5–11.2 days from injection into lunar orbit

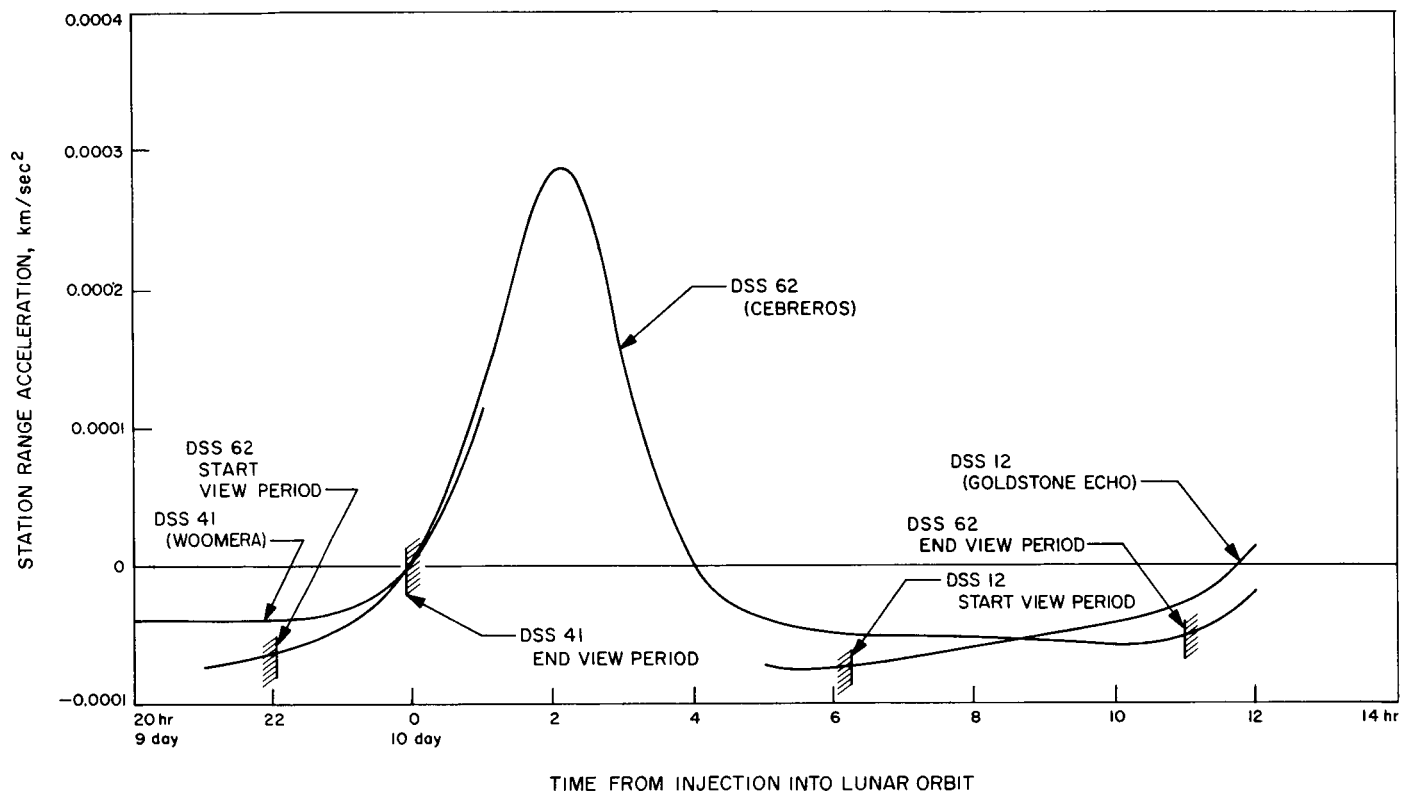


Fig. 15. Lunar Orbiter D slant range acceleration: 9.8–10.5 days from injection into lunar orbit

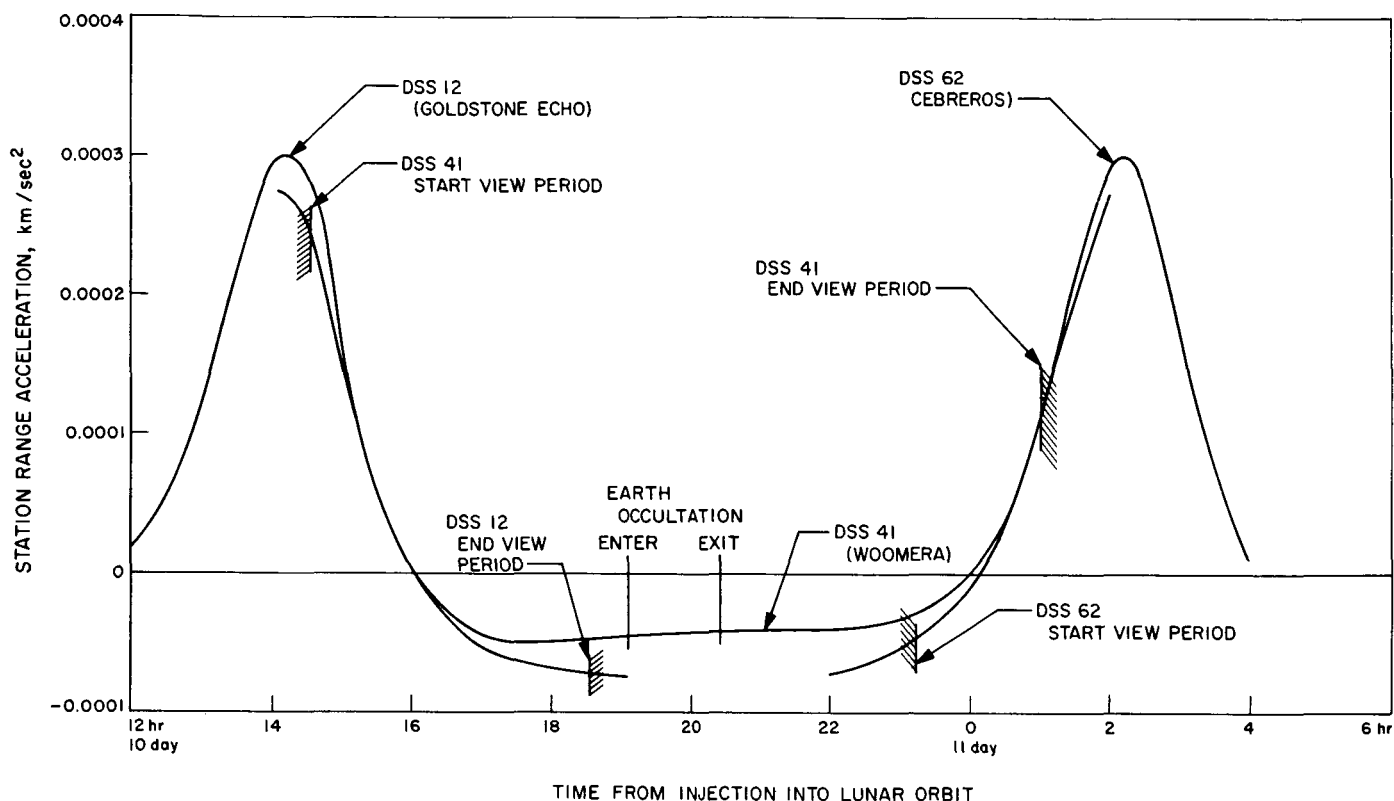


Fig. 16. Lunar Orbiter D slant range acceleration: 10.5–11.2 days from injection into lunar orbit

References

1. Yumi, S., *Annual Report of the International Polar Motion Service for 1962*, International Polar Motion Service Observatory, Mizusawa, Japan, 1964.
2. *Explanatory Supplement to the Ephemeris*, Her Majesty's Stationery Office, London, 1961.
3. Chandler, C. S., *Astronomical Journal*, Vol. 11, p. 65, 1891; Vol. 12, p. 97, 1892 (see articles on polar motion).
4. Markowitz, W., "Latitude, Longitude, and the Secular Motion of the Pole," Reprinted by the U.S. Naval Observatory from *Methods and Techniques in Geophysics*, edited by Runcorn, Interscience Publishers Ltd., London, 1960.
5. Hattori, T., "On the Prediction of Latitude Variation," *Publications of the International Latitude Observatory of Mizusawa*, Vol. II, No. 2, p. 113, 1956.

N67-30373

3 Communications Research and Development 4

A. Demonstration of Error Detection and Correction for DSN Teletype, H. M. Fredericksen and E. C. Posner

1. Introduction

An error-correcting encoder-decoder has been demonstrated on DSN teletype lines. The system uses an SDS 910 computer as "prototype communications processor," together with associated comm buffer. Thirty-six bits are encoded into 60 bits; each teletype character corresponds to a four-bit symbol. The system is capable of correcting up to two symbol errors in a code word of 15 symbols, and detecting up to four symbol errors. In addition, synchronization errors caused by insertions or deletions of characters are detected. The system is compatible with NASCOM constraints, and has been demonstrated over NASCOM lines. The undetected error probability per coded word using this system is about 0.5×10^{-8} in the worst (noisiest) case; the probability of a detected but uncorrected error (including sync errors) is about 1 in 200 in the worst case. These characteristics make the error-correction system ideal for transmitting spacecraft commands generated in the SFOF at JPL to the deep space stations.

2. Design Constraints

For sending commands generated at JPL to the overseas deep space stations for transmission to spacecraft, the utmost reliability is needed. That is, the probability of an undetected error must be extremely small. Furthermore, since the bit rate for teletype is only 25 bits/sec, to repeat a command would add delay to the link. This could prove intolerable in certain situations. Therefore, the probability of needing a repeat should be kept moderately low.

But before designing a coding system to meet these constraints, the characteristics of the inter-DSN teletype circuits must be determined. Experiments performed at JPL to determine the error characteristics of DSN teletype lines are described in SPS 37-30, Vol. III, pp. 91-93; SPS 37-31, Vol. III, pp. 76-78; SPS 37-32, Vol. III, pp. 51-54; SPS 37-33, Vol. III, pp. 109-110; and SPS 37-34, Vol. III, pp. 64-68. It was found that, even in the worst cases, the character error probability is, at most, 0.02. Furthermore, there is a probability of sync error (insertion or deletion of a teletype character) of 10^{-4} ; this latter probability is for the worst case of character error.

It was determined that the proposed system should be judged on the basis of its worst-case performance; so it is assumed that the teletype channel has a character error probability of 0.02 and an insertion-deletion probability of 10^{-4} . The aforementioned experiments showed that an insertion is about as likely as a deletion (this fact is not important in the calculations to follow), and that sync errors occur independently of character errors.

However, there are constraints on a proposed coding-decoding system other than performance. For one thing, DSN teletype destined for Europe goes through speed-change equipment in London to conform to European speeds. If all 32 five-tuples of the five level teletype were used, then such characters as *carriage return* and *line feed* would occur randomly, and those monitoring the JPL transmissions in London might well assume that the equipment was failing and interrupt the transmission. It was therefore decided to use only the first four teletype levels, the fifth being often the noisiest anyway. This is the solution presently adopted also in uncoded DSN teletype for telemetry and commands. The four-bit units we then have at our disposal are called "symbols." By adding a suitable fifth bit to the symbols, the forbidden characters can be avoided. The structure chosen yields all alphabetic characters; sometimes odd parity is used and sometimes even parity.

There are still other constraints on a coding-decoding system due to the fact that all transmissions go through the NASCOM comm processor at Goddard Space Flight Center for switching to the proper destination. This processor does not pass a *blank*; so the *all zero* character must be avoided. Thus, if the *all zero* symbol (four-tuple) is to be sent, the fifth teletype level must be a *one*. Also, the triple *Figures-H-Letters* must be avoided in the message, for the NASCOM comm processor will stop the transmission when it detects this standard *end of message* triple.

Further constraints are imposed by the necessity of having the proper NASCOM header and closing at the end of every coded message. Thus, the encoder for the proposed system must be able to put on and take off such headers, and the decoder must be able to detect the start of the actual encoded message.

A final constraint is that the encoding and decoding are to be done in a standard SDS 910 computer with comm buffer, since this configuration is close to DSN standard.

Now that all the requirements of our encoding-decoding system are known, we can describe the teletype error correction and detection system.

3. The Code

It was decided to use a code over the 16-element field. That is, each symbol of four bits corresponds to one of the 16 elements of the finite field. The field is regarded as consisting of 0 and 15 powers of the quantity β , where

$$\beta^4 = \beta + 1.$$

The four-tuple (d_3, d_2, d_1, d_0) then corresponds to the element

$$d_0 + d_1\beta + d_2\beta^2 + d_3\beta^3,$$

where the coefficients d_0, d_1, d_2, d_3 corresponding to β^k , $0 \leq k \leq 14$, are given in Table 1. Also given are various forms of the field elements. A more detailed description of the algebraic theory behind this coding-decoding scheme will appear in SPS 37-45, Vol. IV.

The code chosen was the Reed-Solomon code over the 16-element field SPS 37-35, Vol. III, pp. 71-76; SPS 37-36, Vol. III, pp. 66-67; SPS 37-37, Vol. III, pp. 49-50; SPS 37-39, Vol. III, pp. 47-48; and SPS 37-40, Vol. III, pp. 8-11. This code consists of code words 15 symbols long. The first nine symbols are information symbols, and the last six symbols are check symbols. Thus, the code has rate $9/15 = 0.6$. Each code word has 36 information bits in it, which is about right for one command, or perhaps half a command, depending on the spacecraft.

Any two code words are at least seven symbols apart, so the code could be used to correct three errors. However, to meet the constraints on error probability, it was decided to use the code so as to correct up to two symbol errors and detect up to four symbol errors. If a detected but uncorrectable error appears, a retransmission is called for.

To take sync errors into account, the following synchronization scheme has been devised: To each encoded word of length 15, add the 15-tuple γ where

$$\gamma = (0, 0, 0, 0, 0, 0, 0, 0, \beta^{13}, \beta^{13}, \beta, \beta^{12}, \beta, \beta^8);$$

as teletype characters,

$$\gamma = (T, T, T, T, T, T, T, T, X, X, L, F, L, Y).$$

The added word is then stripped off before decoding. This word has the property that when added to any code

word, it produces a word at least six places away from any code word. More important, the 14 words

$$\gamma + T^i \gamma, 1 \leq i \leq 14,$$

have the same property. This makes insertion or deletion errors very easy to detect, since they appear as uncorrectable errors. Retransmission is then called for.

Words are encoded as follows: First, information needed for the NASCOM header is entered into the prototype communications processor. This information includes day of month, Greenwich Mean Time, etc. An indication is then given to the machine that the bits of the message start.

Thirty-six bits are read in as nine four-tuples a_0, \dots, a_8 . The check symbols are added, according to the linear recursion rule

$$a_{n+9} = \beta^3 a_{n+8} + \beta^{13} a_{n+7} + \beta^{10} a_{n+6} + \beta^{10} a_{n+5} + \beta^{14} a_{n+4} \\ + \beta^7 a_{n+3} + \beta^3 a_{n+2} + \beta a_{n+1} + \beta^6 a_n,$$

where $0 \leq n \leq 5$.

This produces six more field elements, which form the last six symbols a_9, \dots, a_{14} of the code word. The sync word γ is now added to form the sync-protected code word. The fifth teletype level is now added so as to satisfy the constraints of the preceding section (see the last column of Table 1). All this takes milliseconds on the machine.

As many blocks of 36 bits are entered as necessary to constitute a message, and then the machine is told that the information bits have ended. NASCOM "tailer" information is then added, and the machine now outputs to the teletype lines. First comes the proper NASCOM header as prepared from the input information given to the machine. Then comes the code words, then the NASCOM tailer. The teletype is sent out by a comm buffer under control by the SDS 910 via the SDS 910's interrupt feature. The teletype message now goes to NASCOM, where it is routed to its destination according to information in the header.

Fig. 1 (a) and (b) shows a typical outgoing message and various stages in the encoding. Thus, we have 72 information bits, two nine-tuples of field elements, two 15-tuples of code words, two 15-tuples of sync-protected code words, two 15-tuples of teletype characters which are the two sync-protected code words with fifth level added, the same two 15-tuples in standard teletype correspondence, and the actual transmitted message includ-

Table 1. The 16-element field

Addition: Modulo 2 addition of four-tuples Multiplication: $\beta^i \cdot \beta^j = \beta^{i+j}$; $i + j$ is reduced Modulo 15, if necessary				
Field element	Beta polynomial	Four-tuple	SDS code	Teletype code
0		(0,0,0,0)	0	T
1	1	(0,0,0,1)	1	Z
β	β	(0,0,1,0)	2	L
β^2	β^2	(0,1,0,0)	4	H
β^3	β^3	(1,0,0,0)	8	O
β^4	$\beta + 1$	(0,0,1,1)	3	A
β^5	$\beta^2 + \beta$	(0,1,1,0)	6	I
β^6	$\beta^3 + \beta^2$	(1,1,0,0)	' (12)	N
β^7	$\beta^3 + \beta + 1$	(1,0,1,1)	= (11)	M
β^8	$\beta^2 + 1$	(0,1,0,1)	5	Y
β^9	$\beta^3 + \beta$	(1,0,1,0)	Space (10)	R
β^{10}	$\beta^2 + \beta + 1$	(0,1,1,1)	7	Q
β^{11}	$\beta^3 + \beta^2 + \beta$	(1,1,1,0)	> (14)	V
β^{12}	$\beta^3 + \beta^2 + \beta + 1$	(1,1,1,1)	✓ (15)	F
β^{13}	$\beta^3 + \beta^2 + 1$	(1,1,0,1)	: (13)	X
β^{14}	$\beta^3 + 1$	(1,0,0,1)	9	D

```

000 000 000  0 0 1 1 1 0 1 1 1 } 72 INFORMATION
000 000 000  1 1 1 1 1 0 0 0 0 } BITS (SCAN TOP
000 000 000  0 1 0 1 0 0 1 1 0 } TO BOTTOM,
000 000 000  1 1 1 0 1 0 1 0 1 } LEFT TO RIGHT)

000 000 000   $\beta^8 \beta^{10} \beta^{13} \beta^{11} \beta^{14} 0 \beta^7 \beta^9 \beta^{14}$  } 2 9-TUPLES OF
                                                                FIELD ELEMENTS

0 0 0 0 0 0 0 0 0 0 0 0 0 0 0 0 } TWO CODE
 $\beta^8 \beta^{10} \beta^{13} \beta^{11} \beta^{14} 0 \beta^7 \beta^9 \beta^{14} \beta^7 1 \beta^8 1 1 1$  } WORDS

0 0 0 0 0 0 0 0 0 0 0 0 0 0 0 0 } SYNC WORD
 $\beta^8 \beta^{10} \beta^{13} \beta^{11} \beta^{14} 0 \beta^7 \beta^9 \beta^{14} \beta^5 \beta^6 1 \beta^{11} \beta^8 \beta^2$  } ADDED

T T T T T T T T X X L F L Y } TELETTYPE
Y Q X V D T M R D I N Z V A H } WORDS

```

Fig. 1(a). Sample encoding of information

```

GUS005A
RR JGUS
DE JGUS 005
17/2227Z
JGUS ITY MSG
TTTTTTTTXXFLYYQXVDTMRDINZVAH
17/2227Z APR JGUS

```

NASCOM HEADER
 LINE FEED (101000)—DENOTES TWO CODED WORDS IN MESSAGE
 MMM DENOTES CODED MESSAGE
 NASCOM TAILER

Fig. 1(b). Transmitted message with "header" and "tailer" attached

- ing NASCOM header and tailer. A symbol, in this case, teletype *line feed* denoting *two*, appears before MMM coded message triple (this triple is explained below). This symbol is put in by the machine and denotes that it sent two coded words. Fig. 2 shows the actual input to the prototype comm processor, both the header information and the actual message input consisting of two nine-tuples in SDS code. At the teletype rate of 25 bits/sec, each coded word of 15 characters takes 3 sec to transmit. As explained, only milliseconds are needed for the comm processor to put on the NASCOM header and encode the message. The capability also exists for sending ordinary text, upon proper instructions to the encoder (AAA instead of MMM after the header).

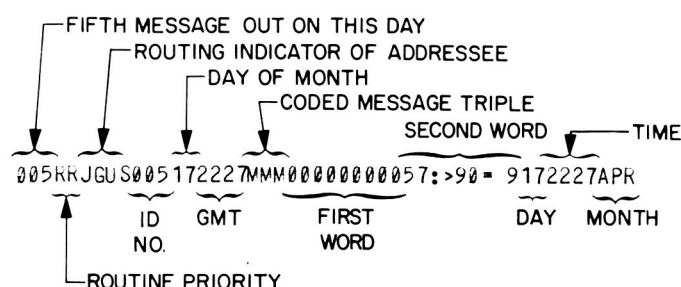


Fig. 2. Typewriter input

4. Decoding

Decoding is much more difficult than encoding and takes more machine time: $\frac{1}{20}$ sec for decoding versus milliseconds for encoding. However, the decoding is much faster than real-time, so that total bit rates of up to 1500 bits/sec (900 information bits/sec) could be accommodated and still allow decoding before the next coded word is fully received.

The message is received in the comm buffer, which alerts the comm processor via an interrupt. The processor first looks for a space in both the 83rd and 84th characters. If it finds them there, as they should be, the header is stripped and algebraic decoding begins. If either a synchronization or character error has occurred in or before these two positions, so that these two spaces are not in their correct position, then the processor searches for *carriage return* and *line feed* until it finds them (normally the 92nd and 93rd characters). Decoding then begins. If the processor does not sync up, it asks for a repeat of the entire message.

Assuming that a point is reached at which the decoder detects that it has correct sync, algebraic decoding begins.

First, the added synchronizing word is subtracted (added, since $1 + 1$ is 0 in the 16-element field). Next, the machine assumes that fewer than three symbol errors have occurred, and computes certain determinants which locate the error positions. A linear or quadratic equation is solved depending upon whether one or two errors were found. These changes (up to two in number) are made in the de-synched received word, and the resulting 15-tuple is run through the code recursion to see if it is, in fact, a code word. If it is, then two or fewer errors have indeed been made, and the information symbols are outputted. If the result is not a code word, an uncorrectable error has occurred. Or if the de-synched received word fails the three tests for no error, one error, or two errors, an uncorrectable error has also occurred. In either case, a repeat transmission is requested.

After all the code words have been decoded and outputted, the NASCOM tailer is erased and the machine reacts to the *ready for new message* condition.

As matters stand now, the encoding and decoding programs sit in the same machine using $3\frac{1}{2}$ K of the 4 K memory. Furthermore, the machine sends to itself in a half-duplex mode. That is, NASCOM routes the message back to the information-processing laboratory, where the system shown in Fig. 3 is located. The routing indicator JGUS has been assigned to the experimental station. After sending, the machine shifts into the *ready to receive* mode. In an operating system for commands, the encoder might be only at the SFOF, the receive portion only at the deep space stations. The $3\frac{1}{2}$ K of storage

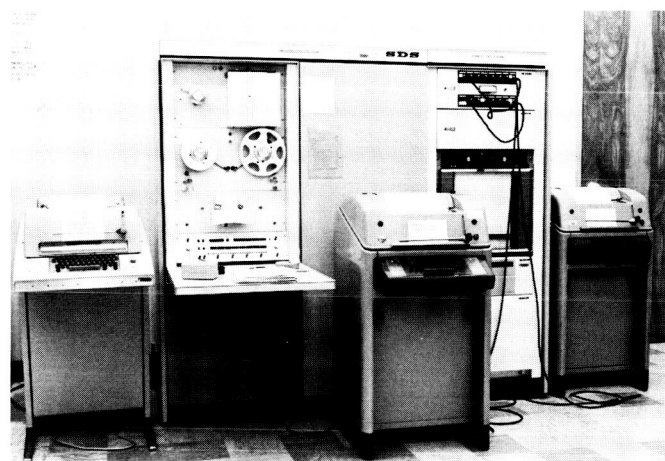


Fig. 3. Prototype communications processor and comm buffer

Table 2. Memory requirements

Encoding		Decoding	
Instructions		Instructions	
Header	20 words	Nonalgebraic	300 words
Encoding	100 words	Algebraic	1700 words
Work space		Work space	
Header	200 words	Nonalgebraic	100 words
Encoding	300 words	Algebraic	600 words
Total for encoding: 620 words		Total for decoding: 2700 words	

breakdown is in Table 2. Almost the entire decoding time of 1/20 sec is used in the algebraic decoding, and that only in the case of a double error.

5. Performance

Under the assumptions of Sec. 1, the theoretical performance of this error correction and detection system can be computed. We are assuming a channel in which there is a symbol error probability of 0.02, and, independently of this, an insertion-deletion probability of 10^{-4} . We know that the code corrects up to double errors, and detects up to four-fold errors. Furthermore, even if a five-fold error is made, the probability of not detecting such errors is still only 0.4×10^{-4} .

Using these facts, we conclude that the probability of an undetected error due to symbol errors only, without sync errors included, is about $10^{-8.2}$. The effect of sync errors together with symbol errors causing undetected errors is so small that the exponent is not affected.

The probability of needing a repeat is also an important parameter of the system. The probability of a detected but uncorrectable error is about 3.4×10^{-3} , due almost entirely to the occurrence of triple errors. The probability of a sync error in a code word is $15 \times 10^{-4} = 1.5 \times 10^{-3}$,

and the probability of detecting the error is so close to 1 that the value of 1.5×10^{-3} is not changed.

All told then, the probability of needing a repeat of a given code word is about 4.9×10^{-3} , or, one in two hundred code words will need to be repeated in the noisiest case. This repeat probability, while not negligibly small, is the price one pays for the extremely low error probability of 10^{-8} .

The properties of the demonstrated error correction and detection system are summarized in Table 3, together with costs involved. In view of the extreme reliability attainable, the system appears attractive for spacecraft command use. When data compression is used between overseas deep space stations and the SFOF at JPL, such coding might also be useful on the inbound telemetry links, since the incoming data will have less redundancy because of the data compression.

B. Frequency Generation and Control: Phase Modulator for Testing Phase-Lock Loops of the Frequency Agile Receiver, G. Lutes

1. Introduction

Testing a phase-lock loop requires a phase modulator as part of the test setup. In the past, a modulator was built for each frequency at which a loop was to be tested. There would be a saving if a module were developed which would cover all the loop frequencies in a system. It was decided to develop such a modulator for testing the frequency agile receiver system, which contains loops ranging in frequency from 500 kHz to 30 MHz.

2. Description

The following requirements were to be met: (1) It should be capable of 5-deg linear modulation over the

Table 3. Characteristics of error-correcting system for DSN teletype

Machine	Cost	Program storage	Running time	Information rate	Information bits per code word	Word error probability worst case	Word repeat probability worst case
SDS 910 with comm buffer	100 K	3.5 K	Encoding milliseconds Decoding 1/20 sec for 3-sec word	0.6	36	10^{-8}	1/200

entire frequency range, (2) the output amplitude should not vary with frequency or modulation, and (3) the input amplitude should not be greater than 10 dbm, and the output power should be at least 13 dbm. The circuit described (Fig. 4) meets all of these requirements.

The modulator is a semibridge R-C phase shifter and requires a signal from a constant voltage source to minimize amplitude variations with phase modulation. It was found that the source impedance (50 Ω) was not low enough to reduce amplitude variations to an acceptable level. A transformer, T1, is therefore used to reduce the source impedance to $\approx 3.1 \Omega$. The second transformer, T2, is used to obtain two out-of-phase signals; however, it also raises the source impedance as seen by the phase shift network to 12.5 Ω . This results in an amplitude variation of < 0.2 db for 10-deg modulation and < 0.3 db for 40-deg modulation. Two transformers are used to facilitate construction. They are extremely broadband and do not affect the bandwidth of the module. Transformer T2, a resistor, and a Capistor diode make up the modulation circuitry.

The Capistor diode is a voltage-variable capacitor diode manufactured by Matsushita Electric Company of Japan. The capacity varies according to the equation $C \propto V_r^{-n}$, where V_r is the reverse voltage and n is

1.222. Most varicaps change capacity according to the same equation but with $n \leq \frac{1}{2}$. The measured change in capacity for the Capistor was from 15 pf at 10-v reverse bias to 250 pf at 1-v reverse bias, a ratio of 16 to 1.

The modulation circuitry is followed by an emitter follower, Q1, so that the input impedance will not load the modulator. This is followed by a broadband voltage amplifier, Q2 (SPS 37-38, Vol. III, pp. 36-38), which is in turn followed by a complementary emitter follower, Q3 and Q4, to lower the output impedance.

The optimum input power to the module from a 50- Ω source is 8 dbm, which provides 13 dbm output into a 50- Ω load. The output amplitude is constant from 50 kHz to 50 MHz.

The modulation input impedance is very high; however, the time constant causes a drop in modulation voltage above about 1 kHz modulation frequency. A different decoupling circuit could raise this frequency considerably.

To test for linearity the signal was phase-modulated with a 5-Hz sine wave from a function generator. The modulation was then read with a vector voltmeter used as a phase detector to supply a voltage proportional to the phase. This voltage was analyzed for distortion with

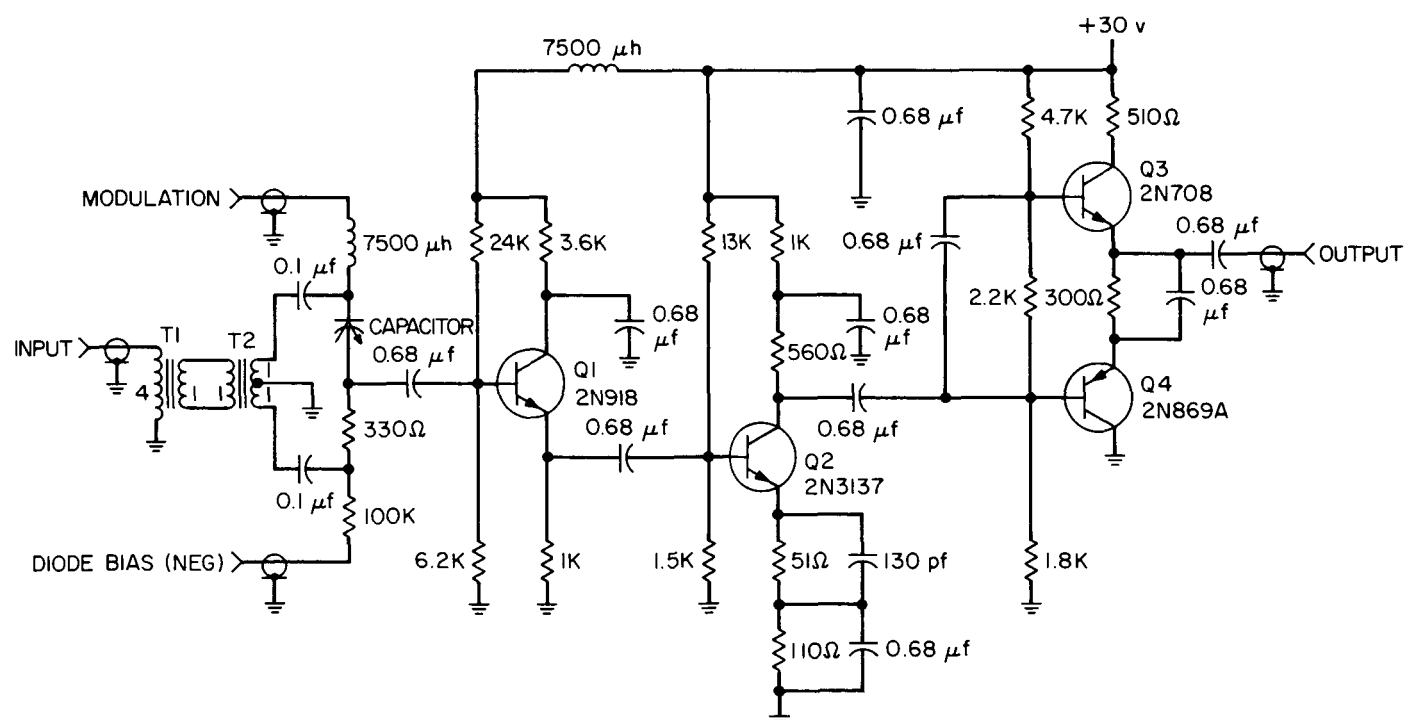


Fig. 4. Phase modulator for testing phase-lock loops

a wave analyzer. These values are given in Table 4 and are direct readings. No attempt was made to compensate for instrumentation error.

In Figs. 5 and 6 a linear modulating ramp voltage is displayed simultaneously with a voltage which is proportional to the phase shift.

The maximum phase shift obtainable at particular frequencies is shown in Table 5.

An analysis of the semibridge R-C phase shifter used in this module is shown in Fig. 7, where

Table 4. Distortion versus modulation

Input frequency, Mhz	Modulation, deg	Distortion, %
0.5	5	2.8
1	5	3.8
5	5	2.0
10	5	4.5
20	5	2.7
30	5	3.7
40	5	2.4
50	5	1.8
0.5	10	3.4
1	10	5.0
5	10	1.7
10	10	2.3
20	10	5.0
30	10	1.6
40	10	4.6
50	10	4.8

Table 5. Total phase shift for 20 v p-p modulation voltage

Input frequency, MHz	Modulation, deg
0.5	80
1	80
5	148
9	150
10	148
20	134
30	120
40	100
50	80

$$I = \frac{2e_1}{R + \frac{1}{j\omega c}}$$

$$e_0 = e_1 - IR = e_1 - \frac{2e_1 R}{R + \frac{1}{j\omega c}}$$

$$\frac{e_0}{e_1} = 1 - \frac{2R}{R + \frac{1}{j\omega c}} = \frac{R + \frac{1}{j\omega c}}{R + \frac{1}{j\omega c}}$$

$$= 1/\pi + 2 \arctan \frac{1}{\omega RC}$$

$$\therefore e_0 = e_1 \left[1/\pi + 2 \arctan \frac{1}{\omega RC} \right]$$

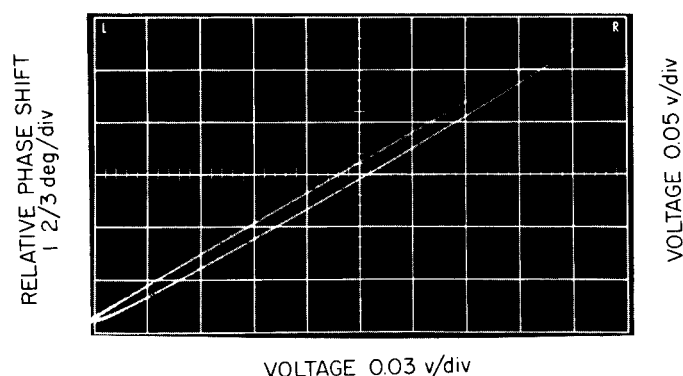


Fig. 5. Relative phase compared to linear modulating voltage (top curve) for 10-deg phase modulation at 10 MHz

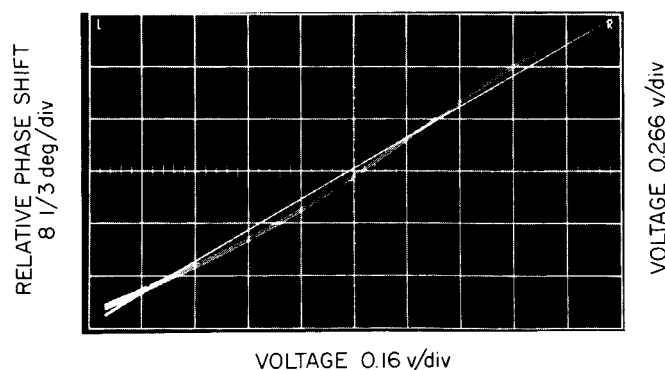


Fig. 6. Relative phase compared to linear modulating ramp voltage for 50-deg phase modulation at 10 MHz

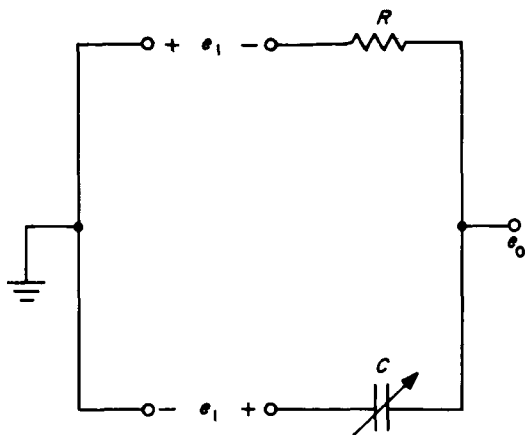


Fig. 7. Analysis of semibridge R-C phase shifter

As C changes from 0 to ∞ the output phase changes from π to 2π or 180 deg. Since C cannot vary from 0 to ∞ , and there is some loading at the output due to the following stage, the maximum phase shift is less than 180 deg (Table 5).

The modulation linearity is dependent upon the capacity versus V_r curve for the Capistor. For small phase shifts (10 deg) the linearity of modulation is good if the diode is properly biased (Table 4). The modulator should be used in conjunction with a vector voltmeter which is used to adjust the modulation and linearity. The best linearity is achieved at 3 to 3.5 v reverse bias on the diode.

3. Conclusion

The use of a new varicap and broadband transformer techniques makes it possible to build broadband phase modulators capable of large phase modulation indices.

C. Frequency Generation and Control: Hydrogen Maser Frequency Standard, W. Higa

Varian Division for Quantum Electronics Devices has recently developed (under NASA contract to Goddard Space Flight Center) a technique for automatically tuning a hydrogen maser frequency standard. A simplified description of the method is given here because of its importance to future field applications.

As explained previously (SPS 37-40, Vol. III, pp. 29-30) the hydrogen maser is susceptible to frequency pulling

due to competition between the resonant cavity and the active atoms. For small detuning the effect is given by the linear relation

$$f_{osc} - f_{atom} = \frac{Q_{cav}}{Q_{atom}} (f_{cav} - f_{atom}) \quad (1)$$

where f_{osc} is oscillator output frequency and is seen to be a function of cavity center frequency f_{cav} . The detuning effect is proportional to the ratio Q_{cav}/Q_{atom} . The Q_{atom} must be taken as the effective Q of all the atoms in the cavity and is subject to line-broadening effects such as doppler shifts and wall collisions. Moreover, it is possible to vary Q_{atom} in a known way by varying the density of hydrogen atoms.

As the gas density is increased, the atoms are forced to come closer to each other and line broadening or lowering of Q_{atom} occurs. The effect is similar to that of increasing the coupling between many synchronously tuned circuits. Conversely a decrease in the gas pressure increases the average distance between atoms and results in a higher Q_{atom} .

The tuning curves shown in Fig. 8 are now understandable. The Q_{atom} is varied by varying the hydrogen beam pressure, p , and the cavity is electronically tuned through resonance. From the foregoing discussion it is seen that $p_3 > p_2 > p_1$. The important point to be observed in Fig. 8 is, of course, the fact that all the tuning curves have one point in common. This is where

$$f_{osc} = f_{cav} = f_0$$

Hence, it is possible to define the "absolute" frequency f_0 .

Qualification of the word "absolute" is necessary here, since the process of measurement to obtain the curves in Fig. 8 requires a reference oscillator. Clearly, the stability of the reference oscillator determines the absoluteness of the frequency f_0 . Fortunately, the hydrogen maser has been proven to have excellent stability (between 10^{-13} and 10^{-14}) over periods of minutes, the time required to obtain the data required for Fig. 8.

The automatic tuning scheme makes use of a servo system which compares one maser against a reference maser. The former is operated at two different pressures to generate an error signal which then electronically corrects the cavity tuning. The electronic tuning is effected

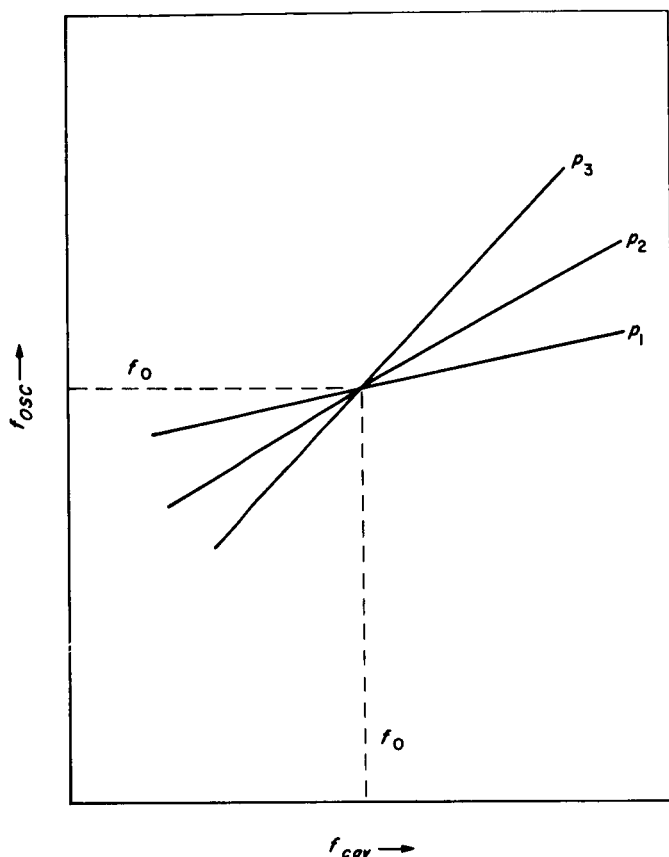


Fig. 8. Tuning curves for a hydrogen maser at various beam pressures ($p_3 > p_2 > p_1$)

by means of a variable capacitor (varactor) loosely coupled to the maser cavity. One sampling period may take several minutes, and the principal feature of the method is to improve the very long-term stability of two already good frequency standards.

More pertinent to the application of these standards to geographically separated tracking stations is the realization that a skilled operator can synchronize his frequency standard, with confidence, with those at the other stations to approximately one part in 10^{13} .

Clearly, each station will require two such standards.

D. Low Noise Receivers: Microwave Maser Development, Block II Traveling Wave Maser, R. Clauss

1. Introduction

Test data obtained with the 3-in. test unit (SPS 37-44, Vol. III, pp. 69-72) has been used to predict the gain,

bandwidth and noise temperature of the proposed Block II traveling wave maser (TWM). A comparison of noise temperature predicted for two values of forward loss is given here.

2. Gain and Bandwidth

The gain and bandwidth of a TWM are related in the following manner (Ref. 1):

$$G_{ab}(f) = G_{ab}(f_0) \frac{1}{1 + [2(f - f_0)/\Delta f_L]^2} \quad (1)$$

where

G_{ab} = electronic power gain in decibels

f_0 = magnetic resonance frequency

f = frequency off-resonance

Δf_L = maser material resonance linewidth

Fig. 9 shows the gain and bandwidth of the 3-in. test unit operating at a center frequency of 2262 MHz. The 3-db bandwidth is 22 MHz at 19 db net gain (electronic gain, 22 db). The maser material (ruby) linewidth, calculated from this data, is 55 MHz.

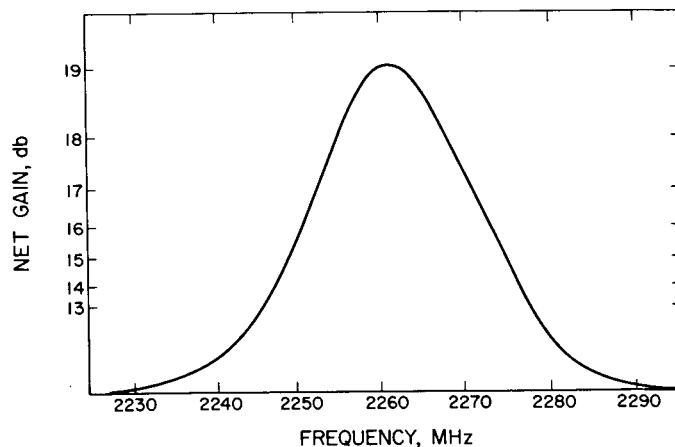


Fig. 9. Bandwidth of 3-in. test unit

Fig. 10 shows the predicted bandpass of two identical 3-in. test units in series, with center frequencies spaced 32 MHz apart (Ref. 1). This combination provides a flat bandpass of approximately 20 MHz, with a 3-db bandwidth of 38 MHz. The net gain (26.9 db) and bandwidth is based on the use of a 16-gauss single step in the magnetic field. This ideal situation will not occur in practice,

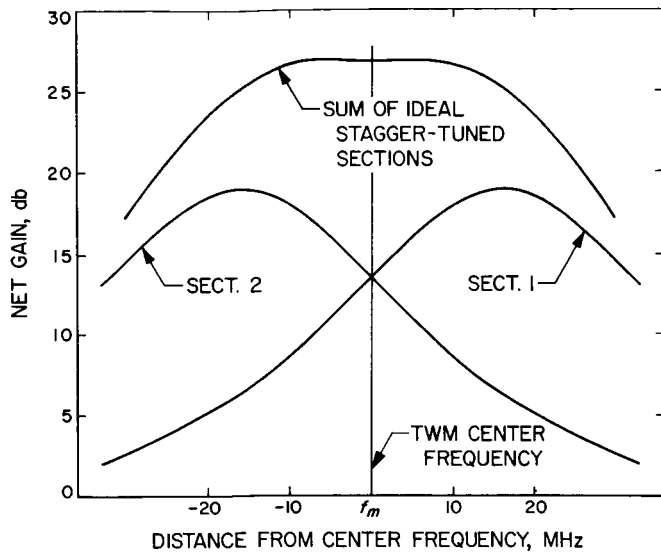


Fig. 10. Predicted bandwidth of two stagger-tuned 3-in. sections

and a 15% reduction in gain is expected. A TWM with an active length of 12 in. should provide the gain and bandwidth indicated in the Block II TWM specification.

3. Noise Temperature

The noise temperature (T_a) of each 3-in. section of amplification is (Ref. 2):

$$T_a = \frac{G-1}{G} \left[T_0 \frac{\rho + \beta}{1 - \beta} \right] \quad (2)$$

where

G = net gain of 3-in. section

T_0 = bath temperature

ρ = 1/inversion ratio

$\beta = \frac{\text{forward loss in db}}{\text{electronic gain in db}}$

The calculated noise temperature for the test unit is shown in Fig. 11. Forward loss degrades the maser noise temperature, especially on the skirts of the maser band-pass where the electronic gain is low. Two examples are shown. The lower curve for a forward loss of 1 db/in. represents a prediction based on the best performance obtained to date with the test unit.

Two or more sections of a TWM, stagger-tuned to provide a wide bandwidth, may be treated as separate

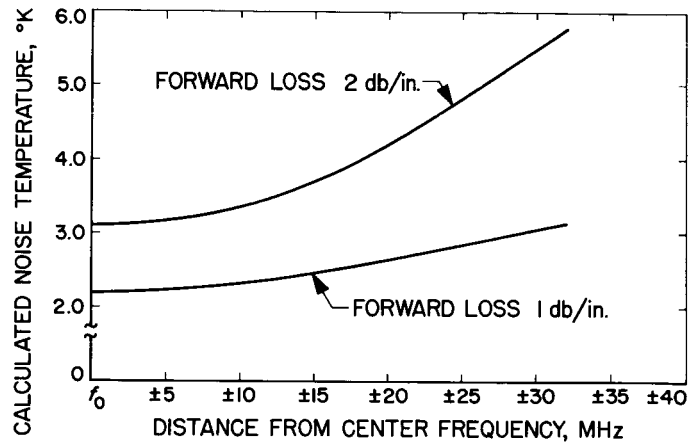


Fig. 11. Noise temperature of 3-in. section

stages of amplification in order to calculate the equivalent input noise temperature of the TWM. In the Block II TWM there will be four 3-in. sections operating in series. The equivalent input noise temperature T_m will be frequency-dependent and is given by the expression

$$T_{m(f)} = T_1 + \frac{T_2}{G_1} + \frac{T_3}{G_1 G_2} + \frac{T_4}{G_1 G_2 G_3} \quad (3)$$

where

$T_{m(f)}$ = equivalent input noise temperature at frequency f

T_1 = noise temperature of Sect. 1 at f

T_2 = noise temperature of Sect. 2 at f

T_3 = noise temperature of Sect. 3 at f

T_4 = noise temperature of Sect. 4 at f

G_1 = gain of Sect. 1 at f

G_2 = gain of Sect. 2 at f

G_3 = gain of Sect. 3 at f

T_m is shown (Fig. 12) for the case where the first and fourth sections of amplification are tuned 16 MHz above the TWM center frequency (f_m) and the second and third sections are tuned 16 MHz below f_m . T_m is shown for two values of forward loss to emphasize the advantage of a low-loss TWM. To determine the equivalent input noise temperature at the waveguide input to the maser package 2.1°K must be added to the value of T_m in Fig. 12 (to account for input line losses).

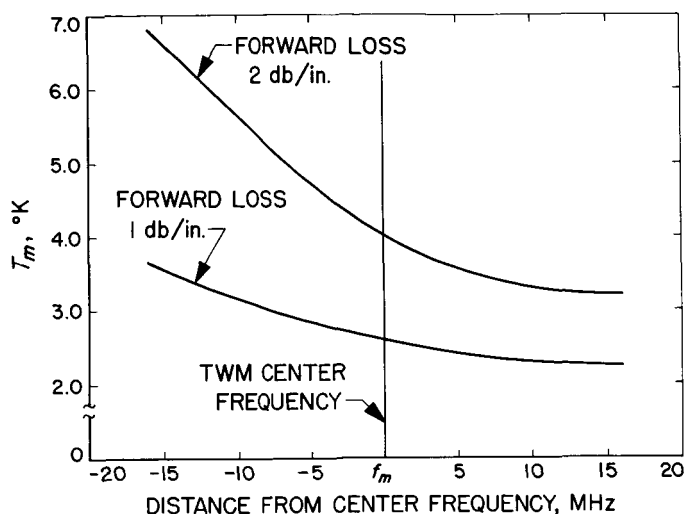


Fig. 12. TWM equivalent input noise temperature

Data obtained during evaluation of the 3-in. test unit indicate that the gain, bandwidth, tuning range, and noise temperature specified for the Block II TWM (SPS 37-44, Vol. III, p. 69) can be met with a 12-in. comb structure, fabrication of which is now nearing completion.

E. Efficient Antenna Systems: X-Band Gain Measurements, D. A. Bathker and B. L. Seidel

1. Introduction

An experimental program has begun to investigate the behavior of the DSIF antennas as they approach gain limit (SPS 37-44, Vol. III, pp. 94-100). Gain measurements have been conducted in the past at S-band; in the future these tests will be planned for C- and K-bands.

The 85-ft Az-El reflector at the Venus Deep Space Station has been partially evaluated at X-band, 8448 MHz, by a combination of radio star (Cygnus A) flux density measurements and measurements using the Tiefert Mountain collimation station. A description of the X-band cone, receiver, and instrumentation may be found in previous reporting (SPS 37-42, Vol. III, pp. 40-51 and SPS 37-43, Vol. III, pp. 56-63). The method used to measure source temperature is a modification of that used in the daily system noise-temperature measurements (SPS 37-42, Vol. III, pp. 25-32). Additionally, certain mechanical measurements of the surface tolerance of the reflector have been made. This report will cover the gain estimates and discuss some of the reflector characteristics observed during the test period.

2. Recent Work

a. Measurement of antenna efficiency. Radio-astronomical methods of measuring antenna efficiency were employed. To this end, a study was made to determine which source or sources to observe. The major criteria in selecting sources were:

- (1) Strength; i.e., the source should be strong enough to observe without using excessive integration times, and the flux density should be well known.
- (2) Distribution; i.e., point sources should be used for ease of data reduction.
- (3) Declination; i.e., the source should appear high in the local sky to reduce atmospheric effects.

A study of the literature and consultation at the California Institute of Technology¹ indicated that Cygnus A (3C405) is the best source for our purposes. The value of flux density of Cygnus A at 8448 MHz (Ref. 3) was taken to be

$$S = 187.6 \times 10^{-26} \pm 28.1 \times 10^{-26} \text{ w} \cdot \text{m}^{-2} \cdot \text{Hz}^{-1}, (3\sigma)$$

The change in antenna temperature, due to the flux density of a point source, is given by

$$T = \frac{SA}{2k}$$

where

T = the change in antenna temperature, due to the source, in °K

S = the flux density of the source in w/m^2 (Hz)

A = the cross-sectional area of the collecting aperture in m^2

k = Boltzmann's constant: $1.38 \times 10^{-23} \text{ w} \cdot \text{°K}^{-1} \cdot \text{Hz}^{-1}$

Cygnus A, though not a point source, can be considered to be two point sources that are separated by 100 sec of arc and have relative strengths of 1.2 to 1.

Assuming that the antenna is pointed at a point between the two sources that comprise Cygnus A, and that this point is analogous to the center of moments in a two-point mass mechanical system, a small correction has to be applied to the conversion from flux density to antenna

¹With Dr. A. Moffett.

source temperature. The corrected equation for the conversion is, for the case of Cygnus A and our expected beamwidth,

$$T = \frac{SA}{2k} \left[\frac{(1.2)(0.95) + (1.0)(0.94)}{2.2} \right]$$

Substituting into the above equation yields $(34 \pm 5.1)^\circ\text{K}$, (3σ) as the increase in antenna temperature due to Cygnus A for a 100% efficient, 85-ft antenna, operated at 8448 MHz. Fig. 13 shows twelve measurements of the temperature of Cygnus A made with the Venus DSS 85-ft Az-El reflector as a function of elevation angle. No apparent correlation exists between the elevation angle and the temperature of Cygnus A as seen by the antenna. The weighted mean of the data shown in Fig. 13 is 15.5°K and has a jitter of about 2.3°K , (3σ) .

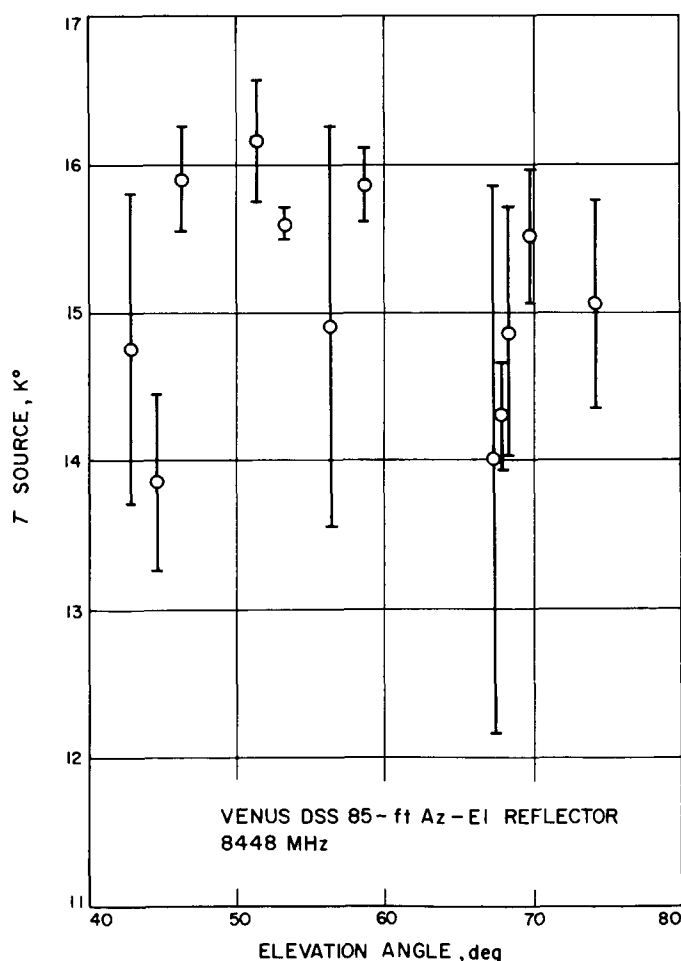


Fig. 13. Temperature of Cygnus A as a function of elevation angle

Since the efficiency η is defined as the ratio of the observed temperature to the temperature for a 100% efficient antenna, the foregoing results in a mean efficiency

$$\bar{\eta} = \frac{15.5}{34} \times 100 = 45.6\%$$

The tolerance on the efficiency is found from the defining equation (Ref. 4):

$$\left(\frac{\sigma_{\bar{U}}}{\bar{U}} \right)^2 = \left(\frac{\sigma_{\bar{X}}}{\bar{X}} \right)^2 + \left(\frac{\sigma_{\bar{Y}}}{\bar{Y}} \right)^2$$

The tolerance is therefore

$$\frac{\sigma_{\bar{\eta}}}{\bar{\eta}} = \left[\left(\frac{0.8}{15.5} \right)^2 + \left(\frac{1.7}{34} \right)^2 \right]^{1/2} = 0.072 = 7.2\%$$

or

$$\sigma_{\bar{\eta}} = (0.072)(0.456) = 0.033 = 3.3\%$$

It must be emphasized that the above value of $\sigma_{\bar{\eta}}$ only takes random errors into account. A bias error that must be considered is that due to antenna pointing. Estimating that a 5% error is made in the source-temperature measurements due to boresight errors (≈ 0.010 deg), we find that

$$\Delta\sigma_{\bar{\eta}} = \frac{(0.05)(15.5)}{34} = 0.023 = 2.3\%$$

Remembering that boresight errors can give rise only to apparent reduction in the efficiency, our final result becomes

$$\bar{\eta} = 45.6\% + 16.8\% - 9.9\%, (3\sigma)$$

and the mean gain of the antenna is

$$\bar{G}_{db} = 63.79 \text{ db} + 1.35 \text{ db } (3\sigma) - 1.07 \text{ db } (3\sigma)$$

as measured at the receiver input reference flange (Fig. 14). Since the receiver input reference flange is the point at which the operational measurements are made,

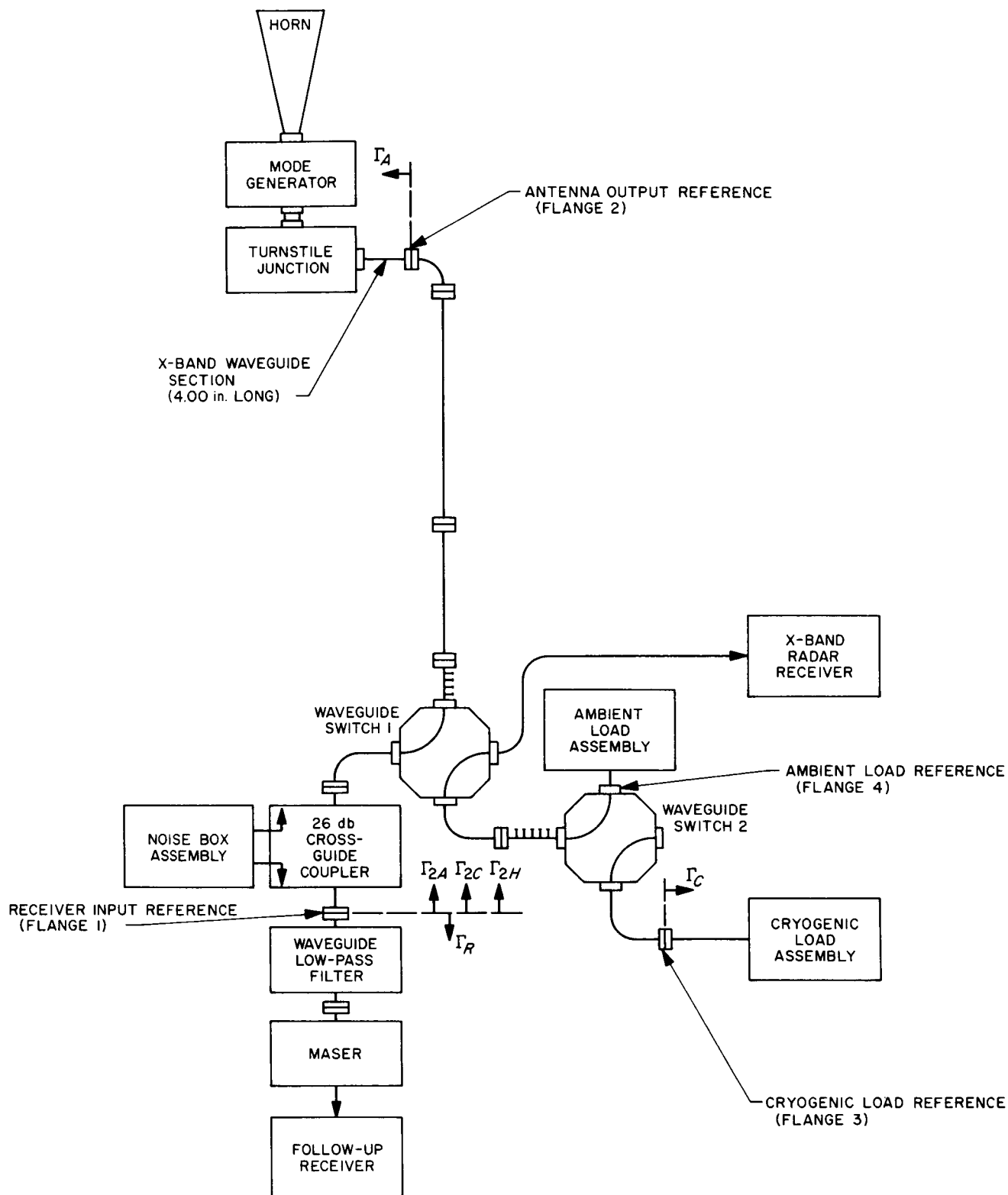


Fig. 14. Block diagram of the X-band cone RF waveguide calibration system

these are the numbers which should be used for keeping track of possible degradation in the system. It is of interest, however, to calculate the efficiency and gain of the antenna at the antenna output reference flange (Fig. 14). The insertion loss between these two flanges is measured to be 0.15 ± 0.0018 db (3σ), as shown in SPS 37-43, Vol. III, pp. 56-63. Correcting for this loss gives rise to a mean antenna efficiency of

$$\bar{\eta}' = 47.2\% \begin{matrix} + 17.4\% \\ - 10.2\% \end{matrix}, (3\sigma)$$

or a mean gain of

$$\bar{G}' = 63.94 \text{ db} \begin{matrix} + 1.35 \text{ db} \\ - 1.07 \text{ db} \end{matrix}, (3\sigma)$$

As indicated in Fig. 13, this result must be qualified as applicable for antenna pointing angles from approximately 45 to 75 deg elevation and does not take into account nonlinearities in the receiving/detecting system. A cursory analysis indicates that errors due to nonlinearities will be small compared to the other sources of error.

b. Surface tolerance effects. Operating a large aperture at high frequency can be a valuable diagnostic tool; for example, certain large-scale perturbations to the paraboloidal surface quickly show up as reduced efficiency unless the system is refocused. For the Cassegrain configuration used we had predicted, on the basis of ray optics, that a hyperboloid movement of approximately 0.25 in. *toward the apex* would be required to focus the system on the Tiefert Mountain collimation station, compared to the true far-field focus. During the tests it was found that the opposite was required, i.e., the hyperboloid had to be positioned 0.28 in. *toward the paraboloid* to focus the system on the Tiefert Mountain station. The refocussing accounts for approximately 8% change in efficiency. While this effect was confusing at first, a later analysis of the paraboloidal structure partially answers the question.

As discussed in SPS 37-44, Vol. III, pp. 106-111, the RMS computing program now has the added capability to best fit using focal length as a parameter. Because the computations are too conservative additional computer runs were obtained with 2 and 3 times gravity deflections.² Table 6 shows computed best-fit focal lengths

²M. S. Katow, private communication.

Table 6. STAIR program computed best-fit focal lengths, 85-ft Az-El reflector

Reflector attitude	Focal length 1 \times Symmetrical deflections, in.	Focal length 2 \times Symmetrical deflections, in.	Focal length 3 \times Symmetrical deflections, in.
Zenith	432.194	—	—
45 deg	432.000	432.000	432.000
Horizon	431.709	431.453	431.199

for the 85-ft Az-El reflector as a function of elevation angle. Assuming one has properly focussed the system on a radio source at approximately 45-deg elevation angle, it can be seen from the predicted 2 times deflections that the focal length will decrease by 0.55 in. when the reflector is oriented to the Tiefert Mountain station at 0.800-deg elevation. Thus, if the Tiefert Mountain station were in the far field, we would expect to move the hyperboloid toward the paraboloid by essentially this amount. Because the Tiefert Mountain station is too close, a first-order correction of 0.25 in. back toward the apex would yield a net near-field focus prediction of 0.30 in. toward the paraboloid. As discussed above, the required movement was experimentally found to be 0.28 in.

Table 7 shows computed best fit RMS of one half the RF pathlength errors for the 85-ft Az-El reflector as a function of elevation angle. These values account only for the panel tie points; effects due to the main reflector and hyperboloid panel shapes have not been included.

A series of conventional surveys using the vertex mounted theodolite technique was made³ to support this program. Although the data yielding RMS at given attitudes has not been reduced, the surveyed changes between 45 deg and horizon indicates the computed

³By DSIF Engineering Sect.

Table 7. STAIR program computed focal length best-fit RMS of one-half RF pathlength errors, 85-ft Az-El reflector

Reflector attitude	RMS 1 \times Sym- metrical deflections, in.	RMS 2 \times Sym- metrical deflections, in.	RMS 3 \times Sym- metrical deflections, in.
Zenith	0.018	—	—
45 deg	0	0	0
Horizon	0.026	0.050	0.074

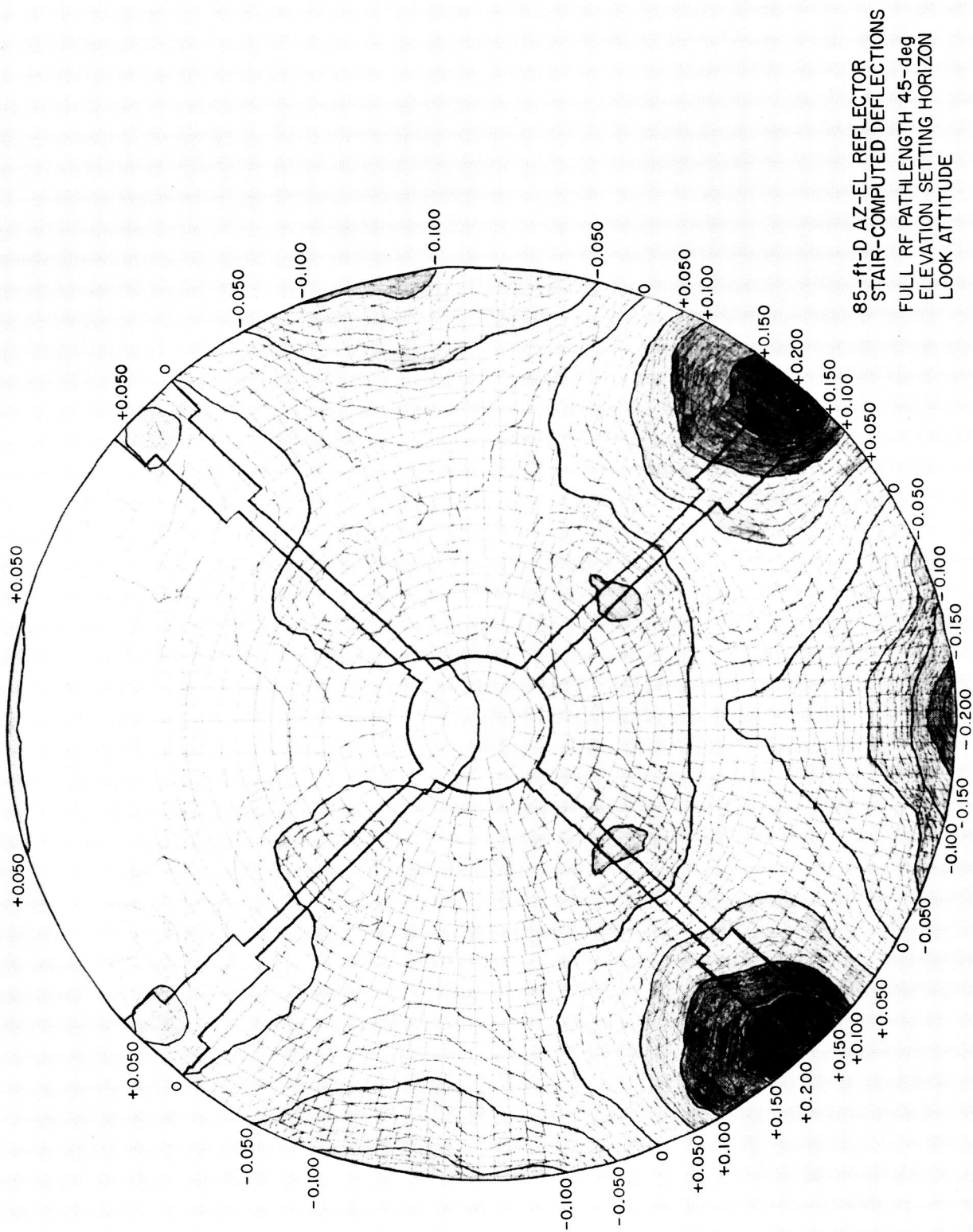


Fig. 15. Computed contour map, 85-ft Az-El reflector

• results using $2 \times$ symmetrical deflections are approximately correct. This is not in disagreement with our experience during focus tests, as discussed above. A certain amount of mechanical hysteresis was found in both the RF tests and mechanical measurements. During the RF tests, we experienced difficulty in repeating bore-sights on both the radio source and the Tiefert Mountain station; presumably some portion of this can be attributed to the reflector surface with some portion possibly due to hysteresis or looseness in the quadripod and/or hyperboloid mechanism. Sample calculations show, for example, the beam pointing is very sensitive to any crabbing or tilting motion of the hyperboloid during focussing.

Fig. 15 is a computer-plotted contour map⁴ of computed $1 \times$ symmetrical deflections of the 85-ft Az-El reflector, after best fitting, at the horizon attitude. Fig. 15 is calibrated in terms of full RF pathlength, a parameter useful for data input to the JPL Radiation Pattern Program. Because the calibration is in terms of full RF pathlength, the figure can also represent the $2 \times$ symmetrical deflections case, which fits the surveyed field data approximately, provided one relabels the legend "one-half RF pathlength." Fig. 15 clearly shows reflector distortions caused by the rectangular box girder as well as the counterweight ties. Subreflector and quadripod shadowing is outlined; the purpose of this map was to arrange data input for the Radiation Program and the subapertures used can be seen. The general characteristic of this map which is noteworthy is the absence of severe astigmatism, such as that found on the 30-ft Az-El reflector (SPS 37-33, Vol. III, pp. 14-18).

Fig. 16 is a graph of gain reduction due to surface tolerance effects for 8448 MHz (Ref. 5). Accepting the radio-astronomical value of flux, and thus the 47.2% mean antenna efficiency for elevation angles near 60 deg, we can compute the surface RMS. Well-known efficiency factors for the feed and blockage are 74.1 and 84.5%, respectively. Assuming the balance is due to surface tolerance effects, we find the surface has a mean efficiency of 75.4% at the above elevation angles, leading to a surface RMS of 0.059 in. The actual surface probably is somewhat better than 0.059 in. RMS since the data is biased by pointing problems.

A gain measurement using the Tiefert Mountain station was not accomplished because of generally poor propagation over the path during the test period. A pre-

⁴IBM 1620 programming by D. L. Nixon; experimental data collected by Venus Deep Space Station personnel.

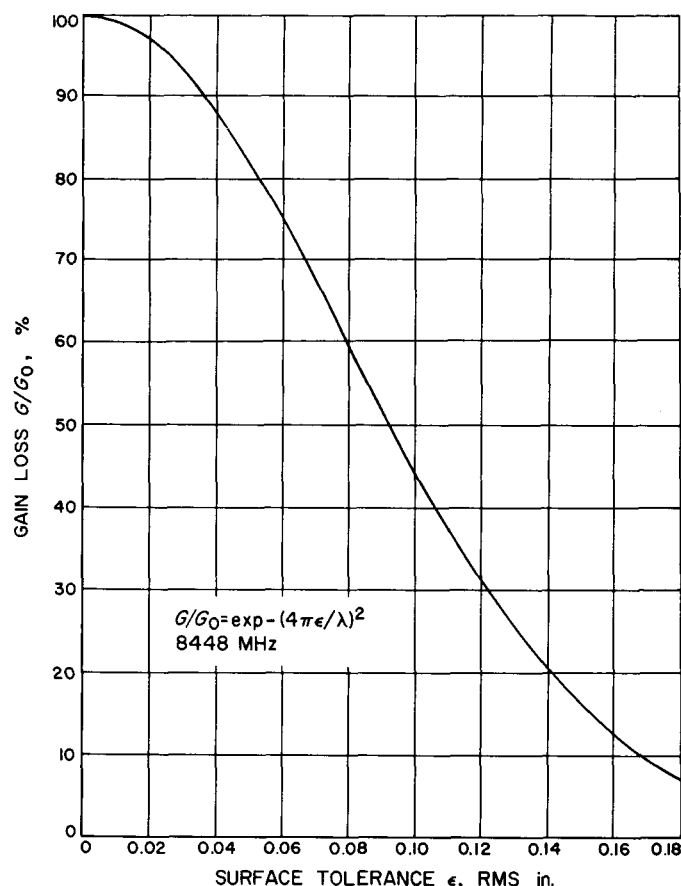


Fig. 16. Gain loss as a function of surface tolerance

diction of gain at low elevation angles is difficult inasmuch as it is not clear if the surface RMS change (Table 7) of approximately 0.050 in. from 45 deg elevation to horizon is to be added coherently or incoherently to the 45-deg elevation surface of 0.059 in. This matter points out the difficulty of transferring a ground-based collimation tower gain figure to higher elevation angles.

3. Conclusions

Accepting the radio-astronomical value of flux density for Cygnus A, we find the mean antenna efficiency of the Venus 85-ft Az-El at 8448 MHz to be approximately 47%. Difficulties in beam pointing were experienced and partially traced to hysteresis in the reflector structure. The amount of hysteresis present is essentially unobservable at S-band but quite noticeable at X-band. It is suspected that a portion of the beam-pointing difficulty also arises during repeated focussing, due to possible crabbing of the hyperboloid mechanism. Further difficulties with the propagation conditions from the Tiefert Mountain station during the period precluded a gain measurement at low elevation angles.

The measured antenna efficiency of the Venus Deep Space Station 85-ft Az-El at 8448 MHz corresponds to a mean gain at the antenna reference flange of +63.94 db at the elevation angles quoted. Based on the expected surface tolerance of 0.059 in. the gain limit of the reflector occurs at 15.9 GHz. Assuming the same feed and blockage efficiencies are realized (a very good assumption) the gain at gain limit will be 66.35 db, about 2.5 db higher than the 8448-MHz system.

Although we are presently operating at a point about 2.5 db below gain limit, pointing has become a difficult matter. At gain limit, however, the pointing requirements will not be significantly more stringent.

F. Multi-feed Cone System for the Advanced Antenna System, G. S. Levy and S. M. Katow

At present, in order to change feed systems on the advanced antenna system (AAS), it is necessary to remove the entire Cassegrain feed support structure and replace it with another unit. The time requirements make it impractical to use different feed systems for different missions. The multifrequency feedcone now in use was designed for maximum versatility at S-band (SPS 37-35, Vol. IV, p. 268) so that one cone could be used for all S-band missions. It has become clear that the use of special-purpose cones would give improved performance and permit experiments at other frequencies, but the time required for changing cones and the necessity of having cone changes between missions has made this approach undesirable. To permit rapid feedcone changing, several feedcone turret configurations have been examined. The three combinations considered are:

- (1) Move feedcone relative to hyperboloid and paraboloid.
- (2) Mount multiple feeds which are fixed with respect to hyperboloid and paraboloid.
- (3) Move hyperboloid relative to multiple feeds and paraboloid.

In the first case the microwave optics are very similar to the existing AAS. If a rotating feedcone turret were used, the blockage would be increased by 1%, and there would be a requirement for high-power rotary joints.

The second case would have a cluster of three horns. The phase center of each horn would be offset from the axis of symmetry of the paraboloid by 50 in. The distance from the phase center of the horn to the focus of

the paraboloid would be the same as in case (1). The phase center of the horns would form an equilateral triangle with the parabola axis passing through the center of the triangle. This configuration would require no

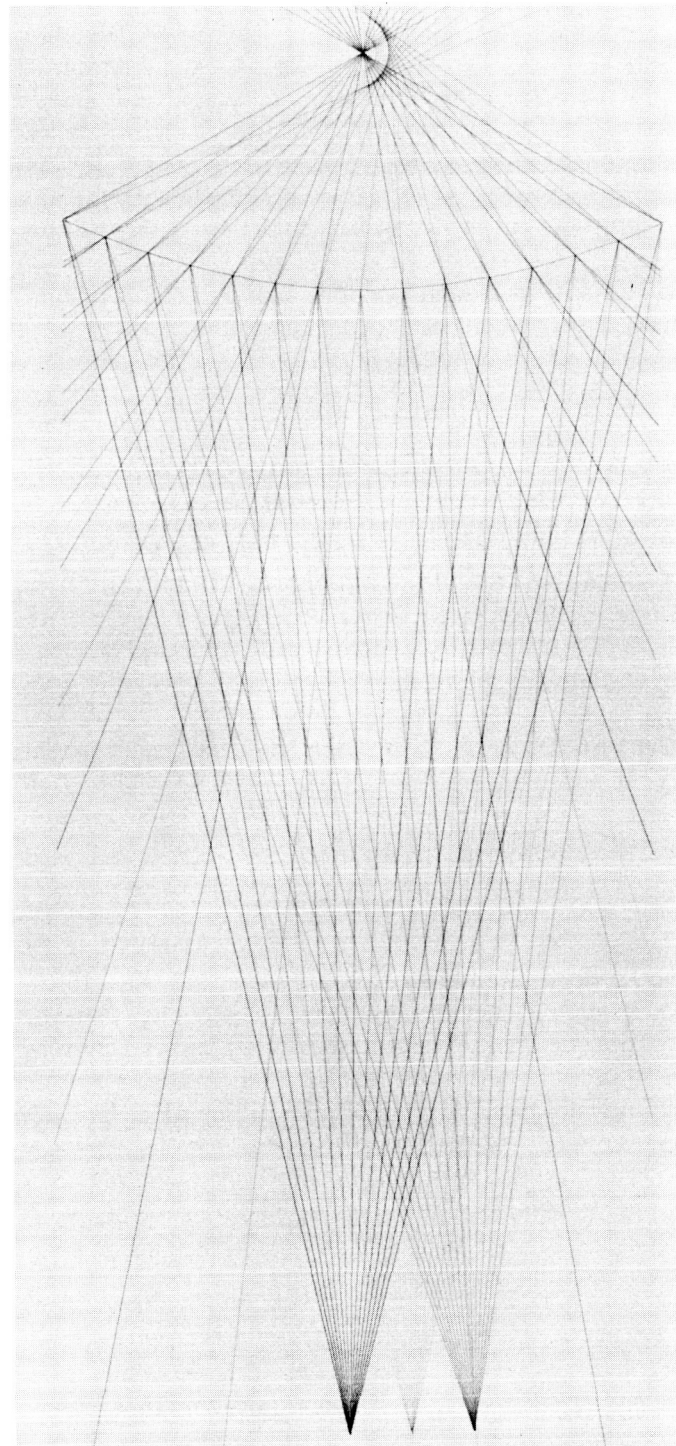


Fig. 17. Hyperboloid with offset illumination

mechanical changes to switch from one feed to another. However it would result in (1) a beamshift which would require pointing corrections, (2) a gain loss due to a phase error introduced by the asymmetrical configuration, and (3) a gain loss and increase in antenna temperature due to energy spilling over the boundaries of the paraboloid.

The third case would involve the same horn configuration as in case (2), but the hyperboloid would be moved to optimum position for each feed.

A ray-tracing program was written to determine the behavior of the virtual focus point of the AAS hyperboloid as the feed was moved off axis. Fig. 17 shows a hyperboloid illuminated from three positions. In one (darkest ink) position the hyperboloid is illuminated from one focus and a virtual image is formed at the second focus. The illuminator is then moved off axis 25 in., while the distance between illuminator and second focus is kept constant (lightest ink). It can be seen that a virtual caustic is formed and no virtual rays pass through the focal point. The third case is a 50-in. offset (medium ink). The caustic is further from the focal point.

The effect of the caustic formation on the performance of the Cassegrain optics was not clear, so the program

was extended to include reflection from a paraboloid (all in two dimensions). Fig. 18 shows the final ray tracing output with the paraboloid reflection included. Since the hyperboloid portion of the program was already written, it was decided to move the feed and paraboloid with respect to the hyperboloid rather than the more obvious case of referring horn and hyperboloid to paraboloid. First (lightest ink) the axis of symmetry of the hyperbola and parabola were considered colinear; the feed was offset 50 in., and the phase center to focal point distance was maintained constant. (For clarity the drawing has only 10 rays; the numerical analysis used 50.) The total length of each ray (from horn to hyperbola to parabola and reflection) was held constant. The end point of each of the 50 rays was then least-square-fitted to a straight line. The standard deviation was found to be 0.126 in., which would produce a gain loss of 0.1 db at S-band, using the approximation of Ruze (Ref. 5): $G/G_0 = \exp -(2\pi\phi/\lambda)^2$ and 1.4 db at X-band. In addition to the gain loss the beam will be offset by approximately 0.5 deg. It must be emphasized that this is a geometric optics two-dimensional analysis, and the results must be regarded as very preliminary.

If it is now assumed that the parabola is rotated about its focus so that the ray from the horn that is reflected from the center of the hyperbola strikes the vertex of the

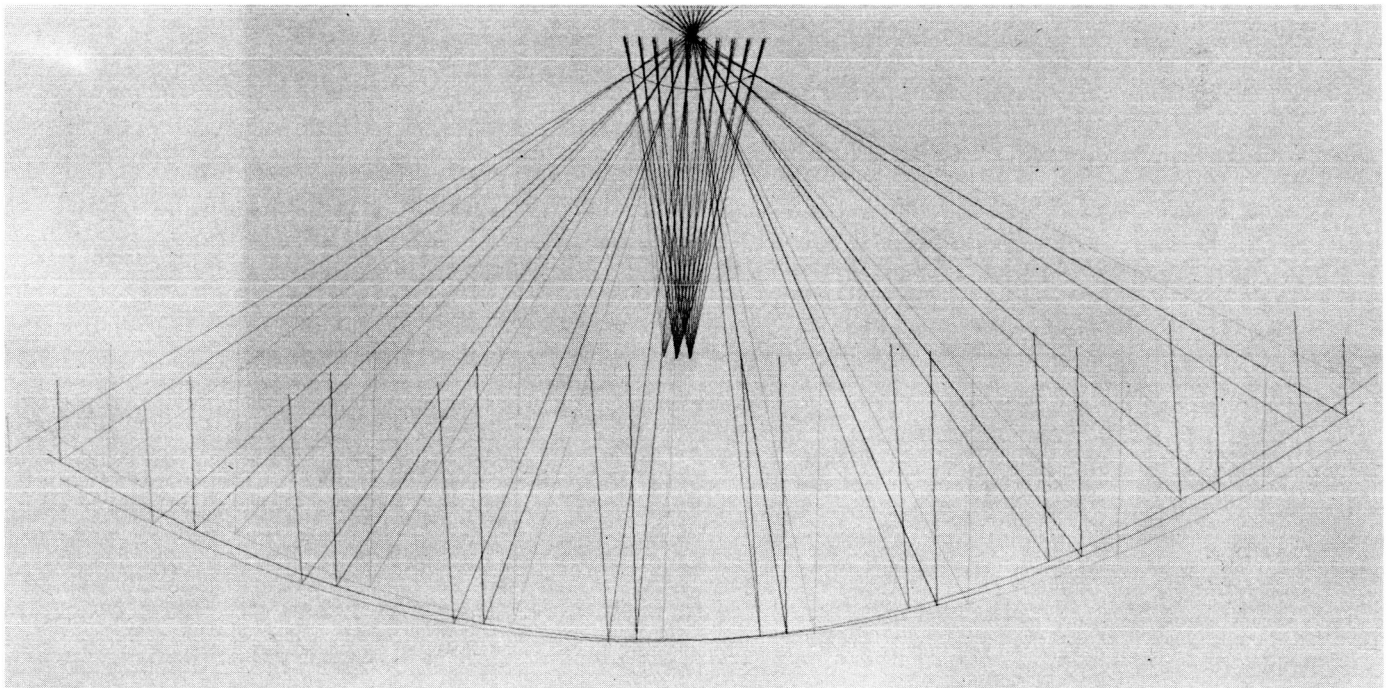


Fig. 18. Cassegrain with offset illumination

parabola, and the feed horn is offset by 50 in. from the axis of the parabola, then the standard deviation is found to be 0.0142 in. (darkest ink). This produces a gain loss of 0.02 db at X-band, due to phase errors and a pointing error of approximately 0.27 deg. The advantage of using a configuration with the hyperboloid axis between the paraboloid axis and the feed-to-focus line is the spillover is reduced. This configuration is particularly desirable if one wishes to use the existing hyperboloid and maintain the capability of returning to a symmetrical feed configuration for special missions.

The configuration which at this time appears the most promising is illustrated in Fig. 19. The hyperboloid axis of symmetry is colinear with the horn phase center. However unlike the medium-colored ink case of Fig. 18, the spillover will be minimized by truncating the symmetrical hyperboloid asymmetrically. This truncation will be initially determined by the boundary formed by the cone, which has its apex at the paraboloid focus and symmetrically circumscribes the edges of the paraboloid. The hyperboloid will be rotated to focus on the cone being used. The advantages of this configuration are that it has

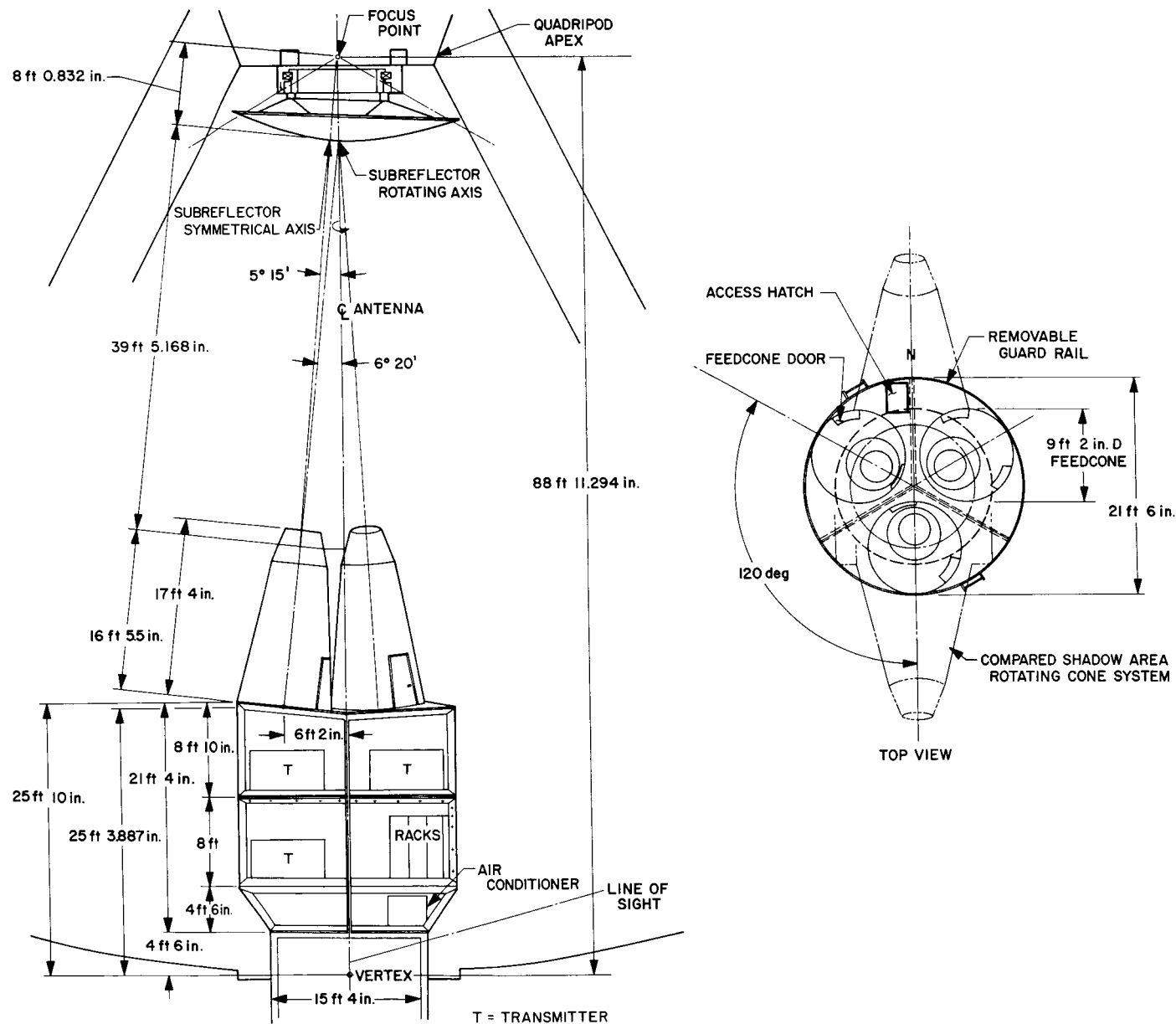


Fig. 19. Possible multiple feed cone configuration

no phase error or boresight shift and should have good spillover performance. This hyperboloid will be made in a scale model which will be tested on the antenna range. The results of the range work will be used to evaluate the feasibility of the configuration.

G. Multi-mission Telemetry Demodulator Project,

R. Petrie and J. W. Layland

1. Introduction

Since its inception, the Deep Space Network (DSN) has carried, and will continue to carry, an ever-increasing load of spacecraft tracking commitments. Each of these various spacecraft has its own particular requirements in the demodulation and decommutation of its telemetry signals. At present, these individual requirements are being met through the use of equipment specifically designed to handle one particular spacecraft or series of spacecraft. The continued use of this mission-dependent equipment (MDE) is both costly and time consuming, not only in its fabrication, but in the time and space required to implement the DSN for each new spacecraft design. Thus, the need became increasingly clear for a general-purpose telemetry demodulation system that was truly mission independent.

Consequently, a program was initiated to develop the methods and equipment necessary to implement such a mission-independent telemetry demodulator. The major phases of this program are summarized briefly as follows.

(a) **Phase I.** The first goal of the program was to establish that telemetry data could, in fact, be recovered by using only a digital computer as a subcarrier demodulator and detector. This goal was successfully achieved in September 1966 on an SDS 930 computer, programmed in Fortran, and operating upon the tape-recorded *Mariner IV* telemetry signals.

(b) **Phase II.** Since Phase I was a non-real-time experiment, the next step was to demonstrate that this same correlation technique could be used for real-time telemetry data recovery. This phase was accomplished in December 1966 using, again, an SDS 930 computer operating on *Mariner IV* telemetry signals as received on the Mars Deep Space Station antenna. The computer data output was appropriately formatted and sent over teletype lines to JPL, thus presenting a real-time telemetry data printout.⁵

⁵Details of Phases I and II, carried out by Dr. R. Goldstein and G. A. Morris, are presently unpublished.

(c) **Phase III.** While the first two phases of the program had been primarily a demonstration of concept, Phase III was the first attempt to implement a system which was a reasonable analog of the proposed operational system. Hence, the Phase III or Type III demodulator was constrained to use an SDS 920 computer (the 920 is one-fifth as fast as the 930 computer) and to do certain operations in external general-purpose demodulation hardware. The external hardware performs the subcarrier demodulation and data stream integration, and the computer performs the detection and the data-dependent controlling operations.

(d) **Phase IV.** Phase IV is the development of the actual operational system. This phase will be covered in detail in future articles.

The purpose of this article is to discuss in detail the Type III demodulation system.

2. Theory of Operation

Fig. 20 is a functional diagram of the Type III demodulator under discussion. The received signal is band-pass filtered to remove noise and subcarrier harmonics, and to limit its dynamic range. It is then demodulated by the local subcarrier reference and correlation detected by a hybrid analog/software integrate-and-dump device. A sampled data, Costas-type phase-locked loop derives a coherent subcarrier reference from the data signal. Bit timing is tracked by a delay lock loop using the sync algorithm used in Phase II and described later in this article. The nonlinear operations required in each of these loops are implemented by software.

The integrate-and-dump devices consist of a low-pass filter followed by a software "dump." Let the impulse response of the low-pass filter be $\exp(-\alpha t)$. The output of the filter is sampled once per bit, and the signal integral over each bit-time is estimated by the operation:

$$I_i = \frac{T_B}{1 - \exp(-\alpha T_B)} [S_i - S_{i-1} \exp(-\alpha T_B)] \quad (1)$$

Where T_B is bit duration and S_i and S_{i-1} denote the current and past bit samples, respectively. If the signal component at the filter input is constant between samples (which it is if the samples are taken at the bit-time instants, t_i), the expected value I_i is equal to the expected value of the integral of the signal $S(\tau)$ from t_{i-1} to t_i .

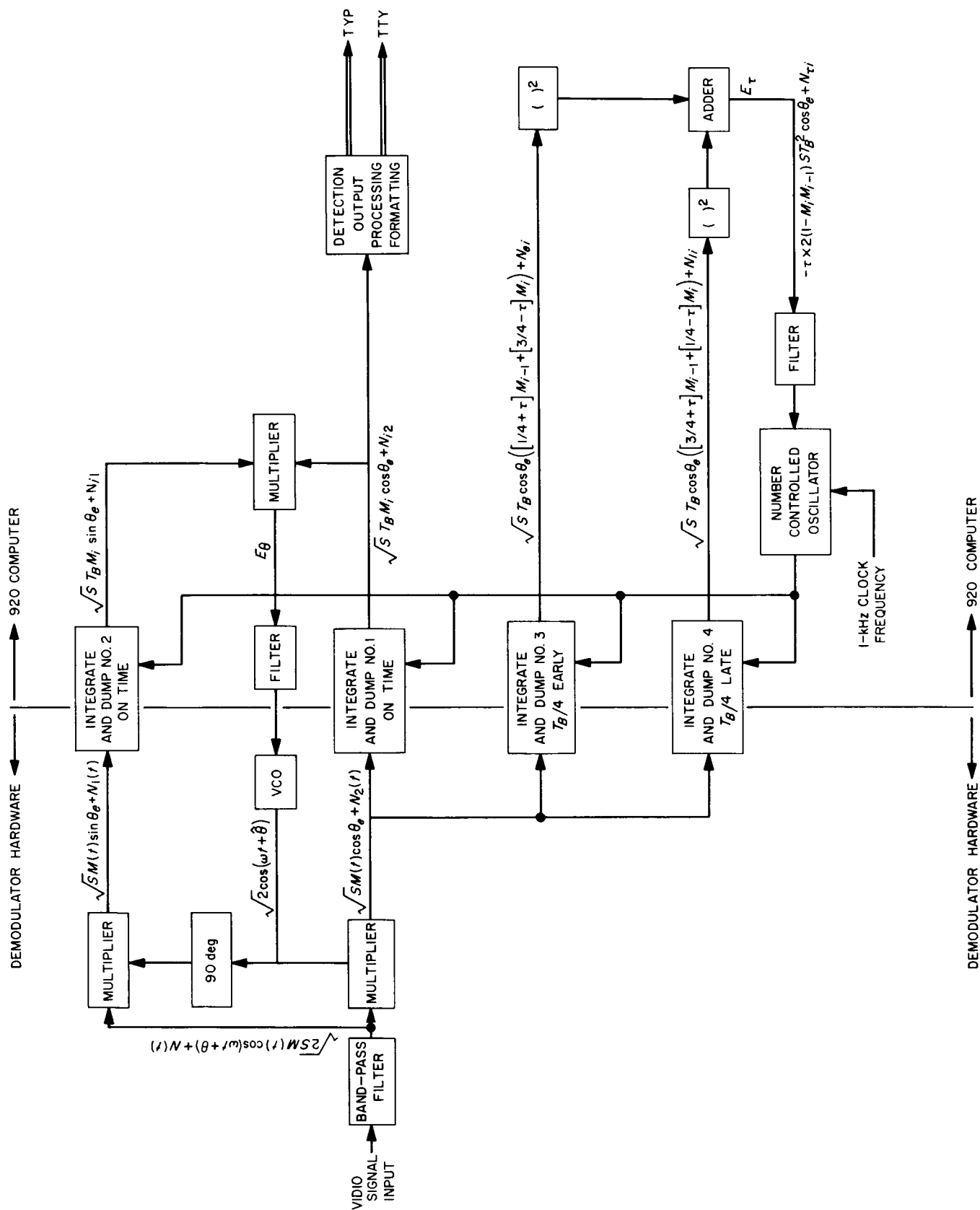


Fig. 20. Type III demodulator functional diagram

The noise component suffers a slight distortion so that the variance of I_i is given by

$$V(I_i) = \frac{1}{2} \alpha T_B [1 - \exp(-2\alpha T_B)] [1 - \exp(-\alpha T_B)]^{-2} \times V \left[\int_{t_{i-1}}^{t_i} S(\tau) d\tau \right] \quad (2)$$

For the case $\alpha T_B = 1/2$, this represents a 0.09-db degradation in signal-to-noise ratio. The degradation is negligible for $\alpha T_B = 1/20$, the value used in the Phase III experiment.

The error signal for the phase-locked loop is generated by multiplying, at each bit-time, the outputs of the data (No. 1) and phase quadrature (No. 2) integrate-and-dump devices. If bit timing is correct, this error signal is independent of the modulation and has expected value

$$\bar{E}_e = ST_B^2 \sin \theta_e \cdot \cos \theta_e \simeq ST_B^2 \theta_e \quad (3)$$

where θ_e is phase error in radians and S is signal power.

If the tracking loop is closed by the relation

$$\hat{\theta}_{i+1} = \hat{\theta}_i + kE_{ei} \simeq \hat{\theta}_i + k_e (\theta_i - \hat{\theta}_i) \quad (4)$$

and the phase error assumed to be small so that the linear approximation holds, the variance of the loop-phase error is given by

$$\sigma_\theta^2 = \frac{k_e}{2 - k_e} \left[\frac{N_0}{2ST_B} + \left(\frac{N_0}{2ST_B} \right)^2 \right] \quad (5)$$

where N_0 is the one-sided noise spectral density.

The error signal for the delay-lock loop is generated by differencing the squares of the two other integrate-and-

dump devices—one operating one-quarter bit time early (No. 3), and the other operating one-quarter bit time late (No. 4) with respect to correct bit timing.

Let τ be the timing error in fractions of a bit-time, and M_i be the data sequence. If $|\tau| \leq 1/4$, the expected value of the i^{th} error sample is

$$\begin{aligned} \bar{E}_{\tau i} &= ST_B^2 \cos^2 \theta_e \{ [(\frac{1}{4} + \tau)m_{i-1} + (\frac{3}{4} - \tau)m_i]^2 \\ &\quad - [(\frac{3}{4} + \tau)m_{i-1} + (\frac{1}{4} - \tau)m_i]^2 \} \\ &= \begin{cases} 0 & \text{if } m_i m_{i-1} = 1 \\ -4\tau ST_B^2 \cos^2 \theta_e & \text{if } m_i m_{i-1} = -1 \end{cases} \\ &= -2\tau ST_B^2 \cos^2 \theta_e \quad \text{for transition probability} = \frac{1}{2} \end{aligned} \quad (6)$$

The situation for τ near $1/2$ is symmetric to that for τ near 0, and the overall error signal is the triangular wave shown in Fig. 21.

If the tracking loop is closed by the relation:

$$\hat{t}_{i+1} = \hat{t}_i + kE_{\tau i} = \hat{t}_i + k_\tau (t_i - \hat{t}_i) \quad (7)$$

and a linear approximation made to the piecewise linear error curve, the variance of the loop timing error is given by

$$\sigma_\tau^2 = \frac{k_\tau}{2(1 - k_\tau)} \left[\frac{5N_0}{32ST_B} + \frac{1}{8} \left(\frac{N_0}{ST_B} \right)^2 \right] \quad (8)$$

Fig. 22 shows σ_τ (in bit fractions) and σ_θ (in radians) as a function of signal-to-noise ratio for $k_e = 0.01$, $k_\tau = 0.005$. The solid lines in this figure correspond to Eqs. (5) and (8). The points were obtained from a Fortran simulation experiment and represent approximately 50,000 data bits at each signal level. Fig. 23 shows the error rate data obtained from the same simulation.

One should, therefore, expect the Type III demodulator to perform with no noticeable degradation from theoretical with a sine-wave subcarrier (e.g., *Mariner IV*) or 0.9-db degradation with a square-wave subcarrier (e.g., *Pioneer*) due to removal of subcarrier harmonics.

3. Implementation

The detailed block diagram of the Type III telemetry demodulator is shown in Fig. 24. The several portions of the system are described in the following paragraphs.

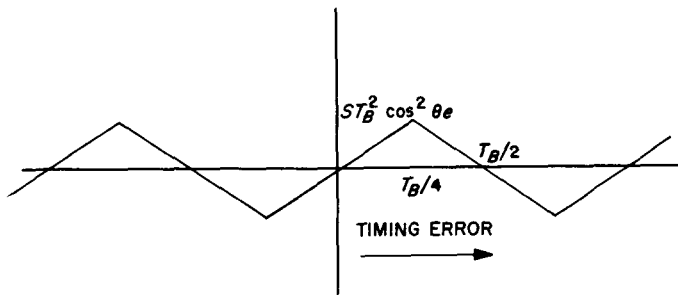


Fig. 21. Mean of timing error signal versus offset

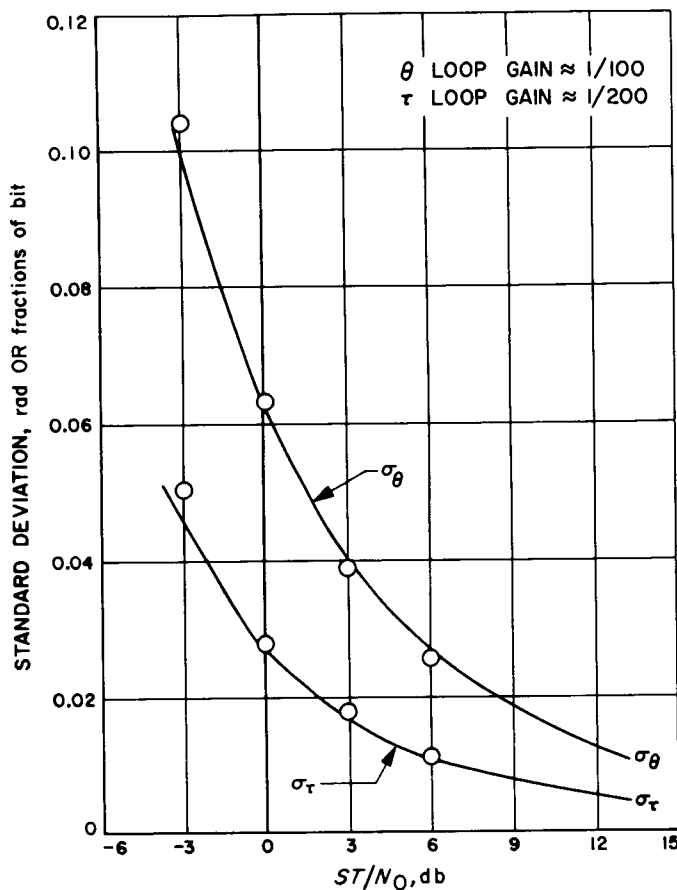


Fig. 22. Phase and timing jitter

a. Signal sources. The input signal source is selected at the analog instrumentation subsystem (AIS) patch panel. Through the use of this patch panel, inputs could be obtained from prerecorded telemetry signals being played back on one or both of the FR-1400 tape machines, or real-time telemetry signals from either the DSIF receiver or the R&D receiver in the Mars DSS alidade room. Two separate coaxial cables were installed for the Phase III Experiment to permit rapid changeovers during operation.

b. Type III hardware. The analog portion of the Type III demodulator performed the band-pass filtration, demodulation, and integration of the telemetry signal; amplification and phase shifting of the local oscillator (VCO) frequency; gain matching of the DC control signal generated by the computer for the VCO; and provided test and monitor equipment for setup and checking of system performance.

Extensive use was made of active networks using operational amplifiers in implementing the band-pass filters,

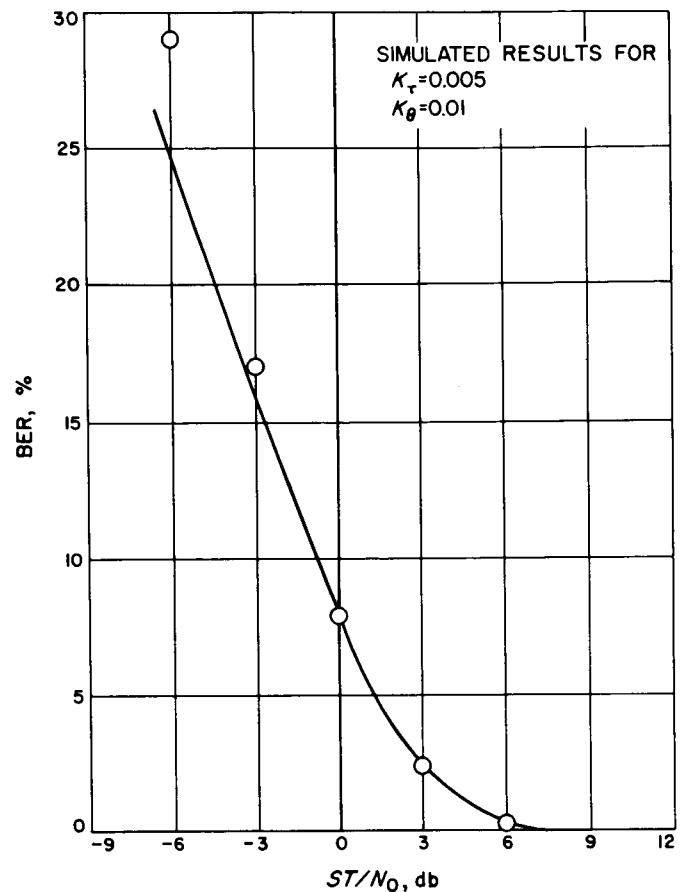


Fig. 23. Error probability, bit error rate, 50,000-bit simulation

amplifiers, phase shifter, and integrators. Diode ring demodulators were employed and a Hewlett Packard 5100A synthesizer was used as the VCO. A number of test points were brought out to a patch panel, which allowed comprehensive monitoring of the entire analog portion. Fig. 25 shows the equipment installation. A brief description of the operating characteristics of the analog portion is presented in the following paragraphs.

The raw telemetry input signal is a nominal 1 v rms composite of subcarrier plus data plus noise. The signal is then band-pass filtered and amplified such that the remaining noise peaks do not exceed ± 20 v. The signal is then demodulated and integrated. The integrator (which can also be considered a low-pass filter) has a time constant τ within the range $2T_B \leq \tau \leq 2^5 T_B$ and a gain such that the peak DC swing is well within ± 5 v (in actual operation, the DC swing was held to ± 3 v p-p) to prevent saturation of the analog-to-digital converters (A/D) that follow.

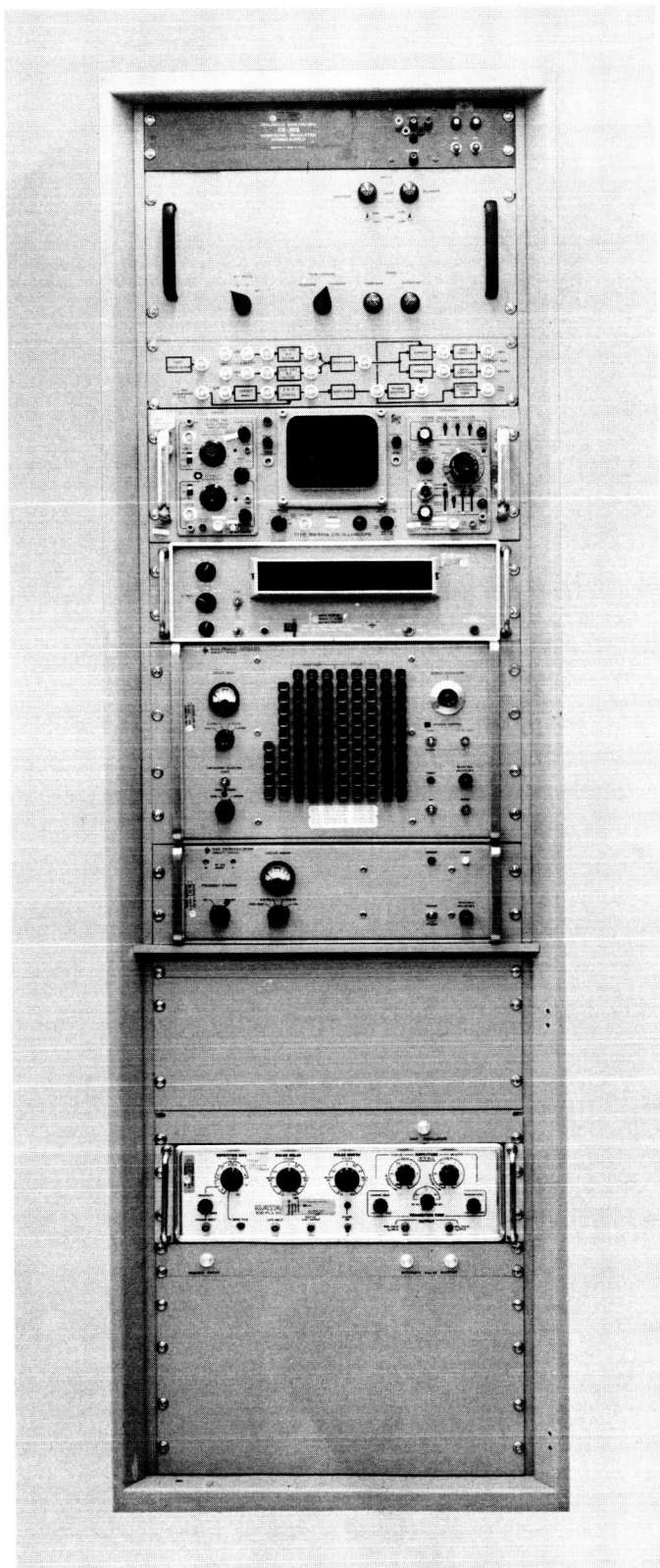


Fig. 25. Type III demodulation equipment rack

The DC control voltage for the synthesizer is generated in a digital-to-analog-converter (D/A) and is in the range of ± 10 v. Since the synthesizer requires a control voltage of -1 to -11 v, a matching device is necessary with a gain of $\frac{1}{2}$ and a DC offset of -6 v.

The VCO output, nominally a 1-v rms sine wave, is amplified and phase-shifted to produce two 25-v p-p sine waves in quadrature as reference signals for the ring demodulators.

Front panel gain controls are used to ensure that all signal voltages are within the required ranges.

c. Computer peripheral equipment. The computer used by the Type III demodulator was the SDS 920 in the digital instrumentation subsystem (DIS) at the Mars DSS. This computer is equipped with a multiplexed 14-bit A/D converter and a 14-bit D/A converter which were used to interface the analog and software portions of the Type III system.

A communications buffer connected to the computer was used to transmit the detected data stream to the displaying teletype machines.

The typewriter shown in Fig. 24 is a standard computer peripheral device on all SDS 900 series computers.

d. Computer program. The software portion of the system, i.e., the program, has been written in SDS Meta-symbol assembly language and is divided into three segments. The first segment accepts parameters via the typewriter keyboard and initializes constants in the remainder of the program. Segment two performs the estimation and control functions described previously under theory of operation. The third segment processes the data stream for output to the typewriter or teletype. Segments two and three use a 1-msec interrupt as a basic clock for the loop timing requirements of the program.

Bit signal-to-noise ratio (SNR) is estimated and used as a lock indicator for the two timing loops. Once these loops are locked, the frame sync point is fixed through a maximum likelihood determination. Once frame sync has been established, data are stacked in an internal buffer until a full frame has been accumulated, then transmitted in octal, word by word, via typewriter or teletype. Frame sync errors are monitored and displayed, along with the bit SNR, prior to transmission of each data frame.

Correlation of the data with the frame-sync words is done by code which is defined by PROC's and a "comma" list parameter. The program will accept different spacecraft formats simply by changing "comma" and other parameter definitions in the program head.

Since the data rates with which this system was required to operate were low (8½ and 16 bps), no attempt was made to optimize its timing. Consequently, certain expedient but unnecessary constraints limit its capacity to 80 bps, or less. Were the program to be so optimized, the limitation would be approximately 600 bps.

e. Output display equipment. The detected telemetry data can be printed out either directly on the console typewriter or, through the communications buffer, on standard teletype machines. Initially, during debugging and testing of the Type III system, the typewriter was used exclusively. During actual operation, however, the teletype option was selected with teletype machines located in the Mars control room and at JPL. Provision was made at Mars to break the data flow, when desired, and manually enter certain observed parameters (e.g., signal strength, bit error rate, antenna elevation angle, etc.) from the local keyboard in order to properly annotate the data printout.

4. Experiments and System Performance

The most important test criterion in evaluating the Type III demodulator was the bit error rate (BER). The bit error rate was predicted from RF system measurements of signal power and noise spectral density using the noisy reference theory of Lindsey (SPS 37-32, and subsequent issues of Vol. IV). The observed error rate was computed on the basis of the number of errors that occurred in the spacecraft frame sync words.

After an initial period of system testing and debugging, a number of BER measurements were made over a period of several weeks. The signal sources used were both real-time and tape-recorded telemetry from the *Mariner IV* and *Pioneer VI* and *VII* spacecraft. The final experiment, in the series, on March 16, 1967, included a simultaneous comparison with the *Pioneer* mission-dependent equipment at DSS 12, using real-time telemetry signals from the *Pioneer VII* spacecraft.

In each case, analysis of the data showed that the observed and predicted BER agreed to within the expected measurement tolerance. Table 8 is a brief summary of BER experimental data.

Table 8. Type III demodulator error rate experimental data

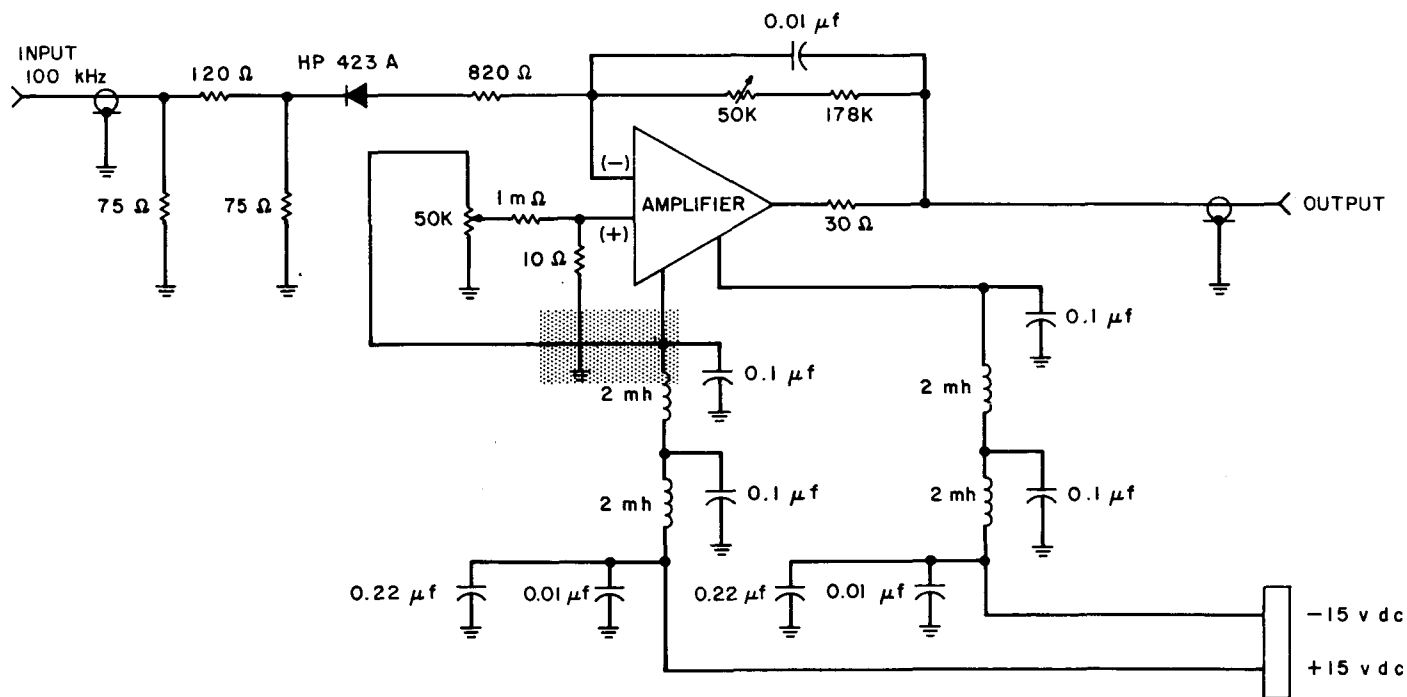
Signal source	GMT	Carrier power, dbm	System temperature, °K	Bit error rate		Comments
				Predicted	Observed	
<i>Mariner IV</i> Pass 825	16:30 to 18:00	-169	32	0.02	0.035	64 Errors in 86 frames
<i>Pioneer VI</i> Pass 438	14:00 to 18:00	-161.2	31	0.001	0.0014	Playback of taped signal
<i>Pioneer VII</i> Pass 212	21:00 to 02:00	-163	40	0.009	0.008	Signal received at DSS 12, microwaved to DSS 14. <i>Pioneer</i> MDE observed BER=0.0063 for same time

References

1. Siegman, A. E., *Microwave Solid State Masers*, pp. 315, 327-331, McGraw-Hill Book Company, Inc., New York, N.Y., 1964.
2. Higa, W. H., *Noise Performance of Traveling-Wave Masers*, Technical Report No. 32-506, Jet Propulsion Laboratory, Pasadena, California, January 1964.
3. Dent, W. A., et al., "The Extension of Non-Thermal Radio Source Spectra to 8000 MC/S," *Astrophysical Journal*, Vol. 144, pp. 568-586.
4. Worthing, A. G., and Geffner, J., "Treatment of Experimental Data," 9th printing, p. 207, John Wiley and Sons, Inc., New York, N.Y., 1960.
5. Ruze, J., *Physical Limitations on Antennas*, Technical Report 248, Research Laboratory of Electronics, Massachusetts Institute of Technology, Cambridge, 1952.

Erratum

This figure replaces Fig. 6 on p. 66 of SPS 37-44, Vol. III. The shaded portion shows the area of change.



100-kHz square law detector schematic

N67-30374

10.3 Communications Development Engineering 8

A. Ultra-Stable Oscillators: 24-MHz Low-Noise VCO Development, A. Kirk

1. Introduction

A new 24-MHz crystal-stabilized voltage-controlled oscillator (VCO) was required to make the existing receiver compatible with a new programmed oscillator (SPS 37-36, Vol. III, pp. 54-63). By adhering to the basic circuit design of existing VCO's (SPS 37-15, Vol. III, p. 34; SPS 37-34, Vol. III, pp. 48-54), it was possible to develop a modified VCO (SPS 37-40, Vol. III, pp. 59-61) that would meet the performance specifications required. The modified VCO which was developed has improved phase noise (about 10 db), better spectral purity, and simplified circuitry.

2. Performance Requirements

Performance specifications established for the 24-MHz VCO are:

- (1) The phase stability must be at least as good as that of the best existing VCO. (The design goal is 0.03 deg rms in a $2\beta_L = 5$ Hz loop.)
- (2) The gain must be adjustable from 40 to 120 Hz/v.

- (3) The linearity of gain must be 5% or better over the ± 1 -v range of error input voltage.
- (4) The VCO must oscillate correctly over the entire error input voltage swing of ± 45 v.
- (5) The VCO must work with power supply voltages (+30 v, -28 v) presently available in the receiver.
- (6) The output voltage into the 50-ohm load must be between 0.5 v rms.

3. Circuit Description

The oscillator section of the circuit (Fig. 1), a 2N918 transistor was chosen to replace the 2N915, primarily because the 2N918 is a lower noise transistor than the 2N915. Actual noise measurements which were made on some of these devices showed the difference to be about 3 db. The collector voltage of the oscillator was lowered from 16 to 7 v and the current decreased from 2 to 1.5 ma. This decreased the transistor power dissipation from 25 to 7.5 mw. The Q of the collector-tuned circuit was lowered by shunting the coil with a 5.1K resistor. This helps to assure stable oscillation over the

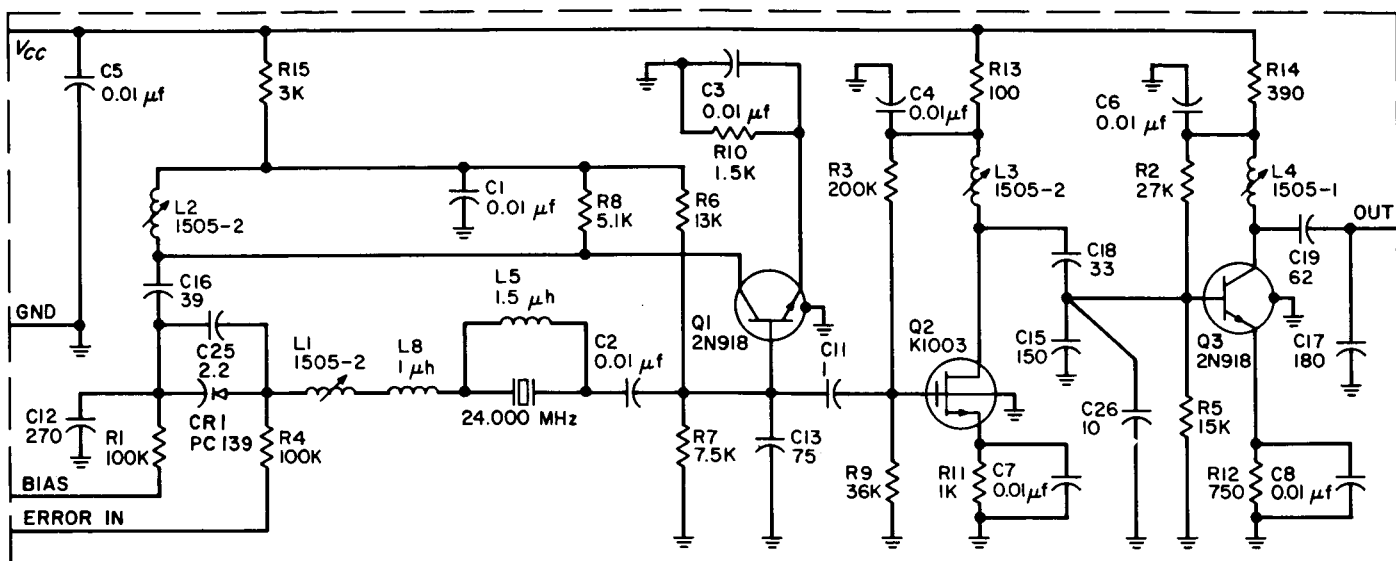


Fig. 1. Voltage-controlled oscillator schematic

full swing of error input voltage. The circuit was breadboarded with a third-overtone 31.84-MHz crystal. Loaded Q was approximately 8×10^4 . Unloaded Q of the crystal was 2.5×10^5 and $R_s = 8.0$ ohm. All performance data in this article, however, are based on the final 24-MHz VCO circuit (Fig. 1). In the buffer stage a K1003 MOS-FET¹

¹Metal-oxide silicon — field effect transistor.

is used. It is a low-noise, high-input impedance device with good gain. This stage is lightly coupled to the oscillator to minimize loading. Since the conductance spread on these transistors is rather large, biasing may have to be selective in order to achieve maximum gain.

Changes in the output stage were confined to lowering the collector voltage somewhat and using a 2N918 transistor.

Collector and varicap bias voltage regulation is accomplished with 1N945 reference diodes that have a temperature constant of $0.0005/^\circ\text{C}$ or less. This assures low drift and error input off-set once the circuit has been tuned.

The automatic gain control (AGC) circuit was deleted entirely. There is no apparent need for long-term AGC action since every VCO is followed by a limiting distribution amplifier. In addition, long-term gain changes in the buffer stage would be translated to oscillator bias shift, which may be undesirable.

4. Test Results

Figs. 2-4 are graphs plotted from data taken with two completed 24-MHz VCO's which were tuned to 50 Hz/v. Fig. 5 shows the phase noise test set-up, and Fig. 6 is a typical phase noise chart.

5. Conclusion

Development of this VCO resulted in a moderate improvement of phase stability; however, more investigation

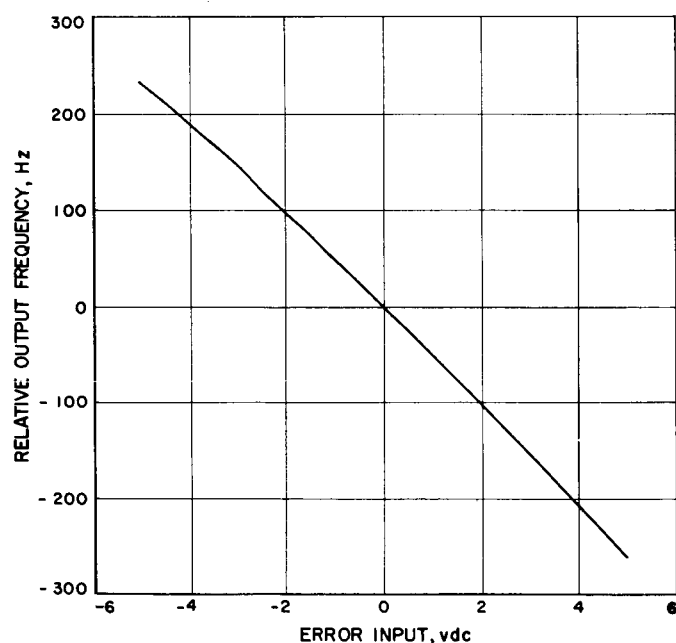


Fig. 2. Typical sensitivity over ± 3 -v error input range at 50 Hz/v

Also shown in the plots are the reflection coefficients which were measured with a laboratory-type high-precision reflectometer system. These reflection coefficient values, however, were measured at some cone physical temperature which was not recorded at the time the measurements were made. It is not presently known if the reflection coefficients measured with the high-precision laboratory reflectometer would also have varied as a function of cone physical temperature. The effect of temperature change on tuning for matched systems has not previously been investigated thoroughly and is a possible problem area which merits future study.

C. Experimental Modification of a Cassegrain Cone Assembly to Reduce System Noise Temperature, R. W. Hartop

The GSDS S-band cassegrain monopulse (SCM) cone assembly was described in detail in SPS 37-33, Vol. III, pp. 43-48. The SCM cone contains the tracking feed, diplexer, filters, and traveling-wave maser (TWM), as well as five waveguide switches used for selecting calibration loads for the TWM and for changing polarization. Two of these switches are in the sum, or reference, channel between the feed and TWM.

Table 1 presents an approximate breakdown of the antenna system noise temperature, using nominal values for contributions which vary from system to system (such as insertion loss and receiver follow-on contributions). This table may be compared with that appearing in SPS 37-34, Vol. III, p. 44, which presented the same breakdown as it was then understood.

Table 1. Nominal S-band system temperature breakdown

Source of noise temperature	Contribution, °K
(1) Extra-atmospheric noise	3.0
(2) Atmospheric absorption	2.5
(3) Quadripod scatter	4.0
(4) Paraboloid spillover and leakage	1.5
(5) SCM feed insertion loss	4.5
(6) Diplexer insertion loss	5.5
(7) Waveguide switch insertion loss (2 each)	4.0
(8) Waveguide insertion loss (12 ft)	3.0
(9) TWM (referred to coupler input)	10.0
(10) Receiver follow-up	4.0
Total system temperature	42.0

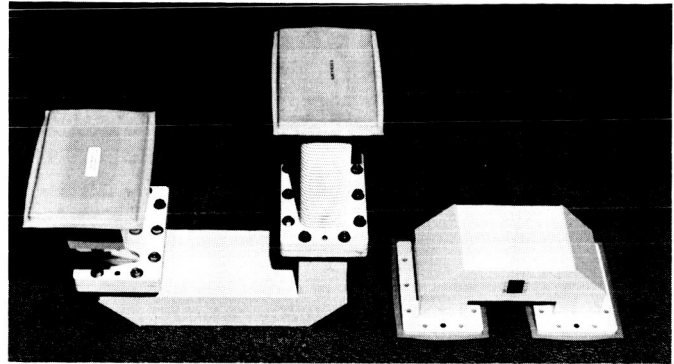


Fig. 12. Low-noise bypass waveguide sections

In order to reduce the system noise temperature for certain critical missions, a special waveguide run consisting of three rigid and one short flexible waveguide sections as shown in Fig. 12 has been fabricated to serve as a temporary low-noise bypass leading directly from the SCM feed RCP sum port to the input directional coupler on the TWM. Thus, contributions 6 and 7 in the table are eliminated, and contribution 8 is reduced to about 1.0°K. The predicted reduction in system temperature is therefore $11.5 \pm 1.0^\circ\text{K}$.

On March 14, 1967, the low-noise bypass was tested at the Goldstone Antenna Test Site on S/N 12 SCM cone assembly, which is awaiting installation at DSS-14. The observed reduction in system temperature was 11.5°K, with about a 2°K tolerance due to measurement errors. For this ground test, a GSDS TWM and receiver were not available; an R&D maser with an effective input temperature of about 6.0°K and a test receiver contributing about 14°K were used for the GSDS/low-noise comparison tests.

As a result of the successful ground test, the low-noise bypass was installed at DSS-12 on March 16, 1967 and used to track *Pioneer VII* for one full pass. The observed improvement in system temperature was $11.5 \pm 1.0^\circ\text{K}$ and resulted in a zenith antenna system temperature of 26.7°K. (DSS-12 has a lower-than-average GSDS system temperature of about 38.2°K, due primarily to higher-than-average TWM gain, thus reducing the receiver follow-on contribution.) Together with the slight increase in effective antenna gain due to reduced insertion loss, the modification results in approximately 1.72-db improvement in system figure of merit.

The low-noise bypass has thus proven successful, though of somewhat limited usefulness in that the transmitter

is needed to determine exactly how much each of the changes contributed to the improvement. Also, the use of low-noise FET's in VCO circuits warrants additional studies. Further analysis of these and other factors may lead to further improvements in overall performance.

B. Improved Calibration Techniques: X-Band Cone Built-in Reflectometer System, C. T. Stelzried and T. Y. Otoshi

This article presents results of reflection coefficient measurements made with the reflectometer which is built into the X-band cone waveguide RF calibration system. Reflection coefficients of the antenna, cryogenic load, and ambient loads are typically measured with the reflectometer whenever a noise temperature calibration of the cone is performed.

The built-in reflectometer system has demonstrated its usefulness in detecting problems in the waveguide system, the antenna, and waveguide terminations. For instance, the reflectometer, built into the multi-frequency cone at the Mars Station, recently was used to detect a problem with a waveguide switch which had degraded over a period of time and was no longer switching properly. It is occasionally necessary to dismantle the input waveguides of operational systems which do not possess the built-in reflectometer in order to verify the match.

The RF instrumentation block diagram (Fig. 7) for the X-band cone shows the reflectometer measurement system. Reflectometer measurements are made by comparison of a CW signal injected into the load under evaluation and into the maser, respectively. The side arm of the 26-db waveguide coupler at the maser input is provided with a waveguide tuner to provide the necessary reflectometer matching.

Reflectometer measurements are nominally performed as follows:

- (1) Set waveguide switches Nos. 1 and 2 to the desired load or antenna measurement positions (e.g., in Fig. 7, waveguide switch No. 1 is properly set for measurement of the antenna reflection coefficient).
- (2) Set the attenuator on the RF signal generator to the 20-db setting. This attenuator reference setting was experimentally determined for this cone. In general, the reference setting will differ for each cone.

- (3) Set switch N2 to the "VSWR" position. This enables the signal from the RF signal generator to be injected into the antenna or load. Any mismatch presented by the antenna or load under measurement will cause a signal to be reflected into the maser.
- (4) Adjust the AIL precision attenuator to give an indication of the reflected signal level on the center of the recorder scale.
- (5) Set switch N2 to the "Gain" position and switch N1 to the "Maser" position. This allows a reference signal from the RF signal generator to be injected directly into the maser.
- (6) Adjust the attenuator on the RF signal generator to return the signal level output indication to the center of the recorder scale. The attenuator setting gives the reflectometer reading directly. Greater measurement dynamic range may require higher signal level for the initial attenuator setting (20 db), which would require a correction to the final attenuator reading.

The reflectometer reading is approximately the reflection coefficient as seen at the maser input flange looking towards the antenna or loads. Comparisons made of reflection coefficients measured with this system and with a high-precision laboratory reflectometer showed that the built-in reflectometer has surprisingly good accuracy (± 1.0 db) when the physical temperature is near the temperature at which the system was tuned. However, as will be discussed, the accuracy of the system is dependent upon the physical temperature of the system.

Measurements of the reflection coefficients for the ambient load, cryogenic load, and antenna were made at 8448 MHz during noise temperature calibrations of the X-band cone (SPS 37-44, Vol. III, pp. 72-85). The measured reflection coefficients are shown plotted as a function of the cone physical temperature T_{02C} in Figs. 8-11. Each figure shows a straight line least squares fit to the data points obtained with a 7094 computer. The $(\sigma_i)_D$ value shown in each figure is the standard deviation of an individual data point due to dispersion of the data points about the least squares curve fit. The data points in Fig. 11 have been omitted for the purpose of clarity.

Changes of measured reflection coefficients as a function of cone physical temperature in Figs. 8-11 are believed to be due to detuning of the built-in reflectometer.

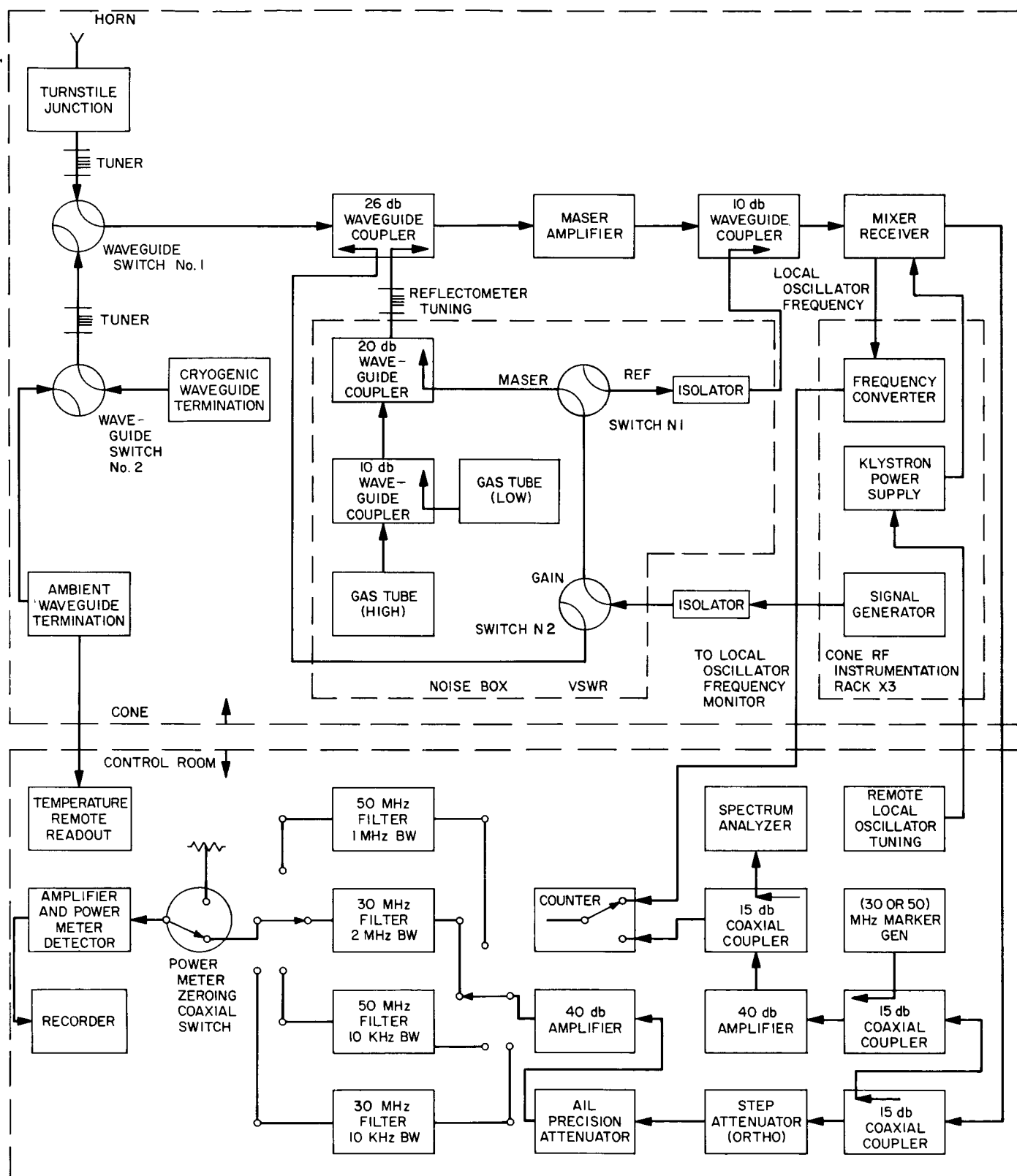


Fig. 7. Block diagram of 8448-MHz cone and control room RF instrumentation

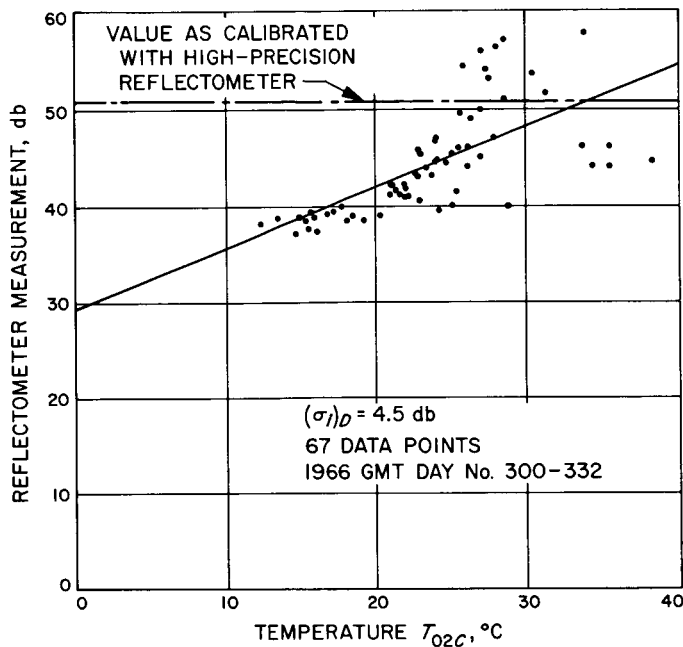


Fig. 8. X-band cone reflectometer readings of the ambient load assembly

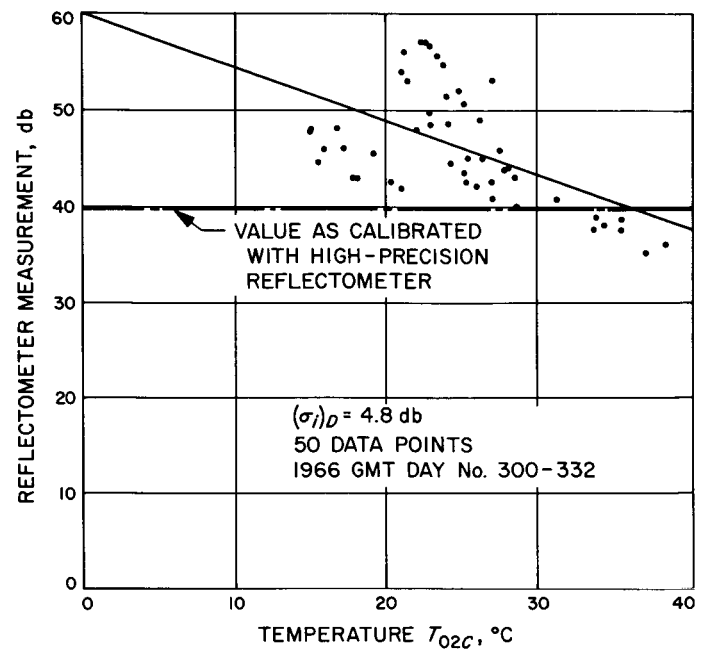


Fig. 10. X-band cone reflectometer readings of the laboratory standard LHe load assembly

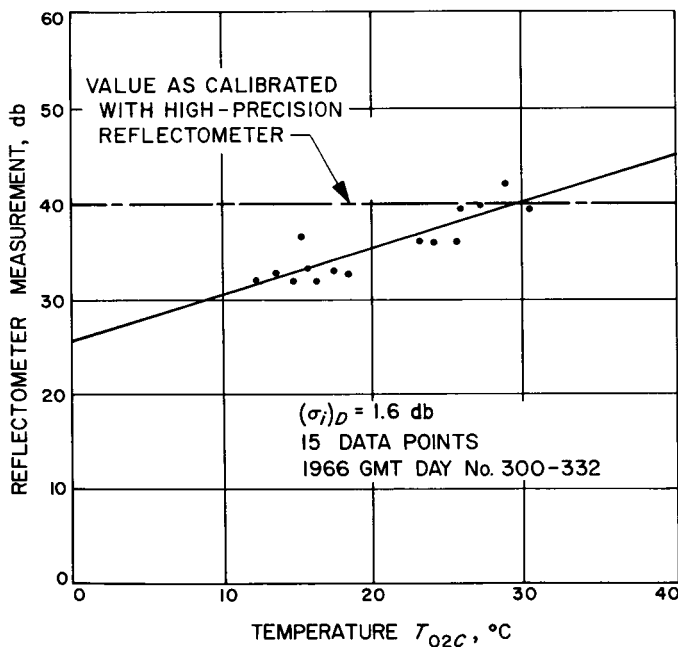


Fig. 9. X-band cone reflectometer readings of the LN₂ load assembly (Model MMC 8023 SN 013)

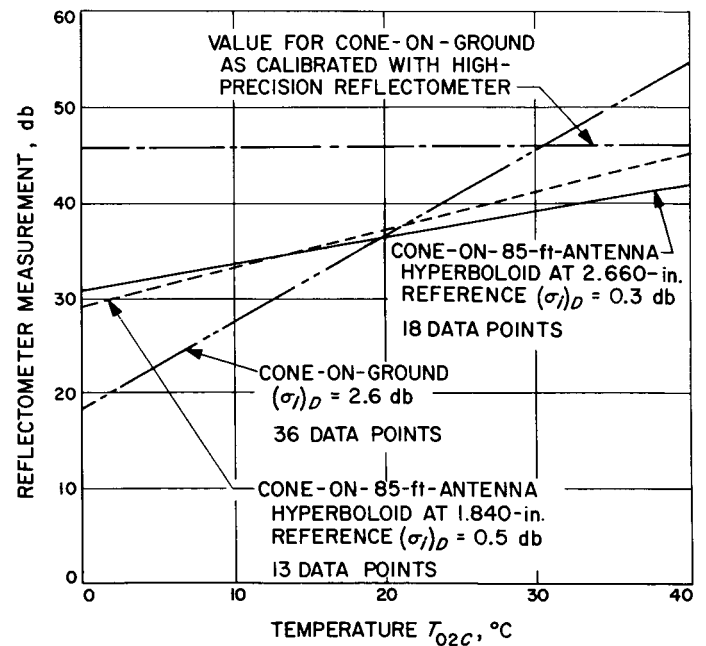


Fig. 11. X-band cone antenna reflectometer readings for cone on the ground and cone on the 85-ft-diameter paraboloid

Also shown in the plots are the reflection coefficients which were measured with a laboratory-type high-precision reflectometer system. These reflection coefficient values, however, were measured at some cone physical temperature which was not recorded at the time the measurements were made. It is not presently known if the reflection coefficients measured with the high-precision laboratory reflectometer would also have varied as a function of cone physical temperature. The effect of temperature change on tuning for matched systems has not previously been investigated thoroughly and is a possible problem area which merits future study.

C. Experimental Modification of a Cassegrain Cone Assembly to Reduce System Noise Temperature, R. W. Hartop

The GSDS S-band cassegrain monopulse (SCM) cone assembly was described in detail in SPS 37-33, Vol. III, pp. 43-48. The SCM cone contains the tracking feed, diplexer, filters, and traveling-wave maser (TWM), as well as five waveguide switches used for selecting calibration loads for the TWM and for changing polarization. Two of these switches are in the sum, or reference, channel between the feed and TWM.

Table 1 presents an approximate breakdown of the antenna system noise temperature, using nominal values for contributions which vary from system to system (such as insertion loss and receiver follow-on contributions). This table may be compared with that appearing in SPS 37-34, Vol. III, p. 44, which presented the same breakdown as it was then understood.

Table 1. Nominal S-band system temperature breakdown

Source of noise temperature	Contribution, °K
(1) Extra-atmospheric noise	3.0
(2) Atmospheric absorption	2.5
(3) Quadripod scatter	4.0
(4) Paraboloid spillover and leakage	1.5
(5) SCM feed insertion loss	4.5
(6) Diplexer insertion loss	5.5
(7) Waveguide switch insertion loss (2 each)	4.0
(8) Waveguide insertion loss (12 ft)	3.0
(9) TWM (referred to coupler input)	10.0
(10) Receiver follow-up	4.0
Total system temperature	42.0

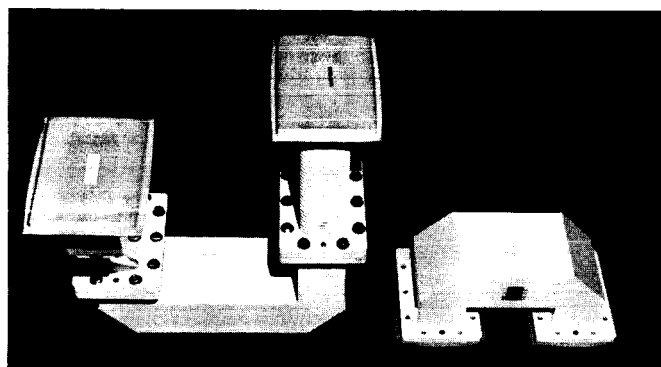


Fig. 12. Low-noise bypass waveguide sections

In order to reduce the system noise temperature for certain critical missions, a special waveguide run consisting of three rigid and one short flexible waveguide sections as shown in Fig. 12 has been fabricated to serve as a temporary low-noise bypass leading directly from the SCM feed RCP sum port to the input directional coupler on the TWM. Thus, contributions 6 and 7 in the table are eliminated, and contribution 8 is reduced to about 1.0°K. The predicted reduction in system temperature is therefore $11.5 \pm 1.0^\circ\text{K}$.

On March 14, 1967, the low-noise bypass was tested at the Goldstone Antenna Test Site on S/N 12 SCM cone assembly, which is awaiting installation at DSS-14. The observed reduction in system temperature was 11.5°K , with about a 2°K tolerance due to measurement errors. For this ground test, a GSDS TWM and receiver were not available; an R&D maser with an effective input temperature of about 6.0°K and a test receiver contributing about 14°K were used for the GSDS/low-noise comparison tests.

As a result of the successful ground test, the low-noise bypass was installed at DSS-12 on March 16, 1967 and used to track *Pioneer VII* for one full pass. The observed improvement in system temperature was $11.5 \pm 1.0^\circ\text{K}$ and resulted in a zenith antenna system temperature of 26.7°K . (DSS-12 has a lower-than-average GSDS system temperature of about 38.2°K , due primarily to higher-than-average TWM gain, thus reducing the receiver follow-on contribution.) Together with the slight increase in effective antenna gain due to reduced insertion loss, the modification results in approximately 1.72-db improvement in system figure of merit.

The low-noise bypass has thus proven successful, though of somewhat limited usefulness in that the transmitter

cannot be operated while in the bypass mode. Since the changeover time after the initial cycle is only about 1 hr, however, the bypass may be important in obtaining telemetry not otherwise available without use of the 210-ft-diameter antenna at DSS-14. A second set of waveguide parts for the low-noise bypass has therefore been placed on order for shipment to an overseas DSS for possible future use.

D. High-Power Transmitter Development,

E. J. Finnegan

1. Controlled 20-kw Power Source

The silicon-controlled rectifier (SCR) power supply described in SPS 37-43, Vol. III, pp. 111-112, has been completed. The power supply has been tested to 25 kw with satisfactory results; full control was realized from near 0 to 100% output. A filter which greatly reduces the AC ripple was added to the power supply output. At small conduction angles, high-frequency components are produced by the power SCR's. These are insignificant when the conduction angle is large, and the DC is quite adequate for a klystron focus magnet. The finished power supply will have a tapped, secondary transformer in order to select an operating point with a large conduction angle and thus assure a low noise output. This power supply will be tested with the 1300-kva, 400-Hz motor-generator set at the Goldstone Venus Site during the next reporting period as a generator field exciter to control the high-voltage klystron power supply.

2. 100-kw SCR Controller and Regulator

a. Generator low-frequency effects. The 20-kvdc klystron beam voltage supplies, which power the DSN 10- and 20-kw transmitters, operate from a 400-Hz motor-generator set. The 400-Hz frequency was chosen instead of 60 Hz to reduce the filter size and the stored energy of the filter. This helps protect the klystron since the dam-

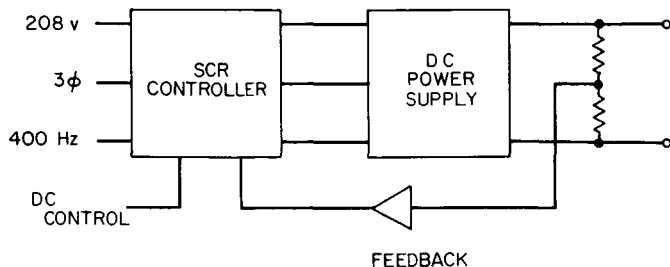


Fig. 13. Controller and power supply test circuit

age caused by an internal arc in a klystron is proportional to the stored energy. The filter is effective for the 2400-Hz ripple frequency but will not remove the 20 Hz produced by the mechanical modulation of the motor-generator sets. The low-frequency modulation is usually caused by variation of the air gap due to irregular pole pieces. With

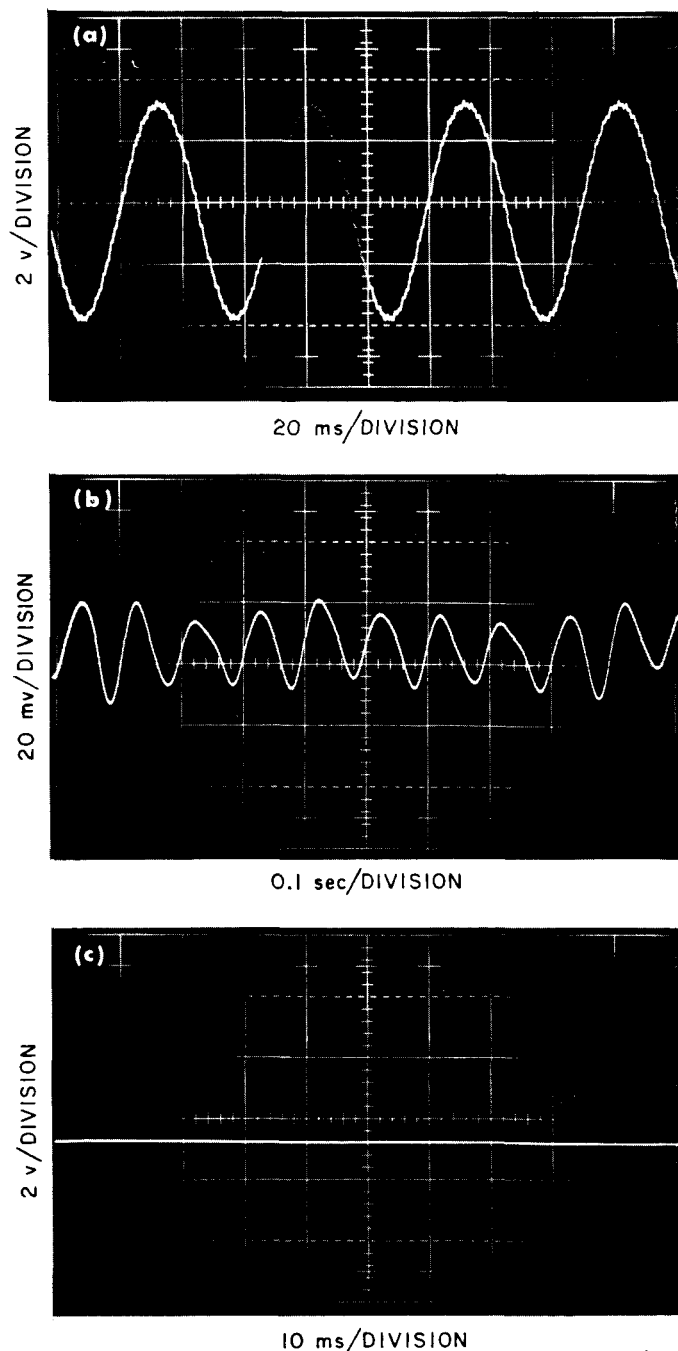


Fig. 14. Power supply modulated output (100 vdc at 20 amp)

- careful design and fabrication of the generator, these frequencies can be minimized. However, some machines now in use by the DSN still have undesirable frequency components in the low-frequency range. This low-frequency modulation is superimposed on the DC beam voltage and phase-modulates the klystron.

b. Frequency response tests. Frequency response tests were made on the SCR power supply (refer to Subsection 1), and it was noted that the three-phase, full-wave AC controller had a 600-Hz response. This unit may be used to regulate the AC input to any device within its capabilities. If the controller were connected between the motor-generator set and the DC klystron power supply, it would then be possible to demodulate the low-frequency ripple by the use of feedback from the DC power supply to the AC control unit. Thus, it should be possible to suppress the undesirable modulation to tolerable limits.

An experiment was performed to test this method. Fig. 13 is a diagram of the test circuit. The AC ripple mainly caused by mechanical modulation from the 400-Hz generator is fed back to the controller and placed on one of the control windings 180 deg out of phase from the original modulation.

Fig. 14a indicates the output ripple of the power supply, which is approximately 20 Hz and 7 v peak-to-peak. The power supply was run at the severest condition in order to amplify the problem. Fig. 14c is similar, with the feedback loop in and the amplifier optimized. Fig. 14b is similar, with the vertical much more sensitive (20 mv/division). As can be seen, this technique reduces ripple and modulation to a more tolerable level.

Fig. 15 shows the modulated output of the power supply with no feedback (open loop) and then with the

feedback gradually increased until all of the modulation is canceled. It is obvious from the data that low-frequency demodulation and voltage regulation are feasible with this technique.

c. Future development and tests. A 100-kw SCR controller with automatic feedback for regulating voltage and demodulation is being developed. It will be tested with a motor-generator set and power supply at Goldstone to determine the effectiveness of the approach described above.

E. RF Voltage-Controlled Oscillator Development, J. H. Wilcher

1. Introduction

The multiple voltage-controlled oscillators (VCO's) previously described in detail in SPS 37-34, Vol. III, pp. 48-53, were initially designed to meet the requirements of the Manned Space Flight Network (MSFN) receiver/exciter. These requirements are:

- (1) Adequate phase stability for operation in the 50-Hz loop.
- (2) Minimum tuning range of ± 9 parts in 10^5 .
- (3) Gain of 400 Hz/v.

Subsequent evaluation of the VCO in a 12-Hz loop verified adequate stability for use in the DSN receiver/exciter subsystem. Recently the stability of the multiple VCO has been evaluated in loops of less than 12-Hz bandwidth. The results of the VCO stability evaluation are described in this article.

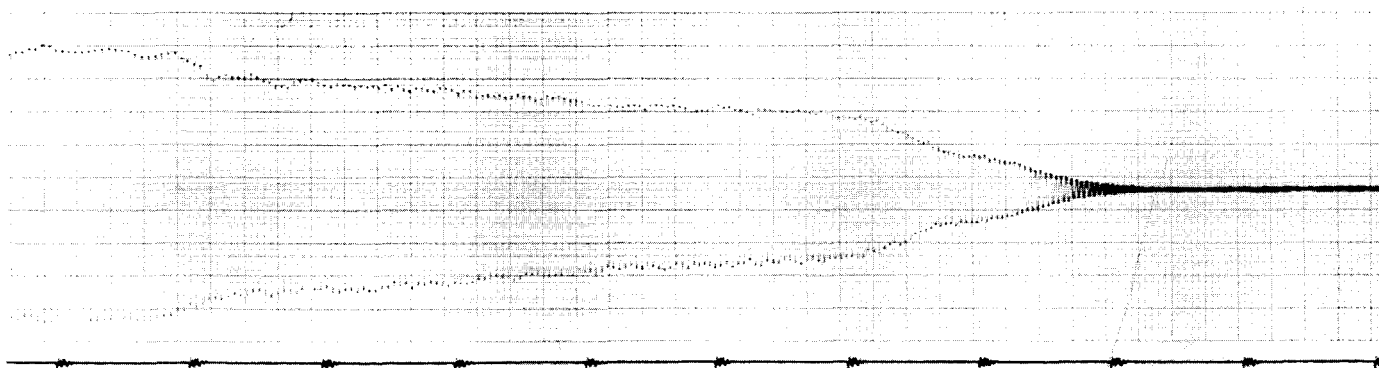


Fig. 15. DC power supply output (100 vdc at 20 amp; 20 Hz, 7 v p-p)

2. Performance

Tracking requirements for some DSSs require receiver loop bandwidths of less than 12 Hz. The phase and frequency stability of the multiple VCO was, therefore, evaluated to determine the capabilities of the existing design at a 3-Hz bandwidth. Table 2 summarizes the results of phase stability measurements in various receiver bandwidths.

Table 2. Phase stability

Network	Loop noise bandwidth $2B_{L0}$, Hz	Phase jitter, deg rms		
		Center frequency f_0	Center frequency - 2 KHz	Center frequency + 2 KHz
MSFN	50	1.2	1.3	3.3
DSN	12	1.8	1.8	4.1
	3	6.8	7.1	10.1

Frequency stability results are shown in Table 3. These measurements were made on the VCO in the laboratory R&D system. Under controlled temperature conditions, where the VCO was placed in a temperature chamber, the VCO exhibited a 10-hr frequency stability of 2.8 parts in 10^7 .

Table 3. Long-term frequency stability

Duration	Frequency stability
1 min	± 1 part in 10^7
5 min	± 1 part in 10^7
20 min	± 3 parts in 10^7
1 hr	± 5 parts in 10^7
10 hr	± 1.7 parts in 10^6

3. Conclusion

The phase and frequency stability of the existing multiple VCO design is satisfactory for operation in receiving loop noise bandwidths down to 3 Hz with negligible degradation in the RF loop threshold. The effect of the phase instability on performance must be considered before using the multiple VCO in a loop with a noise bandwidth less than 3 Hz.

F. DSN Receiver Performance, 3-Hz Loop Noise Bandwidth, J. H. Wilcher

1. Introduction

The effect of noise on the reference signals in the receiver has been analyzed and reported in SPS 37-35, Vol. IV and later issues.² The receiver reference noise at a particular input signal level can be decreased by reducing the noise bandwidth of the receiver. This results in a reduction of the bit error rate (BER) and a consequent improvement in telemetry. The limitations to the improvement, however, are the stability of the receiver voltage-controlled oscillator (VCO) in the narrow bandwidth loop and the stability of the received signal.

The noise bandwidth of the receiver at DSS-12 was reduced from 12 to 3 Hz in order to decrease the BER and so improve the telemetry being received from the *Pioneer* probe. The performance of the RF and AGC loops in the 3-Hz noise bandwidth is described in this article.

2. Receiver Design

The DSN receiver has been designed to operate with a noise bandwidth as narrow as 12 Hz. Reduction of the bandwidth below 12 Hz requires that

- (1) The receiver VCO has adequate stability.
- (2) The linear portions of the system do not saturate with the noise levels encountered in the narrow noise bandwidth loop.

As discussed in the previous article,³ the multiple VCO has been evaluated in a 3-Hz loop with phase instability measurements of less than 7 deg rms at center frequency. This amount of instability has a negligible effect on the RF loop threshold performance. The degradation of the telemetry due to VCO instability, however, is a function of margin between the RF loop threshold and the signal level at which the system is operating. With the anticipated levels of the *Pioneer* signal, greater than 12 db above carrier threshold in the 3-Hz loop, negligible degradation should result.

The portions of the receiver in which it is desirable to retain linearity under the noise conditions of the 3-Hz

²Dr. W. C. Lindsey will further discuss this subject in an article in SPS 37-45, Vol. IV.

³E. RF Voltage-Controlled Oscillator Development.

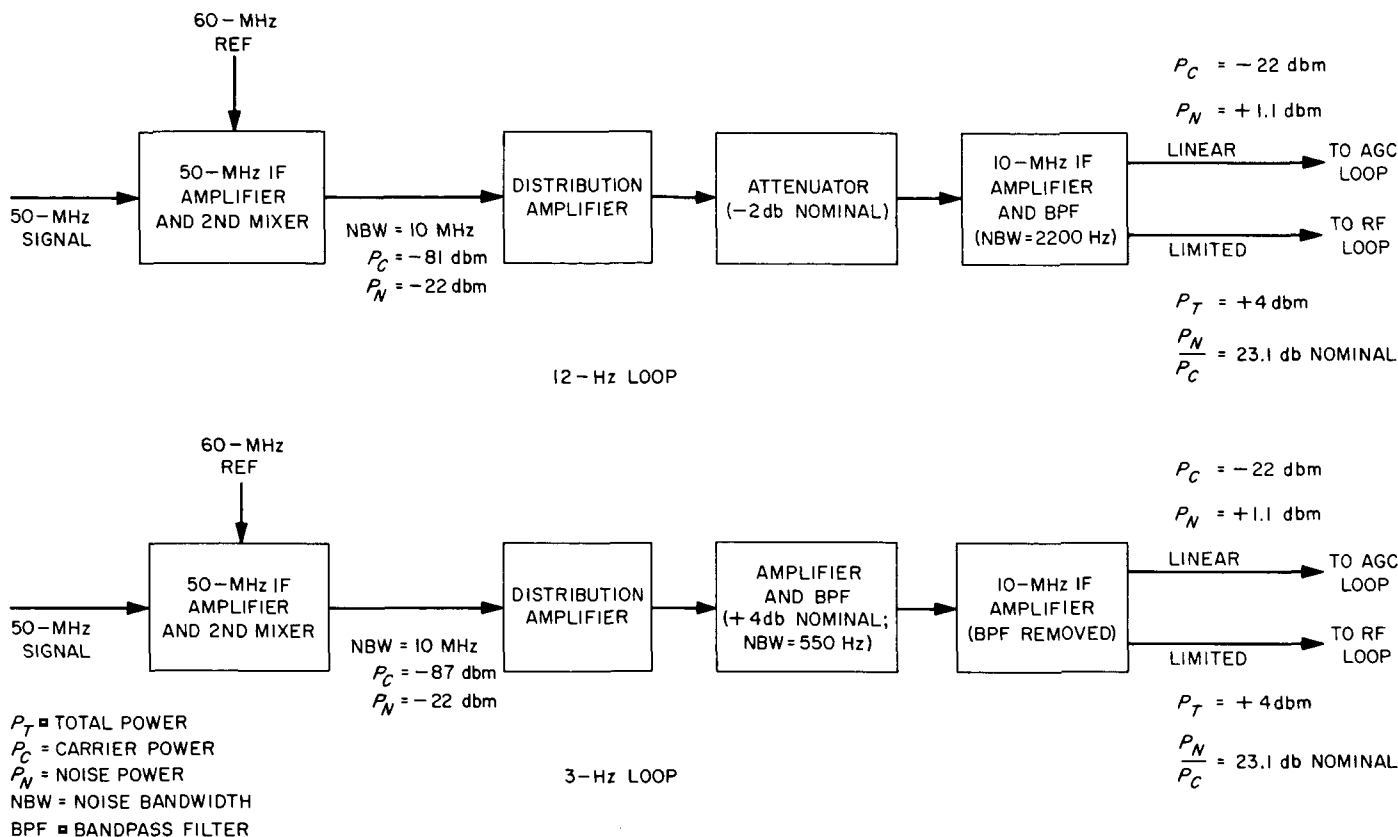


Fig. 16. Receiver block diagram

loop are the AGC loop, undetected telemetry channel, angle channels, and the correlation output of the range receiver. The only portion of the receiver of concern for the *Pioneer* tracking is the AGC loop. None of the other functions are used.

To maintain a linear AGC loop in the 3-Hz bandwidth, the receiver was operated with the same threshold noise level at the output of the second mixer that is obtained in the 12-Hz loop (Fig. 16). This was obtained by providing the additional receiver gain (6 db) following the second mixer. The noise in the 10-MHz IF amplifier was maintained at the level of the 12-Hz loop by reducing the noise bandwidth of the predetection filter by a factor of 4 (12 Hz/3 Hz) from 2200 to approximately 550 Hz.

Linearity in the other portions of the receiver can be maintained in the 3-Hz bandwidth by using the same technique as used in the AGC loop; that is, by changing levels or bandwidths or a combination of both.

3. Receiver Performance

The laboratory R&D receiver and the receiver at DSS-12 were modified to a 3-Hz loop bandwidth. In both

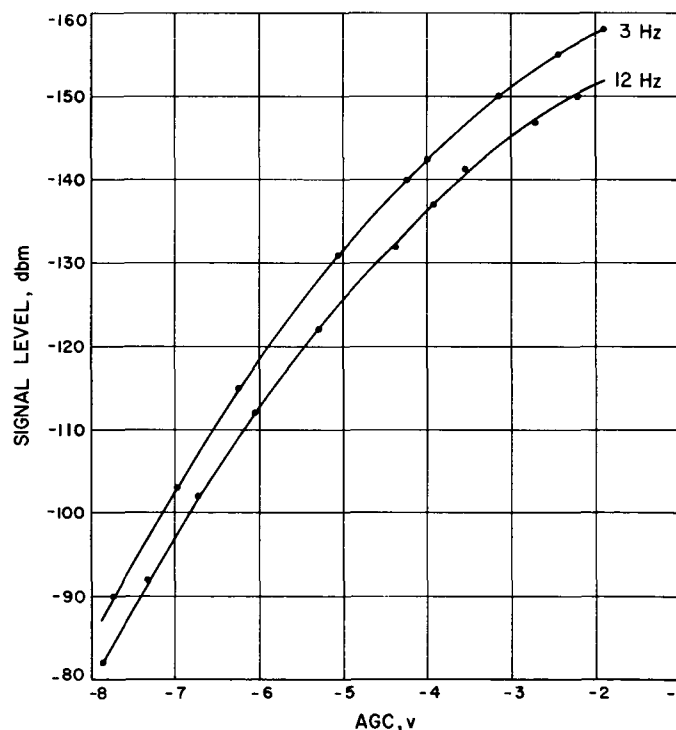


Fig. 17. AGC characteristics

receivers the carrier threshold in the 3-Hz loop was 6 db below that of the 12-Hz loop. Fig. 17 shows the AGC curves of the laboratory receiver for both 12- and 3-Hz loops. The laboratory receiver response at a strong signal level is shown in Fig. 18.

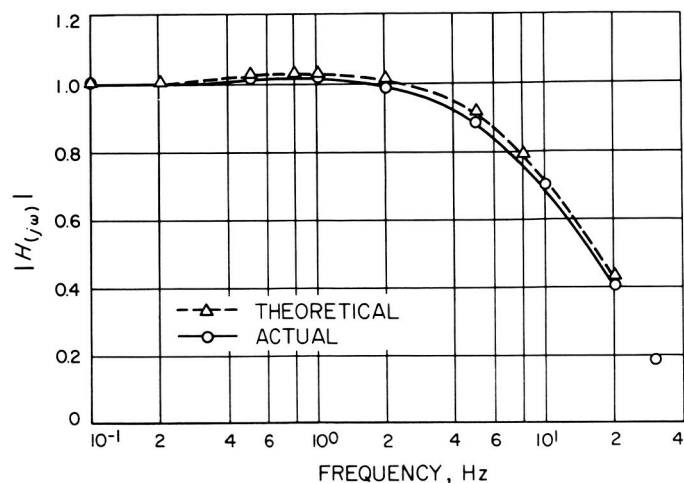


Fig. 18. Receiver response

4. Conclusion

The *Pioneer* probe was tracked using the DSS-12 receiver with both the 12- and 3-Hz loops. The signal levels at the present time are 6 to 8 db above carrier threshold in the 12-Hz loop and 12 to 14 db above threshold in the 3-Hz loop. Under these conditions the receiver reference in the 3-Hz loop is more stable than in the 12-Hz loop. Consequently, there was a noticeable improvement in the telemetry BER performance in the 3-Hz loop over that obtained in the 12-Hz loop.

G. Receiver Subsystem Development, C. F. Foster

A new R&D receiver subsystem completely compatible with present DSIF receiver subsystems has been built and evaluated as part of the *Mariner Venus 67* ranging system. This subsystem provides the R&D receiver designer and experimenter with complete flexibility regarding module location, module addition, or module removal within the subsystem.

The universal R&D receiver housing subsystem (Fig. 19) differs from the standard DSIF subsystem in that complete mechanical and electrical module mounting flexibility is provided. The module mounting plate (Fig. 20) is directly interchangeable with the DSIF standard, but it has been redesigned to provide three vertical slots

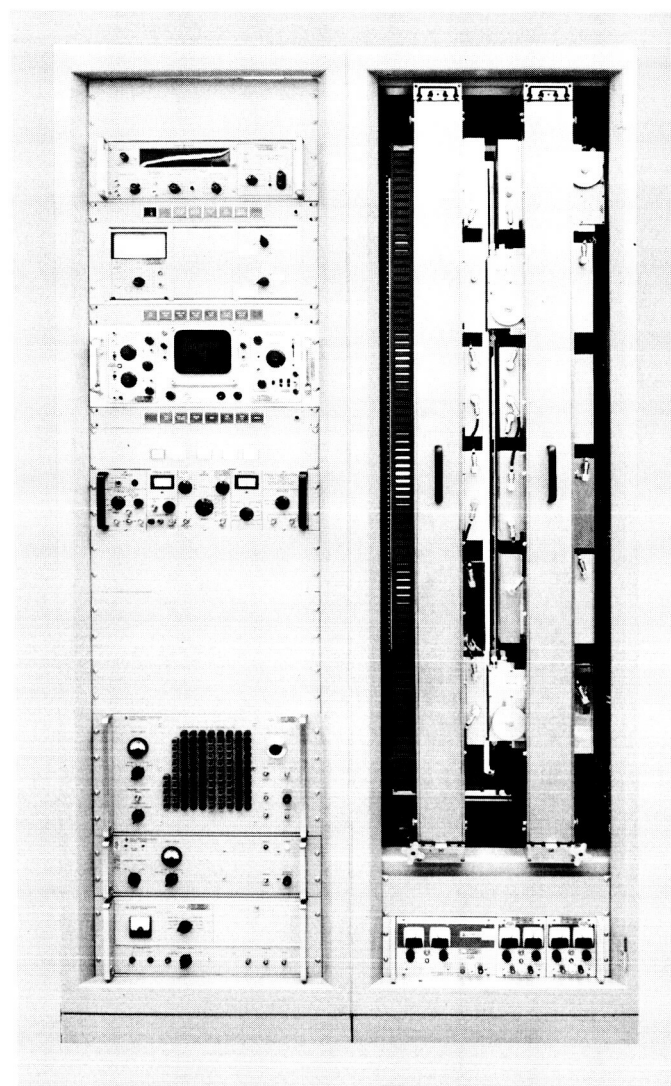


Fig. 19. *Mariner Venus 67* ranging system (front view)

with a standard pattern of tapped holes. A family of module adapter plates and blank filler plates has been designed (Fig. 21) to fit into the slots as the system design dictates. The adapter plates convert standard DSIF receiver components to a modular configuration. The adapter plates also contain a mounting support for the DC power, module control, and monitoring connector and cable.

To provide the degree of flexibility needed, the subsystem has a permanent signal, power, and monitor cabling system between the frames and the cabinet. Each frame has 42 coaxial cables which originate at a jack field on the cabinet side (Fig. 22), and which terminate on the rear of the frame (Fig. 23). The coaxial cables from the modules to the frames are run in a plastic duct which

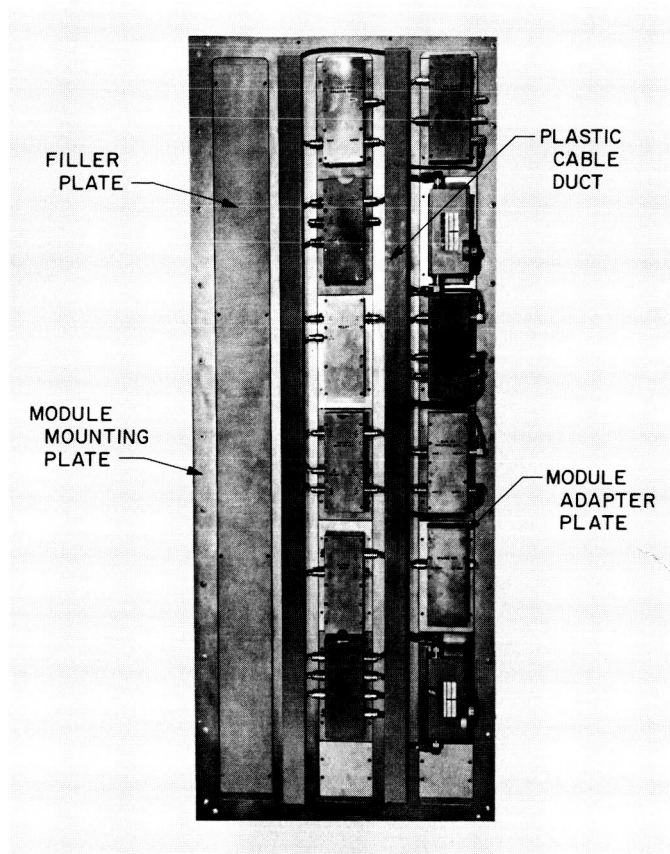


Fig. 20. Module mounting plate

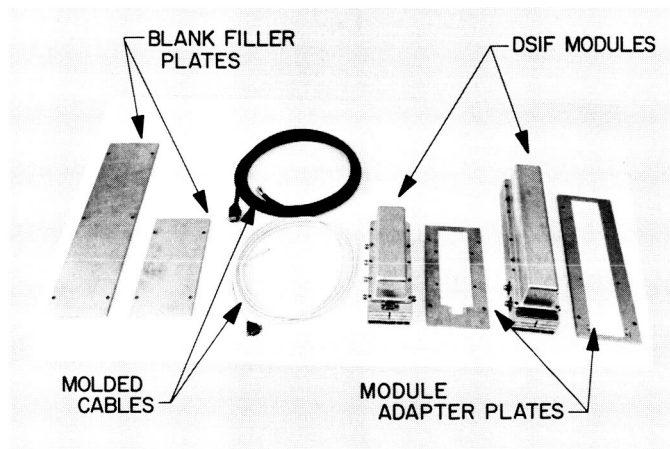


Fig. 21. Modules, module adapter plates, blank filler plates, and molded cables

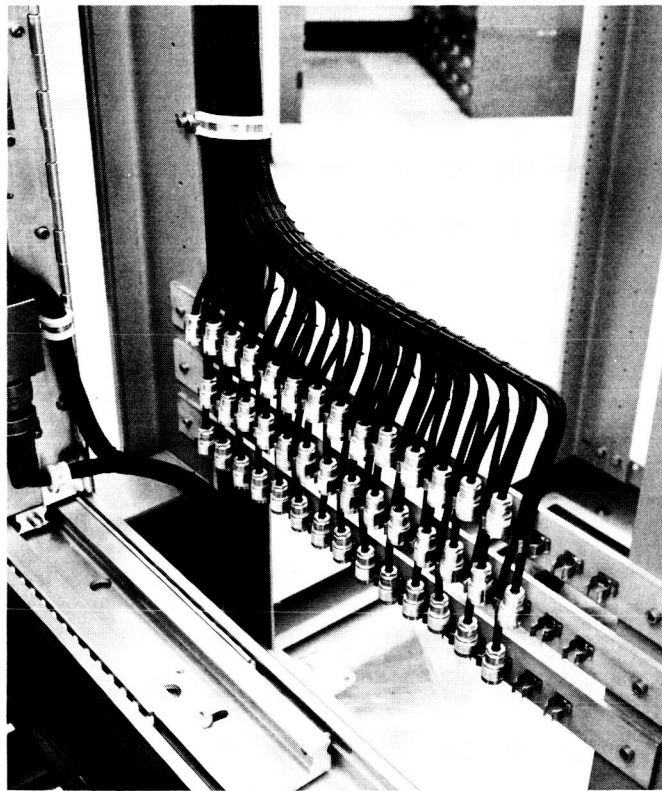


Fig. 22. Cabinet jack field

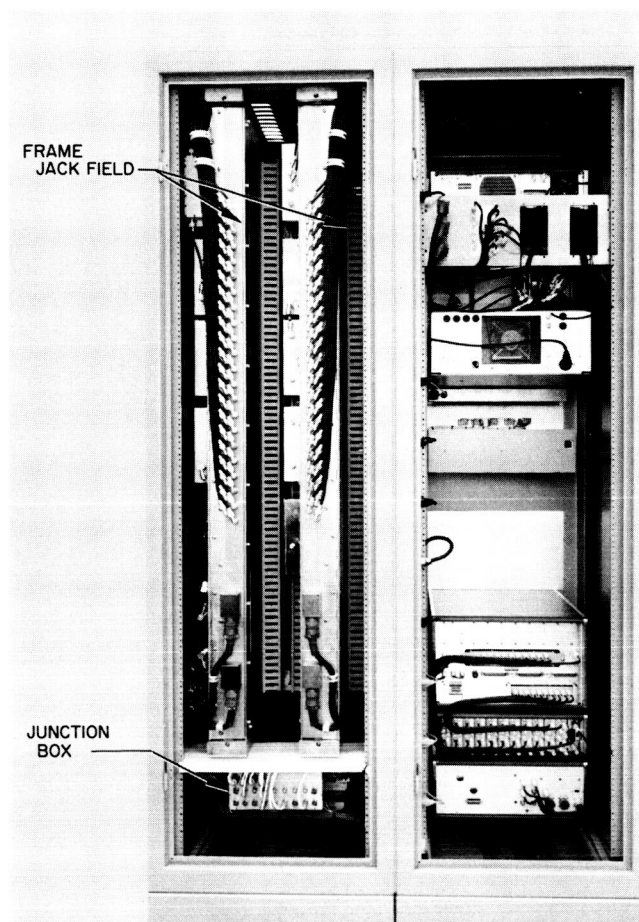


Fig. 23. Mariner Venus 67 ranging system (rear view)

eliminates time needed to relace cables when modules are added or removed. Each frame has 64 DC control and monitoring cables that originate in a junction box at the rear of the cabinet (Fig. 23). All connections within the junction box are made with taper pins inserted into terminal blocks. The junction box is used as a patch-board. The DC power, control, and monitoring cables terminate in terminal blocks located on the module mounting plates (Fig. 24). To connect a new module into this system, a power and control cable (Fig. 21) is attached to an adapter plate, and the open end is inserted into the appropriate socket of the terminal block; then connections to remote locations are made at the junction box.

The universal R&D receiver housing subsystem has been proven in a first prototype destined for experimental use at the Goldstone Mars Site. A second subsystem is now in procurement to be used for advanced development projects for the Goldstone Venus Site.

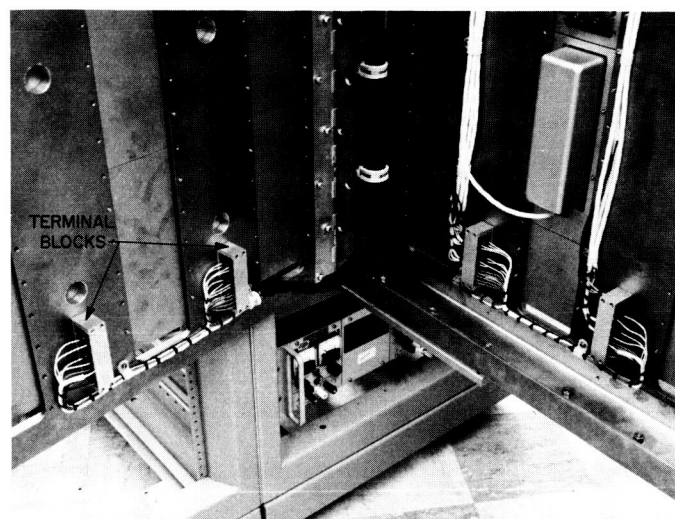


Fig. 24. Terminal blocks

H. Time Synchronization System, R. C. Coffin, R. F. Emerson, and J. R. Smith

The precision time synchronization project was described in SPS 37-43, Vol. III, pp. 92-106. Since that time, system tests have been performed at Goldstone using the 10-kw X-band transmitter and the 30-ft-diameter antenna at the Venus Deep Space Station (DSS); also, the receiver was installed in the communications building at the Echo DSS. No significant problems were encountered during the tests, and the results are in good agreement with the predicted system performance. Only one factor remains to be checked; that the scattering properties of the Moon are essentially the same when the receiver and transmitter are widely separated on the Earth as they are when the receiver and transmitter are very close. To check this factor, the receiver will be installed at the Tidbinbilla DSS in Australia in the near future.

1. Transmitting Station Control

The addition of 4000 words of memory to the computer at the Venus DSS, which is being used to control the transmitting portion of the time synchronization experiment, has permitted expansion of the program to allow improved operator-computer communication. A typewriter input/output package has been added to the program which allows the operator to conveniently monitor and control the computer operations without interfering with the over-all operation of the program. Several of the commands available are similar to those incorporated into the Mars DSS's programmed oscillator control program. In addition, coder commands are included which enable the operator to change the position, offset, width, and speed

of code sweeping. They also enable the operator to start and stop the sweep. These commands permit the operator to simulate many conditions which could cause system failure, a feature which aids in fault diagnosis and correction, thereby assisting in minimizing downtime.

2. Performance

The program has been operating since March 2, 1967. The performance of each of the segments of the program has been determined.

a. Antenna control. The program points the antenna at the ephemeris-predicted location of the Moon to within ± 0.015 deg throughout an entire track and to within ± 0.006 deg throughout 80% of the track.

b. Programmed oscillator. The program drives the frequency of the programmed oscillator to the ephemeris-determined value so well that the error cannot be detected with the equipment available at the DSS. The accuracy is well within the requirements of the system.

c. Modulation control. As with the programmed oscillator, the coder control by the program is well within the accuracy requirements of the system; this error is also below the measurement capabilities of the equipment available at the DSS.

3. Receiver

Since the last report, system tests have been performed at Goldstone, and the receiver can now be described in more accurate detail. The receiver block diagram is shown in Fig. 25. This is a complete receiving system block diagram in that it includes the RF assembly, coder, and receiver.

Table 4 contains the pertinent receiver characteristics. Most of these measurements were made in the laboratory and not at Goldstone. The noise figure was measured by

recording the output noise power, noise bandwidth, ambient temperature, and receiver gain, and then using the familiar relation, $P_N = KTBGF$. Therefore, the noise figure is that of the entire receiver. The modulation index was set by injecting a carrier signal at 8450.1 MHz at the input of the receiver and then using the receiver output as an indication of the amount of local oscillator carrier suppression. It is necessary to set the carrier suppression with a narrow-band detector due to the fact that the length of the modulation code is such that the side bands are about 50 Hz apart. It has been found that a carrier signal, stable enough to set modulation index, may be derived by applying the output of a frequency synthesizer set to 49.70647058 MHz to an HP 10511A spectrum generator. The output of the spectrum generator at 8450.1 MHz (the 170th harmonic) is of adequate level to enable the adjustment of the carrier suppression.

In the SPS 37-43, Vol. III, article describing this system, it was mentioned that by pointing the antenna at the Sun we would see an increase of approximately 1 db in noise power output. By this means it is possible to determine whether or not the receiver gain has changed (assuming a constant noise figure). System tests at Goldstone have shown that an increase of at least 1 db in noise output power is observed when the receiver antenna is pointed at the Sun and that, furthermore, this is a useful check of system operation.

The signal-to-noise ratio (SNR) predicted by the link analysis presented in SPS 37-43, Vol. III, p. 97, is 11.8 db. However, due to a difference in the system noise temperature from that originally expected, the prediction is a little optimistic. With a noise figure of 6.1 db, the system noise power P_N is -157.9 dbm. Using this figure in the link analysis, one finds that the SNR predicted is 9.4 db. On February 2, 1967, with a sample size of 50, the mean SNR was found to be 9.57 db. The standard deviation was 1.32, and the variance was 1.75.

A typical trace from the strip chart recorder at the output of the receiver is shown in Fig. 26. A tangent line is drawn on the trace in order to determine the time at which correlation began and, hence, the clock error. The slope-line should intersect the zero axis at exactly 30 sec after the minute if there is no clock error. There are several factors that affect the accuracy of the system. The first, and possibly the foremost, type of systematic error is that of ephemeris discrepancies. The best available ephemeris of the Moon is accurate enough to predict the position of the center of mass of the Moon within 150 m. A discrepancy of that magnitude would be indicated by the time synchronization system as a clock error

Table 4. Prototype X-band time synchronization receiver measurements

Characteristic	Value
Receive frequency	8450.1 MHz
Noise bandwidth	10.94 Hz
Gain	142.5 db
Noise figure	6.1 db
Time constant (post-detection)	10.5 sec
Carrier suppression (local oscillator)	> 40 db

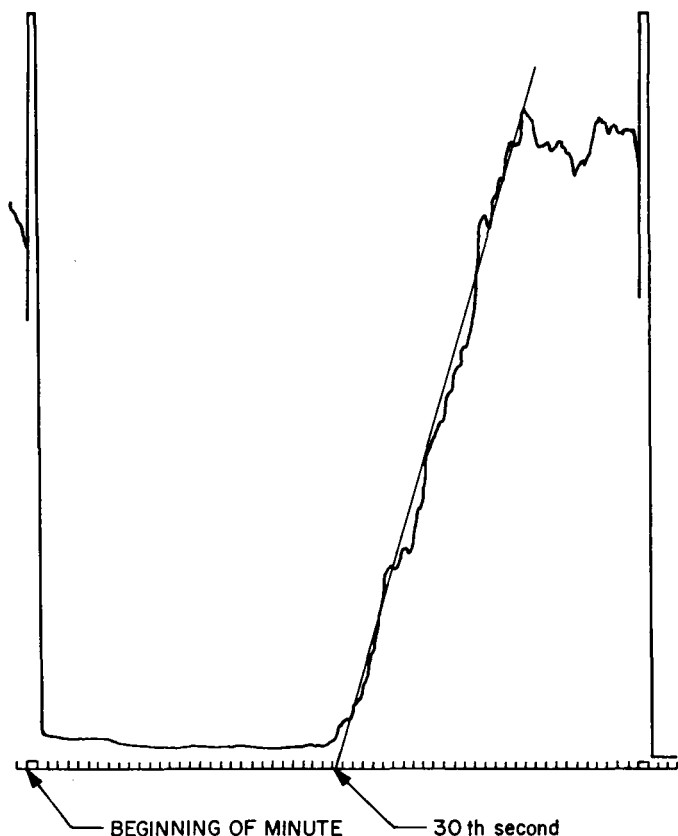


Fig. 26. Typical correlation curve

of $1 \mu\text{sec}$. An error of this type, however, may be corrected through the use of a receiver at the transmitter station operating from the transmitter clock. Before sending signals to a distant station, the transmitter will transmit to its own receiver to verify station time. If the local receiver indicates a timing error, the transmitter operator will assume a systematic error and make the proper corrections before sending information to the distant station.

There is also an error possibility due to the fact that the Moon is not a smooth reflector. It has been noted that there is typically a variation in signal strength of about 2 db peak-to-peak when the range gate is held full on the Moon. This is probably due to reflectivity variations and multipath reflections produced by the motion of the radar reflection point on the Moon's surface. Signal strength variations contribute to the noise on the rise of the correlation curve, thereby producing a possible error in drawing the tangent line and, hence, an error in timing information. The errors of this type can be somewhat nullified through the use of a computer program that would calculate the time error on each minute and then perform certain statistical operations on a number of passes to arrive at the most accurate time error.

There are several other types of system timing errors, most of which will contribute to a lesser extent than those previously discussed. They are mentioned here only for completeness, and it should be kept in mind that their contribution to system error will, in general, be on the order of fractions of microseconds. A timing error will occur when there is an error in the location of the station; that is, the actual station location is different from that given as inputs to the computer programs that compute the ephemeris. Any change in equipment delay will also appear, in the system readout, as a timing error. A clock difference, or timing error, can also occur as a result of code jitter. The code must be moved in time as the Moon changes in range, but the minimum code movement is $1 \mu\text{sec}$. Hence there is some code jitter produced by the code movement corresponding to Moon range changes.

The final source of system error mentioned is that of noise. Phase noise in the local oscillator will contribute system errors in that it will reduce SNR and may cause readout errors. The possible sources of timing error are listed as follows in order of relative importance:

- (1) Ephemeris error
- (2) Rough Moon surface (reflectivity and multipath)
- (3) Error in station location
- (4) Equipment delays
- (5) Code jitter
- (6) Noise sources (phase jitter in reference)

The sources of error that have been mentioned will all contribute to the distribution of clock error as read out by the time synchronization receiver. Variance of clock error as indicated by the system is well within the limits imposed by the system goal of $\pm 10 \mu\text{sec}$. As an example, on day 96 of 1967 with a sample size of 67, taken over an hour's time, the mean zero crossing occurred at 32.707 sec after the minute (a clock difference of $2.707 \mu\text{sec}$). The variance was 1.89, and the standard deviation was 1.37.

In the tests and demonstrations that have been performed so far, the system has proved to be very reliable and the built-in systems tests to be good aids for determining operability. The clock errors indicated by this system have compared very well (better than $\pm 5 \mu\text{sec}$) with those indicated by the portable cesium clock used for calibration checks. The receiver has performed as expected and will need only a minimum of changes before the first commercially built prototype is completed. In general, the system is performing as designed and is well on the way to becoming an operational system.

N67-30375

Facility Engineering and Operations

A. Flight Project Support, J. Orbison

1. Surveyor III Mission

The *Surveyor III* spacecraft was launched from Cape Kennedy, Florida, on April 17, 1967. The Pioneer Deep Space Station (DSS) provided primary tracking and command data transmissions. The Echo DSS performed backup tracking during first view periods, midcourse maneuvers, and landing. After spacecraft landing, the Pioneer DSS continued in command while the spacecraft performed soil sampling and photographic experiments.

2. Lunar Orbiter Missions

a. Spacecraft tracking experiments. The Echo DSS continued tracking *Lunar Orbiters II* and *III*, tracking the two primarily on alternate occultation view periods. The video readout sequence of each had terminated, and the telemetry data received were of normal cruise mode type. Simultaneous tracking of both spacecraft with the S-band receiver was also accomplished, both being tracked for approximately 1.5 hr with a doppler separation briefly approaching 75 Hz.

b. Handover experiments. The Echo DSS and the Goldstone *Apollo* Station successfully performed handover

experiments with a test model of the *Lunar Orbiter* spacecraft (Fig. 1). With the test model installed at the Goldstone test facility screenroom and a passive link antenna installed between Echo, Goldstone *Apollo*, and Pioneer MSFN Stations, adequate two-station testing of handover procedures and station equipment was obtained.

3. Pioneer VII Mission

a. Tracking status. The Mars DSS became unavailable for continuous tracking because of azimuth bearing improvement work, and the Echo DSS assumed temporary prime tracking duties. With the spacecraft over 45 million miles from Earth, the signal received at the Echo DSS was at approximately ground receiver threshold.

b. Modifications at Echo DSS. Two modifications were made at the Echo DSS to reduce the telemetry bit error rate as follows: First, a waveguide section was installed in the cone assembly as shown by the dotted line in Fig. 2. It was connected between the flange connection of the righthand circular polarization sum port and the input port to the 26-db directional coupler so as to bypass the SCM sum channel polarize select and the diplexer. Approximately a 1.75 db lower receiver threshold was

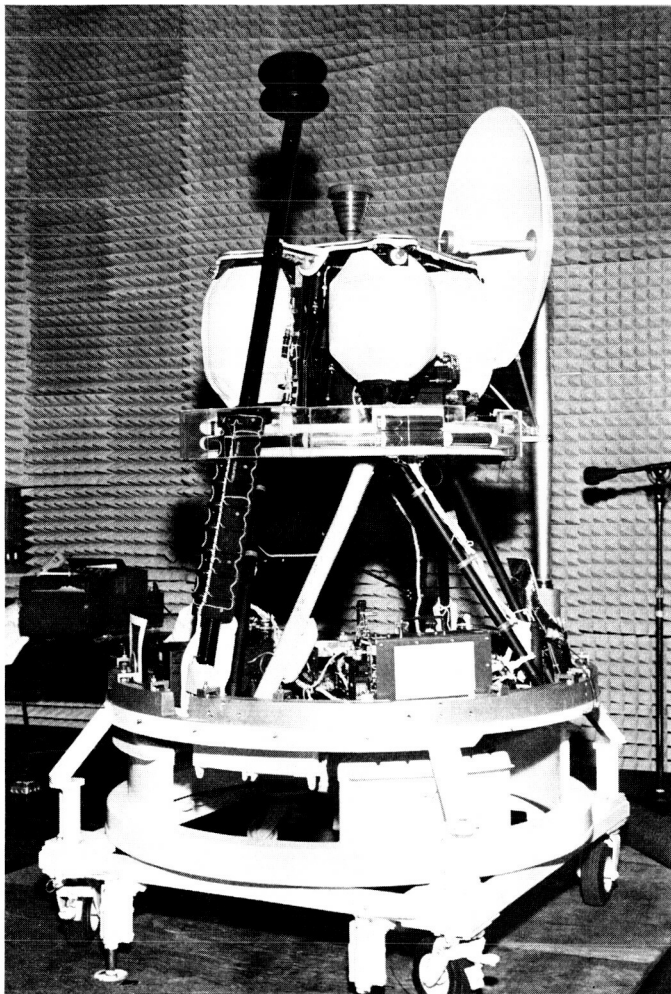


Fig. 1. Lunar Orbiter test model in GDSCC screen room

achieved; however, the modification limited the system to a receive-only configuration. A second modification was made to permit reducing the receiver reference loop bandwidth to 3 Hz and accomplish lowering the ground receiver threshold approximately 5 db. The resulting signal-to-noise improvement was sufficient to allow the Echo DSS to track the spacecraft.

4. Mariner IV Mission

The *Mariner IV* spacecraft was tracked early in March for two view periods, with Venus DSS assisting. However, the halting of Mars DSS tracking operations also stopped all *Mariner IV* tracking because the spacecraft signal strength is below the receiver threshold of all other DSIF antennas. Spacecraft signal strength is increasing as the *Mariner IV* approaches the Earth for its prime conjunction later this year.

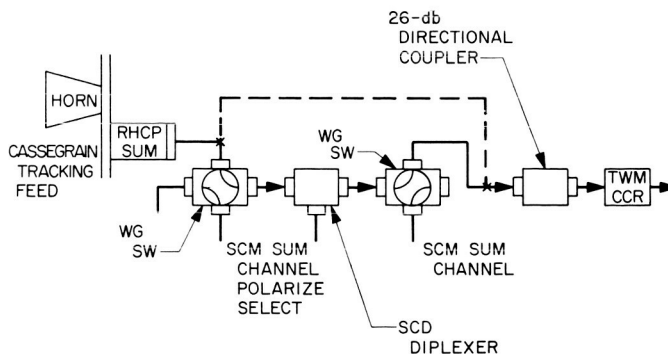


Fig. 2. Block diagram of cone modification for Pioneer VII receiving

B. Facility Construction and Equipment Installation, J. Orbison

1. Echo DSS

a. Building construction. Construction has begun on building extensions to the communications building, G-33 (Fig. 3), to the logistics/stores building, G-38 (Fig. 4), and on a new security building, G-43. The G-33 extension will provide an additional 3200 ft² and the G-38 extension an additional 5000 ft². Both are scheduled for completion during the summer. The security building will provide increased facilities for registration of visitors and vehicles to the Goldstone Complex.

b. Equipment. Installation of the *Mariner Venus 67* read-write-verify and the ground telemetry system (SPS 37-43, Vol. III, p. 123) is completed. System integration testing between DSS 12, DSS 14, and the SFOF is scheduled for early May.

2. Pioneer DSS

a. Building construction. Construction has begun on a building extension to the laboratory building, G-18, scheduled for completion during the summer. The G-18 extension will provide an additional 3200 ft² of space.

b. Station facilities. Installation of two new generators at the Pioneer DSS is essentially completed (SPS 37-44, Vol. III, p. 113). The generators provided primary power for operations, and S-band system, during the period from launch to 5 days after the landing of *Surveyor III*.

3. Mars DSS

Because of azimuth-bearing improvement work, station personnel were primarily concerned with the operational

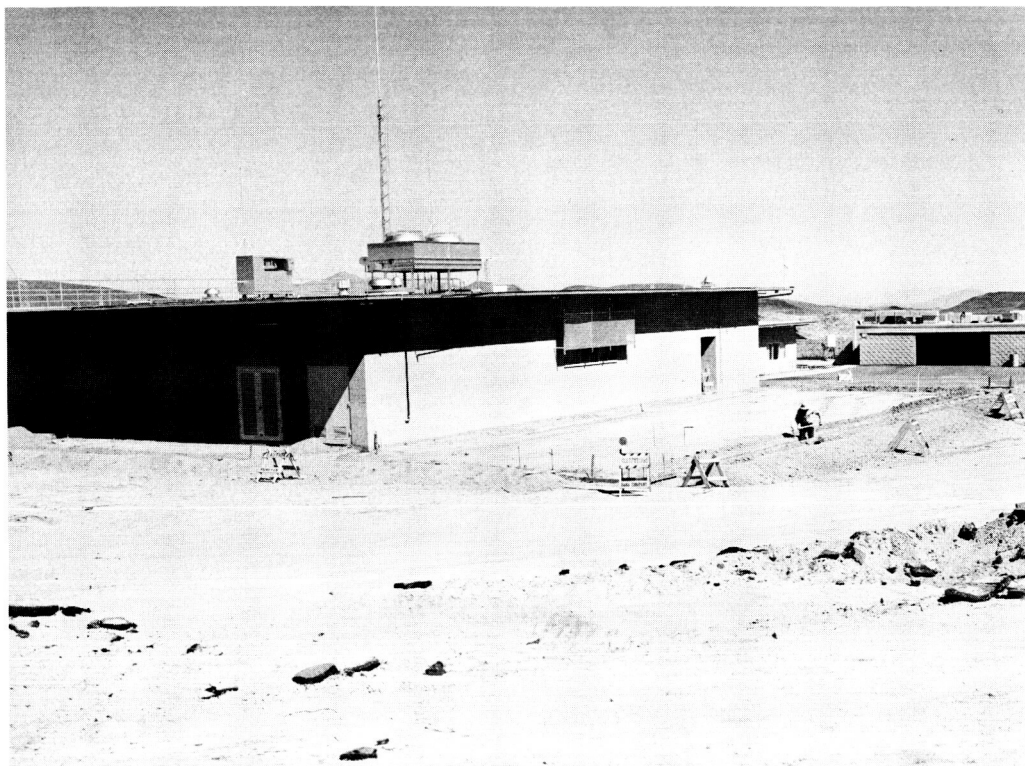


Fig. 3. Building G-33 extension, communications



Fig. 4. Building G-38 extension, logistics/stores

testing and installation of the *Mariner* Venus 67 backup read-write-verify subsystem. Also, the S-band system underwent a thorough testing in preparation for backup tracking of the *Surveyor III* landing.

C. Venus DSS Operations, R. M. Gosline, E. B. Jackson, and A. L. Price

1. Experimental Activities

During the period of February 15 through April 18, 1967, the 30-ft Az-El antenna at Venus DSS was used for a time-synchronization experiment, the 85-ft Az-El antenna was used for a monostatic planetary radar experiment, and reception of the *Mariner IV* spacecraft was accomplished utilizing the R&D equipment at the Mars DSS.

The time synchronization experiment was conducted (successfully) between the Venus and Echo DSSs and also between the Venus DSS and JPL at Pasadena, using the Moon as a reflector in both cases. The monostatic planetary radar experiment, with Mars as the target, is in progress at S-band (2388 MHz). Fig. 5 shows a typical cumulative total spectrum return from Mars.

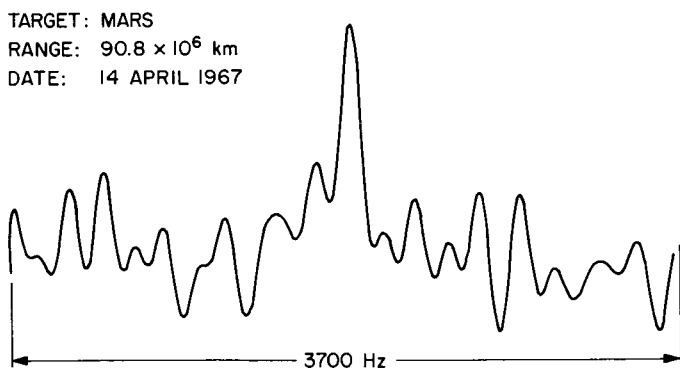


Fig. 5. Mars monostatic total spectrum

2. Subsystem Performance

a. Receiving systems. During most of this period, the Mod IV receiver, as well as the X-band receiver and the *Mariner* receiver, were inoperative due to a scheduled DSS shutdown. This time was utilized in updating receiver cabling documentation and in making receiver cabling modifications and replacements.

The Mod IV receiver is presently being used in a Mars planetary radar experiment at 2388 MHz. The receiver is being operated in its open-loop mode with the received signal being processed in the AM channel.

The *Mariner* receiver is presently being used in an R&D cone polarization loss measurement at 2292 MHz. In order to receive 2292 MHz, an external reference signal was injected into the receiver local oscillator multiplier chain since this frequency is out of the normal tuning range of the programmed local oscillator (PLO).

One failure occurred in the PLO. This involved a -15 volt power supply in the radio frequency (RF) portion of the PLO. The unit was replaced with a spare, and normal operation was restored.

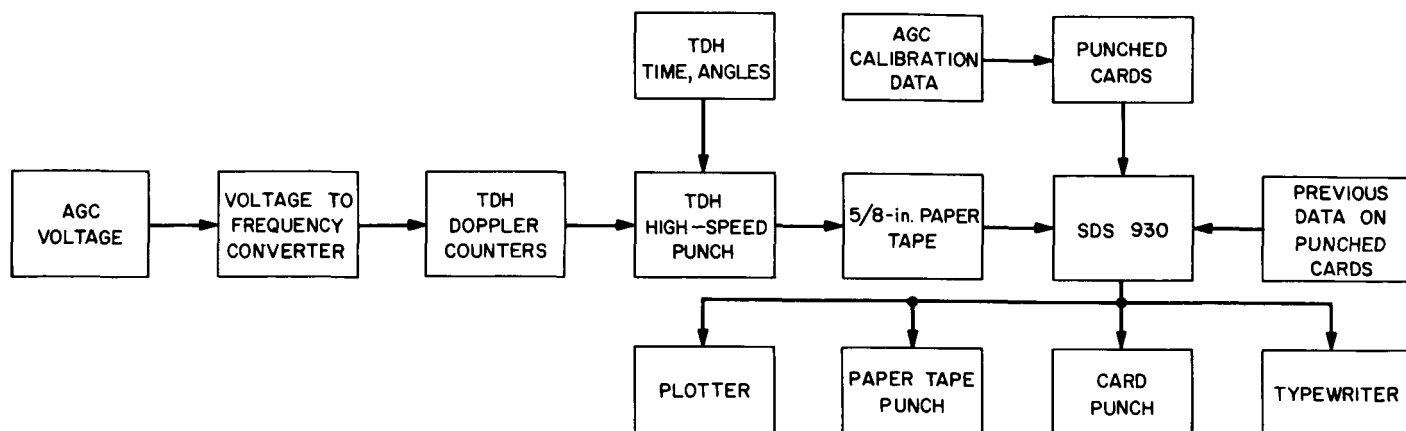
The tape reader in the digital portion of the PLO was overhauled in preparation for the present planetary experiment. The voltage-controlled oscillator (VCO) control potentiometer in the digital portion became intermittent and was replaced.

3. System Improvements

a. Digital systems. To assist in the evaluation of the Venus DSS's 85-ft antenna at X-band, a method was devised to permit the near-real-time data reduction and plotting of antenna patterns received from the Tiefert Collimation Station. A description of the receiving system configuration is contained in SPS 37-43, Vol. III, pp. 61 and 125. The digital system is shown in Fig. 6. As the antenna is manually moved through the received pattern, the automatic gain control (AGC) voltage is converted with a Dymec Model 5207-1 voltage-to-frequency converter and counted in the tracking data handling (TDH) doppler counters. Data samples consisting of time, azimuth, elevation, and AGC voltage (doppler format) are punched on $\frac{5}{8}$ -in. wide paper tape with the high-speed BRPE punch. The TDH samples every second as the antenna moves at slow rates (0.002 to 0.010 deg/sec) to improve the plot resolution.

With the aid of previously stored AGC calibration data, the SDS 930 computer converts the AGC voltage to dbm, and on command it plots antenna patterns for azimuth or elevation. Options are provided to output this data on punched cards, 1-in.-wide paper tape, or typewriter. Provisions are also made to accept this reduced data from cards or 1-in. paper tape (see Fig. 6).

The SDS 930 program is written to accept four-letter mnemonic directives entered from the typewriter which directs the computer to a selected task. Upon completion of the task, control is returned to the main program which waits for the next directive (see Fig. 7).



A brief description of the directives and conditions for their use follows:

(1) *CALB*. The computer will read from 5 to 25 Hollerith punched cards containing AGC calibration data consisting of one calibration point of dbm and AGC voltage per card. The program fits a fourth-order polynomial to the AGC calibration curve data points by the method of least squares.

(2) *TAGC*. The coefficients of the AGC calibration curve fit will be listed on the typewriter, followed by the calibration points, fit, error of each fit, and the overall rms error of the fit in dbm. The curve equation is:

$$Q = C_1 + C_2 G + C_3 G^2 + C_4 G^3 + C_5 G^4$$

where G is the AGC voltage, and $\text{dbm} = -100 (\log_{10} Q)$.

(3) **PAGC.** The computer will plot the AGC calibration data points as X's and draw the fitted curve through them. Erroneous data points may be removed from the card deck and CALB repeated if desired.

(4) *RDTD*. The computer will read from 1 to 300 samples of TDH tape (TTY format) as punched on the high-speed punch. The data is stored in core after converting to binary format. The AGC voltage data is converted to dbm if CALB has been run.

(5) *PCDS*. The data stored in core is output on punched cards in Hollerith format. Erroneous data points may be removed at this point by removing cards and using CRDS.

(6) *TYPE*. The computer will list the data stored in core on the typewriter with the AGC voltage converted to dbm.

(7) *CRDS*. Cards containing antenna pattern data output from PCDS are read back into core.

(8) *DRAW*. The routine provides for setting the plot parameters and scale. Portions of the routine may be bypassed if it is not desired to change the scale. The computer then plots the antenna pattern data points.

The method described is intended for use with the Venus DSS 85-ft and 30-ft antennas but may be used at any station with an SDS 900 series computer and plotter. The AGC curve fit subroutine is useful by itself in automatic plotting of AGC calibration curves.

Since many Venus DSS experiments involve bistatic operation with the Mars DSS at planetary distances, a means of checking angle readouts between the two stations provides an independent check of the predictions and pointing systems. A program was written for the Venus 930 computer to plot the angle differences as a function of the angles. A graph (see Fig. 8), valid for ranges greater than 200,000 miles, illustrates the program capability.

b. Receiving systems. The Venus DSS's rubidium frequency standard, which is set up on an Atomic Time scale, was compared with the Goldstone primary frequency standard. The primary standard is a Cesium Clock set up on a Universal Time scale, UT2. Adjustment is being made to offset the Venus standard by the correct amount from UT2. At present, the frequency error is four parts in 10^{10} parts.

c. The 85-ft Az-El antenna. In an effort to reduce structural distortions caused by variations in gravity loading as the elevation and azimuth change, all the bolts in the

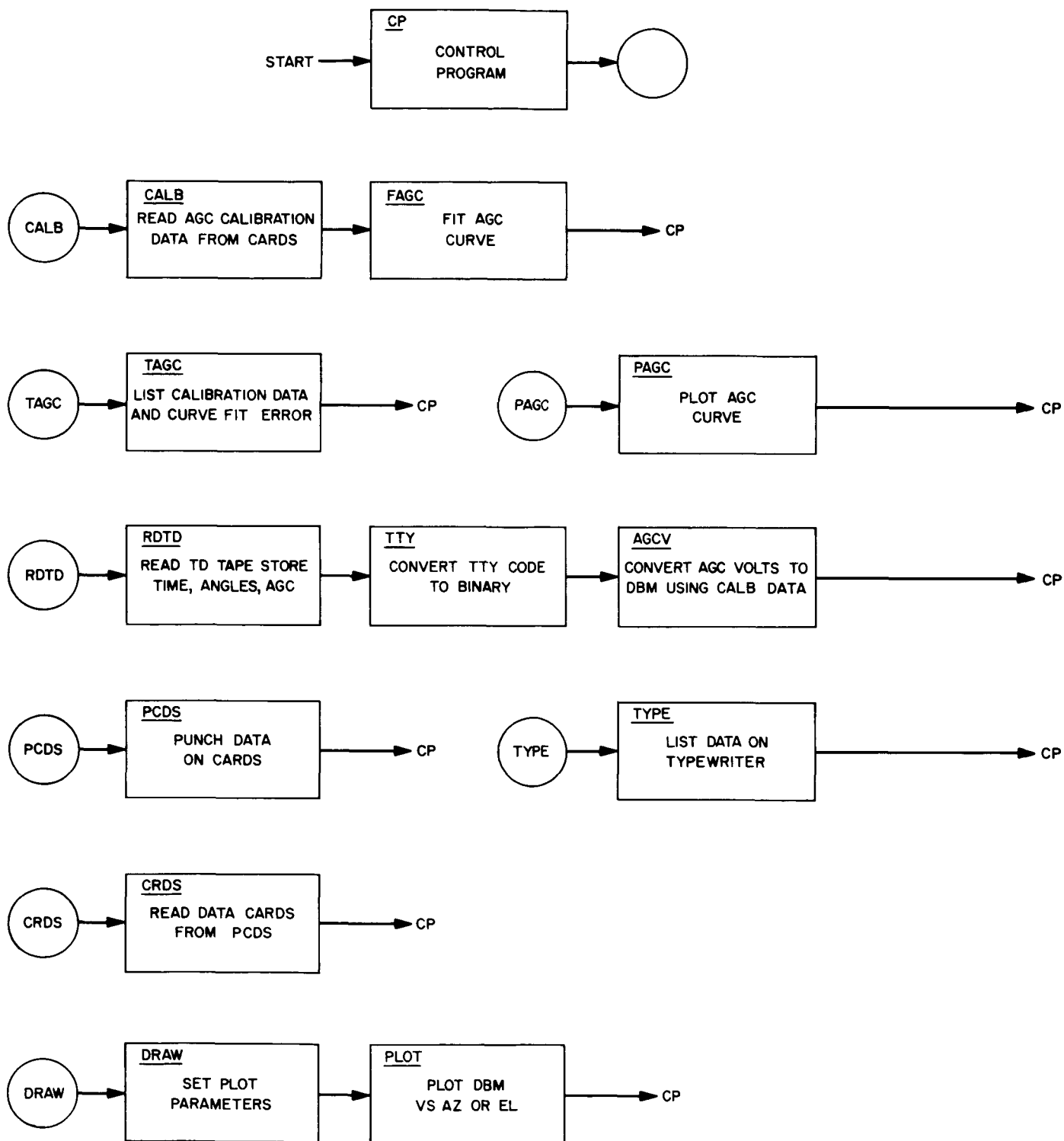


Fig. 7. Program block diagram, Venus DSS antenna patterns

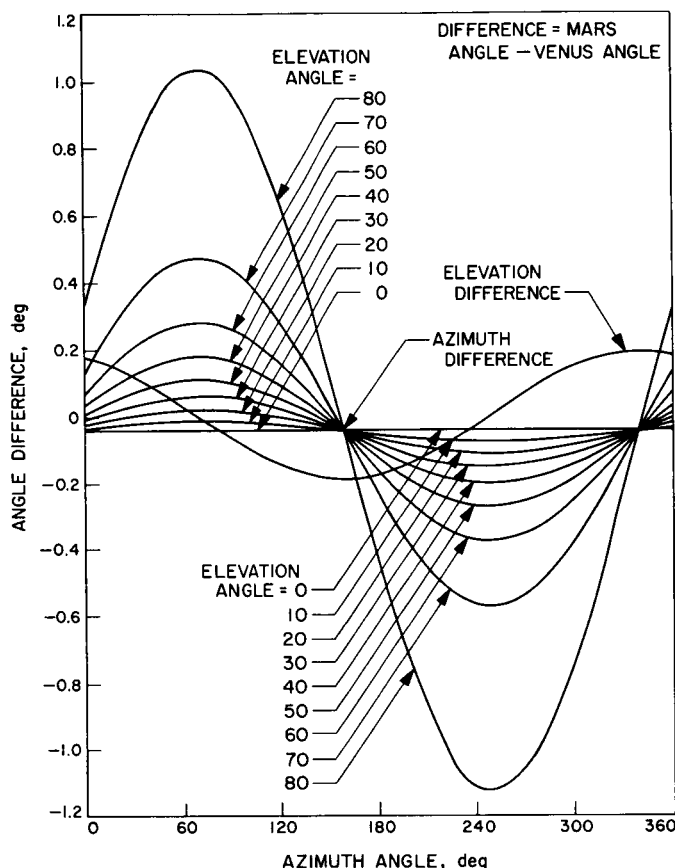


Fig. 8. Venus-Mars DSS tracking angle differences for planetary ranges

antenna backup structure were replaced with high-tensile strength steel and torqued to recommended pressures. Additional measurements of the dish surface will be necessary to establish the effects of this rebolting operation.

d. Transmitting systems. The 100-hp starting motor and magnetic clutch used to bring the 1200-kw motor-generator up to synchronous speed were replaced with a new 200-hp motor and water-cooled magnetic clutch with associated electronics. Past problems with overheating of the starting system should no longer be experienced.

D. DSIF Station Control and Data Equipment,

R. Flanders, J. Woo, G. Jenkins, E. Bann, H. Baugh, A. Burke, and E. Garcia

1. Introduction

The previous status reports on the DSIF station control and data equipment have included reports on the

antenna pointing subsystem (APS), digital instrumentation subsystem (DIS), station monitor and control console (SMC), telemetry and command processor (TCP), and the frequency and timing subsystem (FTS). This report includes the multiple mission support area (MMSA), an additional capability that is being added to the DSIF.

The multiple mission support concept adds flexibility to the deep space station tracking capability by allowing simultaneous support of more than one mission at a given station. The MMSA implementation is being done in two phases; Phase I is to meet the immediate requirements, and Phase II will meet the longer term requirements. The information in this report is primarily limited to the Phase I capability. The follow-on effort will be reported in more detail in subsequent reports.

2. Antenna Pointing Subsystem

The antenna pointing subsystem has been implemented in the DSIF stations to provide capability to point antennas under computer control. Descriptions of the Interim APS and APS Phase I have been given in previous status reports.

The Interim APS, which makes use of existing equipment, has been implemented in DSSs 11, 12, 14, 41, 61, 62, and 72.

The APS Phase I has been implemented at DSS 14 and is scheduled to be implemented at DSSs 11, 12, 41, 42, 61, 62, and 72 at 1-month intervals starting toward the end of July 1967. A fabrication contract has been let for APS control panels with expected delivery July 15, 1967. APS interface racks are close to the end of the procurement cycle, and anticipated delivery of the first unit will be approximately July 15, 1967.

In addition to hardware activity, the APS is presently involved with procurement of subsystem documentation. This documentation is composed of two distinct efforts: (1) Procurement of subsystem assembly and subassembly drawings defining APS Phase I configuration; (2) Procurement of subsystem operation and maintenance manuals required for installation, operation, and checkout of the APS.

Both phases of the documentation are being coordinated with DIS Phase II and TCP Phase II documentation so that subsystem elements common to these systems can be documented with a minimum of duplication.

3. Digital Instrumentation Subsystem Phase II

The digital instrumentation subsystem Phase II implementation is presently concerned with the procurement of subsystem documentation. A program has been initiated to assure the delivery of the documentation coincident with the delivery of the subsystem hardware. This program is composed of the following two distinct efforts: (1) procurement of subsystem assembly and sub-assembly drawings defining the DIS Phase II configuration, including assembly drawings for the DIS Phase I configuration currently in operation; and (2) procurement of the subsystem operation and maintenance manuals required for installation, checkout and operation of the DIS Phase II equipment. Completion of the drawing package is requisite for preparation of the operation and maintenance manuals. As such, the proposal evaluation and order processing are presently proceeding on this phase of the procurement. Upon completion of this effort, the procurement of operation and maintenance manuals will be initiated, and delivery schedules for the various documentation packages established.

The subsystem operation and maintenance manuals are composed of two major sections. Part I of the technical manual is to cover the operation and maintenance of the complete subsystem, as well as each of the subsystem functional elements down to the assembly level. Part II of the technical manual is to cover each assembly down to the level of the detailed parts. The manuals are to be oriented to facilitate their use by the station personnel responsible for the subsystem operation and maintenance.

Both phases of the DIS Phase II documentation procurement are being coordinated with the corresponding programs for the TCP Phase II documentation. In this manner, the documentation covering subsystem elements which are common to both the DIS Phase II and the TCP Phase II can be shared. This will eliminate duplication of effort between the two programs and result in a substantial reduction in both time and funding, since a substantial number of functional elements are identical for both subsystems.

4. Station Monitor and Control Console

Functional descriptions of the station monitor and control console have been given in previous reports and are not repeated here. The SMC Phase I, with the exception of the countdown clock, has been installed and is operational throughout the DSIF. Efforts for completion of the countdown clock have been devoted toward the procurement of components for the Division 33

Hi-Rel digital modules. A contract has been awarded to RCA for the required transistors with delivery scheduled to begin in June.

The logic design and documentation for the countdown clock are being prepared, and the prototype unit will be fabricated in-house. The DSIF operation units will be fabricated to JPL drawings by an outside contractor. The necessary parts will be supplied to the contractor. Completion of the prototype unit is scheduled for August 1967, and the first operational unit is scheduled for November 1967.

The SMC Phase II development is continuing to progress. A procurement is being established for manufacture of the Hi-Rel digital modules for the program alarm and control panel, with module delivery scheduled for August 1967. The implementation plans have been changed with the program alarm and control panel being implemented for 9 stations in 1967, rather than 5 stations as previously reported. The first unit is scheduled to be operational in early 1968.

Delivery of the Phase II prototype X-Y plotter has been delayed from April to May 1967. The procurement has been initiated for the 9 operational units required for the network.

The procurement is still in process for the page printers and line printers for the Phase II configuration.

5. Telemetry and Command Processor Phase II

The telemetry and command processor Phase II provides the Deep Space Instrumentation Facility with a mission-independent telemetry and command data processing capability for real-time operation. The TCP Phase II assembly interfaces with the mission dependent project equipment and provides the capability to decommutate, process, edit, alarm monitor, and format spacecraft telemetry data for transmission to the Space Flight Operations Facility, and to process and verify command data, received at the deep space station from the SFOF, for transmission to the spacecraft.

The basic TCP Phase II implementation has been completed with the installation of the second SDS 920 computer and magnetic tape unit at DSSs 11, 42, and 61.

A modification to the basic TCP Phase II configuration, consisting of the addition of a 4th TTY send module, has been implemented at all DSSs. This establishes a TTY

communications channel between the TCP Phase II and the DIS for transmitting spacecraft automatic gain control and static phase error to the DIS for display purposes.

The TCP Phase II is in the process of expansion to further its capabilities to digital recording of station data (TCP Phase II-B) and the processing support to mission independent telemetry demodulation (TCP Phase II-C).

a. TCP Phase II-B. The principal effort for the past 2 months has been in the procurement of expansion equipment. A purchase order was placed for nine analog-to-digital converters which are scheduled for delivery in May 1967 for partial TCP Phase II-B implementation at all DSSs with the exception of DSS 51. This implementation will provide telemetry processing support to the *Mariner Venus 67* Project. Procurement requisitions and the automatic data processing equipment (ADPE) acquisition plan for the remaining portion of the expansion equipment have been initiated.

The analog equipment (multiplexer, analog-to-digital converter) for each TCP Phase II computer will be housed in an additional equipment cabinet. This will result in a total of ten equipment cabinets for a TCP Phase II-B configuration instead of eight for the present TCP Phase II configuration. The present TCP Phase II computer has facilities for the required memory expansion from 8,192 to 12,288 words.

b. TCP Phase II-C. The principal progress for the TCP Phase II-C expansion has been in the procurement of equipment. Procurement requisitions and the ADPE acquisition plan for the expansion equipment have been initiated. The TCP Phase II-C will be implemented initially at DSSs 12, 14, 41, 62, and 71 for support of *Mariner Mars 1969*. The necessary equipment will be installed and operational prior to September 1968. It is planned to implement the remaining DSIF stations in FY68.

The analog equipment (multiplexer, analog-to-digital converter) for each TCP Phase II computer will be housed in the same equipment cabinet that houses the TCP Phase II-B analog equipment. The TCP Phase II computer has facilities for the required memory expansion from 12,288 (TCP Phase II-B) to 16,384 words.

6. Frequency Timing Subsystem Phase II

Construction of a prototype unit is awaiting delivery of parts for assembly of modules. An order has been placed for one set of digital isolation drivers to be used on the

parallel binary-coded decimal (BCD) outputs from the clock. This one unit will be installed on an experimental basis in an FTS Phase I at Goldstone. If the tests are successful, additional units will be ordered to equip all FTS Phase IIs.

7. Multiple Mission Support

Multiple mission support is a new operating concept for the Deep Space Instrumentation Facility. This new concept provides for an increase in the efficiency and flexibility of the deep space stations and improves the quality and reliability of flight project support.

The design of the multiple mission support concept allows a station to support, simultaneously, two or more projects, one tracking and the others testing. In addition, for those DSSs located in a DSCC having microwave facilities between stations, the utilization of more than one station to support two flight projects located at a single station can be realized.

Implementation of the multiple mission support concept creates three distinct and separate areas, two of which are located within the station's control room. These are: (1) the mission independent area (MIA) which houses the basic tracking station equipment required to support any flight project and is independent of the flight project; (2) the multiple mission support area (MMSA) which houses the standard equipment supplied by the DSIF for supporting and interfacing with each flight project; and (3) the mission support area (MSA) which houses the flight project furnished equipment (outside the control room).

a. Mission independent area. The mission independent area includes all of the equipment which is provided as part of the standard S-band configuration at each DSS. This equipment, its functions and capabilities have been described in various reports and documents relating to the S-band system and is not discussed here.

b. Mission support area. The equipment located in this area is normally furnished by the flight projects and is generally different for each mission. A detailed discussion of this equipment can be found in various flight project documents and is not discussed here.

c. Multiple mission support area. The multiple mission support area will house the necessary equipment to perform five basic functions.

- (1) Process telemetry, command and related project data in real time for the purpose of evaluating and controlling spacecraft operations.
- (2) Record flight project data on magnetic tape recorders, as required, in formats that are compatible with the flight project requirements.
- (3) Provide switching and patching capability for interconnecting flight project support equipment located in the MSA to equipment located in the MMSA and MIA.
- (4) Provide communications system interface capability for transmission of data over available microwave and ground communications links.
- (5) Provide system simulation capabilities for test and verification of flight project equipment and operational procedures.

d. Multiple mission support area implementation. The implementation of the MMSA is being carried out in two phases.

- (1) Phase I provides multiple mission support capability at DSSs 11 and 61 to support *Surveyor* and *Mariner Venus 67*, and at DSS 12 to support *Lunar*

Orbiter and *Pioneer*. The DSS 14 and 62 Phase I configurations will be limited to the extent of aiding the nearby stations to fulfill the multiple mission support capability via the available microwave links. See Fig. 9 for two-station multiple mission support configurations, and Table 1 for the support capabilities among the defined stations.

- (2) The Phase II implementation, which adds permanent capability, will be presented in subsequent articles.

e. Multiple mission support equipment (Phase I). The Phase I multiple mission support equipment provided is formally assigned to the telemetry and command data handling (TCD) subsystem and consists of the following assemblies.

- (1) *Telemetry and command processor Phase II.* The telemetry and command processor assembly has been implemented at all 85-ft S-band DSSs and assigned as an assembly of the TCD subsystem. Additional details for this assembly have been previously published. A status report on the TCP is included earlier in Section 5.
- (2) *MDE transfer rack assembly.* The MDE transfer rack assembly, formerly the only assembly of the

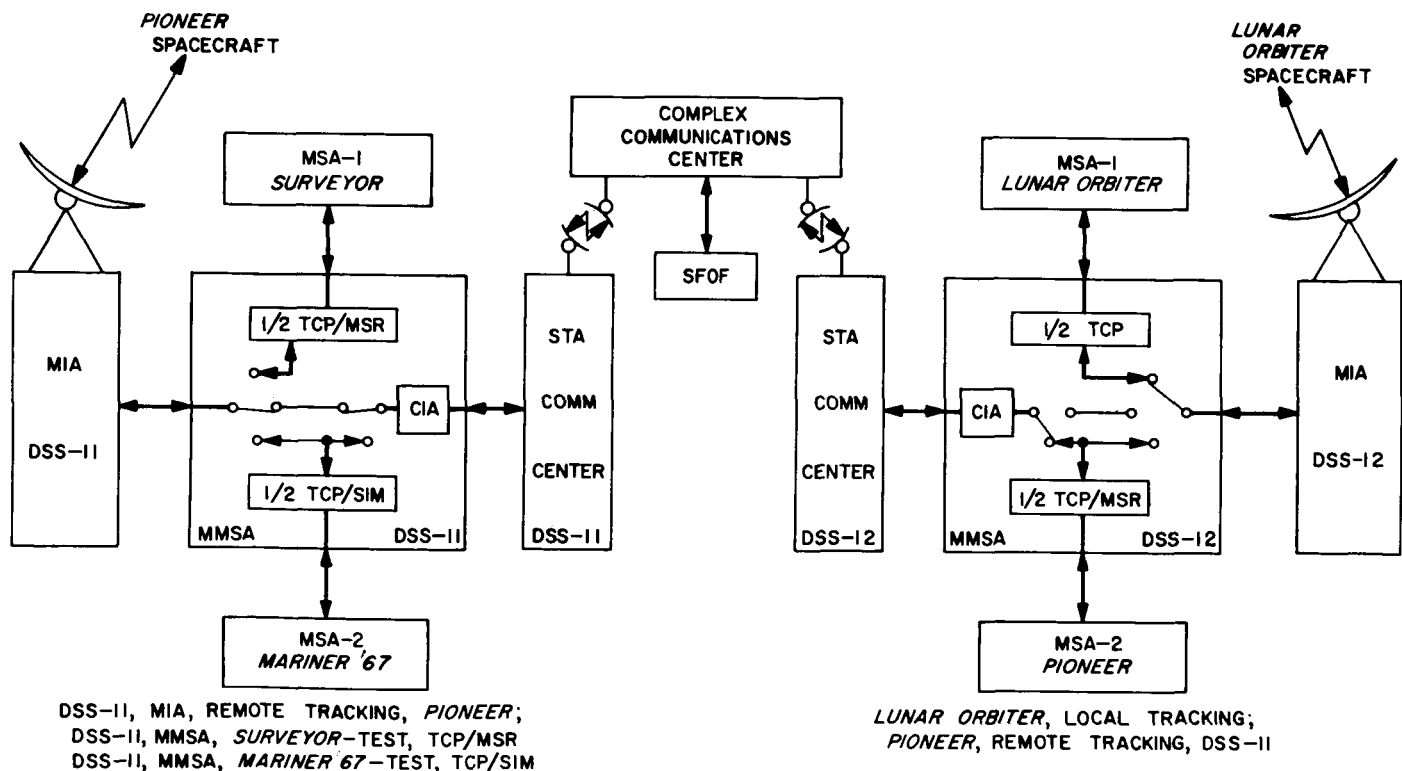


Fig. 9. Two-station multiple mission support configuration

Table 1. Multiple mission support capability

Mission independent area	Mission support area							
	Surveyor		Mariner Venus 67		Lunar Orbiter		Pioneer	
	DSS 11	DSS 61	DSS 11	DSS 61	DSS 12	DSS 62	DSS 12	DSS 62
DSS 11	Local	—	Local	—	—	—	Remote	—
DSS 12	—	—	Remote	—	Local	—	Local	—
DSS 14	—	—	Remote	—	—	—	Remote	—
DSS 61	—	Local	—	Local	—	—	—	Remote
DSS 62	—	—	—	Remote	—	Local	—	Local

TCD subsystem, has been also previously implemented at all DSSs, and additional details may be obtained from previous publications.

- (3) *Mission support recording (MSR) assembly.* The mission support recording assembly provides the additional analog recording capability required for the simultaneous support of two projects. At DSSs 11 and 61, the MSR is assigned to the *Surveyor* project, while *Mariner Venus 67* magnetic tape recording requirements are fulfilled by the TCP, in digital format. The MSR equipment provided at DSSs 11 and 61 consists of a dual FR-1400 recorder/reproducer, one FR-800 predetect video recorder/reproducer, eighteen channels of a CEC 5-133 photographic recording oscillograph and additional MSR peripheral equipment such as coaxial patch panels and voice labeling. At DSS 12, the MSR consists of a dual FR-1400 recorder/reproducer and peripheral support assemblies. The MSR at DSS 12 is assigned to the *Pioneer* Project, while *Lunar Orbiter* is assigned the station's recording subsystem and an FR-900 predetect video recorder/reproducer.
- (4) *Communications interface assembly (CIA).* The communications interface assembly provides the necessary signal conditioning required for isolation and compatibility between the mission independent equipment, the intrasite communications equipment and the mission dependent project equipment. The configuration of the CIA consists of four VCOs, four subcarrier discriminators, two mixer amplifiers, and three DC amplifiers.
- (5) *System simulation (SIM) assembly.* The system simulation assembly prime objective is that of

providing a means of generating simulated ground and spacecraft data and time signals to flight projects requiring test and verification of their operational procedures and equipment. The SIM consists of a time code translator and an FR-1200 magnetic tape recorder/reproducer. The magnetic tape recorder/reproducer was previously part of the station's recording subsystem. This configuration of SIM is being implemented at all deep space stations with the exception of DSSs 13 and 51.

f. MMSA Phase I implementation schedule. Implementation of the MMSA Phase I is as follows:

- (1) *Mission support recording assembly.* The MSR has been implemented at DSSs 12 and 61. DSS 11 MSR will be operational by June 1, 1967.
- (2) *Communications interface assembly.* The signal conditioning subassemblies provided as part of the CIA are scheduled for installation at DSSs 11, 12, and 14 by May 15, 1967. Installations are scheduled for DSSs 61 and 62 by June 1, 1967.
- (3) *System simulation assembly.* The FR-1200 portion of the SIM exists at each of the stations and will be integrated with the time code translator and peripheral subassemblies by September 15, 1967.

E. DSN Discrepancy Reporting System,

G. C. Gilley

1. Introduction

A DSN-wide system of failure reporting, engineering analysis, and management action has been developed for the purpose of (1) aiding in assuring that the DSN is

properly prepared to support flight operations, and (2) improving the reliability of DSN equipment.

In order to realize the above two objectives, the discrepancy reporting system (DRS) was developed in two levels. Level A was made to apply to all operational failures and/or problems which occur throughout the DSN during flight project operational tests or an actual mission. Level B was made to apply to all equipment failures in the DSN whenever they occur. The level A and B systems have been directed at achieving the above objectives (1) and (2), respectively.

The level A system has provided a controlled closed-loop method for systematically reporting and correcting operational failures or problems, including procedural, equipment, and computer program failures or problems. All reported failures or problems are brought to the attention of cognizant personnel for analysis and rectification. In addition, biweekly status reports summarizing the failure reporting activity during the report period are issued to aid management visibility. The level A system has been applied to the flight projects, as well as to the DSN, inasmuch as the flight projects have interfaced with the DSN.

The level B system has provided a method to improve the reliability of DSN equipment on a long-term, sustaining basis. The level B system has served to locate design deficiencies, to identify specific component weaknesses, and to evaluate design integrity and reliability. At present, only the level B system as it applies to the DSIF is operational. The application of the level B system to the SFOF and GCS is currently under development.

Each failure report is brought to the attention of a reliability analyst and the appropriate cognizant engineer for analysis and review. The information on each failure report is also entered into a computerized data bank where it is processed and analyzed statistically. These analysis have been yielding useful data on the long-term performance of the equipment at the deep space stations including the operational mean-time-between-failure figures.

2. Level A System

The level A system was developed to deal with all operational discrepancies. An operational discrepancy has been defined to be a failure or problem which is experienced in one of the major elements of the DSN (i.e., DSS,

GCS, or SFOF) when that element is being utilized in support of flight project operational tests or an actual mission.

Two methods of reporting operational discrepancies have been provided. Time critical problems, such as equipment problems and anomalies in the data stream, are reported by voice in real-time. Problems which are *not* time critical, such as procedural and documentation problems, are reported in writing in non-real-time.

Time critical discrepancies are reported by voice in real-time to the appropriate system chief within the SFOF as follows:

No.	Suspected source of error	Reported to
1.	SFOF Support Systems	Support Chief
2.	Deep Space Instrumentation Facility	Tracking Chief
3.	Ground Communications System	Communications Chief
4.	Data Processing System	Data Chief

After being notified of a discrepancy, the cognizant system chief is responsible for initiating a written discrepancy report and for investigating the reported discrepancy. This method of reporting operational discrepancies has improved the quality of the documentation and corrective action of discrepancies, and has considerably decreased the time required to follow up and close out reported discrepancies.

A group called the DRS Control Office has been established to provide the administrative services necessary to process the discrepancy reports (DRs) and to provide a central agency from which to furnish the necessary status information to aid management visibility into the overall operational readiness of the DSN.

Once initiated, DRs are numbered and logged by the DRS Control Office. Also, a master file of all DRs is maintained by that office. Biweekly status reports, summarizing the discrepancy reporting activity, are issued to appropriate line management by the DRS Control Office.

DRs are retained by the system chiefs until the discrepancy is resolved and the corrective action taken has been documented on the DR form. Suspense copies of all such DRs are submitted to the DRS Control Office on a daily

basis. As soon as the DR has been completed and signed-off by the appropriate Section Manager and/or Group Supervisor, it is sent to the DRS Control Office. A copy of each completed DR is retained by the appropriate system chief.

Non-time-critical DRs initiated by the observer of the discrepancy are submitted daily to the DRS Control Office, where they are numbered, logged, and subsequently submitted to the appropriate group for investigation and corrective action. Once completed and signed off by the appropriate supervision, these DRs are returned to the DRS Control Office where the processing is completed.

3. Level B System

The level B system, as it applies to the DSIF, was developed to provide for the movement of failed DSS equipment, to gather data on failed DSS equipment, and to provide for the analysis of the failure data.

Every equipment failure at each DSS is documented on a trouble and failure report (TFR) by the person detecting the failure. If the equipment cannot be repaired at the subsystem level, it is moved to the appropriate repair location. Copies of the TFR accompany the failed equipment. The action taken to repair the equipment is subsequently documented on the TFR.

Each DSS has assigned to it a station reliability coordinator (SRC) who is responsible for coordinating all failure-reporting efforts at that station. Each SRC collects, reviews, and records all TFRs initiated at the DSS, and then forwards these to the network reliability coordinator (NRC) located at the Goldstone Deep Space Communications Complex (DSCC) who is responsible for coordinating all failure-reporting efforts within the DSIF. The NRC reviews the TFRs and sends a copy of each one to the appropriate cognizant operations engineer (COE) located either at JPL or at the Goldstone DSCC, who is responsible for the control and performance of a specific subsystem. Each COE reviews the TFRs and if he does not concur with the corrective action taken on the failed equipment, he is responsible for further action to be taken on the item of equipment in question.

The NRC also sends a copy of all TFRs to a reliability analyst located at the Goldstone DSCC who is responsible for entering the data contained into a computerized data bank. The reliability analyst, together with DSIF reliability engineering personnel, exercises the data bank for

the purpose of performing statistical analyses on the failure data. The results of these analyses are published by DSIF reliability engineering personnel in a variety of reports, including summary reports to each SRC and the NRC, and engineering analysis reports to each COE and to appropriate line management.

F. Systems Reliability Study for SFOF Power Design, D. C. Card

1. Introduction

In a previous issue of this Summary (SPS 37-43, Vol. III), two parts of the systems reliability problem were discussed; viz, (1) estimation of reliability parameters from empirical data, and (2) the simplest tools for finding the reliability of complex systems. This article, as a continuation of the systems reliability study, addresses the problem of the techniques for finding system reliability in complex configurations. The development and use of a minimum-risk criterion as the optimization criterion for reliability design of the system will be the subject of a subsequent article.

2. Reliability Techniques for Complex Systems

The term "complex system" refers to any system whose designed operation requires more than one distinct element operating in serial, parallel, or combined serial-parallel modes. An element is graphically represented by a single block; it is represented mathematically by a pair

$$[\{a_i(t)\}, \{\mu_i(t)\}, i \in I],$$

where I is an indexing set, and $\{a_i(t)\}$ is a set of failure rates corresponding to the possible failure modes of the element, $\{\mu_i(t)\}$ is the corresponding set of renewal rates; the members of either set may depend upon the time. In this development, all elements will be of the type $[a, \mu]$; i.e., a single failure mode and renewal mode, each with constant rate parameters.

Throughout the analysis, the following notation will be used:

$A(a, \mu), B(b, \nu)$ are elements A and B with their defining parameters.

$\mathcal{F}(A)$ is the event transition of element A into its non-operational state (failure).

$\mathcal{R}(A)$ is the event transition of element A into the operational state (renewal).

$F_A(t)$ is the failure distribution function for element A.

$R_A(t)$ is the renewal or repair distribution function for element A.

The assumptions are:

- (1) The state of an element at any instant does not depend upon the states of its connected neighbors.
- (2) Transitions in complex systems never occur simultaneously,
- (3) The system is required to operate continuously in some (time) interval of interest $(0, T)$.

Furthermore, in order to simplify analysis, the assumption of independent failures and independent renewals for each element will often be used.

3. System 1—"Single-String" Serial System

Fig. 10 represents the simplest two-element serial system. Again, it is assumed that system reliability R_S in some interval $(0, T)$ is the probability that the system S remains continuously operational in $(0, T)$; symbolically,

$$\begin{aligned} R_S &= P [C\mathcal{F}(A) \cap C\mathcal{F}(B) \text{ in } (0, T)] \\ &= P [C\{\mathcal{F}(A) \cap \mathcal{F}(B)\} \text{ in } (0, T)], \end{aligned} \quad (1)$$

where P indicates the probability operator, C represents the complement of the indicated event or set. In cases where the probabilities over an interval, (t_0, T) , do not depend upon events for any $t < t_0$, we can write

$$R_S = [1 - F_A(T)] [1 - F_B(T)], \quad (2)$$

when the operational state of elements A and B are mutually independent. For system unreliability U_S ,

$$U_S = 1 - R_S = F_A(T) + F_B(T) - F_A(T) \cdot F_B(T).$$

It is well known that many systems exhibit element failures whose distributions can be approximated by Poisson distributions; i.e., the times between failures are inde-

pendent, with constant failure rate parameter; if it is assumed that A and B can be treated in this manner, then we have for the distribution of time-to-failure (or operational interval length)

$$\begin{aligned} F_A(t) &= 1 - e^{-at} \\ F_B(t) &= 1 - e^{-bt}. \end{aligned}$$

Therefore, for U_S ,

$$U_S = 1 - e^{-(a+b)t} = F_{AB}(t); \quad (3)$$

which leads to the system probability element for unreliability

$$f_S(t)dt = \sum_1^n a_i e^{-\sum a_i t} dt.$$

For the general case of n mutually independent elements, A_i ,

$$U_S(t) = \prod [1 - F_n(t)] \quad (4)$$

Whether the single-string serial system is maintained or not does not affect the reliability in the case that it must be continuously available.

4. System 2—Parallel Redundant System

Fig. 11 represents the simple two-element redundant system. In order to complete a reliable operation in $(0, T)$, it is necessary that either A or B be operating reliably at every $t: 0 \leq t \leq T$. Let us consider a system which operates in "parallel redundant mode"; i.e., both elements are scheduled to be operational in $(0, T)$. Furthermore, we do not include the reliability of the junction preceding or following the system.

For system failure probability, we can write

$$\begin{aligned} P [\mathcal{F}(S)] &= P [\mathcal{F}(B) \cap C\mathcal{R}(A) | \mathcal{F}(A)] \cup \\ &\cup P [\mathcal{F}(A) \cap C\mathcal{R}(B) | \mathcal{F}(B)] \end{aligned}$$

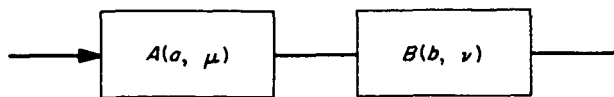


Fig. 10. Two-element serial system

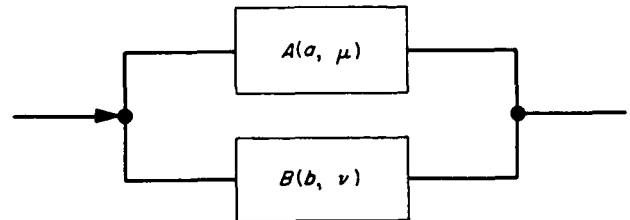


Fig. 11. Two-element redundant system

If it is assumed that the failure rates a , b , and renewal rates μ , ν , are constant and independent of the time, then the system reliability can be treated in the following manner:

Let numerical states 0, 1, 2, 3 be defined by the following events (system states):

$$\left. \begin{aligned} 0 &: \mathcal{CF}(A) \cap \mathcal{CF}(B) \\ 1 &: \mathcal{F}(A) \cap \mathcal{CF}(B) \\ 2 &: \mathcal{CF}(A) \cap \mathcal{F}(B) \\ 3 &: \mathcal{F}(B) \cap \mathcal{CR}(A) \mid \mathcal{F}(A) \cup \mathcal{F}(A) \cap \mathcal{CR}(B) \mid \mathcal{F}(B) \end{aligned} \right\} \quad (5)$$

For the probabilities of finding the system in each of the states at $t + \Delta t$, given that it is in one of the various states at t , we have the following system of equations (ignoring second orders in Δt):

$$\left. \begin{aligned} P_0(t + \Delta t) &= [1 - (a + b)\Delta t] P_0(t) + \mu\Delta t P_1(t) + \nu\Delta t P_2(t) \\ P_1(t + \Delta t) &= a\Delta t P_0(t) + [1 - (b + \mu)\Delta t] P_1(t) + \nu\Delta t P_3(t) \\ \text{etc.} \end{aligned} \right\} \quad (6)$$

From the system, the stochastic transition matrix M is written

$$M = \begin{matrix} & \underline{0} & \underline{1} & \underline{2} & \underline{3} \\ \begin{matrix} 0 \\ 1 \\ 2 \\ 3 \end{matrix} & \begin{bmatrix} 1 - (a + b) & \mu & \nu & 0 \\ a & 1 - (b + \mu) & 0 & \nu \\ b & 0 & 1 - (a + \nu) & \mu \\ 0 & b & a & 1 - (\mu + \nu) \end{bmatrix} \end{matrix} \quad (7)$$

Let I represent the identity matrix of proper dimension, $\mathbf{P}(t + \Delta t)$ represent the (column) vector of state probabilities at $(t + \Delta t)$, and $\mathbf{P}(t)$ represent the same vector at t ; then

$$\mathbf{P}(t + \Delta t) = [I + (M - I)\Delta t] \mathbf{P}(t),$$

or

$$\mathbf{P}(t + \Delta t) - \mathbf{P}(t) = (M - I)\Delta t \mathbf{P}(t),$$

from which comes the system of differential equations, in vector notation,

$$\frac{d}{dt} \mathbf{P}(t) = \lim_{\Delta t \rightarrow 0} \frac{\mathbf{P}(t + \Delta t) - \mathbf{P}(t)}{\Delta t} = (M - I) \mathbf{P}(t). \quad (8)$$

Taking the \mathcal{L} transform of the differential equations, we obtain the following definitions and results:

$$\mathcal{L}(M - I) \mathbf{P}(t) = (M - I) \mathcal{L} \mathbf{P}(t) \triangleq (M - I) \mathbf{P}(S)$$

$$\mathcal{L} \frac{d}{dt} \mathbf{P}(t) \triangleq S \mathbf{P}(S) - \mathbf{P}(0),$$

gives

$$\mathbf{P}(0) = [(S + 1)I - M] \mathbf{P}(S). \quad (9)$$

State 3 defines system failure; therefore, the probability that the system will enter state 3 in $(0, T)$ defines system unreliability in $(0, T)$. In order to find this probability, we can make 3 an absorbing state (i.e., once the system enters state 3, the probability of remaining in the state is 1), and solve the transformed system of equations which result. Assume that the initial condition is $\mathbf{P}(0)^T = \{1, 0, 0, 0\}$; then the resulting system is:

$$\begin{aligned} 1 &= (S + a + b) P_0(S) & - \mu P_1(S) & & - \nu P_2(S) \\ 0 &= & - a P_0(S) & + (S + b + \mu) P_1(S) & \\ 0 &= & - b P_0(S) & & + (S + a + \nu) P_2(S) \\ 0 &= & & - b P_1(S) & - a P_2(S) & + S P_3(S). \end{aligned}$$

The formal solution to this system is

$$\mathbf{P}(S) = [(S + 1)I - M]^{-1} \mathbf{P}(0), \quad (10)$$

which gives the probabilities:

$$\mathbf{P}(t) = \mathcal{L}^{-1} \mathbf{P}(S).$$

However, after some manipulation, $P_3(t)$ can be found:

Let

$$A = b + \mu, B = a + \nu, C = a + b, D = ab\mu, E = b^2\nu;$$

then,

$$SP_3(S) = \frac{D}{\mu} \left[\frac{2S + A + B}{(S+C)(S+A)^2 - D(S+A) + E(S+B)} \right]$$

The roots of the denominator in brackets must be found; let these be represented r_1, r_2, r_3 . Then from

$$SP_3(S) = \left[\frac{ab(2S + A + B)}{S(S+r_1)(S+r_2)(S+r_3)} \right],$$

we find,

$$P_3(t) = \mathcal{L}^{-1} P_3(S) = \frac{ab}{4} \left[\frac{A+B}{r_1 r_2 r_3} + \frac{(2r_1 - A - B)}{r_1(r_2 - r_1)(r_3 - r_1)} e^{-r_1 t} + \frac{(2r_2 - A - B)}{r_2(r_1 - r_2)(r_3 - r_2)} e^{-r_2 t} + \frac{(2r_3 - A - B)}{r_3(r_1 - r_3)(r_2 - r_3)} e^{-r_3 t} \right].$$

In the special case of identical elements, i.e., $a = b, \mu = \nu$, it can be found that

$$P_3(S) = 2a^2 \left[\frac{1}{S(S+r_1)(S+r_2)} \right]$$

where the roots r_1 and r_2 are given by

$$r_1 = \frac{3a + \mu + (a^2 + 6a\mu + \mu^2)^{1/2}}{2}$$

$$r_2 = \frac{3a + \mu - (a^2 + 6a\mu + \mu^2)^{1/2}}{2};$$

therefore,

$$\mathcal{L}^{-1} P_3(S) = P_3(t) = \frac{2a^2}{r_1 r_2} \left[1 + \frac{r_2 e^{-r_1 t} - r_1 e^{-r_2 t}}{r_1 - r_2} \right].$$

In case system 2 is non-maintained, i.e., for all t , $A = A(a, 0), B = B(b, 0)$, the probability of system failure is formally

$$P[\mathcal{F}(S)] = P[\mathcal{F}(A) \cap \mathcal{F}(B) \text{ in } (0, T)].$$

In the case of mutually independent elements, this reduces to

$$P[\mathcal{F}(S)] = P[\mathcal{F}(A)] \cdot P[\mathcal{F}(B)] \text{ in } (0, T)$$

$$= F_A(T) \cdot F_B(T)$$

In the case of conditionally dependent failure,

$$P[\mathcal{F}(S)] = P[\mathcal{F}(A) \cap \mathcal{F}(B)]$$

$$= P[\mathcal{F}(B) | \mathcal{F}(A)] \cdot P[\mathcal{F}(A)]$$

$$= P[\mathcal{F}(A) | \mathcal{F}(B)] \cdot P[\mathcal{F}(B)]$$

$$= F_{B/A}(T) \cdot F_A(T)$$

$$= F_{A/B}(T) \cdot F_B(T).$$

5. System 3—Parallel Redundant Serial Strings

Fig. 12 shows that this is a simple combination of systems 1 and 2. Using the same assumptions as before, and defining strings by the notation $S = AB, S' = A'B'$, we have the events

$$\mathcal{F}(S) = \mathcal{F}(A \cup B)$$

$$\mathcal{F}(S') = \mathcal{F}(A' \cup B')$$

and in the non-maintained case, for the system failure event,

$$\mathcal{F}(\text{system}) = \mathcal{F}(S \cap S') \text{ in } (0, T)$$

$$= \mathcal{F}(S) \cdot \mathcal{F}(S') \text{ in } (0, T)$$

in the case of element independence. For the non-maintained system, assuming Poisson elements,

$$P[\mathcal{F}(\text{System}) \text{ in } (0, T)] = 1 - e^{-(a+b)T}$$

$$- e^{-(a'+b')T} - e^{-(a+a'+b+b')T};$$

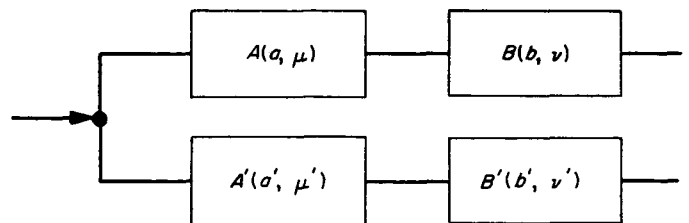


Fig. 12. Parallel redundant serial system

and if $A = A'$, $B = B'$

$$P[\mathcal{F}(\text{system}) \text{ in } (0, T)] = 1 - 2e^{-(a+b)T} + e^{-2(a+b)T}$$

In general, for n identical elements,

$$P[\mathcal{F}(\text{system}) \text{ in } (0, T)] = F^n(T).$$

For the maintained system 3, $[A(a, \mu)]$, $[B(b, \nu)]$, $[A'(a', \mu')]$, $[B'(b', \nu')]$, we use the Markov process method again, in which we define the states for any $t \in (0, T)$:

- 0 = S and S' operating
- 1 = S down and S' operating
- 2 = S operating and S' down
- 3 = S and S' down

Noting that the failure rate for S is $a + b$ and the renewal rate is $\mu + \nu$ (with corresponding rates for S'), and letting $\alpha = a + b$, $\beta = a' + b'$, $\phi = \mu + \nu$, $\theta = \mu' + \nu'$, the system state transition matrix, M , is given by

$$M = \begin{matrix} & \begin{matrix} \underline{0} & \underline{1} & \underline{2} & \underline{3} \end{matrix} \\ \begin{matrix} 0 \\ 1 \\ 2 \\ 3 \end{matrix} & \begin{bmatrix} 1-(\alpha+\beta) & \phi & \theta & 0 \\ \alpha & 1-(\beta+\phi) & 0 & \theta \\ \beta & 0 & 1-(\alpha+\theta) & \phi \\ 0 & \beta & \alpha & 1-(\theta+\phi) \end{bmatrix} \end{matrix}$$

It can be seen that the probability of system failure, $P_3(T)$, is obtained directly from the formulas derived from system 2.

6. System 4—Stages of Switched, Parallel Elements

Fig. 13(a) shows a configuration of serial/parallel elements, with a switchable path, which is often used to provide more serial flexibility. The configuration can clearly be partitioned into a series of stages, S_1 , S_2 , and S_3 , as shown, with system failure then defined as the failure of at least one stage; then,

$$P[\mathcal{F}(\text{System})] = P[\mathcal{F}(S_1) \cup \mathcal{F}(S_2) \cup \mathcal{F}(S_3)]$$

In many cases, it may be possible to assume that the switch (S_2) has a failure rate which is independent of the number of switching operations it must perform. If this assumption is not valid, then the general problem is

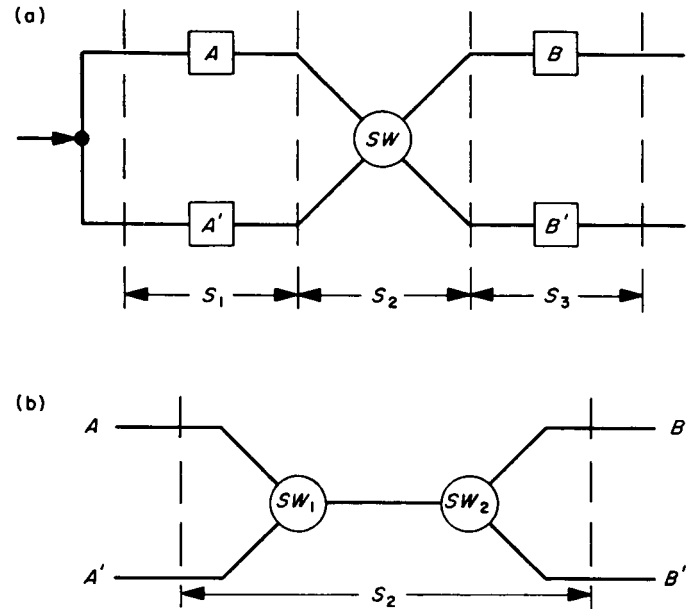


Fig. 13. Stages of serial/parallel elements with a switchable path

complicated by the fact that the state of the switch stage is conditionally dependent upon the states of the preceding and succeeding elements, S_1 and S_3 . In this case, S_2 can be partitioned and represented as in Fig. 13(b). The conditional probabilities of switch failure due to switching operations can then be derived. Assume that both SW_1 and SW_2 have a constant probability, p , of failure at a switching event; then let the operation of switching from A to A' be denoted (A, A') , the operation of switching from A' to A be denoted (A', A) , etc. Define the switching policy to be that the switch changes the path connection from A to A' the instant A fails, and similarly for the remaining three elements. Denoting the probability of (A, A') by $P(A, A')$, etc., and assuming that the system operation begins with A connected, we have

$$P[\mathcal{F}(SW_1) | \text{one } \mathcal{F}(A)] = pP(A, A')$$

$$P[\mathcal{F}(SW_1) | \text{one } \mathcal{F}(A), \text{one } \mathcal{F}(A')] = (1-p)pP(A, A')P(A', A), \text{ etc.}$$

If it is also assumed that A and A' have identical parameters, then we can sum the probabilities for each event to find the conditional probability of SW_1 failure, given n required operations:

$$P_n[\mathcal{F}(SW_1)] = p \sum_{k=1}^n (1-p)^{k-1} p^k P(A, A'). \quad (11)$$

Similarly, for SW_2 we have the probability

$$P_n [\mathcal{F}(SW_2)] = p \sum_{k=1}^n (1-p)^{k-1} p^k (B, B'). \quad (12)$$

The total probability of failure of SW_i is given by P_n as $n \rightarrow \infty$. Let the failure density for A and A' elements be denoted $F_A(t)$; the probability of one or more transitions between elements in an interval $(0, t)$ is then

$$P^1(A, A') = \int_0^t dF_A(x).$$

The probability of two or more transitions is

$$P^2(A, A') = \int_0^t F_A(t-x) dF_A(x) \triangleq F_A(t) * F_A(t). \quad (13)$$

The probability of n or more transitions is the n -fold convolution,

$$P^n(A, A') = F_A(t)^{*[n]}.$$

Assume that times to failure (operating intervals) are exponentially distributed, with parameter a , then,

$$P^n(A, A') = 1 - e^{-at} \sum_{k=0}^{n-1} (at)^k / k! \quad (14)$$

The total probability is obtained by substituting this expression into Eq. (11), and allowing the first sum to have $n = \infty$.

If at is sufficiently small that

$$e^{-at} \simeq 1 - at$$

is a good approximation, then, regardless of the magnitude of p , we have for the total probability (11),

$$P_\infty [\mathcal{F}(SW_1)] \simeq p(at) + (1-p)(at)^2$$

from

$$P_\infty [\mathcal{F}(SW_1)] \simeq p \left[at + (at)^2 \sum_{k=1}^{\infty} (1-p)^k \right].$$

In order for the switch to fail in the conditional mode, it is hypothesized that the A -stage, S_1 , is still in an operating state after the n th transition; therefore, the conditional probabilities of (11) and (12) are weighted by $1 - P_{3,S_1}(t)$ and $1 - P_{3,S_3}(t)$, respectively, where the index 3 represents the non-operating state.

The switching stages may also have an independent failure mode, which is handled in the usual fashion for independent failures in serial systems.

The derivation of the cost optimization formulas for system reliability will be taken up in a subsequent issue of the SPS, Vol. III.

G. DSN 16-Month Loading Schedule System,

R. T. Haenle

1. Introduction

The Deep Space Network consists of eleven deep space stations located at various scientifically advantageous sites around the world; the Space Flight Operations Facility located in Pasadena, California; and the Ground Communications System which ties these facilities together. This network provides tracking and telemetry support to spacecraft missions whose ultimate mission objectives are outside the near-Earth orbit environment. Management of the DSN is the responsibility of the Office of the DSN General Manager, which receives support from a number of organizations. Within this support activity is the DSN scheduling operation.

It is the function of the total DSN scheduling operation to coordinate the availability of appropriate facilities and equipment for the effective support of each flight mission at the proper times and geographic locations. This becomes a complex process when, as is normal, several missions are in varying stages of progress simultaneously, and it is further complicated by the fact that some deep space stations have special capabilities not common to others. Further, all facilities and equipment require varying amounts of time for routine maintenance, major repairs due to climatic conditions or breakdown, and installation of newly developed hardware systems and subsystems.

To cope with this task of coordination, and to integrate all DSN-user requirements into an operationally practical schedule, the DSN scheduling operation is divided into three levels. The first is a long-term forecast of the potential load on major controlling items of equipment, at a time-granularity practical to the long-term visibility. The second is a nearer-term schedule of the probable utilization of detail equipment elements, according to time increments appropriate to the term. The third is a very short-term operational schedule of the utilization of detail equipment elements, on a highly detailed time increment basis. It is intended that potential scheduling

problems observed at the first level be analyzed and generally resolved before they might reach the second level, and residual second-level problems be resolved before reaching the third level.

The first level, i.e., the DSN 16-month loading schedule system, will be discussed below. After a brief examination of the specific parameters of all three scheduling levels in order to compare its degree of detail with those of the others, the functional description of the system will be presented. Form of input, processing of input, and output will then be treated. Present status of compatibility with the other scheduling levels will be discussed, as well as developmental effort in progress. Finally, analytical aids which have been developed adjunct to the DSN 16-month loading schedule system will be described.

2. Relationship Between Scheduling Levels

a. The DSN 16-month loading schedule. This schedule (Figs. 14, 15) is issued monthly and encompasses not less than 16 full calendar months. The number of weeks involved varies between 69 and 72, depending upon how far the first week of interest falls before the start of the first full calendar month. The first 12 weeks of this schedule are the same weeks as those in the concurrently issued DSN 12-week utilization schedule. Elements considered are the antennas of ten deep space stations, (DSS 13, an R&D station, is not included), four operational computer modes, and two simulation computer systems. Data is presented in usage hours per week.

b. The DSN 12-week utilization schedule. This schedule is issued monthly, and encompasses exactly 12 calendar weeks. An extremely detailed list of elements is considered. Data is presented in usage hours per week.

c. The DSN 7-day operational schedule. This schedule is issued weekly, and encompasses exactly 14 calendar days, the first 7 of which are considered operationally firm. The detailed list of elements considered is the same as those in the 12-week schedule, but the data is presented in discretely assigned hours per day.

3. Functional Description

The DSN 16-month loading schedule system is primarily designed to reveal and identify the potential overloading (hereafter termed "conflicts") of any given element during any given week during the period of interest. It does not attempt to resolve such conflicts within a single issue-cycle, but rather, by allowing the

specific DSN users involved in indicated conflicts to see them far in advance, permits re-evaluation and negotiation among the conflictors so that their inputs to the next issue-cycle will not result in the same conflicts. In this manner apparent conflicts should become progressively less, in number and severity, as any week of interest moves closer to the present in succeeding issues.

The system accepts two forms of brief, manually prepared inputs from the DSN users. The shorter-term inputs are the same inputs given to the 12-week schedule system, to avoid unnecessary duplication of input effort by the users, and are processed first by a 1620 FORTRAN program and then by a 7094 COBOL program. The longer term inputs are submitted separately in a simplified format, and are processed manually. All input data thus received and processed is then portrayed graphically on detailed bar graphs for each element involved. The finished material is then reproduced and formally issued to all interested parties for their use in long-range planning as well as for guidance in the preparation of subsequent 16-month and 12-week schedule inputs.

Also, the input data are used in a continuous updating process of the analytical aids provided as part of this system, with such aids being made available to all DSN users for use in planning and input preparation.

4. Input Data Format

Inputs are submitted by each DSN user, i.e., each flight project, DSIF development, SFOF development, and DSN maintenance. Inputs are in hours-per-week for each element of interest to any given user. In the case of the first 12 weeks of the 16-month period, the inputs are in the computer-oriented detailed element format prepared essentially for the 12-week schedule, and therefore must be machine processed to extract only those elements of interest to the 16-month schedule (see below). Inputs for the balance of the 16-month period are submitted on a simple calendar matrix form provided, with the horizontal axis showing time in weekly increments and the vertical axis listing line items of elements.

5. Processing

After the 12-week schedule operation has made use of the 12-week computer-oriented input received under its cognizance, it turns over its new 12-week configuration deck to the 16-month schedule operation to be processed by a 1620 FORTRAN program. This extraction program recognizes only those configuration cards

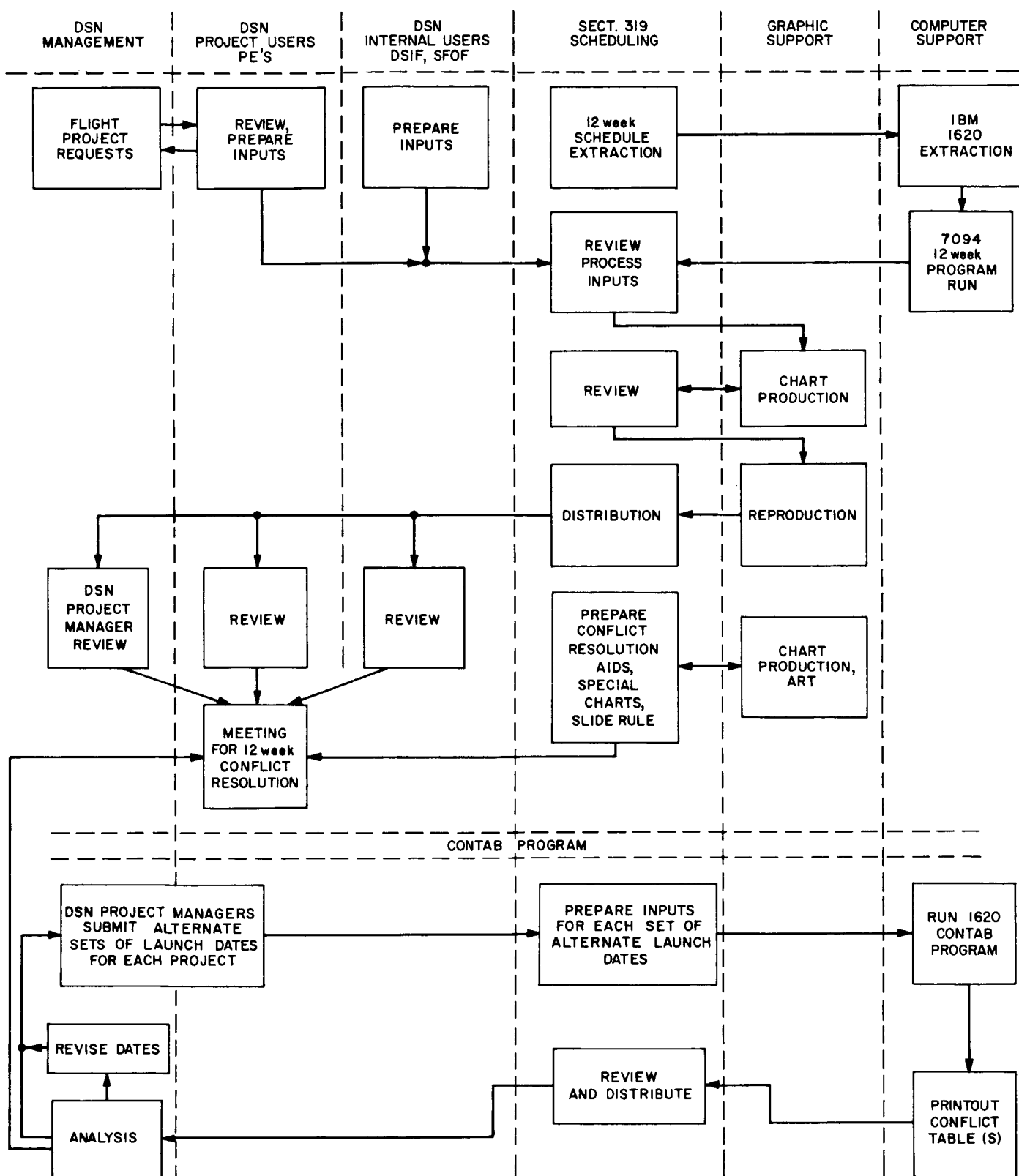


Fig. 14. Flow chart for DSN 16-month loading schedule process

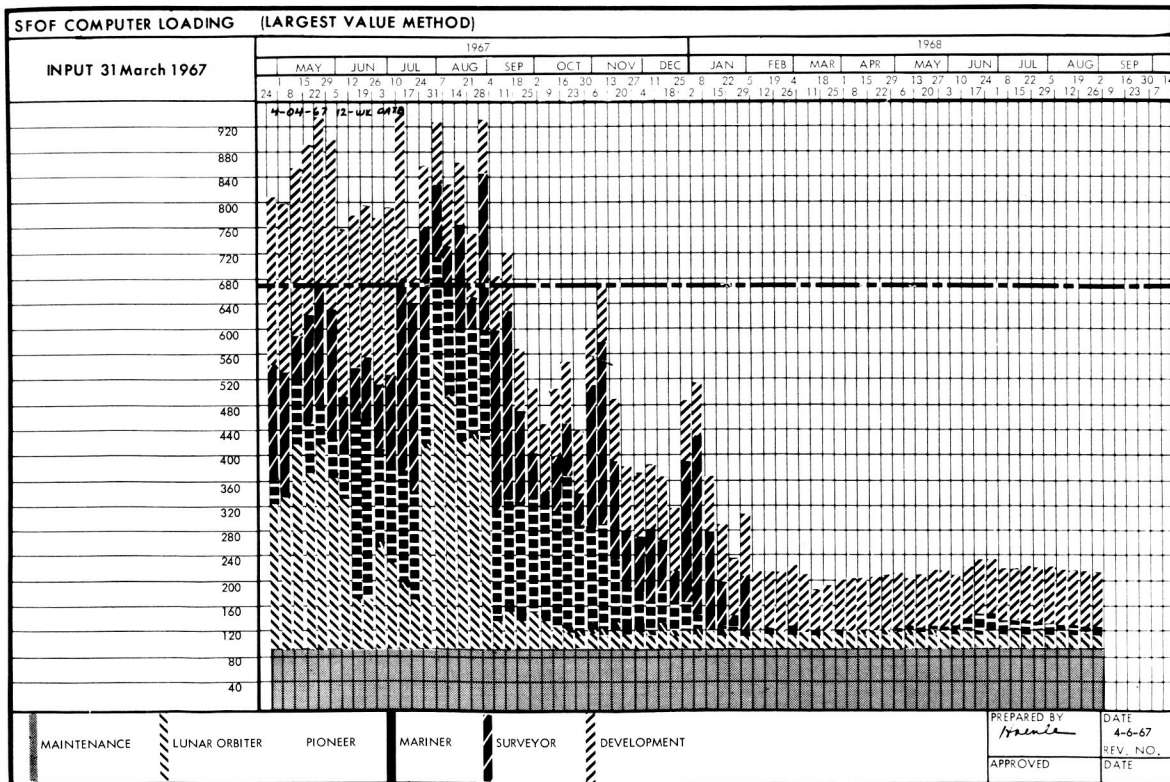
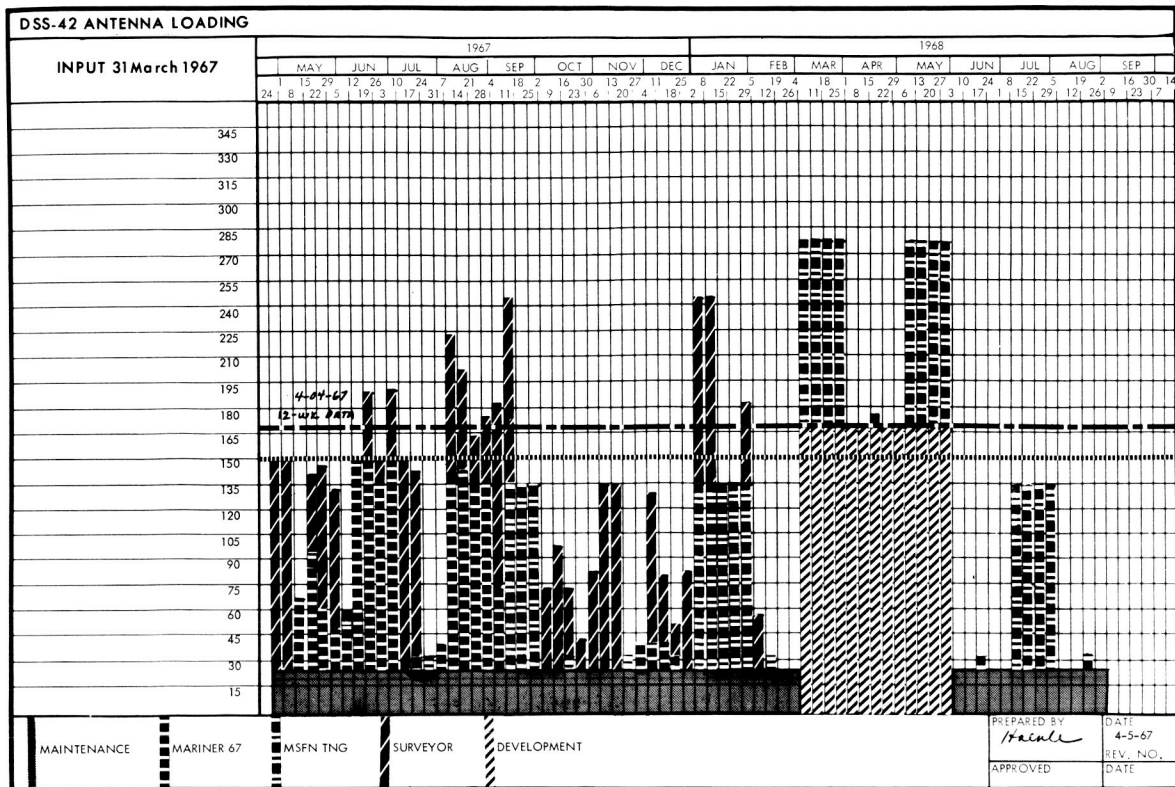


Fig. 15. Typical DSN 16-month loading schedule bar graphs

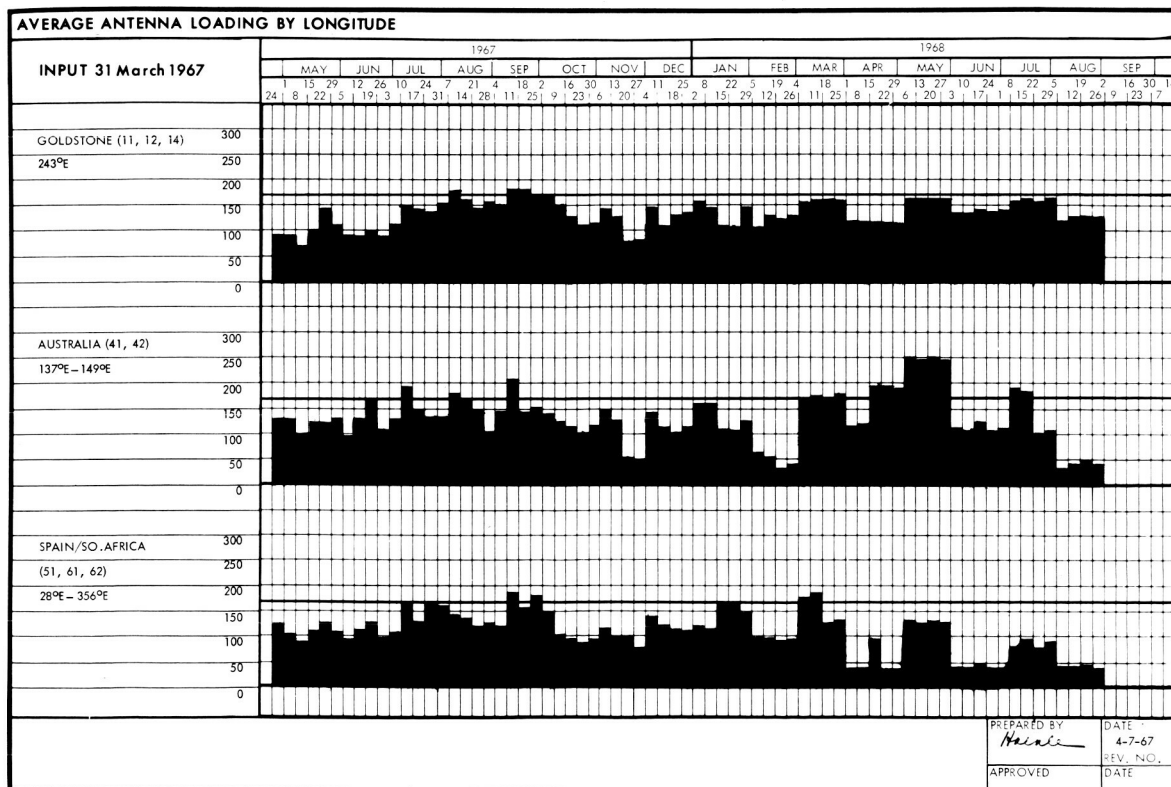
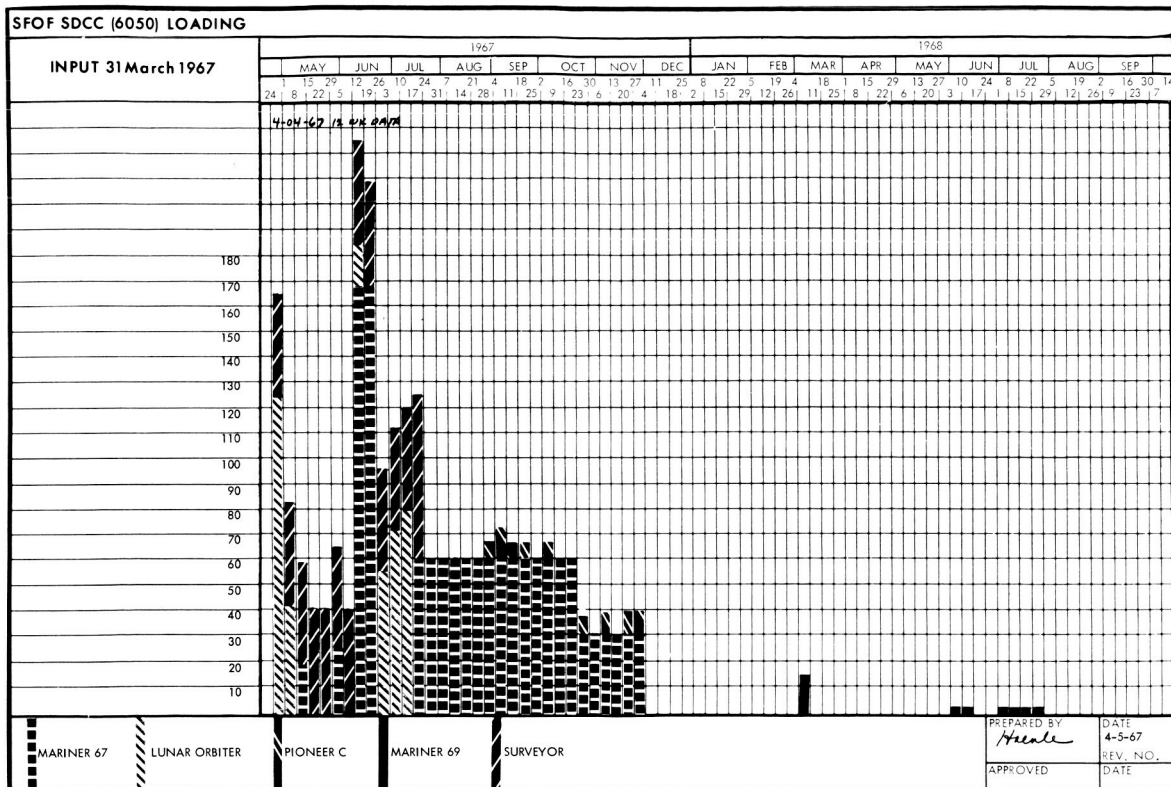


Fig. 15 (contd)

which contain, as part of their total configuration, elements of interest to the 16-month schedule. From these "recognized" cards, it then prepares a new deck whose configuration cards contain only elements of interest to the 16-month schedule, with all other elements deleted. This deck is termed the "16-month extraction deck."

The 16-month extraction deck is then processed by the 7094 COBOL program used for the 12-week schedule, simply by substituting this deck for the normal 12-week configuration deck. The resultant printout produces a listing of the users' requests for 16-month elements (only) by week for the first 12 weeks of the 16-month period of interest.

For the balance of the 16-month period, the data submitted on the calendar matrix input forms are organized by format to show the users' requests for 16-month elements by week. Therefore, in combination with the extracted 12-week data, the total raw data is ready for arithmetic manipulation to achieve the various accumulations, averages, and selective value computations which are then manually plotted on output bar graphs. A flow-chart descriptive of the 16-month schedule process appears as Fig. 14.

6. Output Data

Output data are presented in the form of bar graphs (Fig. 15), with the horizontal axis being calendar time in weekly increments, and the vertical axis being hours per week of requested element usage. Individual graphs are produced for each element, with the only exception being the operational computer modes which are combined in one graph. Also, there are three graphs showing average antenna usage by longitude, resulting in a total of 16 graphs. All graphs, except for the latter three, are both color- and pattern-coded to differentiate between, and identify, each flight project (in the cases of *Pioneer* and *Mariner*, between missions), as well as development and maintenance. All antenna charts contain a horizontal line indicating the present level of manpower staffing at the station represented, as well as a line indicating the total number of hours in a week. Cumulative values extending about these lines portray potential conflicts, and indicate that resolution steps should be taken. Such steps may consist of Project-level negotiation, DSN management decision, or NASA Headquarters decision, and may result in, respectively, such things as revision of station usage plans, revision of station equipment configurations, and revision of launch readiness dates.

7. Compatibility of Systems

The compatibility of the 7-day operational schedule and the 12-week utilization schedule has been treated in SPS 37-44, Volume III. The compatibility status of the 12-week utilization schedule and the 16-month loading schedule is as follows: (1) Both are on an hours-per-week basis. (2) All 16-month elements examined are contained in the 12-week elements list, and thus continuity is maintained. (3) The extraction process for the first 12 weeks of the 16-month schedule can be done using the 12-week schedule COBOL program. (4) An abbreviated conflict list printout, produced as a byproduct of the 16-month extraction, is useful in the 12-week schedule "conflict resolution" meetings. (5) The weeks of both schedules begin on Mondays and end on Sundays (as does the 7-day operational schedule). (6) Finally, the simultaneous start dates of both schedules result in both economy of input preparation effort by the users and a graphic presentation of the 12-week schedule as an adjunct to the 12-week schedule computer printout.

8. Development

The development of the 16-month loading schedule system has thus far been a planned progression and improvement of techniques. Logical subsequent steps in this process are planned, such as the mechanization of the input data in a manner similar to that used by the 12-week schedule, so that manual manipulation of the data to achieve graph plotting values may be eliminated. This will require that a new and rather elaborate computer program be written.

Another development planned, independent of the foregoing, is the preparation of a computer program that will receive the manipulated data and printout bar-graphs in the same element breakdown, using alphabetic characters to differentiate between and identify the various projects, missions, and internal users. This would relieve the present manual plotting and coded-taping effort, and would also simplify reproduction.

9. Analytical Aids

Due to its overview of a relatively long-range period of planned DSN activity, it has been appropriate that part of the 16-month loading schedule effort be devoted to the development of various long-range analytical aids. Following are some of the aids which have proven useful to DSN users, DSN management, and NASA Headquarters.

a. The DSN slide rule. This metal device (Fig. 16) is approximately 12 ft long, folds in four sections, and is portable in its carrying case. Clear Plexiglass overlays on which are depicted various mission profiles can be moved over the background, which indicates on its vertical axis eight deep space stations as well as four operational computer strings, and on its horizontal axis, 16 months in daily increments as well as the launch windows for several flight projects. Movement of the overlays to correspond to various launch readiness dates allows the viewer to quickly determine which combination of such dates will result in the least amount of equipment usage conflicts.

b. The CONTAB computer program. This 1620 FORTRAN program is essentially a mechanization of the DSN slide rule. The program stores all flight mission profiles, and upon the input of a given set of launch readiness dates for all missions, produces a printout (Fig. 17)

which symbolically indicates equipment usage conflicts which would result if this combination of dates were used. Multiple runs of this program, using various sets of launch-readiness dates, would produce printouts of varying conflict severity. Selection of the least severe printout would identify the launch-readiness dates used to produce it as the most favorable, considering the existing mission profiles. This program, as well as the DSN slide rule, have proven to be of value in discussions within and between DSN management and NASA Headquarters.

c. The DSN utilization forecast. This is a large scale display matrix (Fig. 18) on which the horizontal axis indicates time by day for 16 months, and on which the vertical axis indicates eight DSS antennas and computer Dual Mode II. It portrays, by means of color-coded pushpins, the density of anticipated daily utilization of the nine elements by each flight project, for both test and track, on all missions. The data used in this device

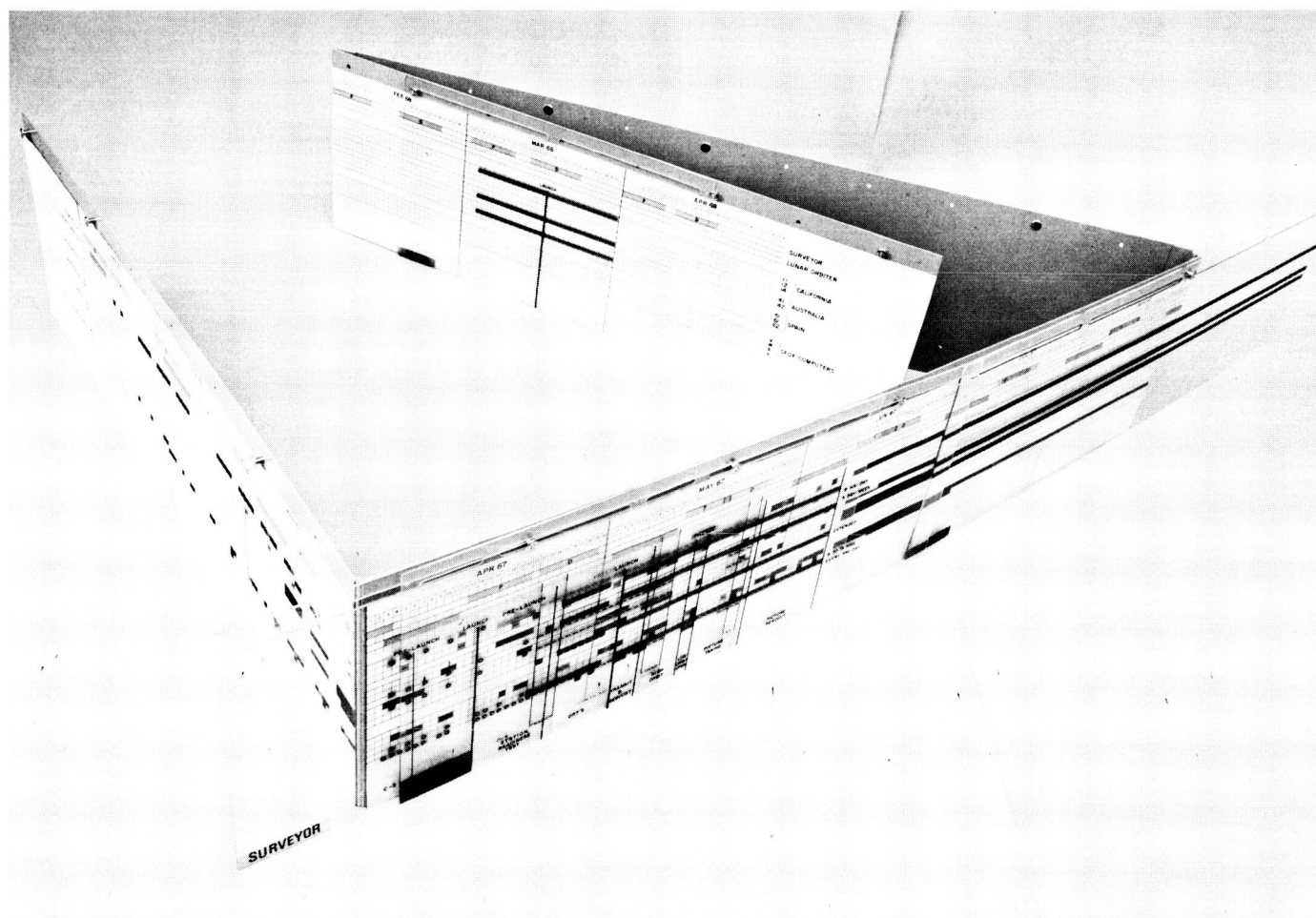


Fig. 16. DSN slide rule

S LAUNCH 6/11 →
M LAUNCH 6/12 →

L LAUNCH 7/3 →

DAY	NET A			NET R			COMPUTERS				TPS		FPAA					
	11	42	61	12	41	62	14	51	71	72	V	W	X	Y	PDP1	6050	1	2
136		M					M					M				M		M
137	SM	SM	S				S	M	S	S		M	S	S	S	M	S	M
138		M						M				M				M		M
139	S	M					S	M				M	S	S	S	M	S	M
140		M						M				M				M		M
141																		
142	M		M				M					M				M		M
143	M	M	M				M	M				M				M		M
144	M	M	M				M	M				M				M		M
145	M		M				M					M				M		M
146	M		M				M					M				M		M
147	SM	S	SM				M		SL	S		M	S	S	S	M	S	M
148									L									
149				M	M	M						M				M		M
150	S	S	S	M	M	M	S	S	S	S		M	S	S	S	M	S	M
151	M	M		M	M	M		M				M	M			M		M
152				M	M	M						M				M		M
153				M	M	M						M				M		M
154				M	M	M		S	L			M	S	S	S	M	S	M
155	S	S	S						S	S			S	S	S		S	
156																		
157	S												S	S	S		S	
158	S												S		S		S	
159	M	M						M				M	M			M		M
160								S					S	S	S		S	
161													S	S	S		S	
162	S	S	S						S	S			S	S	S		S	
163	SM	SM	SM		M			M				M	SM	S			S	M
164	SM	SM	SM		M			M				M	SM	S			S	M
165	SM	SM	SM		M			M				M	SM	S			S	M
166	SM	SM	SM		M		M	M				M	M	S			S	M
167	SM	SM	SM		M		M	M				M	M	S			S	M
168	SM	SM	SM		M		M	M				M	M	S			S	M
169	SM	SM	SM	L	ML	L		M	L			M	ML	S	L	L	S	ML
170	SM	SM	SM	L	ML	L		ML	L			M	ML	S	L	L	S	ML
171	SM	SM	SM	L	ML	L		ML	L			M	ML	S	L	L	S	ML
172	SM	SM	SM	L	ML	L		ML	L			M	ML	S	L	L	S	ML
173	SM	SM	SM	L	ML	L	M	M	L			M	ML	S	L	L	S	ML
174	SM	SM	SM		M		M	M				M	M	S			S	M
175	SM	SM	SM	L	ML	L		M	L			M	ML	S	L	L	S	ML
176	SM	SM	SM	L	ML	L		M	L			M	ML	S	L	L	S	ML
177	SM	SM	SM	L	ML	L		M	L			M	ML	S	L	L	S	ML
178	SM	SM	SM	L	L	L			L			M	ML	S	L	L	S	ML
179	SM	SM	SM	L	L	L			L			M	ML	SL	L	L	S	ML
180	SM	SM	SM	L	L	L	M	L	L			M	ML	SL	L	L	S	ML
181	SM	SM	SM	L	L	L	M	L	L			M	ML	S	L	L	S	ML
182	SM	M	M	L	L	L	M	L	L			M	ML	S	L	L	S	ML
183	SM	M	M									M	M	S			S	M
184	SM	M	M	L	L	L		L	L			M	ML	SL			S	ML
185	SM	M	M	L	L	L						M	ML	SL			S	ML
186	SM	M	M	L	L	L						M	ML	S			S	ML

Fig. 17. Segment of CONTAB program printout: S = Surveyor D, M = Mariner Venus 67, L = Lunar Orbiter E

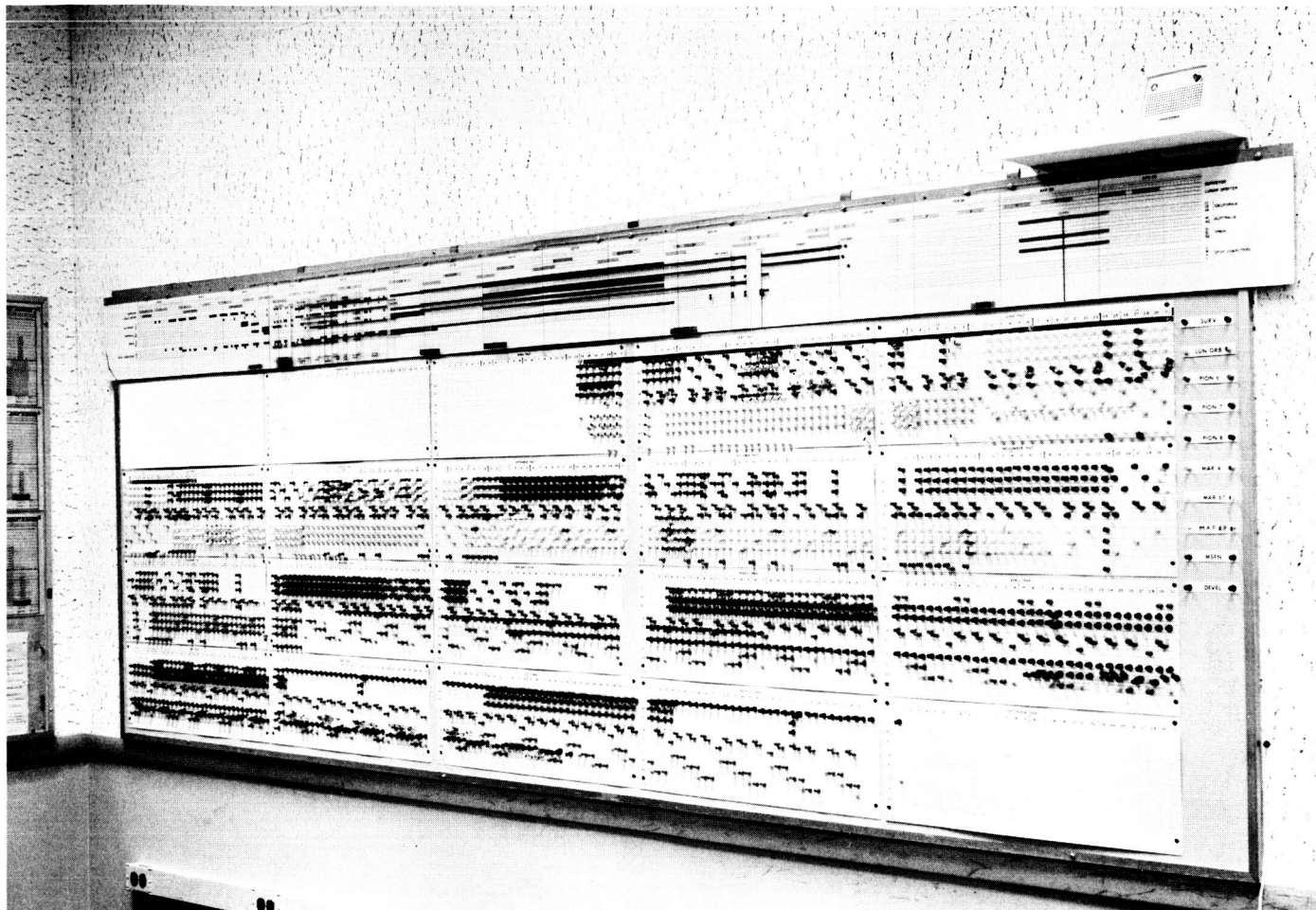


Fig. 18. DSN 16-month utilization forecast

is the 16-month loading schedule inputs further refined to a daily basis, where necessary, by the Project-scheduling personnel. When multiple pins appear in any given element-day, the conflict is obvious. Movement of pins allows flexibility in experimenting with variations of both

time and station selection, leading to possible solutions of the apparent conflicts. While this device has many applications, it has proven to be particularly useful to the Project-scheduling personnel in the preparation of their inputs to the DSN 16-month loading schedule.

N67-30376

3 Operations Programming 6

A. Computer Programming Technology, Part II,

W. Thomas

1. Introduction

A new algorithm for improved recovery of pulse code modulation (PCM) telemetry data was reported in SPS 37-44, Vol. III, pp. 129-131. Refinements to the algorithm are described here which represent a major reduction in the core storage and computational requirements of the program executing the algorithm.

The algorithm previously reported achieves coherency (lock) of phase-shift-keyed PCM telemetry data by using a known pattern within the data stream, which is intended for postdemodulation frame synchronization of the data. A two-dimensional matrix of demodulators (a 2×12 matrix as presented in the report) was used, the output of which was retained in a matrix of dimension $2 \times 12 \times 420$ (*Mariner IV* data Mode II, frame length in bits). This output matrix was then cross-correlated with the known pattern vector in order to determine which of

the demodulators was most nearly coherent with the telemetry data stream.

2. Simulation

The ability of this method to achieve lock depends on the statistics of the cross-correlation matrix C_L^a . The characteristics of such a matrix were investigated by means of a simulation program. In the computer runs, simulated *Mariner IV* data were generated with a signal-to-noise ratio of -13 db. All known bits were included in the data stream, and unknown bit values were assigned randomly. The effect of the number of known bits utilized in the pattern vector on the cross-correlation matrix is shown in Figs. 1-4.¹ As expected, the ratio of highest peak to next highest becomes larger as more known bits are included in the pattern vector (see Fig. 5). The ratio for 55 known bits is such that the dimensions of α may be reduced from 12 to 2, resulting in reduced storage and computational requirements.

$$^1 \frac{ST_a}{N/B} = \frac{\text{received energy/bit}}{\text{noise power/unit bandwidth}}, \text{ db.}$$

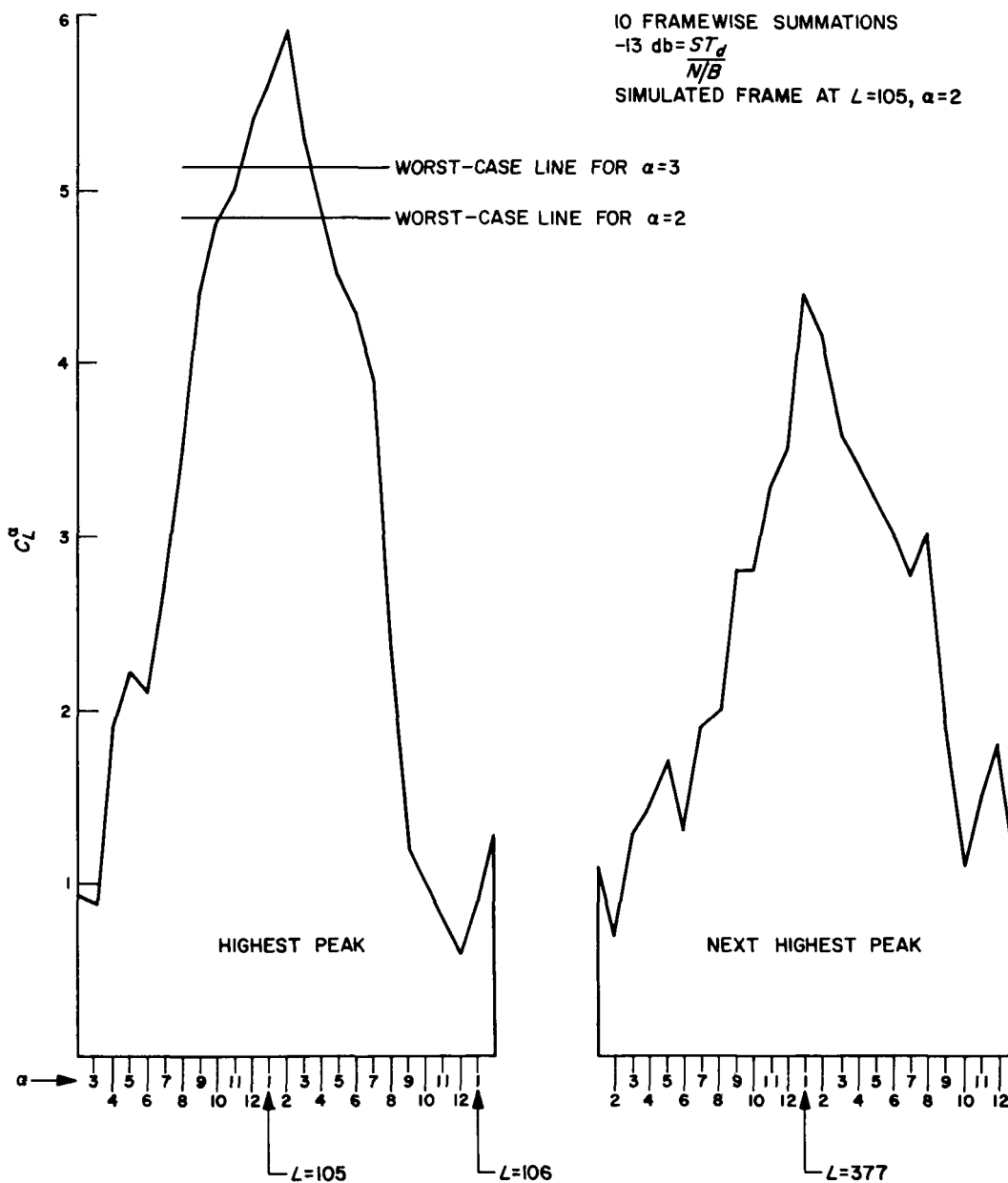


Fig. 1. Cross-correlation coefficient versus α and L for 21 known pattern bits

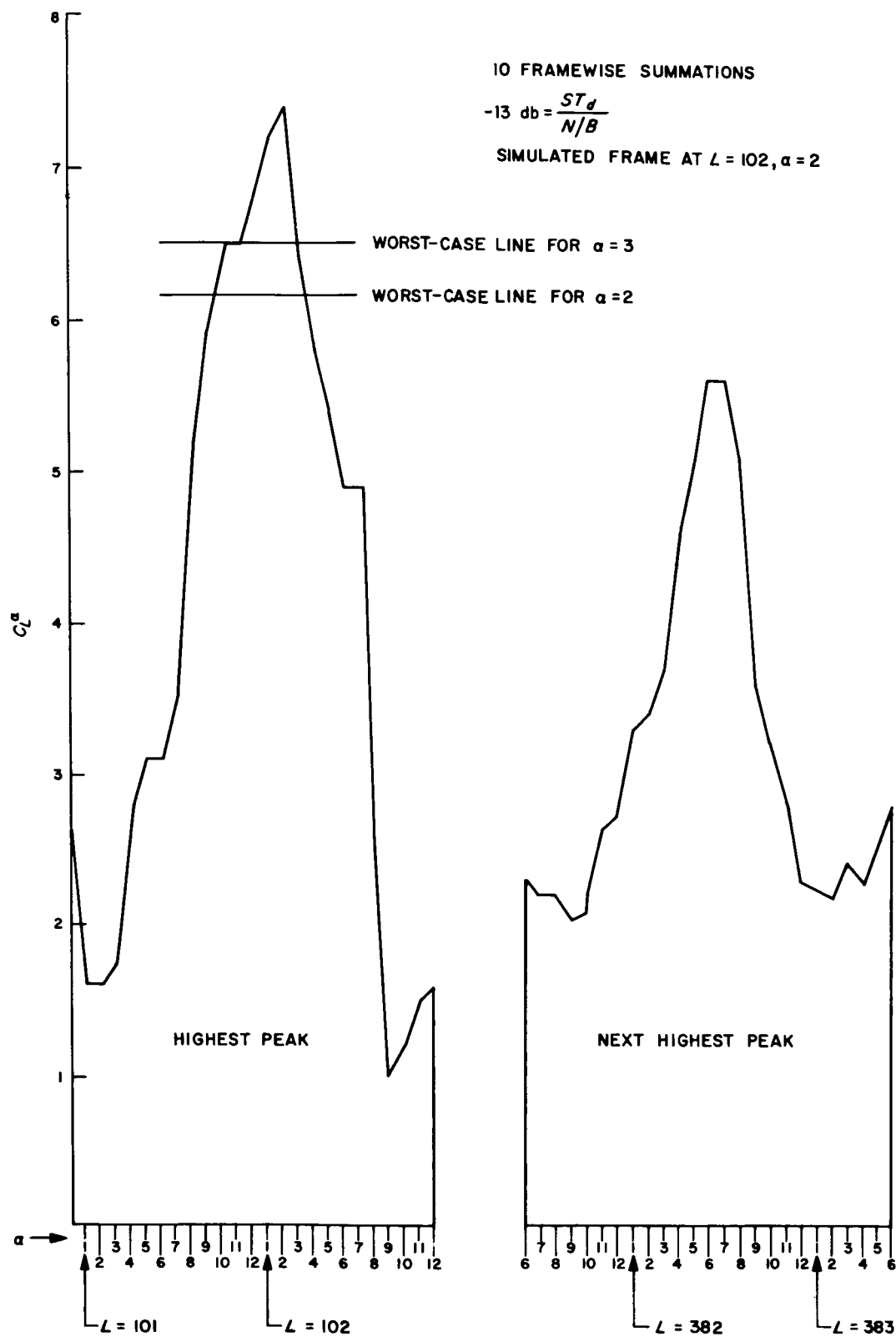


Fig. 2. Cross-correlation coefficient versus α and L for 30 known pattern bits

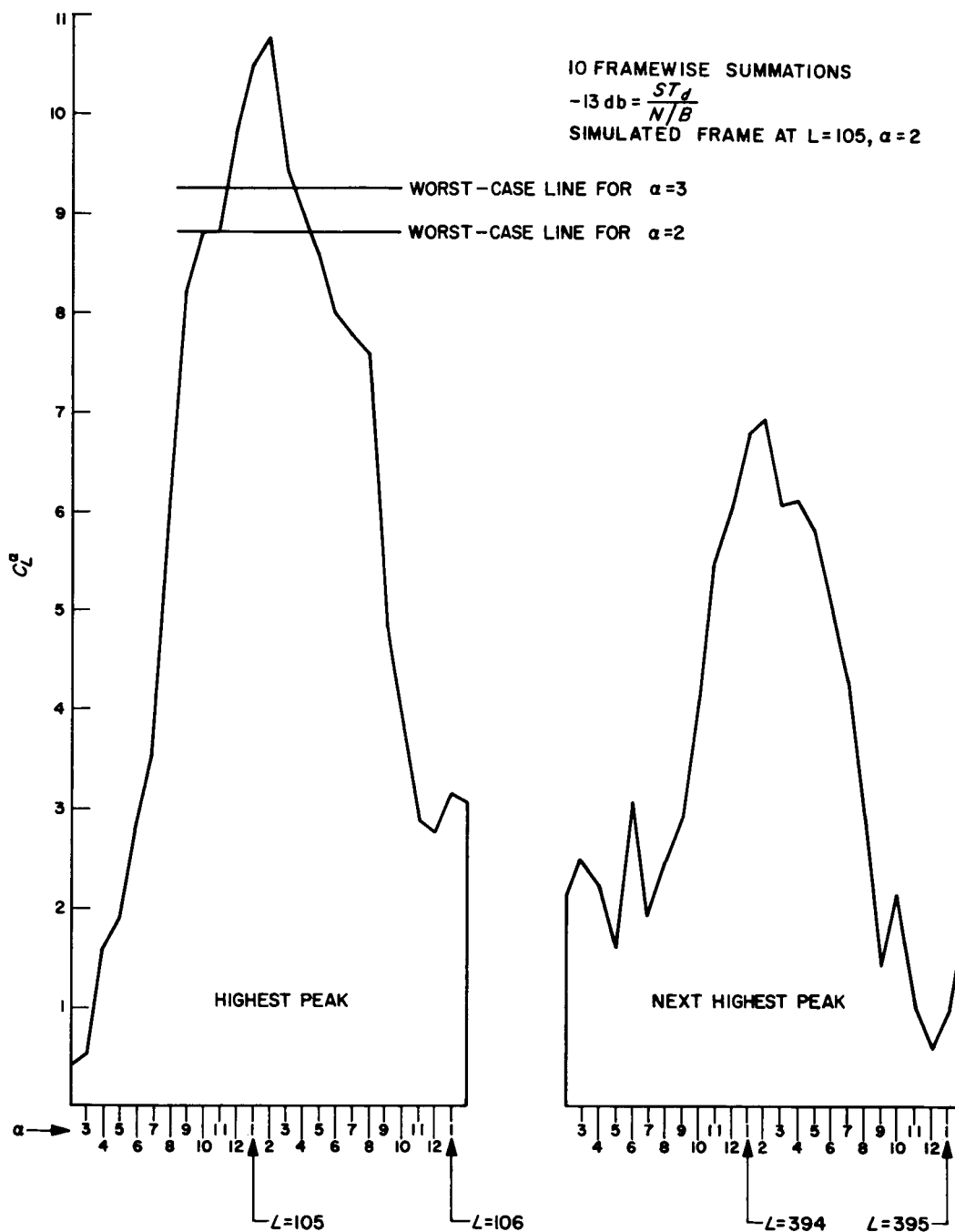


Fig. 3. Cross-correlation coefficient versus α and L for 55 known pattern bits

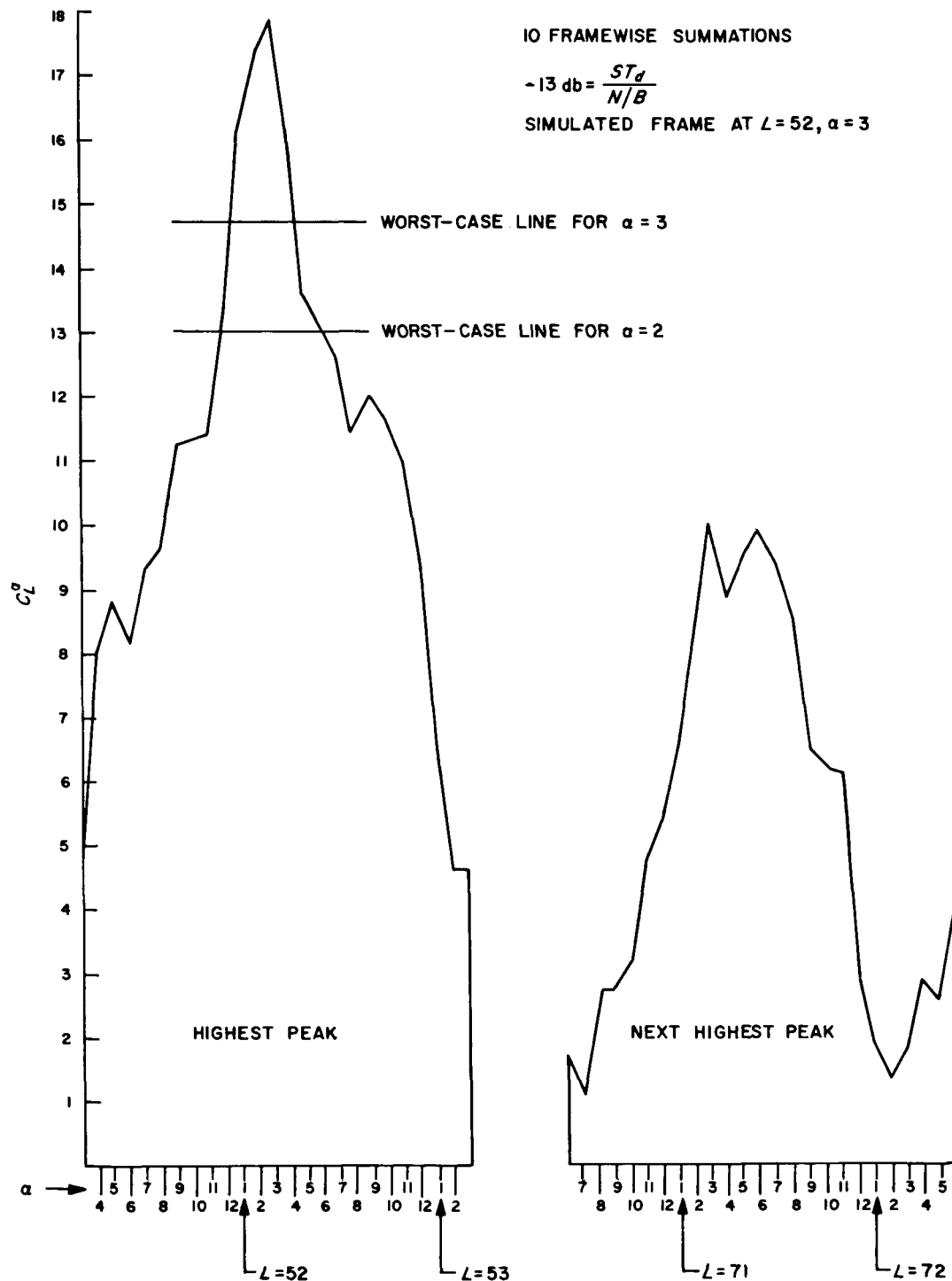


Fig. 4. Cross-correlation coefficient versus α and L for 99 known pattern bits

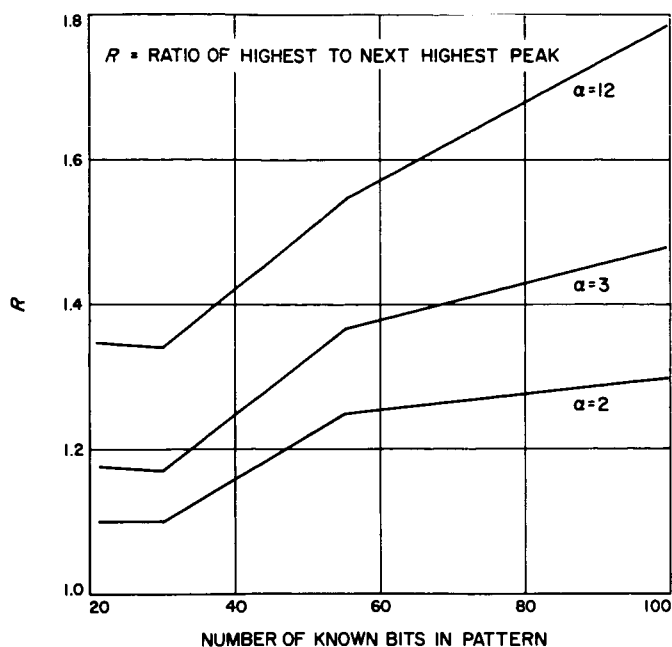


Fig. 5. R versus number of known bits in pattern

3. Acquisition

The reduced variation uses a matrix of demodulators of 2×2 dimension (see Fig. 6). The same procedure as reported previously is then used to determine which demodulator is most nearly coherent with the data stream. The above method is used only for acquisition; i.e., phase transitions are determined only to $\pm 1/4$ of a bit time. Further refinement of bit and frame position is accomplished by a coherency update procedure.

4. Coherency Update

Because only positions adjacent to the approximate frame location need be considered in coherency refinement, the acquisition procedure ($\alpha = 12$) is rewritten as follows to consider only three bit locations:

$$IH_{LL}^{\alpha, \phi} \leftarrow IH_{LL}^{\alpha, \phi} + Y_{L_i}^{\alpha, \phi} \cdot IP_i$$

where

$$i = 1, \dots, M$$

M = number of bits in a frame

$IH_{(1,2,3)}^{(1,\dots,12,1-2)}$ is initially zero

$$LL = 1 \text{ if } L - i + 1 = jM1$$

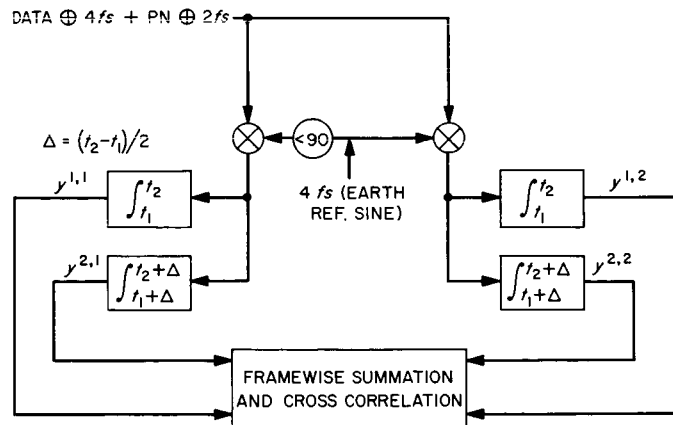


Fig. 6. Reduced demodulation matrix

$$LL = 2 \text{ if } L - i + 1 = jM$$

$$LL = 3 \text{ if } L - i + 1 = jM3$$

$$\begin{aligned} jM1 &= jM - 1 && \text{for } jM - 1 > 0 \\ &= M + jM - 1 && \text{for } jM - 1 \leq 0 \end{aligned}$$

$$= M + jM - 1 \quad \text{for } jM - 1 \leq 0$$

$$\begin{aligned} jM3 &= jM + 1 && \text{for } jM + 1 \leq M \\ &= jM + 1 - M && \text{for } jM + 1 > M \end{aligned}$$

$$= jM + 1 - M \quad \text{for } jM + 1 > M$$

jM defines approximate frame position as determined by the acquisition procedure

α is the index of variation for the limits of integration ($\alpha = 1, \dots, 12$)

ϕ is the index of variation for phase angles
($\phi = 1, 2$)

$$\begin{aligned} IP_i &= +1 \text{ if bit } i \text{ of the frame is a known one bit} \\ &= -1 \text{ if bit } i \text{ of the frame is a known zero bit} \\ &= 0 \text{ if bit } i \text{ of the frame is unknown} \end{aligned}$$

$$= -1 \text{ if bit } i \text{ of the frame is a known zero bit}$$

$= 0$ if bit i of the frame is unknown

After one or more frames have been processed,

$$C_j^\alpha = |IH_j^{\alpha,1}| + |IH_j^{\alpha,2}|$$

$$j = 1, 2, 3$$

$$j = 1, 2, 3$$

The maximum C_j^α determines which of the 12 pairs of demodulators is most nearly coherent. The α index of

this coefficient is defined as αM , and the j index is defined as jN . The variable jM is updated as follows:

$$jM \leftarrow jM - jN + 2 \text{ for } 0 < jM - jN + 2 < M + 1$$

$$jM \leftarrow jM - jN + 2 - M \text{ for } jM - jN + 2 > M$$

$$jM \leftarrow jM - jN + 2 + M \text{ for } jM - jN + 2 \leq 0$$

As before, bit decisions are determined as follows:

$$I3 = \text{SIGN}(MFX_1) \cdot Y^{\alpha m, 1} \cdot |MFX_1 / MFX_2| \\ + \text{SIGN}(MFX_2) \cdot Y^{\alpha m, 2}$$

where

$$MFX_1 = IH_{jn}^{\alpha m, 1}$$

$$MFX_2 = IH_{jn}^{\alpha m, 2}$$

Then, if $I3 \geq 0$, a one bit is detected; if $I3 < 0$, a zero bit is detected.